FACHBEREICH PHYSIK
BERGISCHE UNIVERSITÄT
GESAMTHOCHSCHULE WUPPERTAL

Johann M. Heuser

Construction, Operation and Application of the DELPHI Pixel Detector at LEP2

Dissertation zur Erlangung des Doktorgrades des Fachbereichs Naturwissenschaften I – Physik der Bergischen Universität-Gesamthochschule Wuppertal

WUB-DIS 99-1
Januar 1999

Kurzübersicht

Die vorliegende Arbeit diskutiert das Projekt des DELPHI Pixeldetektors, die erste Anwendung eines hybriden Silizium-Pixeldetektors in einem Collider-Experiment. Der Pixeldetektor ist Teil des "Very Forward Tracker", einer der neuen und erweiterten Detektorkomponenten des DELPHI Experiments zur optimierten Spurrekonstruktion bei LEP2, der Hochenergieperiode von CERN's "Large Electron Positron"-Collider mit angestrebten e^+e^-–Schwerpunktenergien von bis zu 200 GeV.
Der DELPHI Pixeldetektor wird in Pixeldetektor-Entwicklungen eingeordnet, die gegenwärtig bei CERN für die zukünftigen Experimente am "Large Hadron Collider" durchgeführt werden. Die physikalische Motivation für die Anwendung eines Pixeldetektors bei DELPHI wird dargestellt. Die Entwicklung und Konstruktion des Siliziumdetektors werden behandelt und Erfahrungen zusammengefaßt, die während der ersten drei Betriebsjahre gewonnen wurden. Die Leistungsfähigkeit des Pixeldetektors und sein Beitrag zur Spurrekonstruktion in den Endkappen des DELPHI Experiments werden charakterisiert und diskutiert.
Die Untersuchung der Produktion von W-Bosonen zählt zu den wichtigen physikalischen Forschungszielen bei LEP2. Der Very Forward Tracker wurde zur Identifizierung von Elektronen in den Endkappen des DELPHI Experiments eingesetzt, um semileptonische W-Boson-Ereignisse bei 183 GeV Schwerpunktenergie zu selektieren.

Abstract

This thesis discusses the DELPHI pixel detector project, the first application of a hybrid silicon pixel detector to a collider experiment. The detector is part of the Very Forward Tracker, one of the upgrades of the DELPHI experiment to optimize its track reconstruction at LEP2, the high energy period of CERN's Large Electron Positron collider aiming at e^+e^- collisions at 200 GeV center-of-mass energies.
The DELPHI pixel detector is classed among other pixel detector projects currently under development at CERN for future application with experiments at the Large Hadron Collider. The physics motivation for the application in DELPHI is discussed. Design and construction of the detector are described and experience gained during the first three years of operation presented. The performance of the pixel detector is summarized and its impact on the track reconstruction in DELPHI's end-caps is detailed.
The study of W boson production is one of the important physics tasks at LEP2. The Very Forward Tracker was applied to electron identification in DELPHI's end-caps to tag events with semi-leptonic W boson decays at 183 GeV center-of-mass energies.

Contents

1 Introduction **1**

2 Development of pixel detectors at CERN **5**

2.1 Objective and design aspects 5

2.2 RD19 pixel detectors 7

2.3 Pixel detectors for LHC experiments 11

2.4 The DELPHI pixel detector 15

3 Motivation for the DELPHI Pixel Detector at LEP2 **17**

3.1 The DELPHI Experiment at LEP 17

3.2 Main physics topics at LEP2 21

3.3 DELPHI detector upgrades for the operation at LEP2 27

4 The DELPHI Silicon Tracker **31**

4.1 The microstrip vertex detector 34

4.2 The Very Forward Tracker 36

4.2.1 Design Considerations 36

4.2.2 Ministrip Detectors 39

4.2.3 Pixel Detectors 41

5 Development and construction of the DELPHI pixel detector **43**

5.1 The front-end electronics 44

5.2 Sparse Data Scan Readout 54

5.3 Bonding technologies 58

5.4 The detector substrate 62

5.5 Module pre-production and test beam results . . . 65
5.5.1 Test of the electronics wafer . . . 65
5.5.2 Test of the detector wafer . . . 69
5.5.3 Test beam characterization of the first module . . . 69
5.6 Module production . . . 75
5.6.1 Module assembly . . . 75
5.6.2 Final functionality test . . . 83
5.6.3 Production yield and breakdown of errors . . . 85
5.7 Assembly of the detector layers . . . 89
5.8 Integration into the Silicon Tracker and installation into DELPHI . . . 91

6 Experience with the pixel detector operation 97
6.1 The power supply system . . . 97
6.2 The data acquisition system . . . 99
6.3 Detector control and data quality monitoring . . . 101
6.4 Operational status . . . 103
6.4.1 Detector configuration in 1996 . . . 103
6.4.2 Detector configuration in 1997/98 . . . 103
6.5 Threshold setting and detector noise . . . 107
6.6 Event size and protection against excess occupancy . . . 111
6.7 Protection against high radiation dose . . . 116

7 Performance of the pixel detector 119
7.1 Detector noise . . . 119
7.2 Alignment, detector stability and spatial resolution . . . 120
7.3 Contribution to the track reconstruction . . . 122

8 Electron identification in semi-leptonic W events 125
8.1 Production of W bosons at LEP2 energies . . . 125
8.2 Electron identification with the DELPHI detector . . . 127
8.3 Event selection from the data sample at $\sqrt{s} = 183$ GeV . . . 134
8.4 Assessment and further improvements . . . 139

9 Conclusions **143**

List of Figures **145**

List of Tables **149**

Bibliography **151**

Acknowledgements **161**

Chapter 1

Introduction

The DELPHI[1] experiment at CERN[2]'s Large Electron Positron Collider LEP is the first collider experiment at which hybrid silicon pixel detectors contribute to the track reconstruction. The pixel detector was built in the framework of detector upgrades, performed by the DELPHI collaboration when preparing its experiment for LEP2, the high energy period of LEP aiming at e^+e^- collisions at 200 GeV center-of-mass energies.

Pixel detectors are novel semiconductor tracking detectors. The term has been proposed with respect to electronic imaging, where "pixel = picture element" denotes the smallest unit of a digitized image [1]. Related to established silicon microstrip detectors [2, 3], linear arrays of diodes on high resistivity silicon substrates with usually less than 50 μm pitch, pixel detectors extend their high spatial resolution to two dimensions. They consist of two-dimensional arrays of detector elements with pitches of less than 1 mm, contain active signal processing electronics for every element and provide unambiguous space points of tracks of charged particles.

True two-dimensionally segmented silicon detectors are a supposition for tracking and vertexing applications in high occupancy environments as experiments at CERN's approved Large Hadron Collider project LHC or linear colliders in order to manage the ambiguity problem present with microstrip detector systems and their projective geometry. Future "micropattern" detectors have been considered as ideal imaging and tracking detectors for their high spatial resolution, short readout time and possible built-in pattern recognition facilities [4].
The development of such detectors requires new approaches and is possible since even fewer than ten years. Detectors with high spatial resolution in two dimensions imply a large number of small detector cells which can only be handled with appropriate low power and fast microelectronic readout circuits. The large number of necessary interconnections demands for reliable micromechanic techniques or alternative methods

[1]Detector with Lepton Photon and Hadron Identification

[2]Conseil Européen pour la Recherche Nucléaire, Geneva, Switzerland

developed with microelectronics processing. Special readout strategies have to be integrated into the detector to manage the data stream in an adequate time as required in high energy physics experiments. Radiation hardness is an important aspect both for detectors and electronics circuits to guarantee operational systems even in high luminosity conditions.

Considerable effort has been made both in Europe and the United States to develop pixel detectors for applications with the next generation of high energy physics experiments [5, 6, 7, 8]. Also present collider experiments can benefit from the outstanding track reconstruction capabilities of pixel detectors. The DELPHI experiment at LEP was equipped with a pixel detector system to enable efficient standalone pattern recognition and track reconstruction in its end-caps close to the interaction region. For the first time experience was gained with the construction of a large-scale pixel detector system for a collider experiment, its operation and application to physics measurements [9, 10].

The concept of the DELPHI pixel detector originates from developments of the Detector Research and Development Collaboration 19 at CERN [11]. Since 1990 this research group has worked on the development of hybrid and monolithic silicon micropattern detectors for vertex detector and tracking applications with experiments in high luminosity environments. Although a rather general approach open for potential application in future high luminosity experiments has been envisaged, first experimental and large scale detector systems have been provided for intermediate physics experiments at fixed targets and colliders.
RD19 has demonstrated with a step-by-step approach the feasibility of true two-dimensional semiconductor detector arrays for tracking applications. Several technological approaches have been studied over the years, using to a large extent latest resources and available technologies from microelectronics industries. Hybrid silicon pixel detectors with binary output turned out to be the most successful ones. A series of detector generations has been developed, improving the performance and complexity of the detector system with every generation.
One of the front-end electronics was ideally suited for the DELPHI pixel detector system where only moderate readout speed, no extremely reduced power consumption and no radiation hardness were required compared to the LHC environment. From the beginning of RD19 on a team also active in the DELPHI collaboration studied the possibility of adding pixel detectors to the DELPHI vertex detector. First concepts which were not realized foresaw to replace full modules and layers of the microstrip vertex detector with pixel detector assemblies.
Associated to RD19, the DELPHI pixel detector group adapted the pixel electronics to the DELPHI needs. A sparse data readout was added to match the low occupancy expected in DELPHI and the pixel geometry enlarged with respect to the moderate spatial resolution required. The macro-pixels allowed to study several “cheap” bonding technologies attractive to minimize considerably the costs of the project. The

development of a multi-chip detector module that could be produced with sufficient yield and installed into DELPHI's new Very Forward Tracker was one of the main efforts with the DELPHI pixel detector project.

This thesis discusses the steps of the DELPHI pixel detector project from the design and prototyping phase to its application to physics measurements. The first two chapters classify the DELPHI pixel detector among other pixel detector projects currently under development at CERN, introduce the DELPHI experiment and provide the physics motivation for the construction of the DELPHI pixel detector. Design aspects, first prototypes, the production, assembly and integration into the experiment are discussed then. Experience with the operation of this first large-scale pixel detector system and the performance yielded are presented. The application of the Very Forward Tracker to electron identification in semi-leptonic W boson events at LEP2 energies is the objective of the last chapter.

Chapter 2

Development of pixel detectors at CERN

The development of pixel detectors at CERN started at the end of the 1980s in a research group associated to the CERN-LAA project [12]. New structures in research projects on modern detector technologies at CERN for experiments at the coming generation of high luminosity colliders as well as the complexity of the objective led to a wider approach then.
The "Development of Hybrid and Monolithic Silicon Micropattern Detectors" was assigned to the Research and Development Collaboration 19, where universities and research institutes as well as industrial partners contributed in a complementary way to the development of two-dimensional semiconductor particle detectors.
With the concepts and technical designs of LHC experiments becoming more elaborate, separate activities on pixel detector development started in several of those collaborations.

2.1 Objective and design aspects

Pixel detector development at CERN aims ultimately at the construction of high performance, large area tracking detector systems for the innermost parts of LHC experiments. Such detectors will have to cover areas of up to several square meters, need to provide track points with spatial resolutions of the order of a few micrometers, will comprise about 10^8 pixels and will be installed in a difficult environment. Luminosities of up to the order of 10^{34} $cm^{-2}s^{-1}$ and bunch crossing intervals of 25 ns will lead to an enormous number of detector hits.
Figure 2.1 illustrates a scenario with the future ATLAS[1] detector at LHC. The event

[1] A Toroidal LHC ApparatuS

simulation shows a radial view of reconstructed tracks in the barrel inner detector and corresponding signals detected in the electromagnetic calorimeter for the process H(130 GeV) → ZZ' → 4e, overlaid by vast background. The enormous number of hits and tracks requires tracking detectors which provide unambiguous space points. The internal layers where the track density is maximal will consist of pixel detectors which are able to fulfill this task.

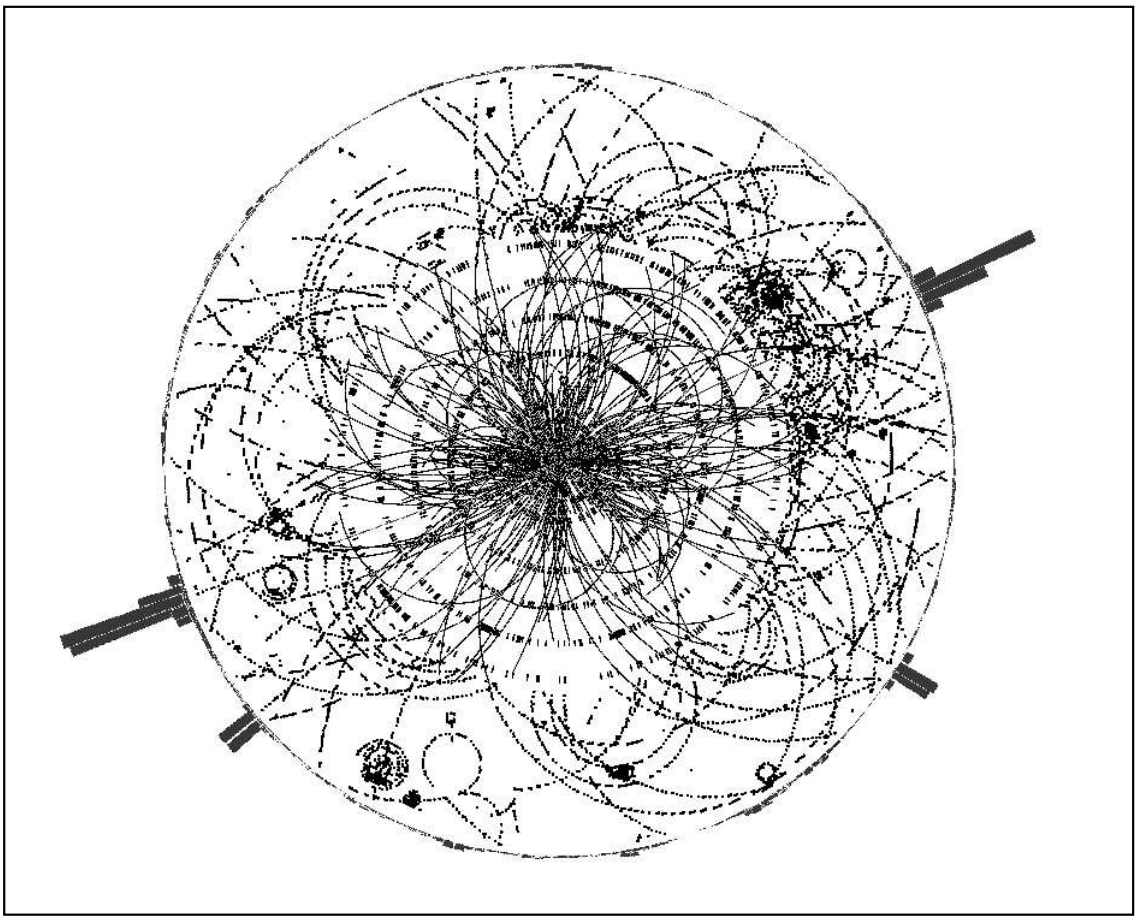

Figure 2.1: Event simulation for the ATLAS experiment at LHC. The graphics shows reconstructed tracks in the barrel inner detector and signals in the electromagnetic calorimeter (radial position not to scale) for the process H(130 GeV) → ZZ' → 4e at a luminosity of 5×10^{33} $cm^{-2}s^{-1}$ [13]. The inner detector has a diameter of 2.2 m.

A variety of often conflicting aspects has to merge into the design of large scale pixel detectors.
High particle detection efficiency very close to 100% is mandatory for efficient pattern recognition while at the same time little material has to be involved. Thin detectors and readout electronics and low-mass but stiff mechanical support are required. The signals in thin detectors, however, are small and sensitive low-noise electronics necessary for the detection.

With large numbers of readout channels there is a strong requirement for extremely low noise in the detector system. The levels of signals and noise have to be well separated therefore. Low noise can be achieved with small input capacitances to the electronics circuits, i.e. small detector cells. Also aspects of the readout electronics as time constants of signal shaping play an important role with respect to the noise.
High spatial resolution requires low cross talk to neighboring detector cells but also at the same time charge sharing in case of tracks crossing regions between adjacent cells.
Leakage currents which increase in the detector with time and under irradiation of the detector material have to be as small as possible to minimize noise. The dynamic range of the front-end electronics has to be large enough to cope with a certain increase. Radiation hardness of detectors and electronics are important aspects in high luminosity conditions.
Low power consumption is required for the electronics itself which contradicts fast circuits and precise timing. Already with a consumption of only a few tens of microwatts per pixel the heat dissipation of the entire detector systems will be significantly high.
Uniform behavior of the pixels is mandatory for operational detectors where several hundreds or thousands of modules with several thousands of pixels each are operated together.
Data selection and readout strategies which enable the handling of the large data stream have to be foreseen on detector level.

2.2 RD19 pixel detectors

RD19 has considered the development of front-end electronics as most important and challenging for the success of such large scale detectors. Consequent use of microelectronic processes for the design of pixel readout electronics enabled the development of a family of detector systems. Two basic design philosophies have been considered.

Monolithic pixel detectors contain detector and readout circuits integrated in a single device. Provided appropriate production technologies, this approach would minimize production steps, lead to high production yield and would finally reduce costs. The wafer processing, however, is difficult and not industrial standard. Reference [14] describes an approach where the wafer was processed from one side only. Double-sided processing of p-type substrates where n-doped wells shielded the detector volume from the electronics was studied as well and a fully functional demonstrator chip built [15]. Conflicting aspects of electronics implementation and properties of the charge collection volume are a principal weakness with this approach. A modified design in Silicon On Insulator technology avoids such interference. Detector material and electronics layer are still combined in a monolithic device but separated from each others by an insulating oxide layer [16].

Hybrid pixel detector systems provide the advantage that detector and electronics components can be optimized separately and provide freedom for custom specific needs. Figure 2.2 illustrates schematically that every hybrid pixel consists of a detector part which is connected to readout electronics covering the same area as the detector but located on a different chip. The connections are established by small solder balls ("bump bonds") or other conductive material deposited on contact pads on one of the components. In a "flip-chip" process detector and electronics are precisely aligned and the electric connections established. The large number of interconnections necessary for a detector module or even a full detector system demands for a very low failure rate, implying a well controlled mechanical setup. A variety of flip-chip processes is industrially available presently. Suitable techniques need to be carefully chosen to match the detector design and application [17].

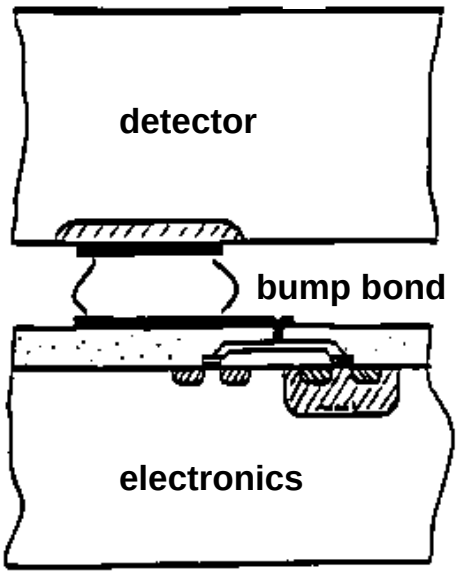

Figure 2.2: Principle of hybrid pixel detectors. Bump bonds establish the interconnections between detector and electronics chips [18].

The concept of the pixel detectors developed by RD19 is based on a hybrid approach and solder bump bond connections. The amount of integrated electronics has been kept to a minimum applying a binary readout. Provided low noise, the spatial resolution of binary pixel detectors[2] with small detector cells and staggered planes is comparable to systems with analog readout.
Every pixel is DC-connected to an amplifier followed by an adjustable discriminator circuit. The threshold can be set externally via control currents and defines the signal to be exceeded before it is stored in a 1-bit memory inside the pixel. Different readout strategies can be applied, depending on the requirements of the experiment. A shift

[2] pitch/$\sqrt{12}$ or better if two-pixel clusters are considered [11]

register readout is realized with the RD19 detector systems. After the memories have been reset and the chip has been activated by a gate signal for a certain period of time, the matrix is read row by row. A bitted word, representing the hit status of the pixels, is retrieved and sent to the data acquisition system.

detector generation	pixel size [μm^2]	bump $\oslash$ [μm]	pixels per chip	technology [μm]	electronics specification
1. LAA (1988)	200 × 200	30	9 × 12	SACMOS 3	current + voltage amplifier, discriminator, 1 bit memory
2. OMEGA-D (1991)	75 × 500	30	64 × 16	SACMOS 3	charge amplifier, discriminator, leakage current compensation, shift register output, tunable delay
OMEGA2 (1993)	75 × 500	30	64 × 16	SACMOS 3	+ improved uniformity
3. LHC1 (1995)	50 × 500	10	128 × 16	SACMOS 1	+ adjustable delays, facilities to test/mask individual pixels
4. LHC2 (1997)	30 × 590	10	128 × 2 test chip	MIETEC 0.5	+ radiation hardness

Table 2.1: RD19 pixel detectors.

Table 2.1 summarizes important characteristics of RD19 pixel detector electronics as overviewed in reference [19].
A first prototype chip ("LAA") focused on the demonstration of the concept of binary pixel detectors [20]. The feasibility of a particular production technology[3] was verified, chosen for the especially dense design. Single-chip assemblies were produced. Every pixel of 200 × 200 μm^2 area in the 9 × 12 array contained a combination of two preamplifiers, a discriminator, a memory as well as a pad for bump bonding the small matrix to a matching detector array. Threshold uniformity and noise were measured for the first time with a binary pixel detector. Electrical test pulses which simulated particle

[3]SACMOS, a CMOS process from FASELEC/PHILIPS

induced signals were applied to dedicated test pixels across the readout chip. Absolute calibrations of thresholds, signal heights and noise were obtained from integrated γ-spectra, measured with radioactive sources on top of the 300 μm thick detector. This laboratory procedure proved to be very successful to characterize the detectors, even though it was time consuming due to lack of a trigger signal and subsequent random readout. This procedure was applied also to the later developments [21, 22, 77].
The LAA pixel detector was fully functional. The electronics behaved according to the design expectations, the detector was efficient and the bump bond connections reliable. Noise of about 500 e^- r.m.s. at signals of 2×10^4 e^- for minimum ionizing particles was measured.

Based on these results the second generation of pixel detectors ("OMEGA") was built in the same technology. The electronics contained a different amplifier providing lower noise and a circuit for detector leakage current compensation was added. Aspects for applications in larger systems were taken into account with a shift register output and a tunable delay matching a trigger timing.
The OMEGA-D chip [23] comprises an array of 64×16 pixels. A rectangular pixel geometry with a small edge of 75 μm allows for high spatial resolution if two crossed detector planes are applied. The pixel detector was extensively tested in laboratory [24], followed by test beam characterizations and a first application in the tracking system of experiment WA94 at the OMEGA spectrometer at CERN [25, 26]. An improved version of this chip, OMEGA2 [27], was designed for better uniformity in the array and application in larger assemblies. The detector yields noise of (170 ± 25) e^- and efficiencies of more than 99.9% at thresholds below 10 ke^-. Spatial resolutions of 24 μm and 6 μm were obtained with tracks passing through single and double pixel clusters, respectively. At thresholds of 6000 e^- uniformities corresponding to 800 e^- have been measured across the chips.
Based on the comprehensive experience with the OMEGA design and the application of the devices, larger detector arrays for realistic tracking applications were set up subsequently [28]. Planar arrays of 12 modules each containing 6 readout chips were built forming active areas of about 5×5 cm^2. Design, first operation and experience with the performance in the silicon telescope of experiment WA97, the successor of WA94, have been reported in references [29] and [30]. The plane comprised about 72 000 pixels. 10% of the area were inoperative, mostly because of entire chips not working. After final adjustment of timing and control signals and masking of about 1% always noisy pixels, a fraction of less than 10^{-8} spurious hits was achieved. The important conclusion from the construction and operation of this pixel detector was that careful design and understanding of the multi-parameter detector enabled to yield a successful device. Emphasis was placed especially on the characterization of all components prior to the final assembly. With the noise rate achieved, envisaged pixel detector systems of 10^8 elements have been demonstrated to be reachable.

Further telescopes successively involved several detector planes [31, 32, 33]. A 500 000 channel telescope with planes of OMEGA pixel detectors was installed 1995/96 in the heavy-ion fixed target experiment WA97 [34]. The pixel detector telescope was placed in 0.4 m distance from the target and was not embedded in a magnetic field. Figure 2.3 provides a perspective event display of the setup [35]. In an environment comparable to the track occupancy in an LHC experiment, the detector contributed essentially to the track reconstruction. For the first time hybrid pixel detectors have been involved in physics measurements there.

Recent RD19 pixel detector designs aim at performance items with respect to the LHC environment. The LHC1 [36] detector generation has been built in a 1 μm process. In even smaller pixels than with the OMEGA design, more electronics has been integrated to allow for threshold adjustment, masking and testing of individual pixels, improving vastly the uniformity of the detector arrays. The small pixel size demands for the smallest bump bonds available [37]. In 1997 a telescope comprising 600 000 pixels has been commissioned for the CERN experiment NA57. A telescope of total 1.1×10^6 pixels will be operational there.
In a further step, radiation hardness has been added to the electronics. The LHC2 design is foreseen to be used in the ALICE[4] experiment at LHC. A first circuit implementation in 0.5 μm technology tolerated up to about 1 Mrad of radiation. Chips designed in 0.25 μm technology remained functional up to an x-ray dose of 30 Mrad [38]. With the end of the RD19 project in December 1997, this work continues in collaboration with the ALICE experiment and the RD49 project[5].

2.3 Pixel detectors for LHC experiments

ALICE The ALICE experiment [39] has been proposed as a dedicated heavy-ion experiment to study nuclear collisions at LHC. Track finding in the environment of heavy-ion collisions has been considered as the most challenging aspect for the detector. Three-dimensional hit information with many track points in a weak magnetic field are necessary for a successful pattern recognition.
The inner tracking system of ALICE will be built from silicon detectors on a total area of 6.6 m^2. Next to silicon drift detectors and microstrips the use of pixel detectors is foreseen. The pixel detectors will build the first two out of six layers at radii of 3.9 and 7.6 cm from the beam and will cover an area of 0.23 m^2.
The design of the ALICE pixel detector is based on the latest radiation tolerant chip version of RD19 and the positive experience with the pixel detector telescope in the recent heavy-ion experiments WA97 and NA57. A possible scheme foresees a pixel size

[4] A Large Ion Collider Experiment at the LHC

[5] RD49 collaboration: radiation tolerant techniques and strategies of electronics systems for the LHC experiments

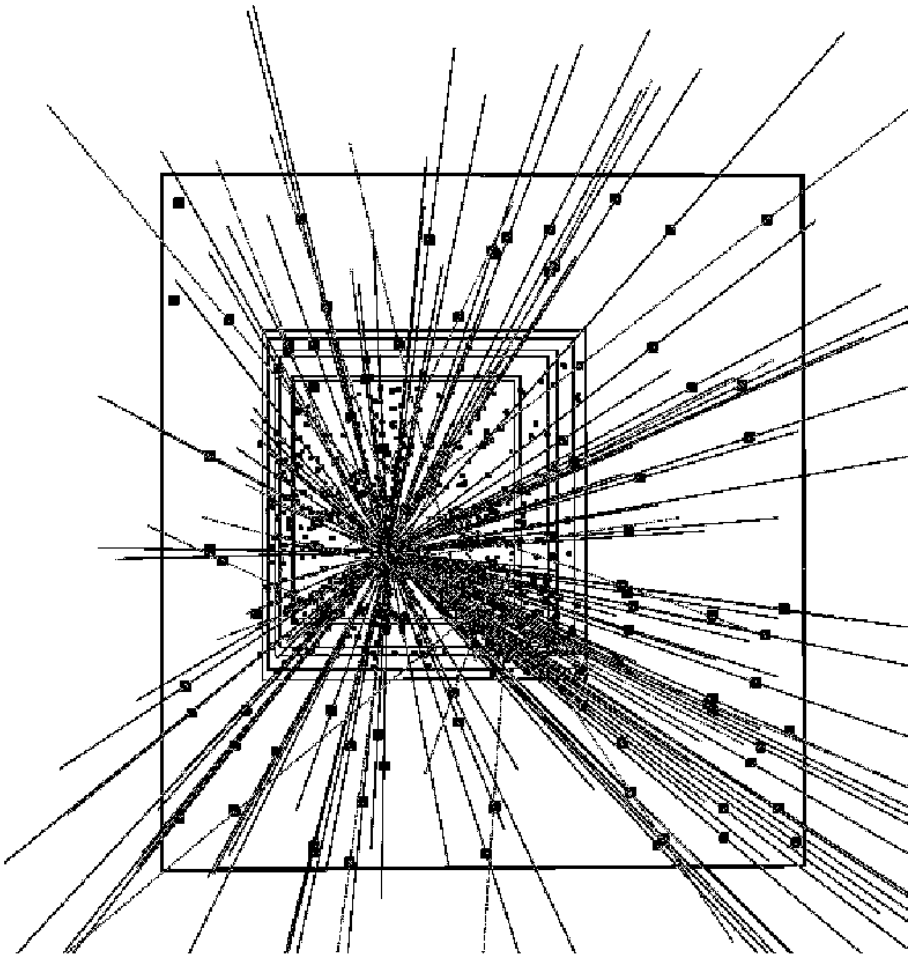

Figure 2.3: A high multiplicity event with 153 tracks recorded with the pixel detector telescope in the CERN's fixed target experiment WA97. Seven planar detector layers of 5×5 cm^2 active area each are staggered to form the telescope. The average occupancy of 30 hits per plane is comparable to the ones expected in LHC experiments.

of 50×300 μm^2, yielding 15 and 90 μm spatial resolution and two-track resolution of 100 and 600 μm. The basic unit of the pixel detector is a ladder of 80×13 mm^2 size, bump bonded to 16 readout chips. A thin multi-layer bus is glued to the rear side of the detector to allow wire bond connections to the chips. A total number of 220 ladders with 1.4×10^7 pixels is foreseen. With occupancies of up to 10^{-2}, the readout could be performed in less than 200 μs at 5 MHz clock. The power dissipation will amount to 500 watts.

ATLAS The general purpose proton-proton experiment ATLAS at LHC will use hybrid binary pixel detectors in its inner tracking detector [45]. The collaboration developed own designs and approaches concerning front-end electronics, readout architecture and module structures. The project status has been published in detail recently [46]. Different front-end and readout architectures as well as module technologies are still under investigation.
Excellent pattern recognition in the high multiplicity environment, high transverse impact parameter resolution and three-dimensional vertex reconstruction capability as well as b-tagging and triggering are the essential performance requirements for the pixel system. Simulation studies yielded that three pixel hits per track with good efficiency are needed in the entire acceptance range.
The ATLAS pixel detector will consist of three barrel layers and five forward and backward disks. The barrel layers will be organized in ladders and the disks in sectors of modules. All modules are nearly identical. The building blocks will contain 16 chips. The barrel pixel detectors are arranged in three cylindrical layers at radii from 4.3 to 13.2 cm. The modules are nearly 80 cm long. The internal layer ("B-layer") is placed as close as possible to the beam axis to provide optimal impact parameter resolution. Radiation hardness is a key item for the detectors there. The exchange of the B-layer has to be planned already in the detector design and is projected after about four years of operation. The layers at larger radii are considered to survive ten years.
The pixel disks in the end-caps surround the beam axis at z-positions between 0.5 and 1.0 m and carry modules from 12 to 19 cm radius.
The ATLAS pixel detector will comprise 1.4×10^8 pixels of 50×300 μm^2 size on about 2.200 detector modules and will cover a total area of 2.2 m^2.

CMS The CMS[6] experiment [47] at LHC has been designed to detect cleanly diverse signatures from new physics in high luminosity proton-antiproton collisions over a large energy range. It will use two layers of pixel detectors for the barrel part and two layers for the end-caps of its central tracking detector [48]. The high granularity tracking system has been extensively simulated and pixel detectors have been found to offer advantages in pattern recognition and track finding over alternative designs.
CMS decided to use pixel detectors with analog signal output for enhanced spatial resolution by signal interpolation. A resolution of 11 μm has been required. Squared pixels of 125×125 μm^2 size are the basic detector elements.
The barrel layers will be located at radii of 4.1, 7.0 and 11.7 cm. During LHC's low luminosity operation, the two inner layers will be installed and operated. The innermost layer will be removed then and the third layer installed for the high luminosity period.
The basic detector unit covers 1.6×6.4 cm^2 with 16 bump-bonded readout chips. Several units are grouped to modules of 65 cm length. The disks in the end-cap region

[6] Compact Muon Solenoid

shall cover the radial region from 6 to 15 cm and will be positioned at distances of 32 and 46 cm from the interaction region. The entire detector will comprise 4.5×10^7 pixels on 1 m^2 area.

FELIX FELIX[7] is a full acceptance detector for the Large Hadron Collider presently under study. It focuses on comprehensive and broad-range observation of strong-interaction processes at LHC energies [40, 41].
About 50 tracking detector systems ("stations") are foreseen to ensure full tracking acceptance and uniform resolution. Great attention has been payed to occupancy considerations with the tracking detectors, since high particle densities close to the beam impose significant pattern recognition problems. Each station should therefore be able to reconstruct track segments locally. The conceptual design for most of the tracking stations foresees pixel detectors out to radii of about 8 cm, supplemented by other tracking devices at larger radii.
It is supposed to use pixel readout chips originating from RD19 developments. The geometry of the modules and the operational conditions will be adapted to the specific situation. Arrays of 5 ladders of the design applied to WA97 are foreseen. It is foreseen to arrange 12 arrays in a module which are mounted on ceramic substrates. MCM-D[8] techniques might be considered to integrate bus and supply lines into the detectors and minimize the number of external connections.
A sensitive thickness of 120 μm silicon is sufficient for the required signal-over-noise performance. An overall module thickness of 770 μm silicon equivalent is assumed for the final layout. A full module will cover 250 cm^2, comprise 1.8 million pixels and dissipate about 90 watts.

LHCb The LHCb[9] experiment [42] will perform precision measurements on CP-violation and rare decays. It intends to use pixel detectors for photon detection in its ring imaging Cherenkov detector. Two photo-detector planes will cover an area of almost 3 m^2 where single photons with highest possible efficiency and a spatial resolution of 2.5 mm have to be detected. Wavelengths in the visible and ultraviolet range have to be covered. The photo-detectors must operate fast enough to match the 25 ns bunch crossings at LHC. With about 340 000 detector channels, the noise has to be low. Radiation hardness of the device is an important aspect (the expected dose is up to a few krad per year) and the device has to work in magnetic fields of up to 100 Gauss. Multi-anode photo-multipliers and hybrid photo-diodes are considered as detector candidates to meet these requirements.
In association to RD19, a pixel based photon detection tube has been developed already in the LAA project [43]. The hybrid photo-diode is based on the technology

[7]Forward ELastic and Inelastic EXperiment at the LHC
[8]Deposited Multi-Chip-Module on high resistivity wafers
[9]Large Hadron Collider beauty experiment

of standard image-intensifier tube geometries. Photo-electrons are focused onto a segmented silicon pixel array which is bump-bonded to a readout chip. The pixel detector structure is placed in the tube's vacuum. It needs to stand the bake-out cycles which are required during the production of the photo tubes.
No extreme spatial resolution but high photon detection efficiency is required with this application. Objective of current developments is to rise the sensitivity of the pixel detector for low energetic electrons, to improve the necessary threshold uniformity in the pixel array and to enlarge at the same time the pixel size to 2×2 mm^2 [44].

2.4 The DELPHI pixel detector

DELPHI is the only LEP experiment that has participated in the development of pixel detectors and has applied this new technology in the pre-LHC era. The basic design of the DELPHI pixel detector originates from RD19's OMEGA-D electronics. A detector with 1.2×10^6 pixels on 152 modules comprising 16 readout chips each has been developed and constructed. The pixel size of 330×330 μm^2, the readout strategy and the module structure are specially adapted to the DELPHI requirements. The detector covers an area of 0.15 m^2.
The luminosities at LEP are significantly lower (at least two orders of magnitude) than with the future hadron collider. The motivation for the decision to apply a pixel detector to DELPHI is the topic of the next chapter.

Chapter 3

Motivation for a Pixel Detector in the DELPHI Experiment at LEP2

3.1 The DELPHI Experiment at LEP

DELPHI is one of the four large experiments for e^+e^- physics studies at LEP, operated by an international collaboration of research institutes and universities [49, 50, 51].

The Large Electron Positron collider is CERN's largest accelerator, installed about 100 m below ground in a 26.7 km long and almost circular tunnel of 3.8 m diameter [52]. Beams of electrons and positrons circulate slightly separated from each others in opposite direction in LEP's vacuum chamber. They are kept in orbit by several thousands of magnets. Radio frequency cavities correct for energy loss by synchrotron radiation. Four of eight possible intersection points are equipped with experiments. Fig. 3.1 overviews CERN's accelerator systems with the LEP collider.

The LEP storage ring is the last accelerator in a chain of five. Electrons and positrons are generated by an electron gun and a positron converter. The LEP Pre-Injector (LPI) consists of two linacs (LIL) which accelerate the particles to 200 and 600 MeV before they are stored in the Electron Positron Accumulator (EPA). The Proton Synchrotron (PS) is used as a 3.5 GeV e^+e^- synchrotron. Further acceleration is performed by the Super Proton Synchrotron (SPS) which operates as a 20 GeV injector for LEP. LEP itself is equipped with cavities to accelerate the bunches of electrons and positrons to their final energy. During the LEP1 period (1989-1995) copper cavities allowed to operate at center-of-mass energies of around 91 GeV (Z boson physics). Further (super conducting) cavities subsequently installed since then [54] allow to access higher energies during the LEP2 period (W boson physics). LEP operates at 189 GeV center-of-mass energy currently. The aim is to reach 200 GeV before the year 2000 and deliver an integrated luminosity of about 500 pb^{-1} per experiment [55], with instant luminosities of the order of 10^{31} $cm^{-2}s^{-1}$.

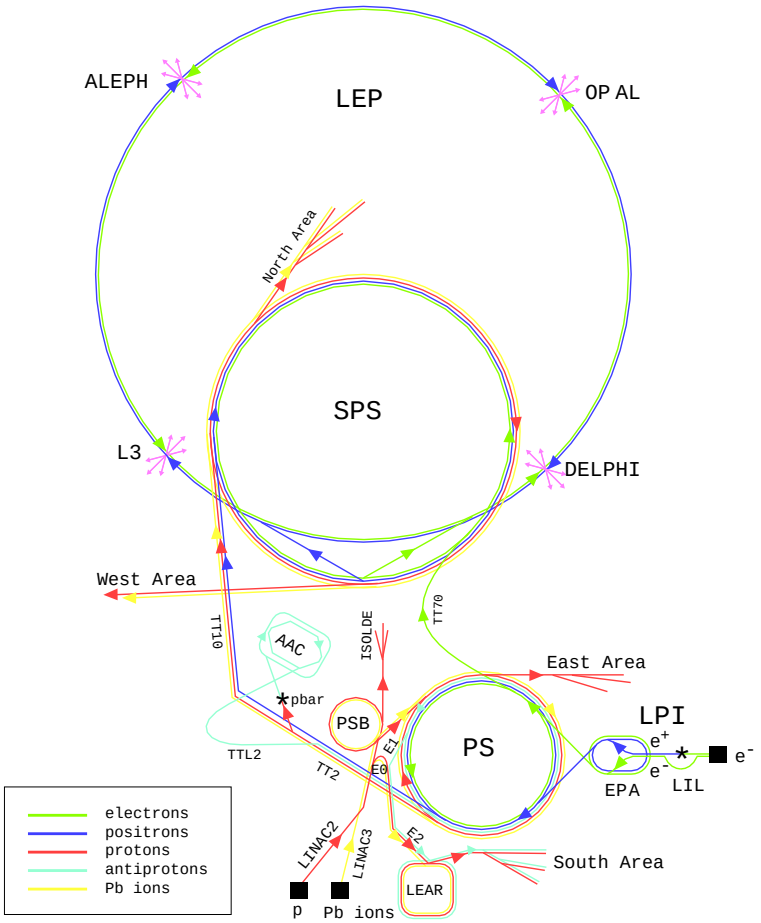

Figure 3.1: The LEP Collider and CERN's accelerator complex [53].

DELPHI's name insinuates the main design concept: the detector components are highly granular and allow for a high quality particle identification in almost the entire solid angle, supposition for precision measurements to test the Standard Model.
DELPHI is structured into a barrel-like central part of about 10 m diameter where concentrical layers of sub detector systems surround symmetrically the LEP beam pipe with the interaction region in its center, and matching end caps which close the barrel region almost completely on both sides (see fig. 3.2). The end-caps can be moved and DELPHI opened for maintenance purpose with access to all detector components.
The cylinder symmetry of the experiment suggests to use polar coordinates for the description of its geometry. Per definition, the z axis points along the direction of the electron beam, the x axis towards the center of LEP and the y axis points upwards. With the origin of this coordinate system located in the center of DELPHI, space points are preferably described by their polar angles θ to the z axis, azimuthal angles ϕ around the z axis and the radial coordinate $r = \sqrt{x^2 + y^2}$.

DELPHI operates since the startup of LEP in 1989. During the LEP1 period emphasis was put on high statistics precision measurements at the Z resonance, requiring

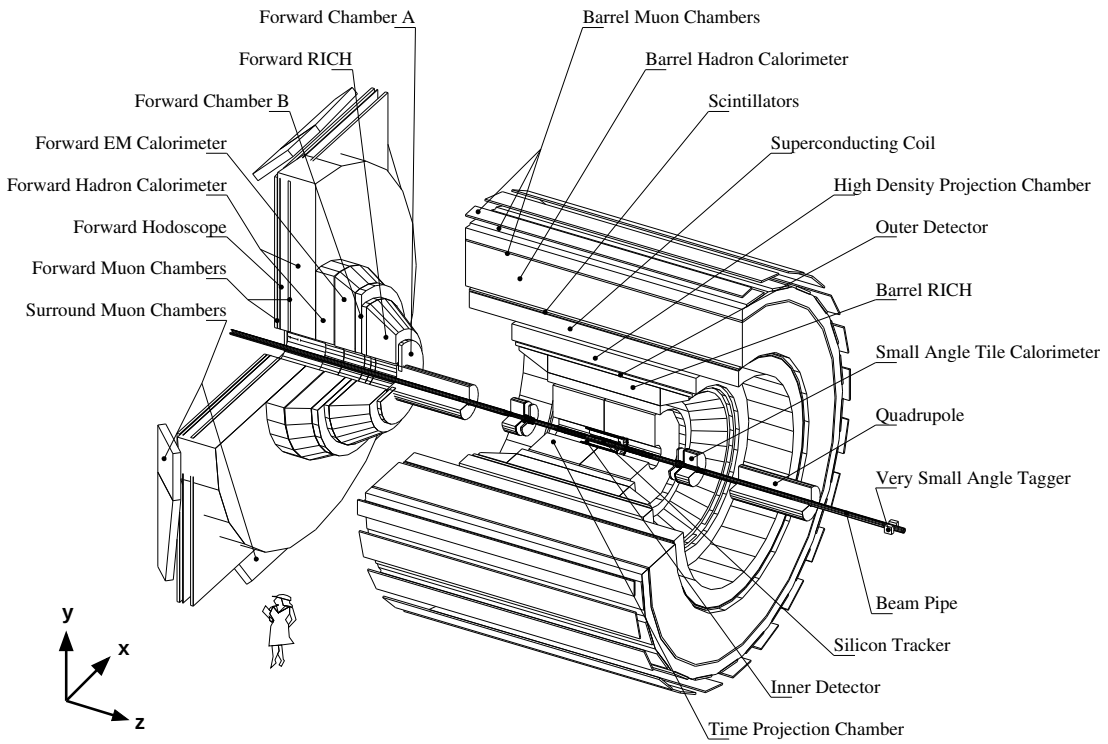

Figure 3.2: Layout of the DELPHI Detector [51].

accurate alignment and calibration of the detector components as well as precise track reconstruction in the central part. At LEP2 the study of W boson production and the search for new particles are the main issues and demand especially for detector hermeticity and overall high efficiency.

The DELPHI detector systems allow for event reconstruction according to the following aspects:

- measurements of decays and life times of short-lived particles with a silicon microstrip vertex detector close to the interaction region
- track reconstruction of charged particles in the central and end-cap ("forward") region in a 1.2 Tesla solenoidal magnetic field
- identification of charged hadrons with a system of ring imaging Cherenkov detectors in the central and end-cap regions
- calorimetry for particles with electromagnetic and hadronic interaction in detectors of high granularity
- beam luminosity measurements from small angle bhabha scattering
- muon detection with track chambers outside the magnetic field

DELPHI's system of independent tracking detectors for charged particles is embedded in a highly uniform magnetic field of 1.2 Tesla parallel to the beam axis, provided by a super-conducting solenoid.
In the central region, it consists of the Vertex Detector (VD, built from silicon microstrips), the Inner Detector (ID, a jet chamber), the Time Projection Chamber (TPC) and the Outer Detector (built from drift tubes). In the end-cap region, the wire chamber detectors Forward Chambers A and B (FCA, FCB) and the Very Forward Tracker (VFT), a new silicon detector attached to the Vertex Detector forming the Silicon Tracker, are the tracking devices.
Several components overlap from the central into the end-cap region and ensure continuous coverage and redundancy.

DELPHI comprises two independent systems of Ring Imaging Cherenkov detectors aiming at hadron identification from Cherenkov photon angle reconstruction. Both in the central detector part (Barrel RICH) and the end-caps (Forward RICH) liquid and gas radiators cover a large momentum range.

A system of calorimeters enables to detect particles with hadronic and electromagnetic interaction and to measure the beam luminosity close to the experiment. The Hadron Calorimeter is the most massive detector component of DELPHI. It is integrated into the iron of the magnet's yoke where layers of gas detectors sample showers originating from penetrating particles with hadronic interaction.
The High Density Projection Chamber is the central electromagnetic calorimeter. It applies the time projection principle to calorimetry in order to achieve a highly granular three-dimensional measurement of electromagnetic showers with a minimum number of electronic readout channels.
The Forward Electromagnetic Calorimeter (EMF) in the end-caps of DELPHI is built from arrays of lead glass blocks which enable to detect charged particles from their Cherenkov radiation and to measure the deposited shower energies.

The Small Angle Tile Calorimeter (STIC) is a sampling lead-scintillator calorimeter in both end-caps of DELPHI, used for beam luminosity measurements and photon detection close to the incoming beams. The Very Small Angle Tagger provides online measurements on the relative luminosity and beam background information which is sent from the DELPHI experiment to the LEP control room.

Three independent detector systems for muon identification form the external layers of DELPHI. The iron of the Hadron Calorimeter provides a filter to distinguish between hadrons and muons. Hadrons are absorbed in the iron core but muons with momenta larger than 2 GeV/c pass through and are detected in the muon chambers.
The central detector part is covered by the Barrel Muon Chambers. The Forward Muon Chambers are installed in each of the two end-caps. The intermediate region between Barrel and Forward Muon Chambers is covered by the Surround Muon Chambers.

3.2 Main physics topics at LEP2

The high energy period of LEP started in 1995 with center-of-mass energies of 130 and 136 GeV. It enables to complement the knowledge on the Standard Model parameters obtained from Z boson measurements at LEP1. The important aspects of LEP2 physics as well as theoretical and analytical background have been elaborated during a series of workshops at CERN in 1995 and summarized in its final report [56]. A brief overview shall be given here, mentioning main topics and leading to the motivations for the detector upgrade projects of DELPHI during its preparation for LEP2.

The total cross section at LEP2 is typically of the order 1/100 with respect to the one at the Z peak. The DELPHI detector has to be as efficient as possible therefore to yield a sufficiently large statistics of events. Figures 3.3 and 3.4 compare the total cross section from $e^+e^- \rightarrow Z/\gamma \rightarrow q\bar{q}$ to cross sections of several Standard Model processes as a function of the center-of-mass energy.

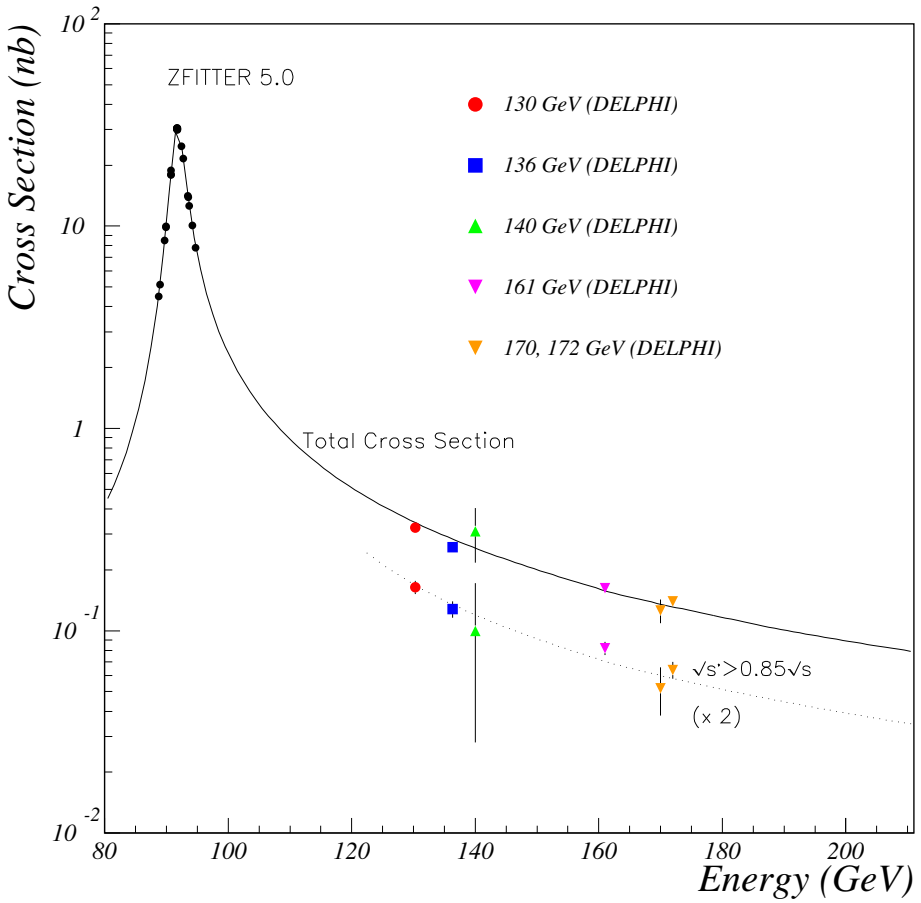

Figure 3.3: Total hadronic cross section from LEP1 to LEP2 energies [57].

Two photon physics $e^+e^- \rightarrow e^+e^-X$, with $\gamma\gamma \rightarrow X$, is the dominant process at LEP2. The tagging of one of the outgoing electrons enables to probe the photon in deep-inelastic scattering experiments to study QCD items.
Two fermion processes yield the largest cross sections; the production of quark pairs even exceeds the W boson pair production. With increasing center-of-mass energies $\sqrt{s}$ above the Z peak, initial state radiation has to be considered where the incoming electron or positron radiates an energetic photon before the annihilation occurs. This effect leads to enlarged cross sections at reduced effective interaction energy $\sqrt{s'}$. The measurement of two fermion processes enables to extend the study of Standard Model parameters continuously from LEP1 to LEP2 energies.

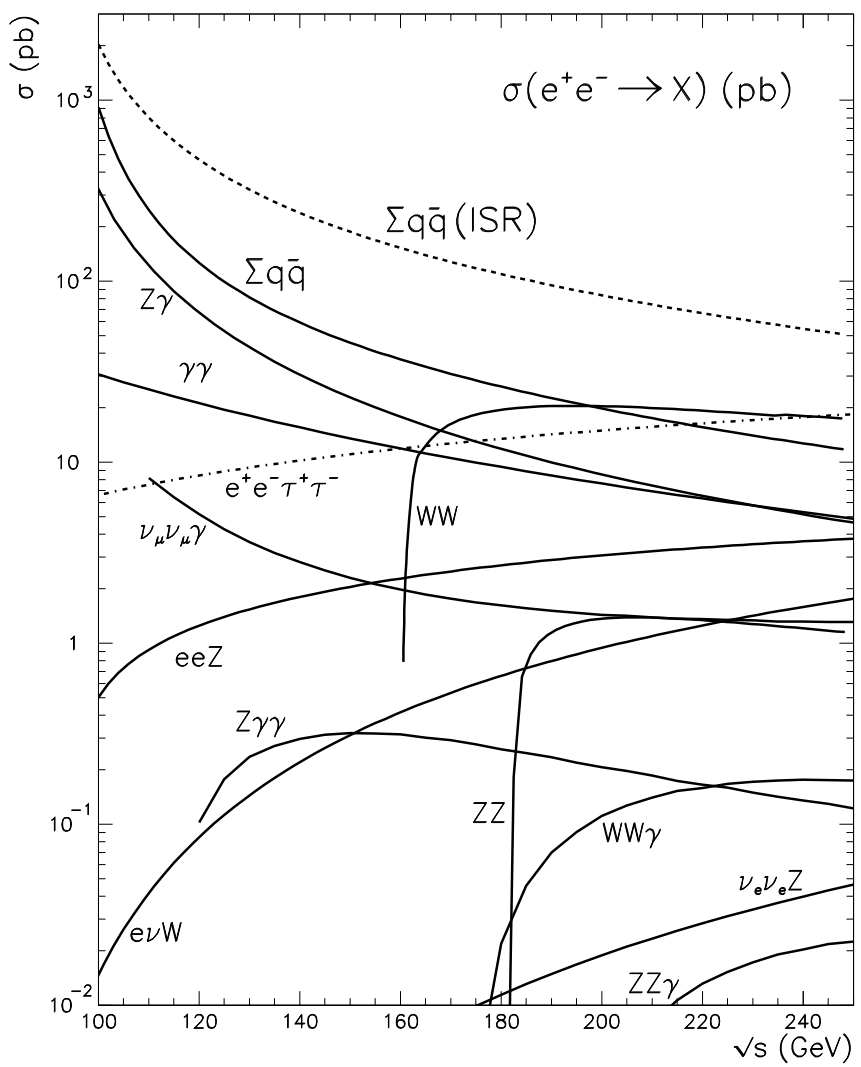

Figure 3.4: Cross sections of Standard Model processes at LEP2 [56].

LEP2 is the domain of W boson physics. The threshold for W pair production was reached for the first time in 1996 when LEP was operated at center-of-mass energies of 161 and 172 GeV. The measurements of mass and width of the W boson belong to the main tasks at LEP2. M_W is one of the important input parameters of the Standard Model. Together with the precise knowledge of the Z boson mass, its measurement is sensitive to loop corrections where the masses of Higgs boson and top quark enter and performs an essential test of the Standard Model predictions.

At LEP2 triple gauge boson couplings enter the cross section calculations at tree-level, playing an important role for the renormalization of the electroweak theory. For the first time at LEP the structure of these couplings is accessible to measurements. The search for evidence for anomalous couplings, i.e. deviations from the Standard Model expectations, can be performed studying W pair differential cross sections or several four fermion processes as e.g. single W boson production $e^+e^- \rightarrow We\nu$.

W or Z boson pair production with their subsequent decays belong to the class of four fermion processes. Their final states are produced with large cross sections at LEP2 and originate from several production mechanisms. Some of them are not associated to the real boson pair production but act as background e.g. with the search for the Higgs boson and new particles. Their study and accurate calculation is therefore of interest; deviations from the Standard Model expectation would signal new physics.

The search for new particles is another main reason for the high energy period of LEP. The search for the Higgs boson with masses up to M_Z or even beyond is one of the top tasks. Aiming at the understanding of the mechanism which is responsible for symmetry breaking in the electroweak theory and which leads to particle masses, several scenarios involving Higgs bosons have been described in theoretical approaches. The most simple one is realized in the Standard Model. The dominant production mechanism is $e^+e^- \rightarrow H^0Z^0$ where both bosons are on-shell. The Higgs boson is emitted from a virtual Z boson and decays with highest probability into b qarks. Several hadronic and leptonic decay modes of the Z^0 boson lead to multiple event types, being affected by other processes acting as background.

With the super-symmetric extensions of the Standard Model, new particles are predicted as partners of the standard ones. The Higgs sector is enlarged. Mixing of Higgs partners and standard bosons yields new physical mass eigenstates. The search for super-symmetric particles at LEP2 is therefore of special interest.

Many of the processes mentioned above are characterized by final state particles involving the entire solid angle or cross sections peaking at small polar angles. It is important to distinguish between signal and several background processes which often appear with similar experimental signature. Next to an efficient detector, hermeticity with tracking and particle identification are essential for measurements at LEP2. These items led to upgrades of several detector components of DELPHI.

Two event displays shall provide examples for the detector performance needed. The event shown in figure 3.5 was recorded by DELPHI at 189 GeV center-of-mass energy. It was tagged as a candidate for the process $e^+e^- \rightarrow ZZ$ or HH. Two muons are detected in the central detector part and one jet in every end-cap. Both jets involve polar angles in the "very forward region". With the LEP1 configuration, DELPHI's track reconstruction was not efficient there. At LEP2 the pixel detector in the new Very Forward Tracker provided important track information to fully characterize the event.

A four-fermion event with a pair of Z bosons decaying into two electron-positron pairs (discussed in [58]) is shown in fig. 3.6. The threshold of Z pair production was exceeded for the first time in 1998. The electrons were produced in the forward direction and tracked by Vertex Detector and Very Forward Tracker. The charge of one of the electrons was determined wrongly, unfortunately, because the momentum was measured with a large error. This is a general problem with tracks in the very forward region being almost parallel to the solenoid's magnetic field.

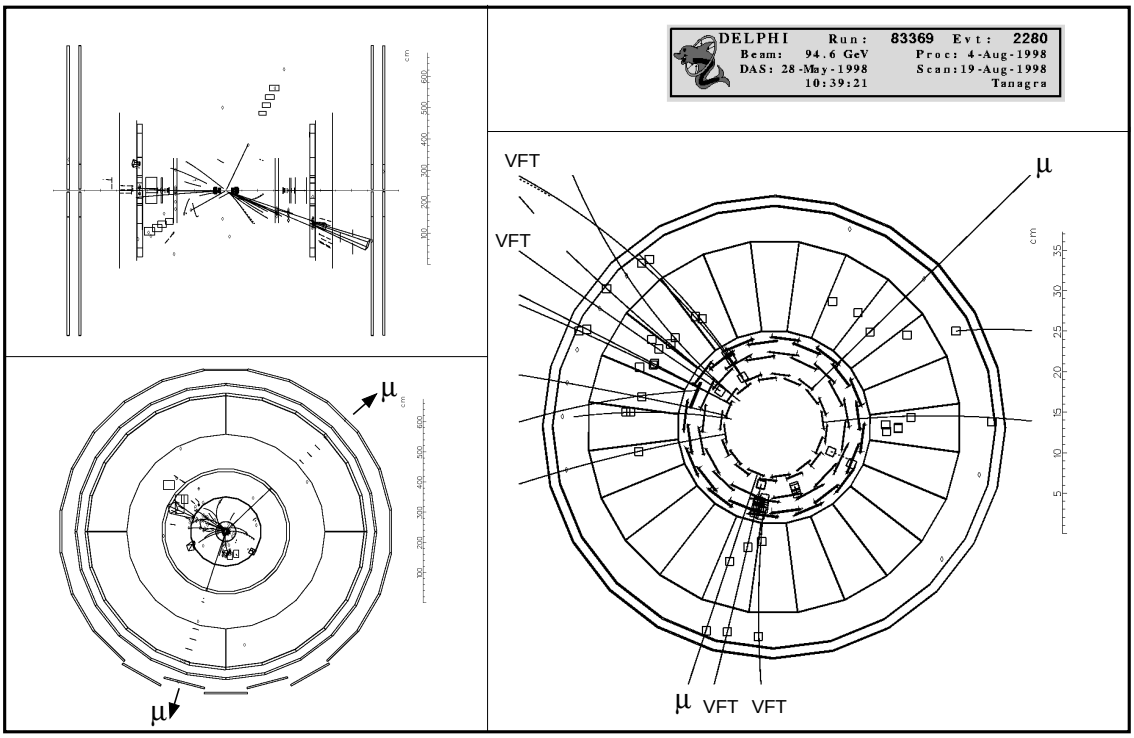

Figure 3.5: An event candidate for the process $e^+e^- \to ZZ$ or HH at $\sqrt{s} = 189$ GeV. Top left: zx-projection with the end-cap detectors indicated. Bottom left: xy-projection of DELPHI. Right: xy zoom into Silicon Tracker and Inner Detector. Track elements measured by the Inner Detector and Very Forward Tracker are indicated as squares, reconstructed tracks as solid lines. Tracks with VFT participation are marked. The symbols of Vertex Detector track elements have been suppressed in the graphics.

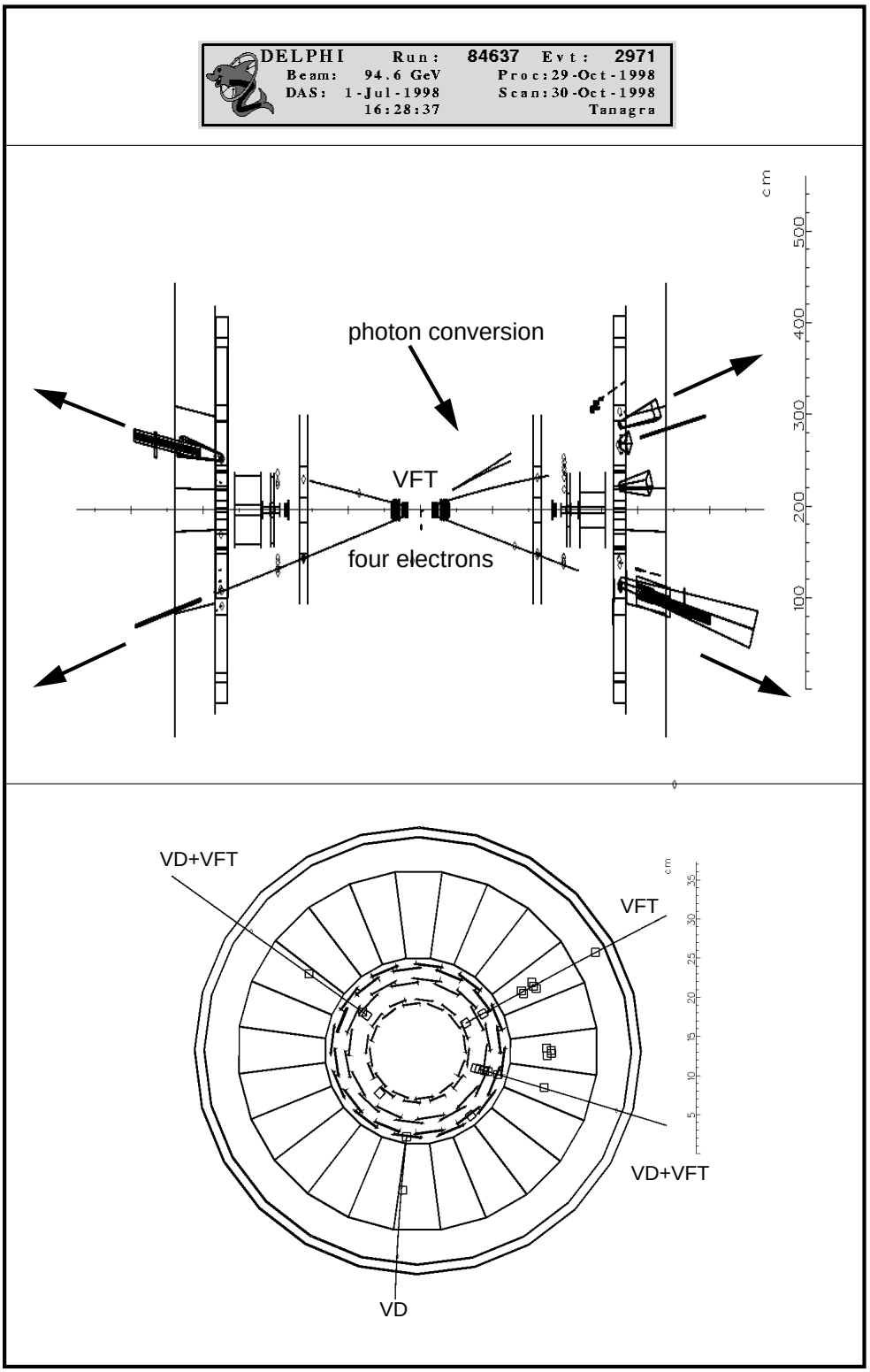

Figure 3.6: An event candidate for the process $e^+e^- \rightarrow ZZ \rightarrow e^+e^-e^+e^-$ at $\sqrt{s} = 189$ GeV. The electrons are produced in the very forward direction. Three of them are tracked by the Very Forward Tracker.

3.3 DELPHI detector upgrades for the operation at LEP2

Several detector upgrades concerning the end-cap region of DELPHI have been proposed and performed with respect to the LEP2 physics requirements [59, 60]. They cover general detector hermeticity aspects in the forward region at $\theta < 25°$ and an enlarged vertex detector for extended b-tagging capabilities.

Electromagnetic calorimetry in the end-caps of DELPHI is performed by the Forward Electromagnetic Calorimeter, covering the polar angles $8° < \theta < 35°$. A gap existing between this calorimeter and the Small Angle Tagger, the former luminosity detector close to the beam pipe, was closed by the new Small Angle Tile Calorimeter. It ensures electromagnetic hermeticity in the forward region by its enlarged acceptance $1.7° < \theta < 10.7°$ [61].

The DELPHI detector comprised already large-area muon chambers for its central and forward part. A gap between the Barrel and Forward Muon chambers at $\theta = 40°$, however, was unsatisfactory at LEP2. It was closed by adding the Surround Muon Chambers to provide hermeticity with muon identification [62, 63].

Charged track hermeticity in the end-cap region is provided by several new and modified detectors. With the DELPHI setup at LEP1, the tracking was limited by several radiation lengths of unavoidable support material in front of the forward tracking chambers A and B, covering the polar angles $11° < \theta < 36°$ in every end-cap. Figure 3.7 visualizes the material distribution. At the same time the central tracking detectors subsequently dropped out of the tracking for polar angles $\theta < 25°$. The Time Projection Chamber, DELPHI's main tracking device, does not provide track elements below 22°. Below $\theta = 20°$ the tracking chambers used to have no supporting tracking device at all. No redundancy with the detection of charged particles was ensured and the stand-alone pattern recognition efficiency low [64, 65].

A straight forward solution would have been to extend only the length of one already existing detector considerably, the silicon microstrip vertex detector ($40° < \theta < 140°$), yielding both an enlarged solid angle for b-tagging and track information to be linked to the tracking chambers further outside.
Little space in the central opening of DELPHI, however, where the vacuum chamber of LEP intersects the detector, limits the total length of the vertex detector and did not allow for this approach. A longer vertex detector was still possible, but had to be completed by an additional silicon tracking device, the **Very Forward Tracker**, and a longer Inner Detector. The new Vertex Detector covers polar angles down to 20° [67]. The jet chamber and straw tube layers of the new Inner Detector [51] cover the polar angles down to 12°. The task of the Very Forward Tracker is to perform stand-alone pattern recognition in the acceptance range $10° < \theta < 25°$ close to the interaction region [64]. It is built from two detector components. Ministrip detectors

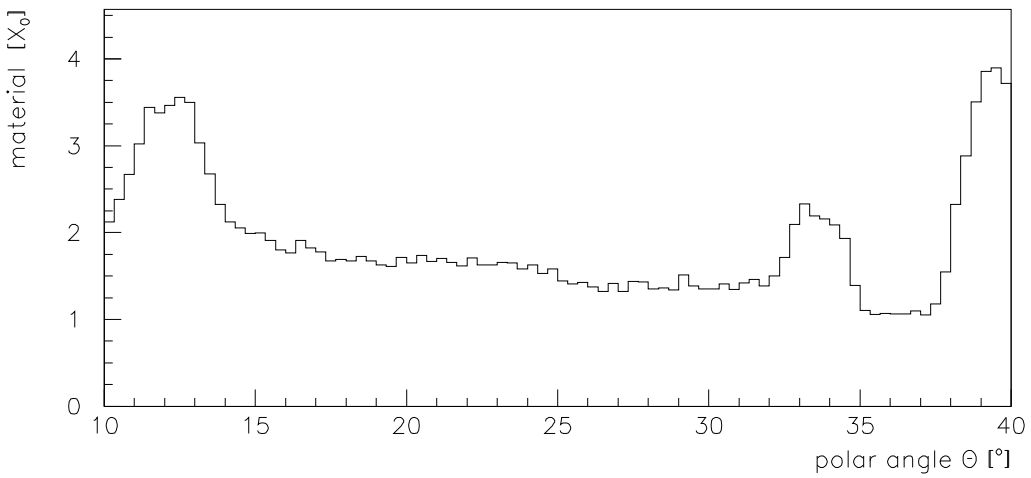

Figure 3.7: Mean material distribution in units of radiation lengths as a function of the polar angle in the end-cap region. Particles were simulated to traverse the DELPHI detector. The DELPHI material data base was read and entries considered from the interaction region to the Forward Electromagnetic Calorimeter [66].

minimize the number of readout channels by their large strip pitch, are highly efficient and provide the advantage of an approved technology. The **pixel detectors** keep the combinatorial background with the ministrip detectors low and are essential to yield the required pattern recognition efficiency.

The upgraded system of tracking detectors in the end-cap region covers polar angles down to $\theta = 10°$. The situation for the innermost tracking detectors is illustrated in figure 3.8, which shows the number of $r\phi$ and z coordinates measured per track as a function of the polar angle.

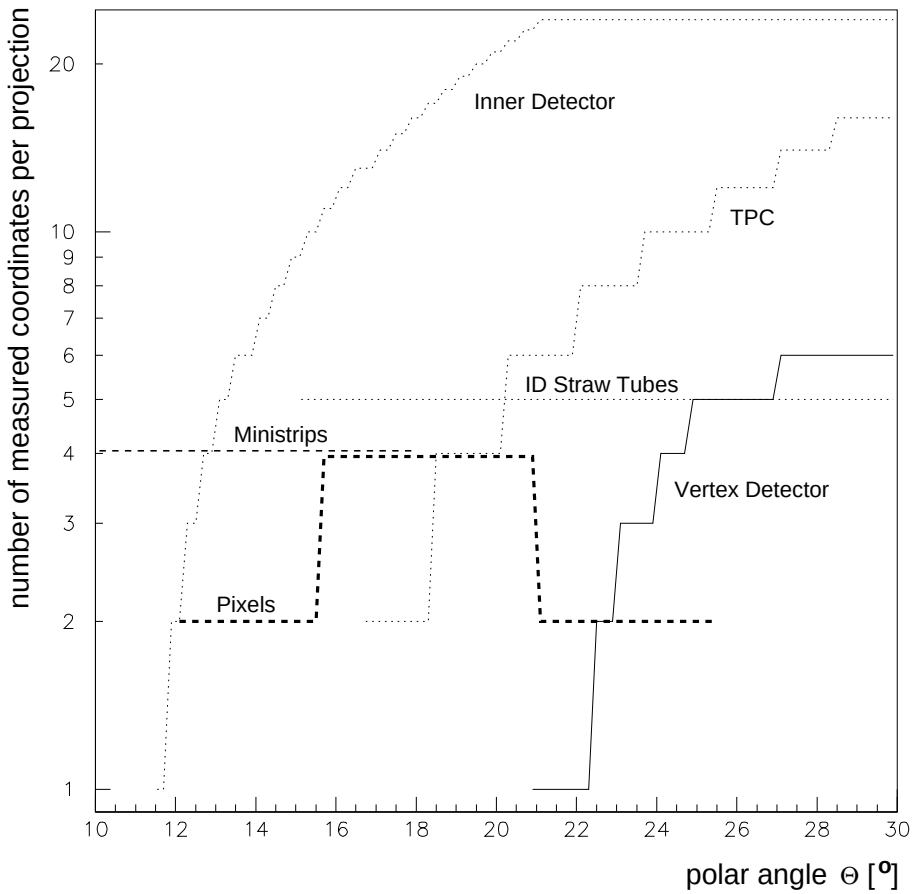

Figure 3.8: Number of coordinates measured by the innermost tracking detectors in the forward region as a function of the polar angle [67].

Chapter 4

The DELPHI Silicon Tracker

The Silicon Tracker is the final state of the upgraded DELPHI vertex detector, optimized for the physics program at LEP2 [67]. It consists of the 3-layer microstrip vertex detector in the central part and the Very Forward Tracker [64] in the end-caps of the detector. Every end-cap is built from two layers of ministrip and two layers of pixel detectors. The heterogeneous components of the Silicon Tracker are mechanically connected and share common resources.
The task of the vertex detector is to enable the reconstruction of primary and secondary vertices with high spatial resolution. The Very Forward Tracker is a self-sufficient tracking detector close to the interaction region to cover polar angles below 25°. The combined silicon detectors cover the polar angles $10° < \theta < 170°$.
The micro- and ministrip detectors were fully upgraded and installed for the running period in 1996. The pixel detector was installed to 5 over 8 parts in 1996 and completed for the data taking period in 1997. With a total sensitive area of 1.78 m^2 the DELPHI experiment comprises the largest silicon vertex detector currently existing.

The Silicon Tracker is placed in the opening between the vacuum pipe of LEP and the internal wall of the Inner Detector. It covers the available space of 12 cm radius nearly entirely. The outline of the detector is shown in the cut-out view of figure 4.1, and figure 4.2 provides a cross section view of a quarter of the detector.

The central part of the Silicon Tracker is 55 cm long. Modules of microstrip detectors, linear arrays of segmented silicon plaquettes, are mounted in concentrical layers surrounding the beam axis. The end-caps of the Silicon Tracker extend the detector length to 80 cm. Cone-shaped arrangements of ministrip and pixel detector modules are mounted inclined with respect to the beam axis to cover an enlarged polar angle at limited detector length. Including repeater electronics on either sides the total detector length is 1 m.
The design of the Silicon Tracker ensures hermeticity by sufficient overlaps of all modules and components. The microstrip detector covers the azimuthal angle entirely. Holes between neighboring detectors are closed by transposed modules. Depending on

length and radius of the layers, polar angles down to 24°-21° are covered. The internal pixel detector layer reaches into the microstrip vertex detector and links the central detector part to the forward region. In the central region up to 6 hits by crossing charged particles are measured, starting from the interaction region. The Very Forward Tracker provides up to 3 hits in its four layers at polar angles below 25°.
Detector and support material have been minimized as far as possible to yield high spatial resolution at minimum multiple scattering. Figure 4.3 describes the material of the Silicon Tracker as a function of the polar angle. The central detector region contains the least amount of material. The most important term for high impact parameter resolution there is given by the 1.1% radiation length after the first measured point. In the very forward region, the material increases to about one radiation length due to support structures.

The photograph in figure 4.4 shows an end-cap region of the Silicon Tracker prior to the installation into the experiment. Modules of the external microstrip and pixel detector layers are visible as well as ministrip detectors and circular boards of repeater electronics outside the detector acceptance.

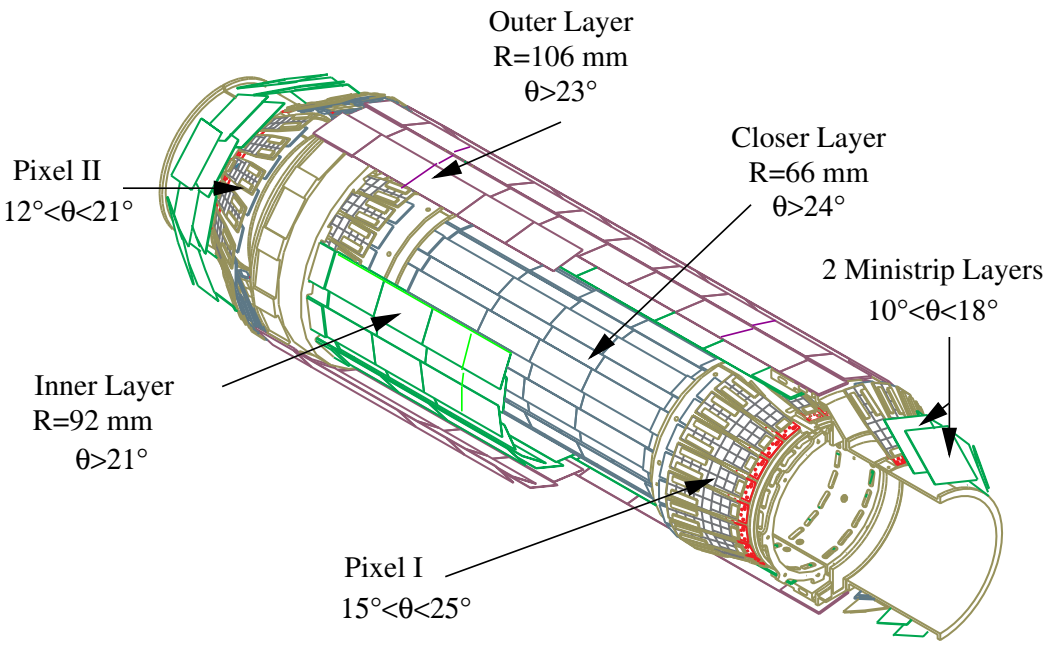

Figure 4.1: Outline of the DELPHI Silicon Tracker.

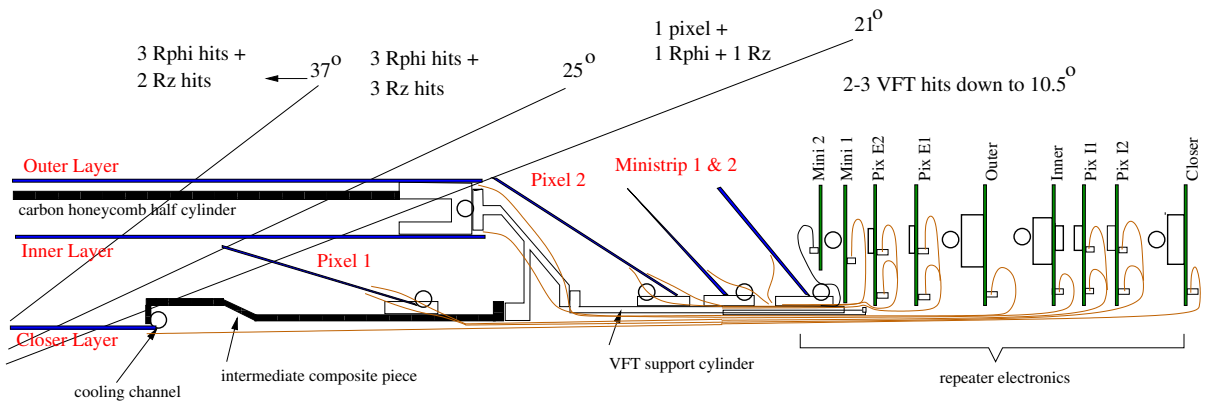

Figure 4.2: Cross section of a quadrant of the Silicon Tracker, $|z| > 10$ cm.

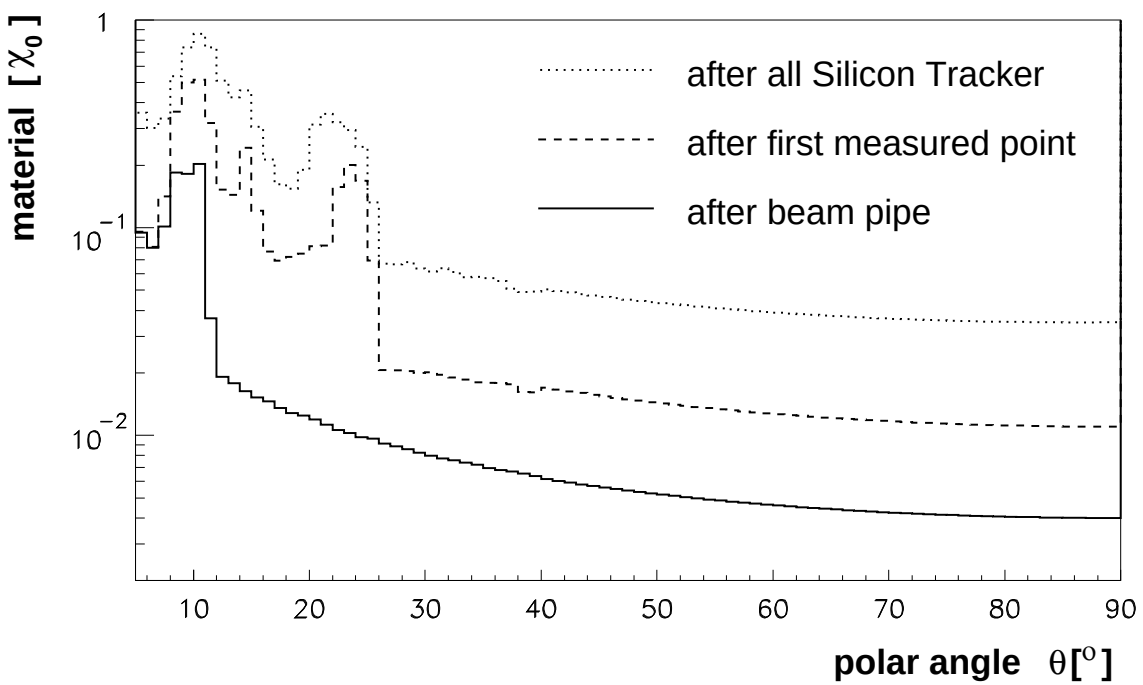

Figure 4.3: Material of the Silicon Tracker as traversed by particles at polar angles θ.

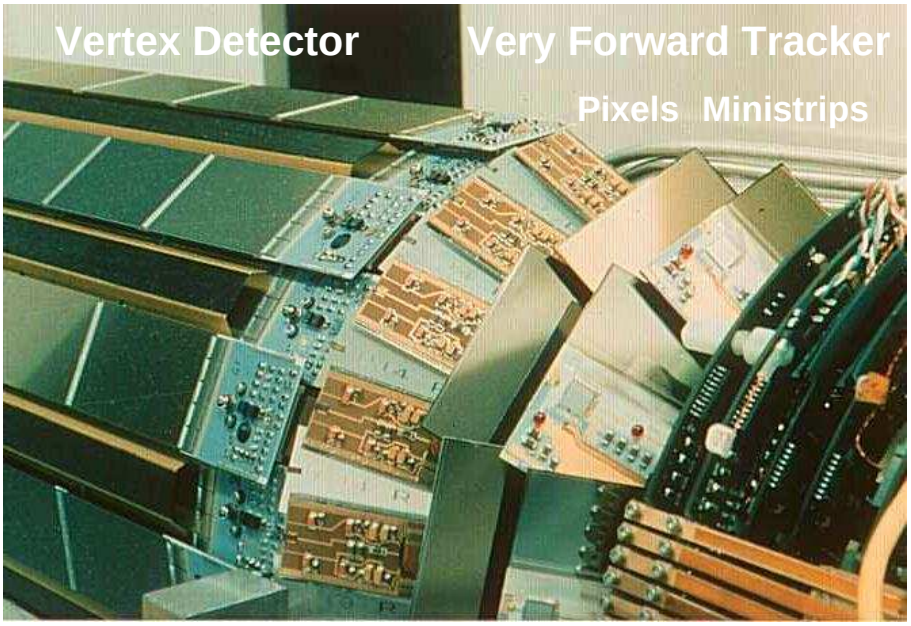

Figure 4.4: End-cap of the Silicon Tracker.

4.1 The microstrip vertex detector

The microstrip vertex detector consists of three concentrical layers of microstrip detector modules with two-coordinate readout. The modules are placed at average radii of 6.6 cm, 9.2 cm and 10.6 cm, chosen to provide best track resolution by maximum lever arm and closest possible distance to the beam pipe. The configuration of the detector layers is shown in figure 4.5. Table 4.1 summarizes overall properties of the microstrip vertex detector. A detailed description of the modules has been given in reference [68].
The intermediate "Inner" microstrip layer consists of 20 modules, the internal "Closer" and external "Outer" layers of 24 modules. They are mounted in a staggered way to provide overlaps for full azimuthal coverage and redundancy. Residuals measured in the overlapping regions of one layer, taking into account tracks defined by the two other layers, enable to perform a stand-alone geometrical alignment which is the seed for the final alignment of the entire DELPHI experiment [69].
A module is built from two electrically independent half-modules which are joined in the center. Up to 8 silicon plaquettes are used per module. With the Outer layer where multiple scattering is less severe, a back-to-back solution with 16 single-sided plaquettes has been chosen.
The silicon is 300 μm thick and and contains up to 1280 strips of 25 μm pitch. The readout pitch is 50 μm for rϕ coordinates and varies with the z coordinate to match

enlarged clusters of hit strips and high spatial resolution with inclined tracks at low polar angles. A double metal layer for the re-routing and multiplexing of z strips, i.e. the diodes orthogonal to the beam direction, has been integrated into the silicon to limit the number of external wire bond connections and readout channels. Wire bonds connect the strips of adjacent plaquettes of a half module.
Hybrid electronics circuits with front-end chips for the readout of 384 and 640 analog strip channels are wire bonded to the plaquettes at both ends of a module. They serve as the only mechanical support and fix the module on water-cooled aluminum end rings from where the heat dissipated by the electronics draines off. The modules themselves are supported by omega-shaped kevlar structures with karbon fibre beams. Neighboring modules carry their supports on alternating sides to allow a dense arrangement. The support has been designed as lightweight but stiff as possible to ensure minimum multiple scattering at high mechanical stability.
A low-mass carbon fibre honeycomb cylinder joins the end rings on both detector sides and provides mechanical stability to the entire structure. The internal microstrip modules and the internal pixel detectors are supported by an extra composite material piece.
The entire microstrip detector provides 150 000 readout channels on 1.37 m^2 area.

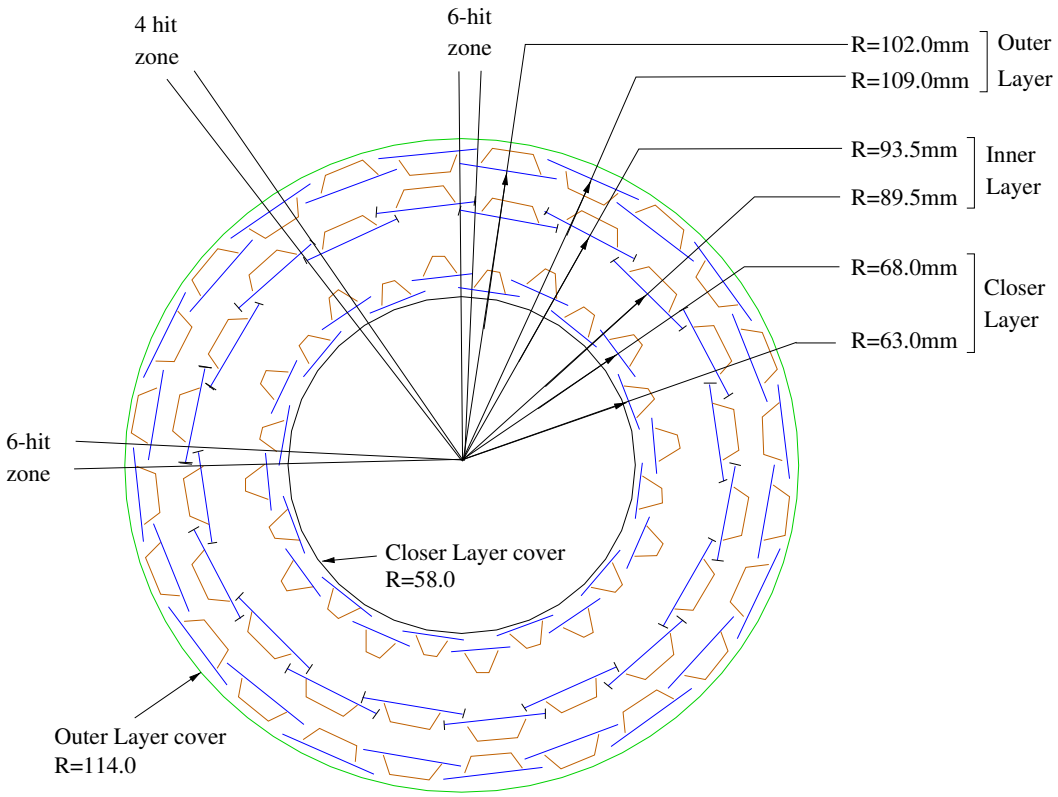

Figure 4.5: rϕ cross section of the 3-layer vertex detector.

microstrip vertex detector	
number of layers	3
radii [cm]	6.3, 8.9, 10.8
modules/layer	24, 20, 24
detectors/module	4, 8, 16
silicon length [cm]	28, 48
acceptance in θ [°]	21-159
modules overlap [%]	12-15
channels	150,000
front-end chips	MX6, TRIPLEX
AC coupling	integrated
2-coord. readout	double + single
z readout	double metal
readout pitch [μm]	rϕ: 50, z: 44–176
material [χ_0]	<1
sensitive area [m^2]	1.37

Table 4.1: Characteristics of the DELPHI microstrip detector.

4.2 The Very Forward Tracker

The Very Forward Tracker achieves stand-alone pattern recognition at minimum combinatorial background with two layers of ministrip and two layers of pixel detectors. It complements DELPHI's tracking capability at small polar angles close to the interaction region.

4.2.1 Design Considerations

The spatial resolution requested from the Very Forward Tracker is of the order of 100 μm. This precision is sufficient taking into account Coulomb scattering already in material in front of the Very Forward Tracker. Furthermore, its track elements are extrapolated towards the Forward Chambers and the Forward RICH detectors which are located further outside after several radiation lengths of additional material. No extreme resolution as with the microstrip vertex detector is necessary therefore and the task restricts to unambiguous and efficient pattern recognition.
Ministrip and macro-pixel detectors, characterized by rather large strip pitch or element size, respectively, meet this situation. They are able to provide the moderate spatial resolution and allow at the same time a module design minimizing the total number of detector and readout channels. The pixel detector contains an on-module

readout scheme with zero-suppression that keeps the data size small. The development of ministrip and pixel detector modules which could be produced with sufficient yield was a major goal of the Silicon Tracker project.

Detailed simulations on the configuration of detector modules and layers were performed for the design study [64]. Unlike the microstrip modules of the Vertex Detector which are arranged parallel to the z axis, the complex geometrical situation enforced a design with the new silicon detectors inclined with respect to the beam. Complicated mechanics, however, delicate handling during construction and assembly as well as aggravated alignment result from the little available space. A first approach considered a reduced radius of LEP's beam pipe in DELPHI. The extra available space from 54 mm to 45 mm radius would have been advantageous for a relaxed design with three silicon layers. This approach was finally not realized because of the increased beam background rate to be expected with the vertex detector at the lower radii.

Four detector layers are necessary to cover the desired polar angles, considering the available space between beam pipe and the outermost radius as well as possible detector module lengths. Best results concerning minimum ambiguities and maximum track reconstruction efficiency in different polar angle sections were obtained with two internal layers of pixel detectors and two external layers of ministrip detectors. Additional improvement was gained by rotating the external strip layer with respect to the internal one. This information led to a ministrip detector design with slightly tilt strips. The kind of support material and different ministrip pitch widths turned out to be less important than the order of pixel and ministrip layers.

detector configuration	θ range	ambiguities [%]
layer 1–2	15°–22°	
pixel mini		24
pixel pixel		**17**
layer 1–2–3	15°–22°	
pixel mini pixel		24–10
pixel pixel mini		**17–9**
layer 2–3–4	10°–17°	
mini pixel mini		10
pixel mini mini		9
pixel mini (mini tilt)		**6**

Table 4.2: Track ambiguities with different Very Forward Tracker configurations [64].

The detector modules are arranged in "cones" as illustrated in figures 4.6 and 4.7. The ministrip detector layers are inclined by 50° and the pixel detectors by 12° and 35° with respect to the beam. They are fixed to the support at one end only. Every layer is mounted on a separate aluminum ring support which allows a pre-assembly in the laboratory and to insert the final cones one by one into the Silicon Tracker during assembly.
The internal pixel layer is placed between the Closer and Inner layers of the vertex detector, mounted on a carbon fibre composite support that also carries the internal microstrip detector layer. The mechanical properties of this composite support match closely the behavior of the barrel's carbon fibre support to avoid thermal stress. The second pixel layer together with the ministrip cones is mounted on an aluminum cylinder outside the central acceptance.

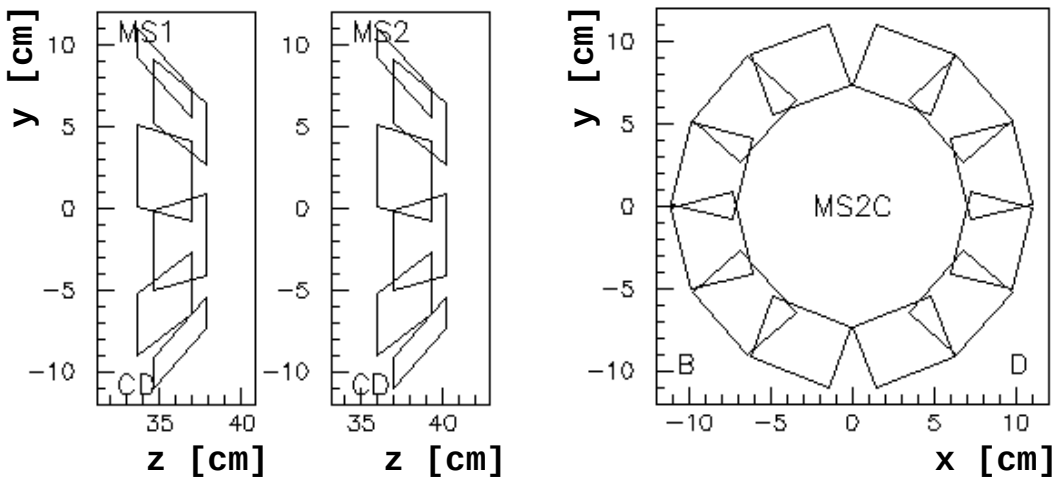

Figure 4.6: Arrangement of ministrip detectors.

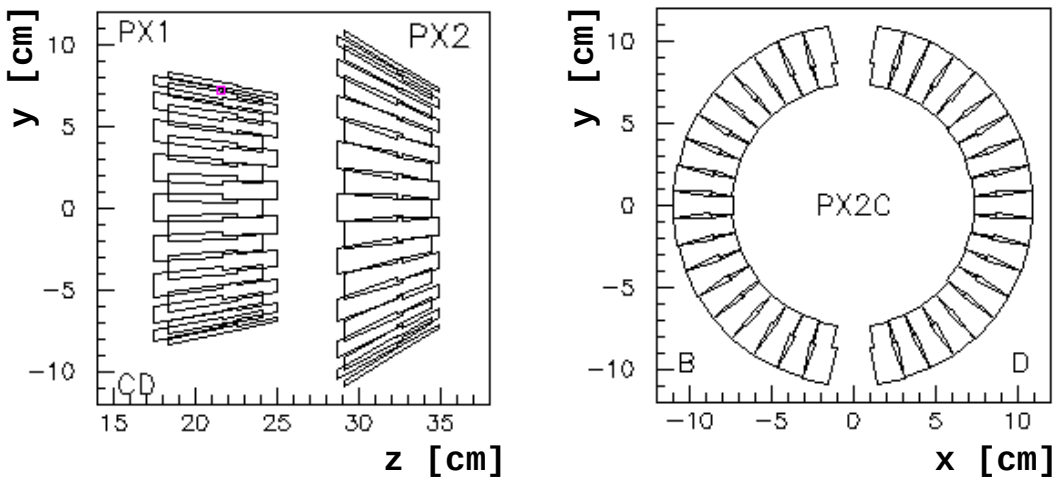

Figure 4.7: Arrangement of pixel detectors.

The Very Forward Tracker represents a significant obstacle for the routing of cables and cooling pipes to and from the microstrip detector and also its own components. Almost all space in the end-caps is already occupied by silicon modules. Flat kapton cables can pass between the tracker's aluminum support and the detector cones close to the beam pipe (see fig. 4.2). Space for water cooling pipes has been made available by splitting the cones into independent halves, corresponding to the half-shell structure of the Silicon Tracker. A few degrees in azimuth near $\phi = 0°$ and $\phi = 180°$ are not covered by detectors. The pipes reach into the detector through these gaps, visible in figures 4.6 and 4.7.

Table 4.3 summarizes important characteristics of the Very Forward Tracker. The ministrip detector provides 24.500 readout strips on 0.26 m^2 sensitive area. The pixel detector covers 0.15 m^2 and is segmented into 1.2 million pixels.

Very Forward Tracker	mini strip detector	pixel detector
layers/end-cap	2	2
radii [cm]	6.9–8.4	6.9–8.4, 7.5–11.2
inclination [°]	50	12, 32
modules/layer	12	38
detectors/module	2	1
silicon size [cm^2]	5.3 × 5.3	6.9 × 1.7→2.3
acceptance θ [°]	10–18	12–25
modules overlap [%]	15	12, 37
channels	24.500	1.2 million
front-end chips	MX6	SP8
coupling	AC, integrated	DC
2-coord. readout	single sided back-to-back	sparse data scan
readout pitch [μm]	200 (1 intermediate strip)	330 (pixel size)
sensitive area [m^2]	0.26	0.15

Table 4.3: Characteristics of the DELPHI Very Forward Tracker.

4.2.2 Ministrip Detectors

The ministrip detectors are a special development for the application in the DELPHI Very Forward Tracker. Research topic was to study the detector physics of silicon strips with large implant width and to design a detector layout which fulfilled the important aspects of a tracking device as high efficiency, high signal-to-noise ratio and sufficient spatial resolution at a low number of electronics channels. The design had to match the tight space constraints and to be compatible with the vertex detector

supply and data acquisition systems. A layout with enhanced inter-strip capacitance and an additional metal layer on the strip side matched these requirements [70].

The ministrip detector comprises 96 detector plaquettes, assembled into cones of 12 modules each. The construction of the detector has been reported in reference [71]. A module is formed from two 5.3 $\times$ 5.3 cm^2 single sided silicon strip detectors, tilted by 90 degrees and glued back-to-back to measure two orthogonal coordinates. The strip pitch is 100 μm. Every second strip is capacitively coupled to a readout line, yielding a readout pitch of 200 μm. Charge sharing with the intermediate strips, however, results in higher spatial resolution than imposed by the readout pitch only. Neighboring modules are shifted in z direction and overlap slightly.

The assembly of a module is illustrated in figure 4.8. Two hybrid circuits carry the readout electronics and are glued directly onto the strip side of the detectors, coping with the lack of space in the region of the Very Forward Tracker. The hybrids' substrates are made from beryllium oxide, matching closely the thermal expansion of silicon. Specially designed fan-in structures on the hybrids match the strip pitch to the pitch of the readout chips' input pads.

The strip implants are tilted by two degrees with respect to the detector edges. In a single detector layer with two-coordinate readout, multiple-strip hit combinations have ambiguous intersection solutions. They need to be resolved or at least minimized in a tracking device. The stereo angle of four degrees between strips of top and bottom detector in a module supports the reduction of space point ambiguities with multi-hit events in two detector layers. The high signal-to-noise ratio of about 30 to 40 efficiently avoids background from unphysical hits.

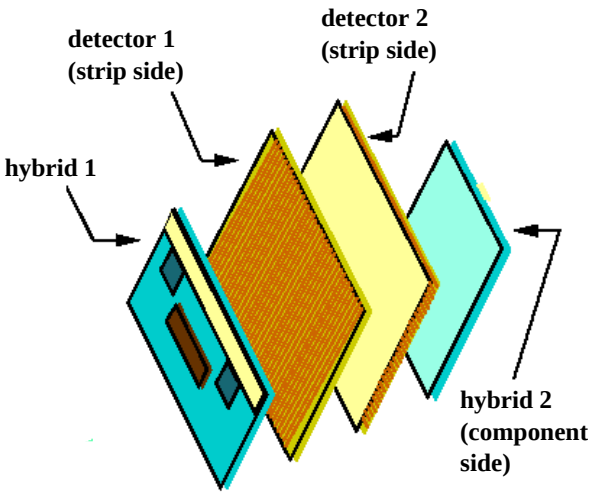

Figure 4.8: Assembly of a ministrip module.

4.2.3 Pixel Detectors

The pixel detector is a DELPHI specific development. It comprises 152 multi-chip detector modules, arranged in two cones per end-cap similar to the ministrip mounting. The shape of the module takes into account the small opening angles of the cones. In order to use the available space optimally, a racket-like layout has been chosen with one of the short sides wider than the other. The modules are fixed with the small side to an aluminum support.

The detectors are built in hybrid technique, with the detector substrate carrying all components. They are covered by readout chips containing the signal processing electronics for every pixel. Bus lines for both analog and digital signals as well as the power supply are integrated into the detector substrate. Solder bump bonds establish the connection to all chip contacts. Kapton cables, glued on top of the electronic chips and wire bonded to the integrated bus, route the lines to repeater electonics outside the Silicon Tracker's acceptance.

Pixel detectors are characterized by the large number of detector elements, requiring a readout strategy matching the low-occupancy environment with DELPHI. Data size and readout time are minimized applying an on-module zero-suppression. The numerous detector elements required many interconnections between detector and readout electronics. Working modules demanded for assemblies with a very low failure rate especially with power lines and control signals.

The design and construction of the pixel detector is discussed in detail in the next chapter.

Chapter 5

Development and construction of the DELPHI pixel detector

The pixel detector project is a joint effort of several institutes of the DELPHI collaboration. Linked by the Silicon Tracker group at CERN, research work on different aspects of the detector system as well as production and test of prototypes and components took place mostly outside CERN. The tasks and sharing of responsibilities related to the pixel detector hardware are overviewed in table 5.1.

	Karlsruhe University	Marseille CPPM	Milan Univ./INFN	Paris CdF	Wuppertal University
chip design/testing		×	×	×	×
detector design		×			
bonding study		×	×		
module production	×	×	×		×
assembly/testing	×	×	×	×	×
mechanics		×			
slow control					×
data acquisition				×	
online monitoring					×

Table 5.1: Institutes and responsibilities within the pixel detector project.

Main goal of the DELPHI pixel detector project was the development of a multi-chip detector module which fulfilled the DELPHI specifications. High particle detection efficiency had to be provided at 100 μm spatial resolution and random noise of about 10^{-6}. The detector had to match the DELPHI timing, implying a selective readout to limit the size of the output data, had to fit into the limited available space, and the

modules had to be produced with a sufficient yield. For the first time a large-scale production of pixel detectors was planned and performed.

Chapters 5.1 to 5.4 discuss the evolution, design and performance of the front-end electronics, describe the detector layout and present the choice of the interconnection technology.
The first detector modules assembled in a pre-production provided important information on the characteristics of the overall design and led to a significant change of the modules' layout. Experience with the detector prototype and the performance yielded in a test beam is presented in chapter 5.5.
The detector module production itself is topic of chapter 5.6. The components of the module, its assembly, the test procedure and the yield of the production are discussed. Chapter 5.7 describes the assembly of the detector layers, the geometrical survey and the integration into the DELPHI Silicon Tracker.

5.1 The front-end electronics

The front-end electronics of the DELPHI pixel detector is based on RD19's OMEGA-D design which was just released when the DELPHI project started. Every sensor diode of the hybrid detector is directly coupled to its readout cell which covers a congruent area and contains a full chain of electronics circuits for signal amplification, discrimination and storage of the binary output signal.
The OMEGA-D electronics performance was ideally suited as a starting point for the application in DELPHI. The binary signal processing and hit information was fully sufficient for DELPHI's moderate pixel pitch of 330 μm. The power consumption of about 40 μW per pixel was low enough to consider an additional detector system of 1.2 million pixels and its cooling needs in the center of the DELPHI experiment. The sensitivity was high, i.e. detector signals down to about 5 000 e^- could be cleanly measured. The original pixel layout was small enough to fit an enlarged bond pad into DELPHI's pixel geometry, allowing for "cheap" bonding methods without major changes of the electronics concept.

Chip design

The electronics layout was adapted to the DELPHI requirements by the teams of the particle physics laboratories at Collège de France, Paris, and CPPM, Marseille. The chip development required several iterations until the performance satisfied the DELPHI specifications. Table 5.2 summarizes the basic steps and characteristics and also indicates the elapsed time. Comprehensive tests of every prototype version were

performed in several of the collaborating institutes before the next design steps were started.

DELPHI chip version	pixel size [μm^2]	bump $\oslash$ [μm]	pixels per chip	design step
CDFTEST 05/91	–	–	–	SACMOS 3 μm test chip
CDF2 05/91	84 × 288	30	8 × 6	front-end from RD19, + output switches
CDFSPARSE 12/91	84 × 288	30	16 × 8	+ sparse data scan prototype
CDFSP2 10/92	84 × 288	30	16 × 64	+ sparse data scan
CDFSP3 12/92	84 × 306	30	16 × 64	+ DELPHI gate
CDFSP4 07/93	330 × 330	150	24 × 24	+ DELPHI pixel geometry, large bond pad, adapted amplifier
CDFSP5/5b 12/93	330 × 330	150	24 × 24 24 × 16	modified current distribution; two chip sizes
CDFSP6 12/93	330 × 330	150	24 × 24	modified timing
CDFSP8/8b 06/95	330 × 330	100	24 × 24 24 × 16	modified bond pad, amplifier, timing; $\Longrightarrow$ final chips

Table 5.2: Chip development for the DELPHI pixel detector.

After an initial test chip which enabled the electronics engineers to learn about specific properties of the SACMOS process, the first small array of readout pixels was designed and produced in the framework of the EUROCHIP[1] program. From multi-project wafers, small batches of chips were obtained at an affordable price. The CDF2 chip contained the OMEGA-D preamplifier, discriminator and an output latch in original

[1]initiative by the European Union to promote design of integrated electronics in public education

dimensions, including the bond pad with 30 μm diameter. Circuitry to add a selective readout was already foreseen. The selective readout "Sparse Data Scan", developed at the Collège de France (see chapter 5.2), was subsequently added with the next versions. Chip CDFSP3 contained a fully operational sparse readout together with a gated input necessary with the timing of the DELPHI trigger system.
The electronics was adapted to the final pixel size with chip version CDFSP4. A large-size bond pad of 150 μm diameter fitted into this cell. The extra capacitive load was taken into account with the design of the input stage to reach low noise and fast timing. The chip geometry itself was re-designed. The final array contained 24 $\times$ 24 pixels, and the circuitry of the sparse readout was placed along the chip contact side rather than next to every pixel row to avoid dead area.
A problem with the distribution of the threshold current, however, led to a significant non-uniformity in the behavior of the pixels. With increasing column numbers, the pixels' thresholds decreased. As a result the full chip could not be adjusted commonly and was not operational therefore. The design was corrected with chip version CDFSP5, produced in two sizes matching the tapered shape of the DELPHI pixel detector modules. The CDFSP5/5b chips were ordered in larger batches. Most of the wafers were used to perform studies on different bonding technologies to connect detectors and readout chips (see chapter 5.3).
Two more iterations were necessary to reach the final readout chip. Chip CDFSP6 was designed in order to study a modified timing for sensitivity improvements. This approach was not approved. Resulting from careful electronics characterizations and bump bonding studies, the final front-end chips CDFSP8/8b contained a bond pad with reduced diameter, providing less capacitive load at the adapted input stage and ensuring correctly placed interconnections also with slightly misaligned bump bonds.

The layout of the final chips is shown in figure 5.1 [72]. On approx. 0.8 and 0.6 cm^2 area, the arrays comprise 24 $\times$ 24 and 16 $\times$ 24 pixels, respectively, of 330 $\times$ 330 μm^2 size. 24 bias cells in an extra row supply the pixels in their associated column with all currents and voltages. Two more specific pixels sense the leakage current from the detector's guard ring to take into account with the signal amplification. The chips contain 30 and 29 input/output contacts, respectively, arranged with 200 μm pitch along one of their sides. The Sparse Data Scan logic is placed outside the pixel array close to the contact pads.

The front-end electronics of the DELPHI pixels has been described in reference [73]. Every pixel contains the building blocks shown in figure 5.2. The detector is connected to the signal processing electronics through a bond pad. The input stage is built from a charge preamplifier, a folded cascode circuit with static feedback. The amplifier's peaking time is close to 120 ns. A filter of about 200 ns peaking time improves the signal-to-noise ratio. The output signal from the amplifier is digitized by a fast discriminator which can be adjusted by an external control current and is stored locally in a 1-bit memory inside the pixels. The writing only takes place while a gate signal is

provided. Discriminator and memory need to be reset before the next detection cycle. The pixels are arranged in rows and columns, with the design of pixels in pairs of columns being mirrored to share the same bus of supply lines. Figure 5.3 illustrates the pixel layout of chip version CDFSP6 and the final design with CDFSP8, appropriate for bump bonds with 100 μm diameter.

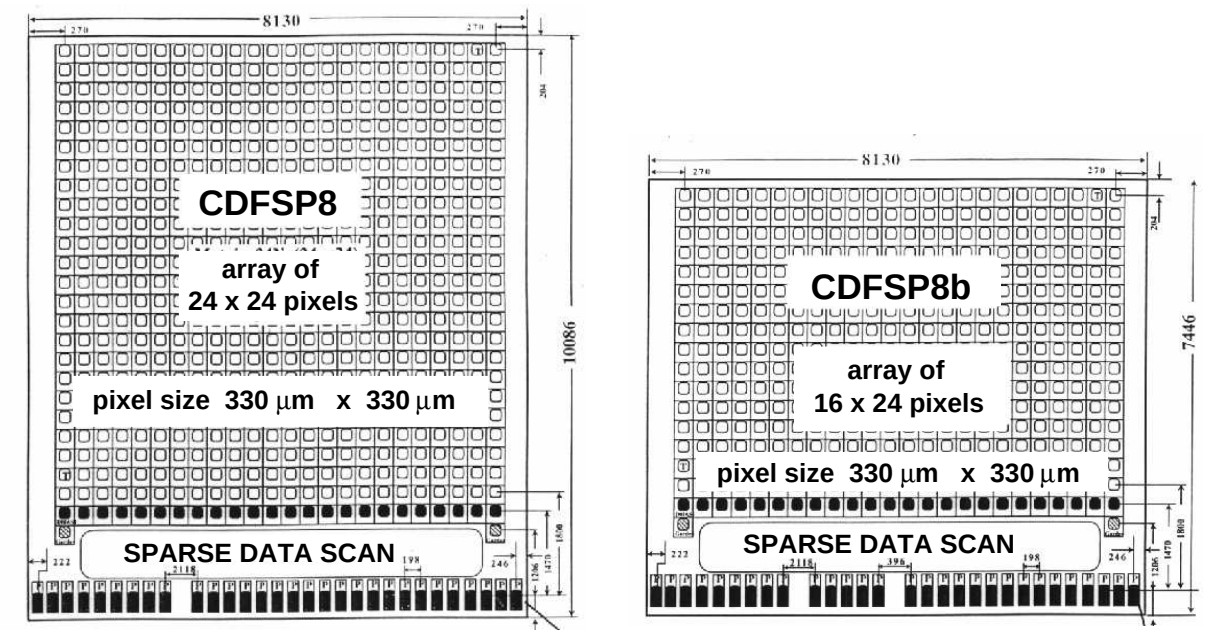

Figure 5.1: Layout of the readout chips CDFSP8/8b.

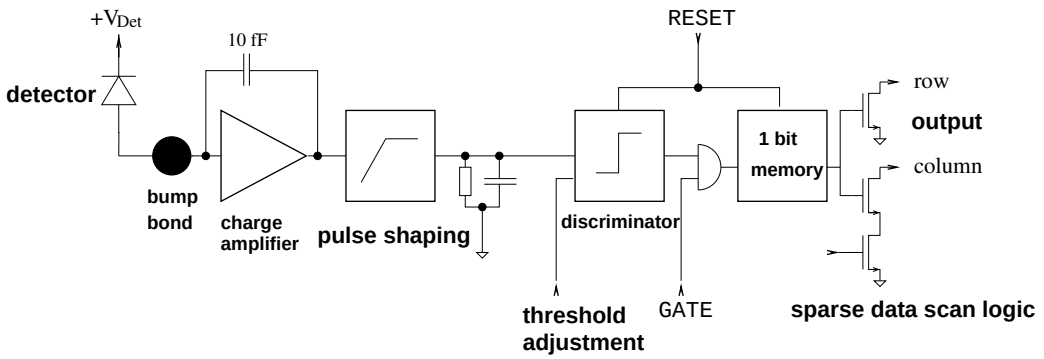

Figure 5.2: Block diagram of the electronics components in every pixel.

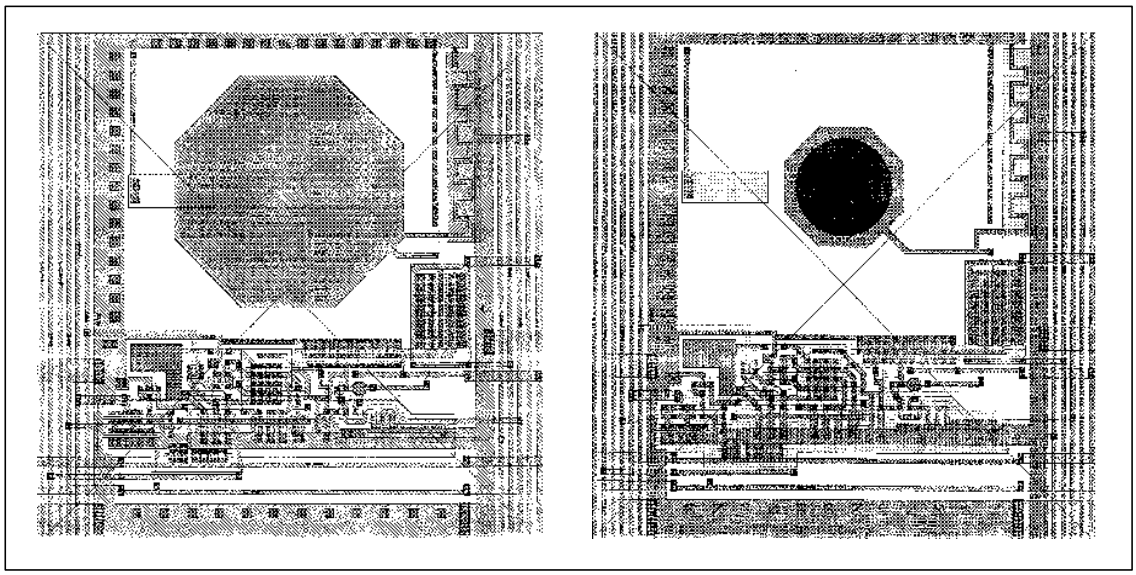

Figure 5.3: Layout of the pixel electronics. The electronics covers about 1/3 of the 330×330 μm^2. The remaining area contains space for the flip-chip interconnection. Left: 140 μm bond pad with chip version CDFSP6. Right: final design with chip version CDFSP8. Bond pads with 80 μm diameter allow for 100 μm bump bonds.

Performance of the pixel electronics

The performance of the front-end electronics was carefully analyzed during the design and prototyping period. Single chips and assemblies connected to small detector arrays were tested in the laboratories of several collaborating institutes [74, 75, 76, 77].

The important electronics characteristics with binary pixel detectors are the minimum threshold adjustable, the noise and the signal resolution. Results for the latest DELPHI pixel prototypes are summarized here, emerging from the work published in reference [77].

Threshold adjustment: The threshold curve in figure 5.4 shows the height of the detector signal which has to be exceeded in order to pass the pixel electronics and switch the state of the 1-bit memory. It was obtained by injecting generated charge pulses into the amplifiers of two dedicated test pixels per chip. These test pixels are equipped with input capacitors ($C_{test} \approx 30$ fF) to allow the application of fast voltage steps for the charge generation. The discriminator was adjusted by a control current. The circuit's behavior was scanned at various discriminator settings by counting the relative response of the output latch to 1000 input triggers with increasing test pulses. The 50% mark was considered for every entry in the graph. The threshold went almost linearly with the control current. Detector signals exceeding 5 ke$^-$ were detected. An

offset of several thousand electrons was found with the two test pixels, depending on the adjusted threshold.
Stable detector thresholds are reached several μs after the discriminator circuit has been reset. The timing for two test pixels in chip version CDFSP5 and CDFSP6 is shown in figure 5.5. The threshold is affected by initial oscillations and rather unstable within the first 3 μs, independently from the absolute threshold. The situation is also present with the final chip version. It was taken into account with the detector operation and the timing chosen accordingly in the experiment. The reset signal is sent to the pixel detector early enough to provide stable thresholds when particles from e^+e^- collisions cross the detector (see chapter 6).

Threshold calibration, spread and noise: Since the small input capacitance is only vaguely known, absolute calibration of the threshold measurement is essential to judge the performance. Readout chips connected to detector arrays were used to perform a threshold scan with γ calibration sources. The amount of charge generated by the energetic photons in silicon is well known. About 3.6 eV are required to create an electron-hole pair in silicon at room temperature. Figure 5.6 shows the normalized count rate obtained from ^{109}Cd and ^{241}Am lines as a function of the detector threshold. With every source 50 integrated spectra of single pixels were measured. The count rates drop sharply with the discriminator setting exceeding the generated signal and are well separated from noise seen without source. These positions calibrate the adjusted threshold and are indicated also in figure 5.4.
From both figures it is obvious that the thresholds of individual pixels spread across a chip. The effect originates from tolerances and non-uniformities with the chip production. For the final SP8 chip, the mean minimum threshold has been determined as 7.8 ke^- with 1.2 ke^- r.m.s.. The noise of the pixel detector has been determined from the width of the comparator's relative response as a function of the signal height. It was cross-checked with the ^{109}Cd spectrum shown in figure 5.7. The electronics bump bonded to a detector yields a noise of 230 e^- r.m.s..

The results matched the electronics specifications needed for an efficient particle detection. The situation for inclined tracks with the DELPHI pixel detector geometry has been studied in a dedicated Monte Carlo simulation at CPPM, Marseille, and is shown in figure 5.8. Full efficiency is obtained with thresholds up to 10 ke^-. This result was verified in a test beam run before the final production started (see chapter 5.5).

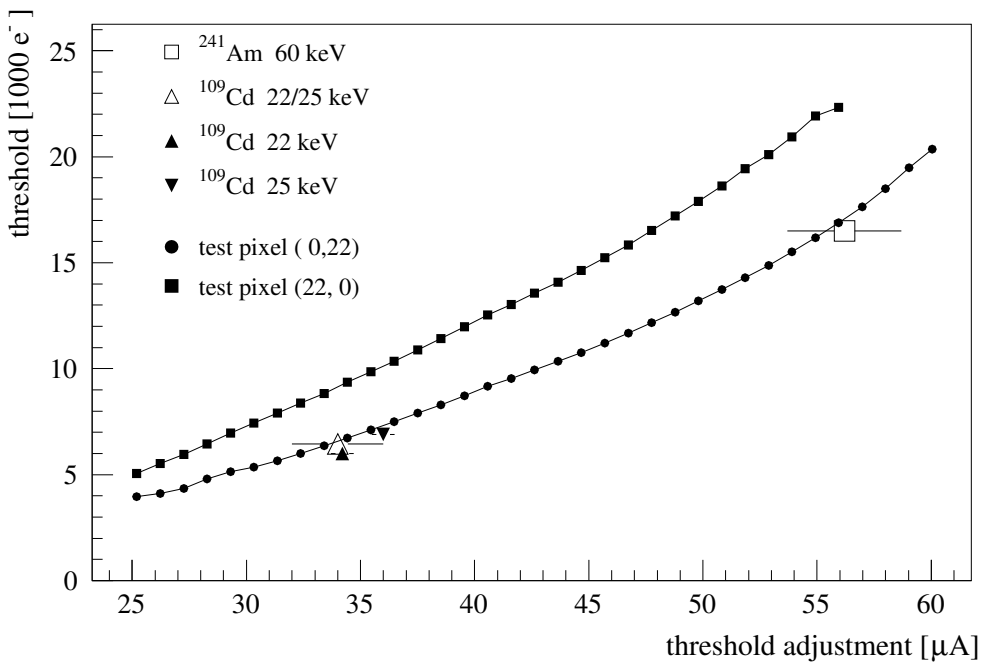

Figure 5.4: Threshold behavior of the CDFSP6 chip. Two pixels in the corners of the chip, equipped with analog test signal inputs, were used to probe the minimum detector signal to be seen as a function of the discriminator adjustment. The threshold varies almost linearly with the control current. Both pixels have a different threshold offset. The measurement was calibrated with γ sources.

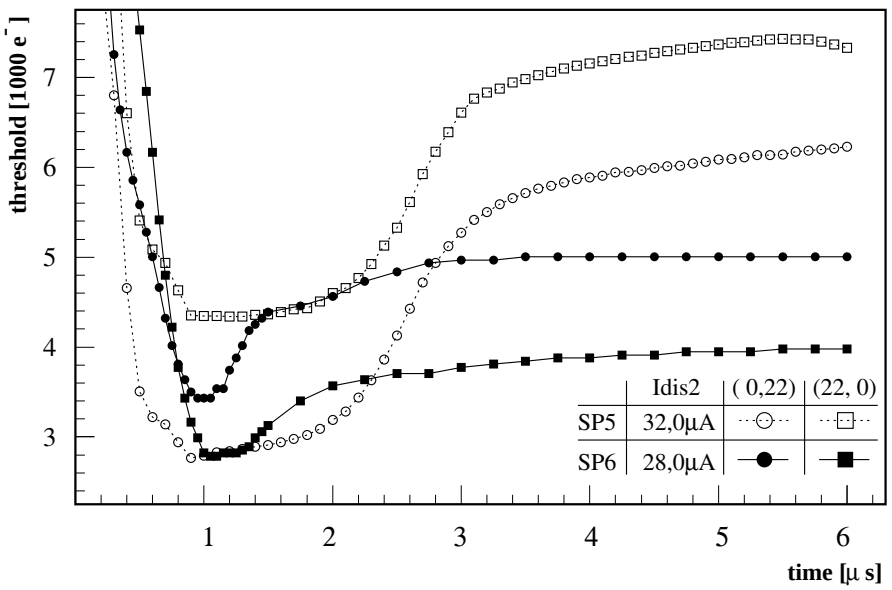

Figure 5.5: Timing of the pixel detector threshold. Stable thresholds are reached several μs after the comparators have been reset.

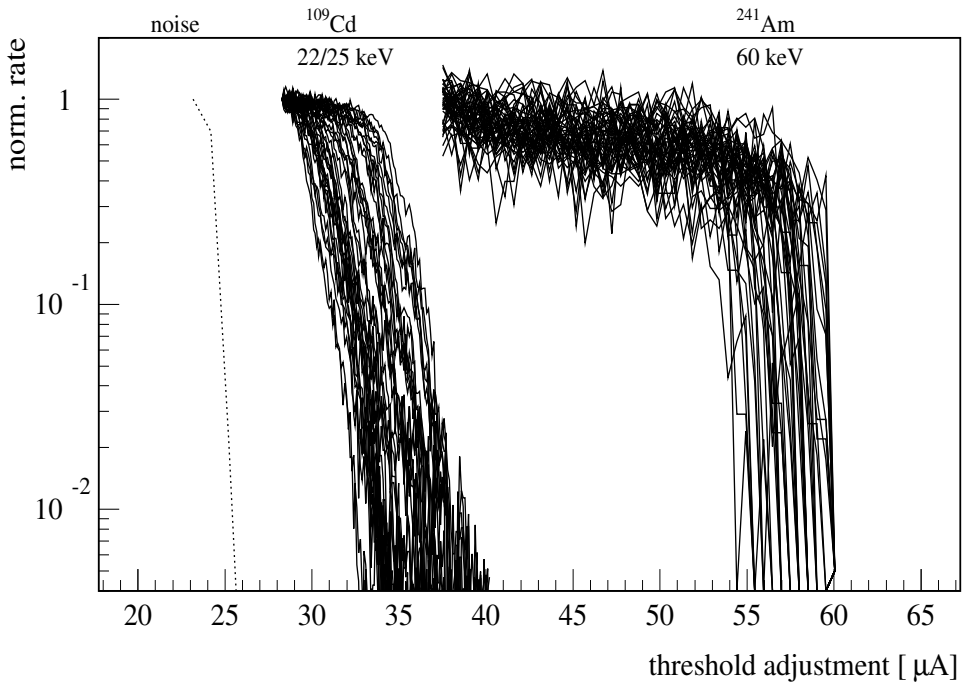

Figure 5.6: Calibration of the threshold current with ^{109}Cd and ^{241}Am γ lines.

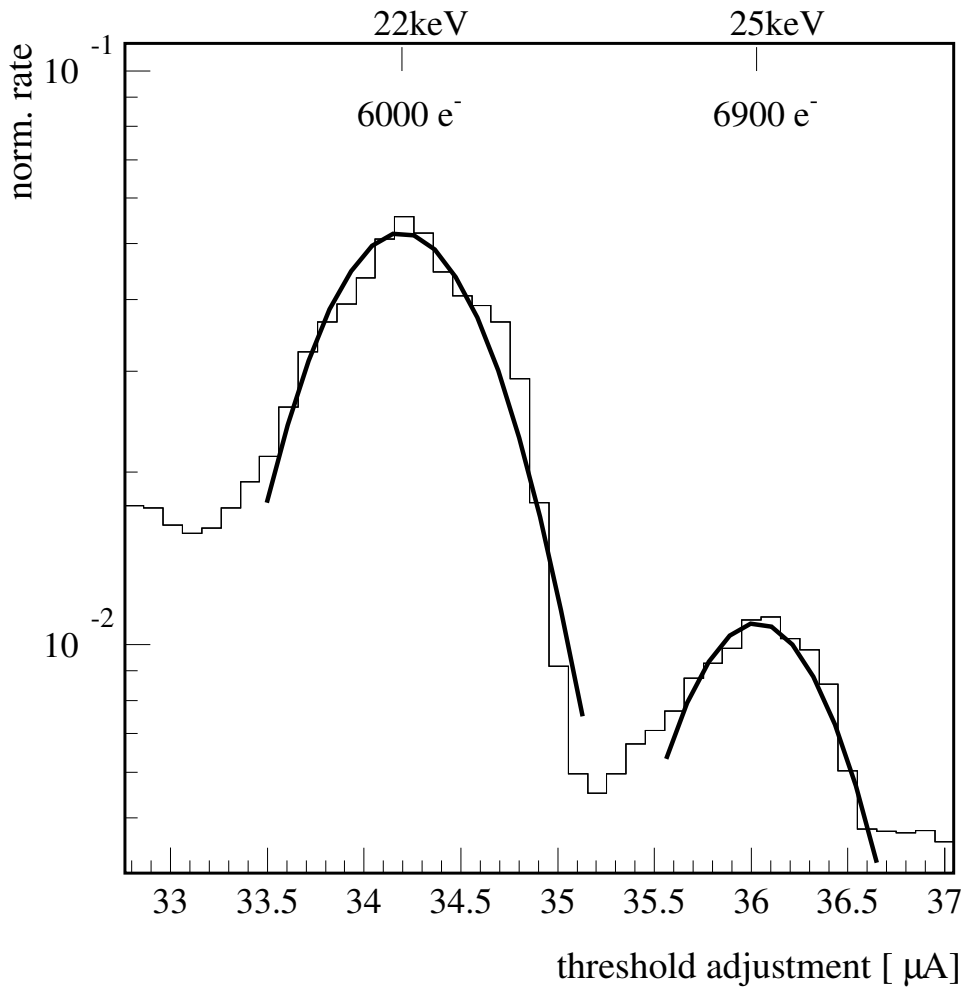

Figure 5.7: Spectrum of ^{109}Cd γ lines measured with the CDFSP6 chip. The two lines at 22 and 25 keV are distinguished. The corresponding charge released in silicon is 6 000 and 6 900 e^-, respectively. From the widths of the lines, an equivalent noise charge of 230 e^- r.m.s. has been determined. The pixel detector yields a signal-to-noise ratio of about 100 for minimum ionizing particles in 300 μm silicon.

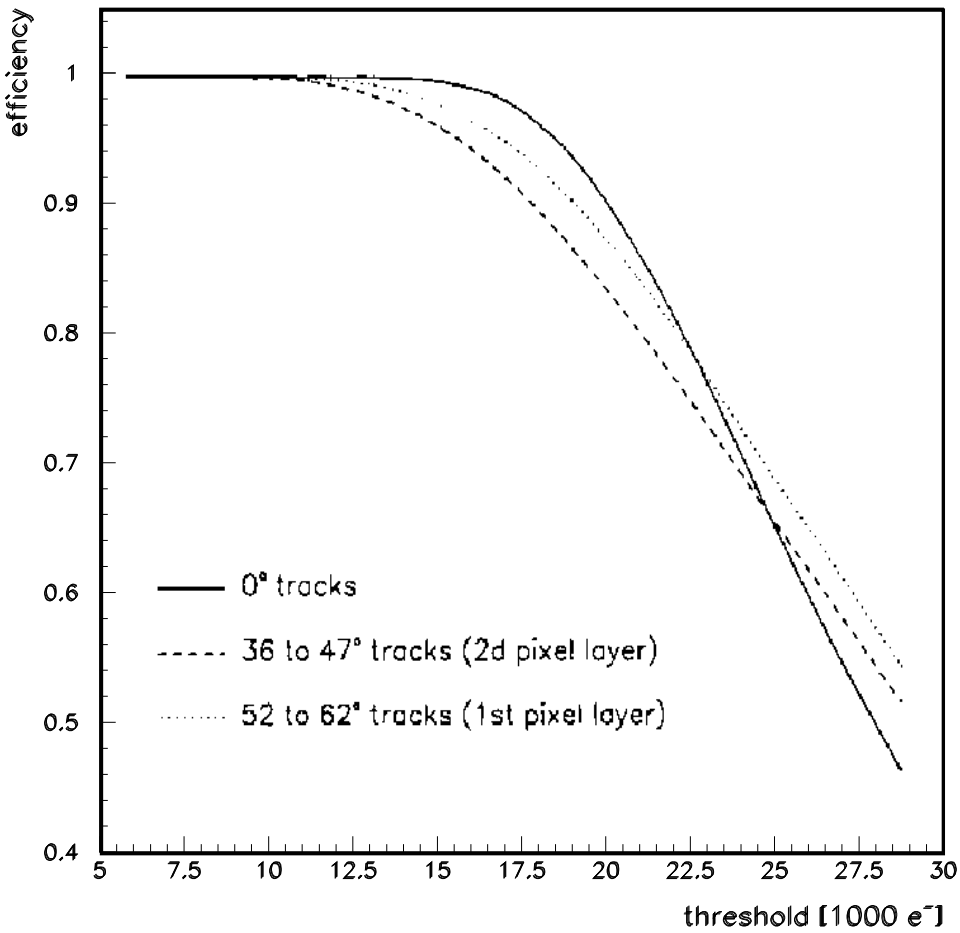

Figure 5.8: Particle detection efficiency as a function of the detector threshold. The curve was obtained from a Monte Carlo simulation with particles releasing charge at different track angles and track lengths in detectors of the DELPHI pixel module geometry [78].

5.2 Sparse Data Scan Readout

The DELPHI pixel detector is equipped with a selective readout scheme, implemented in the front-end electronics and yielding ambiguity-free coordinates of active detector cells. With respect to the expected low occupancy of less than 10^{-4} of all pixel per event, zero-suppression is applied during the readout. Areas with no hits are skipped and need no readout time, improving vastly the detector readout speed.
The "Sparse Data Scan" circuit has been developed at Collège de France as a part of the RD19 project. Details have been described in reference [79] where also the implementation in the DELPHI front-end chips is reported.

The Sparse Data Scan readout is fully hardware-implemented. The principle is visualized in block diagram 5.9, representing a small array of 2 × 3 pixels. If a pixel is traversed by a particle and the signal exceeds the threshold settings, or if a pixel is noisy and yields a fake signal, its output latch switches and stores the detection result. Hit pixels close two extra "switches" to enable contact to row and column logic lines. An active row logic line indicates that at least one pixel in the corresponding row was hit and needs to be read (switch A closed).
Priority logic blocks associated to every row and column of pixels scan the states of these logic lines synchronously to a clock signal. A row priority logic sets the scanning to the hit row which has the highest priority, e.g. the first one of a chip containing hit pixels. As soon as the readout trigger is received, this row is analyzed. A validation signal is returned to the hit pixels of this row and connects through the switches B to the column logic lines, thus marking the hit pixels there and solving the ambiguity. The columns are now scanned by a similar column priority logic. With every clock cycle one hit column is scanned. Switching to the next active row needs one extra clock cycle.
For every hit pixel, a pair of binary encoded line and column addresses as well as a synchronous validation signal are sent to a data bus which can be read by an external acquisition system. Empty rows and columns are skipped without loss of time. Several chips containing the Sparse Data Scan can be chained to yield larger areas with autonomous sparse readout. The overall readout duration for a contiguous area equipped with the sparse data scan is

$$\mathrm{t} = \mathrm{T} \times (\text{no. of rows with hits} + \text{no. of hit pixels}),$$

with T being the clock cycle period. The maximum design clock speed is 10 MHz with the SACMOS process.

The Sparse Data Scan was tested with several of the chip prototypes. Results have been reported in references [80, 81, 82].
The readout circuit contains a self-test where all pixels in the array are simulated to be hit. During the scanning the sequence and order of addresses can be checked and

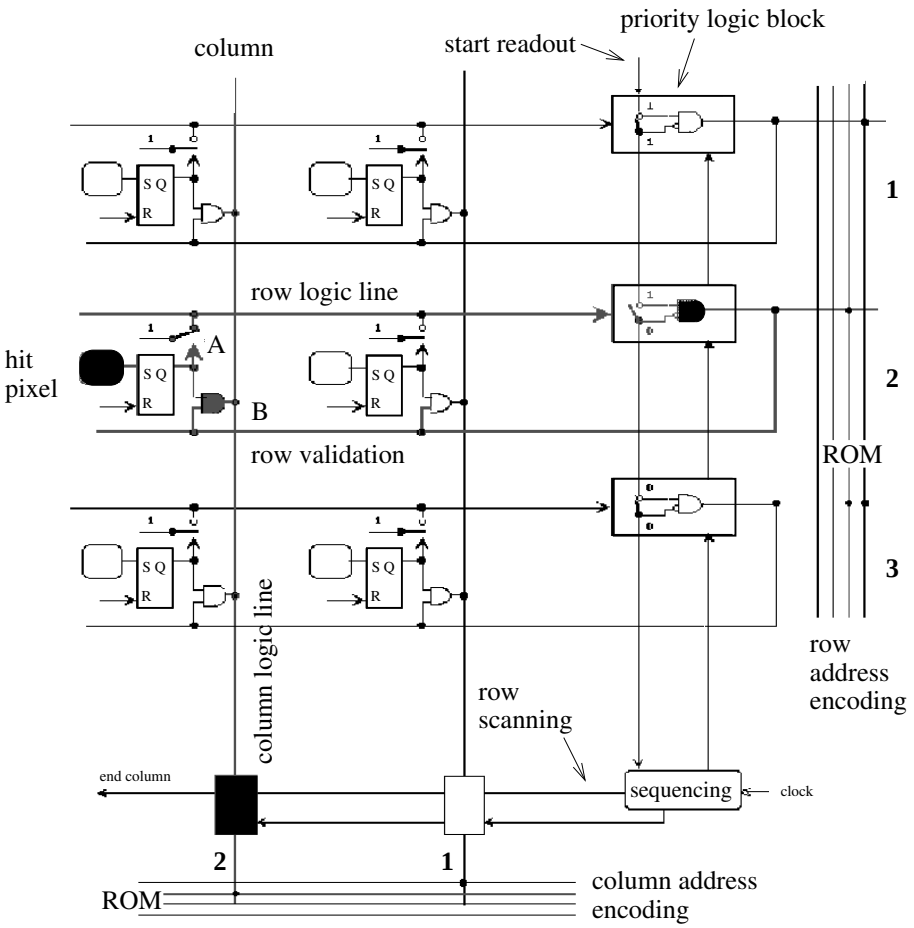

Figure 5.9: Principle of 2-dimensional sparse data scan readout.

analyzed for errors.
Single pixels or more complicated patterns had to be activated externally. For single pixel studies a laboratory set-up was constructed that directed a focused infra-red laser beam onto the pixel array of the readout chip. This way of signal generation exploited the fact that the transistor structure responsible for the leakage current compensation in every pixel was sensitive to light and injected charge into the pixel's amplifier. Since there was no need for calibrated signals, pulsed and quasi-static light sources could be used. Laser spot diameters of less than 10 μm were reached, enough to stimulate single pixels.
Complex patterns were studied with visible light, generated by a mask and projected through a microscope onto the pixel arrays. Figure 5.10 shows the situation with a diagonal pattern on the CDFSP3 chip. The sequence of output signals was recorded as given in figure 5.11. The clock cycle was 2 μs. After the start of the readout with the

CIN signal switching to active state, 5 data ready pulses (DTR) indicate that 5 valid pixel addresses were read and output to the address bus. The addresses are encoded with the column bits C0-C3 and row bits L0-L5. The readout is finished with COUT switching to active state.

The tests stated an operational Sparse Data Scan readout. No readout errors occurred up to 10 MHz readout speed.

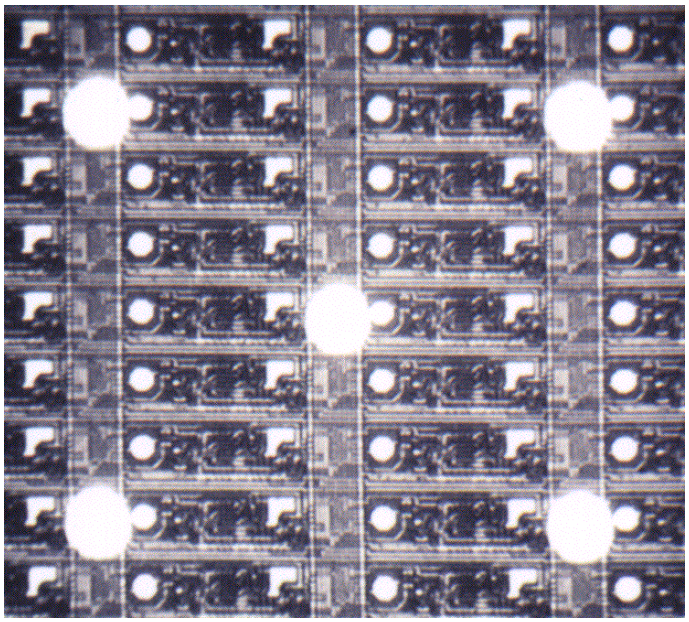

Figure 5.10: Pattern of light spots projected onto a CDFSP3 chip.

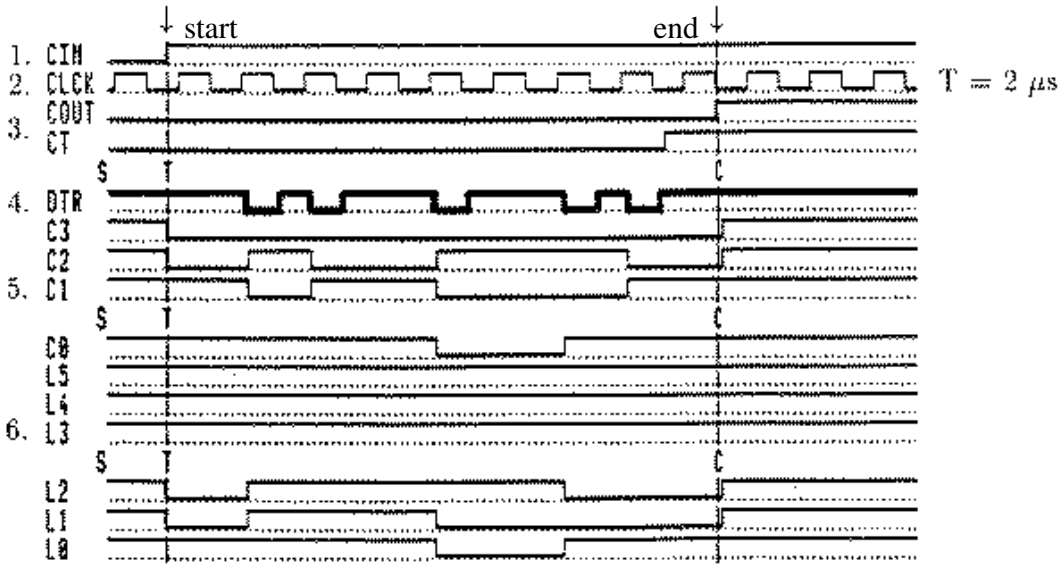

Figure 5.11: Sequence of output signals from the pattern in fig. 5.10. Synchronously to the clock signal CLCK, the addresses of hit pixels appear on the data bus (column bits C0-C3, row bits L0-L5). The presence of valid data is indicated by the data-ready signal DTR. Active pixels in the same row were output with every subsequent clock cycle. Switching to the next row with active pixels required an extra clock cycle.

5.3 Bonding technologies

The very high number of electrical interconnections between the detector and electronics components in hybrid pixel detector systems is a real challenge and requires a high bonding efficiency. A certain failure rate might be tolerable within the pixel matrix and would affect the overall efficiency only sightly. With multi-chip modules, however, where also the electrical contacts of readout chips are established with the same bonding technology, failures on the chips' supply contacts might result in the loss of large fractions of the detector.
Next to the design and production of the detector components, the bonding represents a considerable effort of the construction which reflects also in the costs if patented industrial micromechanic processes are considered. The availability of alternative, "cheap" bonding technologies was therefore very attractive for the realization of the DELPHI pixel detector project, even a supposition at the beginning of the planning to stay within the given financial budget. Modern flip-chip interconnection techniques have been overviewed recently in reference [17].
The rather large size of DELPHI's macro-pixels allowed to study interconnection methods using anisotropic film and conductive glue next to the established and usually expensive industrial bump bonding.

Anisotropic film bonding

Anisotropic conductive adhesives are widely used in electronics industry for connectorless connections in all kinds of commercial products. The method has been especially developed for connecting flexible printed circuits to printed circuits boards, characterized by a rather low number of wide-spaced contact pads.
Anisotropic film bonding uses polymer films filled with grains of conducting material, e.g. silver. The insulating thermoset adhesive has a higher coefficient of thermal expansion than the composite conductive particles. The film is placed between the components to join. A thermo-compression process is applied to melt the polymer and to establish electrical contact between the conductive pads of the hybrid's components.

The feasibility of this low cost method has been tested for passive connections with microstrip detectors [84]. At CPPM, Marseille, anisotropic film bonding has been applied to pixel detectors [85]. Metal jigs have been engineered where detector, adhesive film[2] and readout chips are sandwiched and mechanical pressure is applied while heating the setup.
Working assemblies of single readout chips connected to small detector arrays were obtained. While the contact resistance of about 200 mΩ, measured with several hundreds of individual pixels, matched the requirements, the yield was not satisfactory when connecting 16 chips to a common bus. Even with a rather low probability p

[2] 5303R z-axis adhesive film by 3M

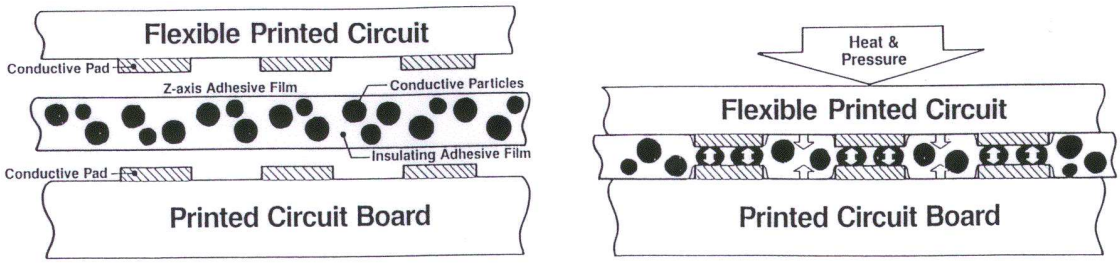

Figure 5.12: Film bonding technology [83]

for single chips to fail, the total probability for a module is significant and calculates as 1 - (1 - p)^{16}. The problems arose on the edges of the readout chips where loss of contact with input/output pads occurred. The method of film bonding tended to lift off these contacts when applied to two rigid components and could not be used for the detector production therefore.

Serigraphy bonding

A working group of INFN Milan has studied serigraphy bonding for the use with the DELPHI macro-pixel detector [86]. A similar process was already applied before at CERN to contact structures with microstrip detectors.
Serigraphy bonding or screen printing is a technology developed originally for thick film circuit processing where two components of a flexible circuit have to be connected electrically at low costs. Conductive glue is deposited on a substrate by the means of masks with precisely machined holes matching the contact pads. The glue is deposited by a blade, sliding on the mask with a certain pressure. Both the holes' dimensions and the pressure of the blade determine the size of the deposited glue drops. Substrate and screen need to be precisely aligned in parallel in order to yield uniform glue drops. A screen printing machine has been set up in Milan where different masks could be applied. Holes with diameters from 70 μm to 120 μm were realized by chemical etching of 50 μm iron foils. Best results were obtained with 80 μm holes. With smaller diameters, insufficient amounts of glue reached the contacts. Larger holes led to short circuits to the neighboring drops.
After the glue has been deposited onto the detector the readout chips are flipped and precisely aligned by optical means. Both the horizontal and vertical alignment is surveyed. The glue polymerizes finally in an oven at 110°C and a mechanically robust assembly is obtained.
After optimization of the machines' parameters, a missing contact rate of (0.05 $\pm$0.03)% was reached, estimated from a sample of single readout chips bonded to matching detectors. Resistance measurements resulted in 1 Ω per contact for normal pads. Gold

bumps deposited additionally on the aluminum pads yielded 150 mΩ. No significant increase of the detectors' leakage currents was observed before and after the bonding.

The serigraphy bonding was finally not considered for the serial production of the DELPHI pixel detector. It turned out to be very difficult to control many subtle mechanical parameters of the screen printing machine, resulting in non-operational modules when connecting 16 chips to the detectors.

Bump bonding

The technology of chip interconnection by arrays of solder, gold or indium balls ("bump bonding") was developed by IBM during the 1960's [87]. The intention of this method was to provide an alternative to wire bonding and to obtain a higher density of contacts and packaging. In a "flip-chip" process (see fig. 5.13), chips are attached face-to-face to other circuitries, with contact pads matching on both components. Solder balls deposited on the pads of one of the components are heated and form contacts in a *Controlled Collapse Chip Connection (C4)*, providing self alignment and chip separation by the surface tensions of the solder alloy in its molten state (see fig. 5.15). While IBM used the bump bonding technology only for in-house products over a long time and did not offer the process as a product of its own, other companies developed similar bonding techniques. The RD19 collaboration developed their hybrid pixel detector systems together with GEC Plessey, United Kingdom, which concentrated especially on small bumps down to 10 μm diameter [37]. IBM bump bonding with less extreme parameters became available for customers during 1994 [89]. The attractively low price made this approach affordable for the DELPHI pixel detector project.

C4 bumps are deposited through a bump mask onto solder wettable chip pads, forming truncated cones of lead. The metallurgy is shown in figure 5.14. The high lead content is necessary for increased reliability of the bond and high melting temperature in case that subsequent processing is foreseen. Tin reduces solder oxidation and forms strong inter-metallic bonds with the copper in the pad limiting metals. A non-oxiding re-flow process yields the final round C4 bump, ready for the flip-chip process.
Electrical and mechanical interconnections are formed simultaneously by thermal re-flow with flipped and aligned chips in an inert atmosphere at 360°C.

IBM offers four options of C4 processing as listed in table 5.3. For the DELPHI pixel detector design, standard option A was chosen initially. Bump bond diameters and pitches matched the electronics cell and chip design. Systematic shifts of the bump bonds by up to 30 μm which occurred on several wafers during the prototyping and which affected the electronics performance by adding capacitive load to the amplifier inputs led to a revised pad size. The layout of the pixel cells is shown in figure 5.3. On pads with 80 μm diameter bump bonds with 100 μm diameter and heights of 30 μm according to option C are grown. IBM describes option C as difficult to manufacture

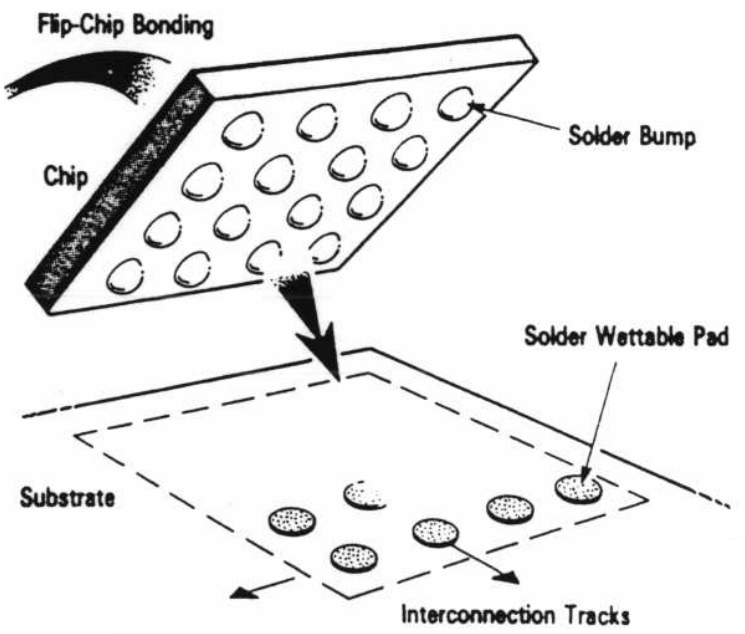

Figure 5.13: Schematics of the flip-chip bonding process [37].

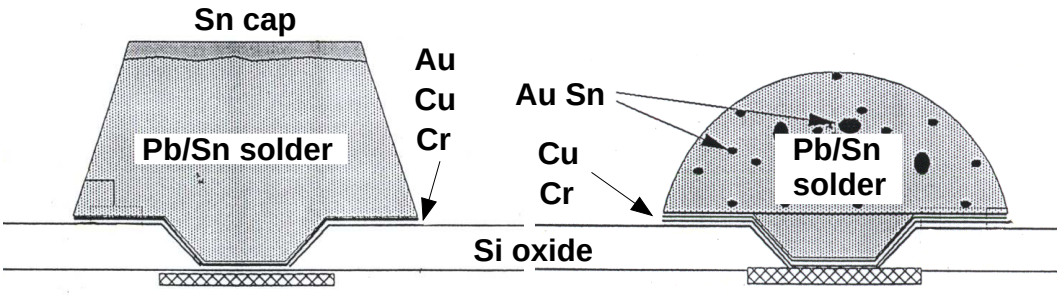

Figure 5.14: Principle of the C4 bump bonding technology by IBM. Left: solder deposited on bond pad. Right: bump after thermal re-flow, ready for the connection to the hybrid component [89].

resulting in a lower wafer yield compared to the standard options A and B. The photo in figure 5.16 shows chip CDFSP8 after this metallization. A contact failure rate of $(2.4 \pm 0.2) \times 10^{-4}$ was achieved, matching the aspired maximum rate of 5.0×10^{-4} necessary for 80% yield of the assembled detector modules [78].

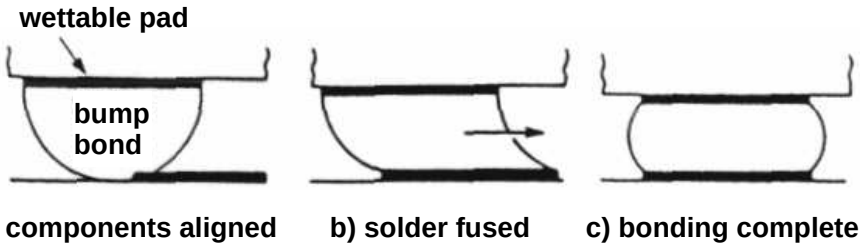

Figure 5.15: Process of self aligning and bonding [37].

C4 bump bonds	bump diameter [μm]	min. pitch [μm]
option A	150	300
option B	125	250
option C	100	225
option D	150	350

Table 5.3: IBM C4 bump bond process options [88].

5.4 The detector substrate

The detector substrate has been designed at CPPM and manufactured from 300 μm thick high resistivity silicon wafers by CSEM[3]. The layout is shown in figure 5.17. Two of the 6.9 cm $\times$ 1.7/2.3 cm wide structures fit on a 4 inch wafer.
The active surface is sub-divided into 10 regions of 24 $\times$ 24 pixels and 6 regions of 16 $\times$ 24 pixels where the large and small readout chips are bump bonded to. Pixels at the boundaries of neighboring readout chips have doubled or fourfold dimensions to ensure a fully sensitive surface.
Next to the pixel structures bus lines have been integrated into the silicon. They run along the rim of the detector, bringing input and output signals to each of the readout chips and providing power supply. A double metal process was applied. The aluminum lines are 0.5 μm thick at widths of 20 μm (logic signals) and 150 μm (power lines). Contacts from the bus to the chips are established by the same bump bond process as with the pixel array. Two rows of pads are placed next to the small chips to allow to connect the bus to an external readout cable.
The integrated bus minimizes the amount of material associated with the detector,

[3]Centre Suisse d'Electronique et de Microtechnique, CH-2007 Neuchâtel, Switzerland

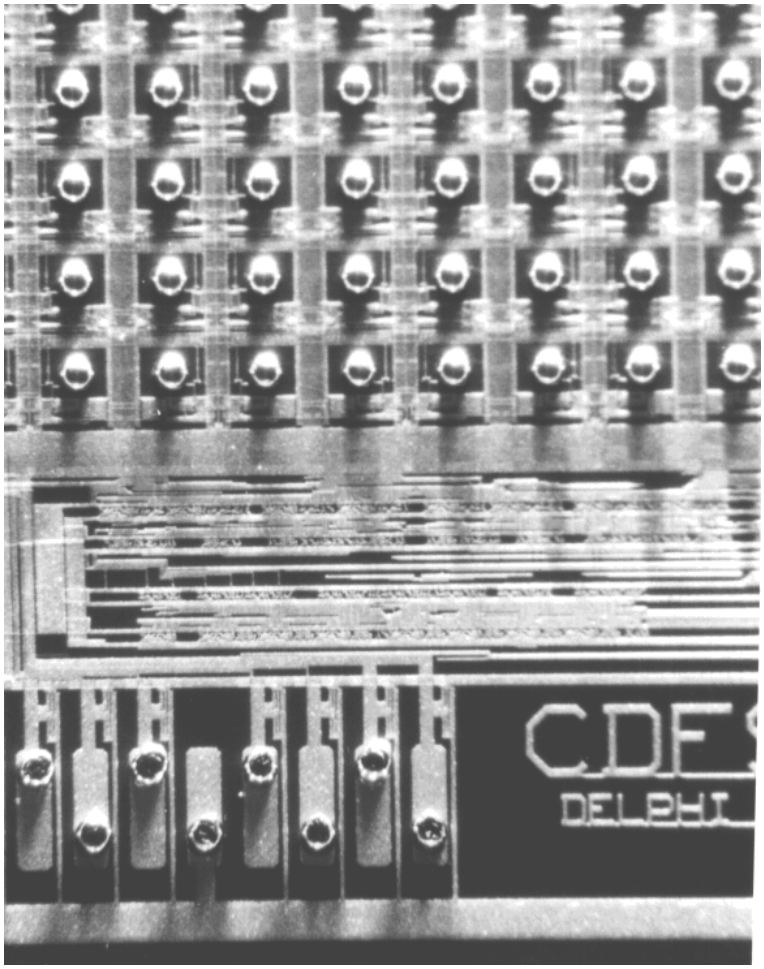

Figure 5.16: SP8 readout chip with bump bonds in the pixel array and on chip pads.

and multiplexing limits the number of signal lines. The conceptual advantage, however, demands for a high-quality interconnection technique with low failure rate. The bus structures on the detector required extra test procedures to detect possible interruptions or short circuits.
The photograph in figure 5.18 shows a close-up view of a detector region where a small readout chip was removed for test purpose after the bump bonding. Remaining solder is visible both in the pixel array and on the chip contact row. Pads for the connection of the bus to the readout cable are seen close to the detector rim.

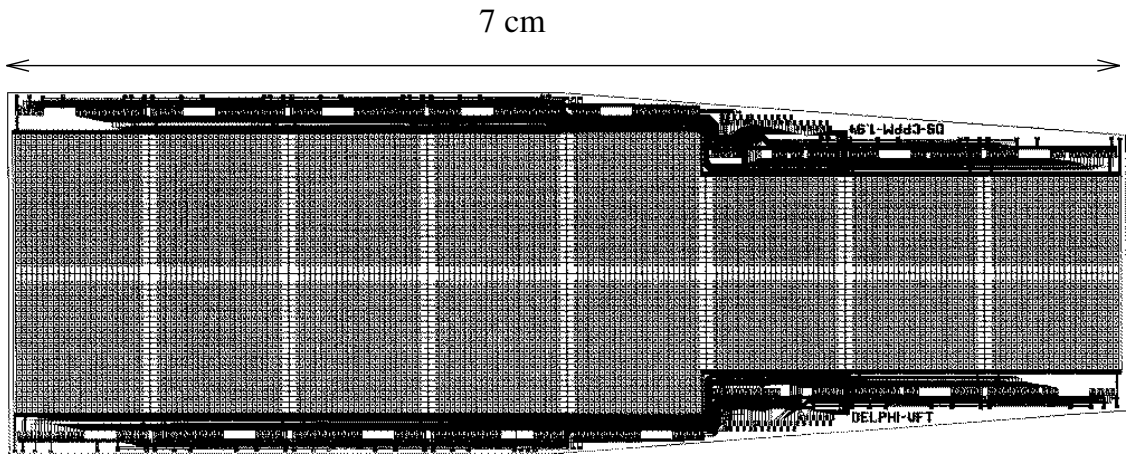

Figure 5.17: Layout of the pixel detector substrate with integrated bus.

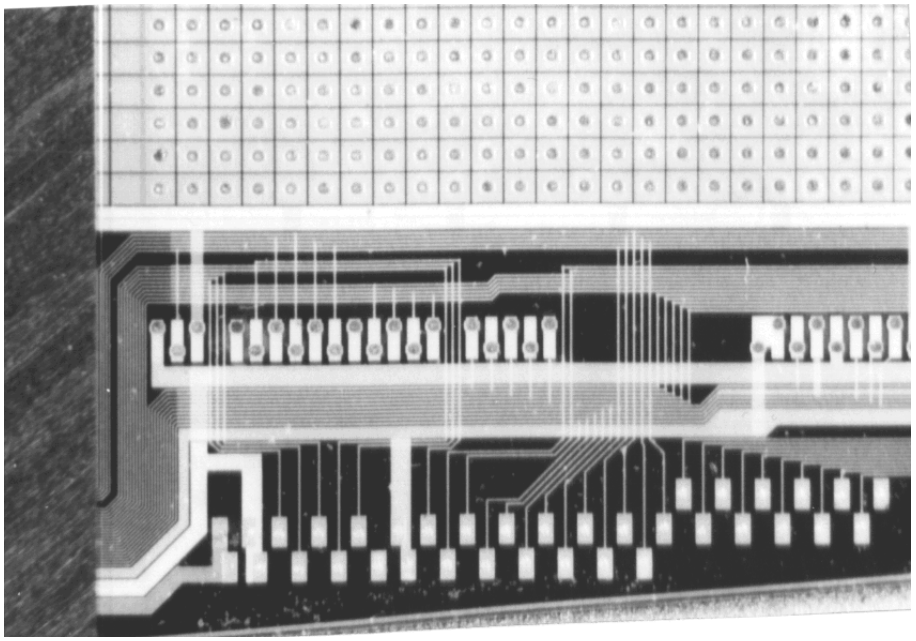

Figure 5.18: Detector region with integrated bus, chip contact row and pixel array. For test purpose a chip was removed again after the chip flipping. Remaining bump bonds are visible both in the pixel array and on pads to connect the chips to the integrated bus.

5.5 Module pre-production and test beam results

A first verification of the concept of the DELPHI pixel detector module was performed in spring 1995. A pre-production was started to prove that all selection and construction steps were appropriate. Two modules were assembled and characterized in a test beam run.
A 6 inch CDFSP5 wafer equipped with C4 bumps was delivered untested from the foundries. A semi-automatic wafer test station was concepted and set up at CPPM Marseille for probing and selection of the 180 chips. The detector wafer was delivered by CSEM and tested at Karlsruhe University. Test procedures already with the foundries would have increased the costs of the project significantly. Extra flexibility was gained with the selection of good components performed in the collaborating institutes.

5.5.1 Test of the electronics wafer

The method to characterize basic properties of the readout chip has been described in references [73, 90].
A semi-automatic probe station accessed every chip on the wafer. The machine was controlled by a personal computer, describing the wafer's geometry and orientation, the number of chips and their pitch. For every chip, a probe card equipped with contact needles with convex tips reached to the bumps on the chips' input/output pads. When a chip was connected to the probe card, a test program was started, activating a system of power supplies, pulse generators and readout facilities. Once the probe station was aligned to the wafer, the entire test proceeded autonomously. Up to 7 hours were required to characterize the 180 chips per wafer.

The tests were performed in hierarchical order. Two steps were distinguished. Functionality at nominal settings was verified first according to the items listed in table 5.4. For every chip, a positive or negative result was yielded and the minimum threshold at $\leq 1\%$ noisy pixels determined.

The second step intended to select working chips with similar characteristics to be grouped on a module. Mean operation parameters were adjusted, determined from the data of the first test. Chips which passed the first test were measured again and their supply currents, voltages, thresholds and threshold slopes filed. The chips were classed into two[4] groups of matching parameters, mainly taking into account the absolute thresholds and their slopes. During the module production, more options in the multi-parameter space were considered when grouping the chips. Nevertheless, it has to be pointed out that the decision on how to group the chips strongly involved the experience gained by the physicists with the electronics prototypes before.

[4]only two detectors were available at that time

step	objective for functionality test
1.1	power consumption within certain limits
1.2	Sparse Data Scan test
1.3	no noisy pixels at very high threshold
1.4	noisy pixels in all columns at very low threshold
1.5	fast threshold scan, find setting yielding 1% noisy pixels
1.6	fine threshold scan, find minimum threshold with test pixels
1.7	measurement of applied supply voltages
1.8	test on even/odd column asymmetry

Table 5.4: Basic functionality tests of readout chips.

Figure 5.19 provides the result with the first wafer of CDFSP5 chips, equipped with C4 bumps. Large and small chips are neighboring in pairs. 64 large and 56 small versions of the chip were found to be operational, represented by the shaded area and yielding 70% and 62%, respectively, of all chips. The result was typical for all later wafer tests. The symbols "r1" and "r2" denote selected chips and indicate the detector they were assigned to after final grouping.
The chips in the top region of the wafer were found to suffer from a misbehavior caused by misaligned masks during the metallization and leading to displaced bumps. This situation is shown in figure 5.20. The mirrored geometry of pixels in neighboring columns was sensitive to the asymmetric input capacitances induced by this effect. Pixels in even and odd columns, operated at a common threshold, did not own the same sensitivity. The measurement shown in figure 5.21 details this "even/odd" effect. Chips with this characteristic had to be rejected. In order to improve the yield, these results led to a revised bond pad size and the use of 100 μm bumps instead of those with 150 μm diameter. The correct placement of smaller bumps supported by the self-alignment improved the situation significantly.

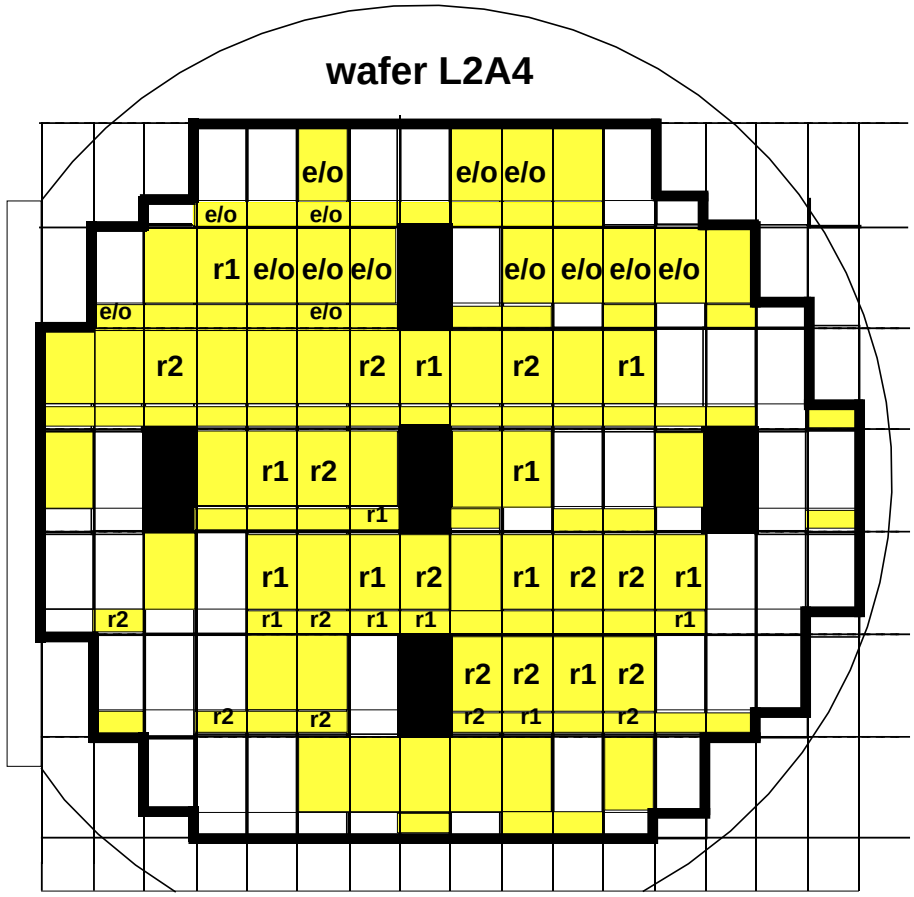

Figure 5.19: Selection of chips for the first two prototype detector modules. Large and small chips are placed in pairs on the 6" wafer. The shaded area marks readout chips which passed the basic functionality test. According to their properties, they were classed into two groups of matching parameters to be used for the first two detector modules ("r1, r2"). Chips from the top part of the wafer were affected by misaligned bumps, resulting in asymmetric pixel sensitivity with even/odd columns ("e/o").

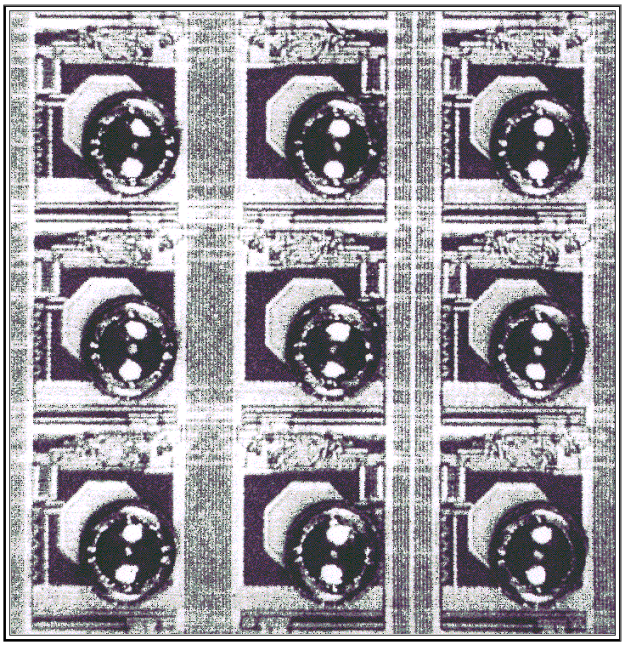

Figure 5.20: Shifted bumps on electronics chips from the border of a wafer.

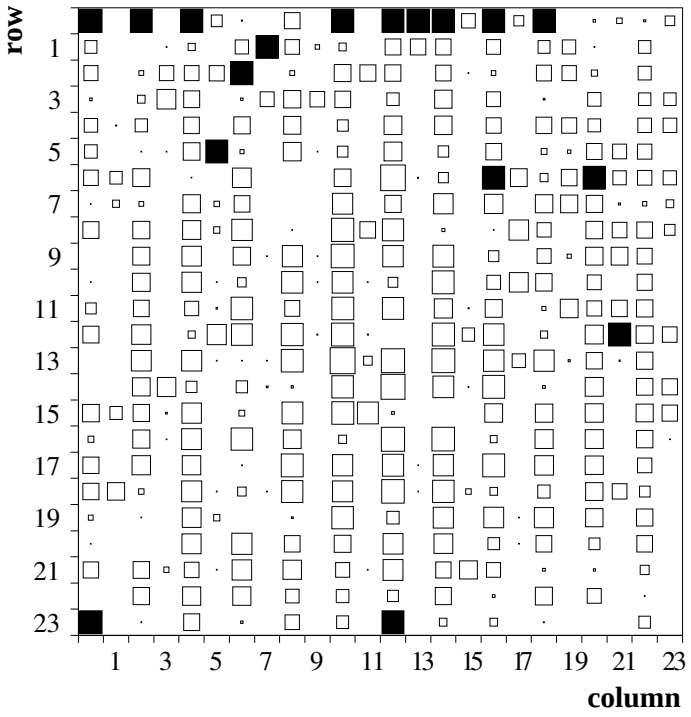

Figure 5.21: Asymmetric hit rates with a CDFSP6 chip bump bonded to a detector array and irradiated with $^{241}_{95}$Am. Even column numbers show correct sensitivity, whereas odd columns deviate significantly. Pixels marked by filled squares were systematically noisy.

5.5.2 Test of the detector wafer

The design of the DELPHI pixel detector module with flip-chip bonding and integrated bus required careful selection of the detector substrates prior to the placement of orders for bump bonding. The test procedure applied at Karlsruhe University evolved from experience with the construction of microstrip modules for the DELPHI vertex detector and has been described in references [91, 92]. The reverse current was measured and every bus line probed individually to sort out detectors with defects.

Full functionality was ensured by measuring the detector capacitance and the leakage current as a function of the depletion voltage. Backplane voltages of up to 100 V were applied. Detectors with leakage currents exceeding 10 μA were rejected; about 3% were affected. Excellent detectors had currents of about 1 to 250 nA.

An automated capacitance measurement was applied when testing the bus lines. The quality of these structures expresses in terms of a capacitance. The important items are the thickness of the passivation or oxide layer, the dielectric constant of the insulator and the geometrical dimensions of the line. Layer thickness and dielectric properties are usually constant. Deviation from the expected capacitance therefore indicates geometrical effects as interrupted lines or short circuits. The method was successfully applied using an automatic probe station. CV-meter measurements yielded typical line capacitances of around 1.5 pF with variations within 20%.
Per detector 607 pads were contacted. In a first step, all pads connected to the same line were checked for similar capacitances. With relative differences exceeding 5%, the line was considered as interrupted. The second step tested on short circuits between neighboring lines. Capacitances exceeding a difference of 20% with respect to a reference value were considered to indicate such a case. In a third step the partner lines of the short circuit were searched to allow for possible repair.
The photographs in figure 5.22 show several classes of defect lines. A mask fault was likely for the short circuits between neighboring lines on several wafers (left). The material was removed by applying high currents to the lines . Dust as shown in the center of the figure could not be removed and interrupted lines (right) not repaired. 9% of all detectors turned out to be affected by bus faults.

5.5.3 Test beam characterization of the first module

A test beam run with the first bump bonded pixel detector module was performed in August 1995 [93, 94]. Two modules were assembled before. One of them was noisy and considered only as a backup. The other detector was installed in a microstrip telescope operated in the H8 beam at CERN's SPS. The beam provided electrons with momenta of 100 GeV/c and pions with 120 GeV/c. The telescope was already in use for the very first test of a single DELPHI pixel chip in 1994, tape bonded to a small detector array [95]. It comprised four scintillators to build the trigger and four double sided

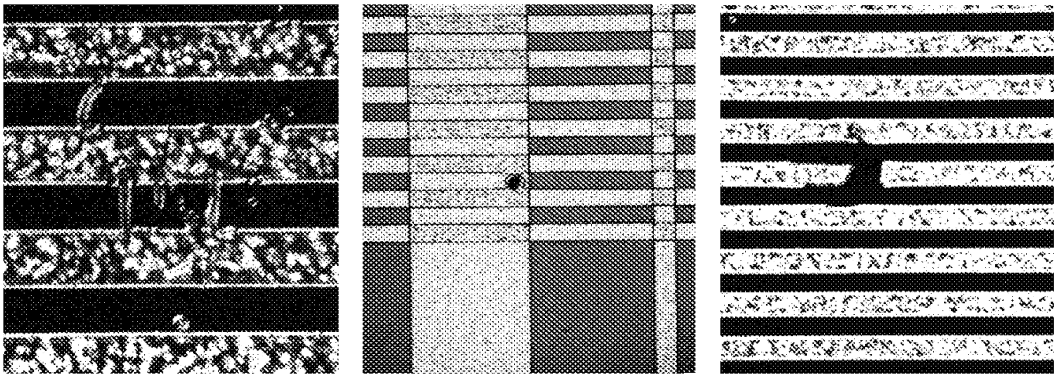

Figure 5.22: Failure classes of the integrated bus. Left: short circuits by metallic pieces; center: shorted lines by dust particle; right: interrupted line [92].

microstrip detectors for the track definition. The pixel detector module was installed in the central part of the 1 m long telescope where the mechanics allowed to turn it around the vertical axis. An inclination of 40° with respect to the incident particles was chosen, corresponding to the situation later on in DELPHI.

The detector module was mounted on a printed circuit board as seen in figure 5.23. Both integrated busses were connected to the power supply and readout systems by 2×36 wire bonds. Decoupling capacitors with lines to the external connector enabled the parallel operation of the 16 readout chips. The backplane of the detector substrate was glued to a large copper pad on the circuit board to provide the depletion voltage.

A first characterization of the detector module in the laboratory yielded an important result which required a significant modification to the final design. It turned out that parts of the integrated bus did not satisfy the necessary specifications. The lines responsible for the power supply of the chips were too resistive ($R \leq 10\ \Omega$). The double metal process was not sufficient for this task. A subsequent drop of the supply voltages occured along the module. Readout chips at the end of the module operated significantly different than the ones in the central part. A common setting and operation was not possible.
Considering the available space on the detector substrate, no improvement with wider lines was possible. This situation enforced a supplementary power bus parallel to the integrated bus. A solution was found using the third dimension and gluing a flexible circuit with the supplementary power bus on top of the bump bonded readout chips. Wire bonds to the power lines on the detector in the proximity of every readout chip provided the appropriate supply. The price for this modification was a module with more material involved, an extra component to manufacture, test and pay, and a more complex module assembly.

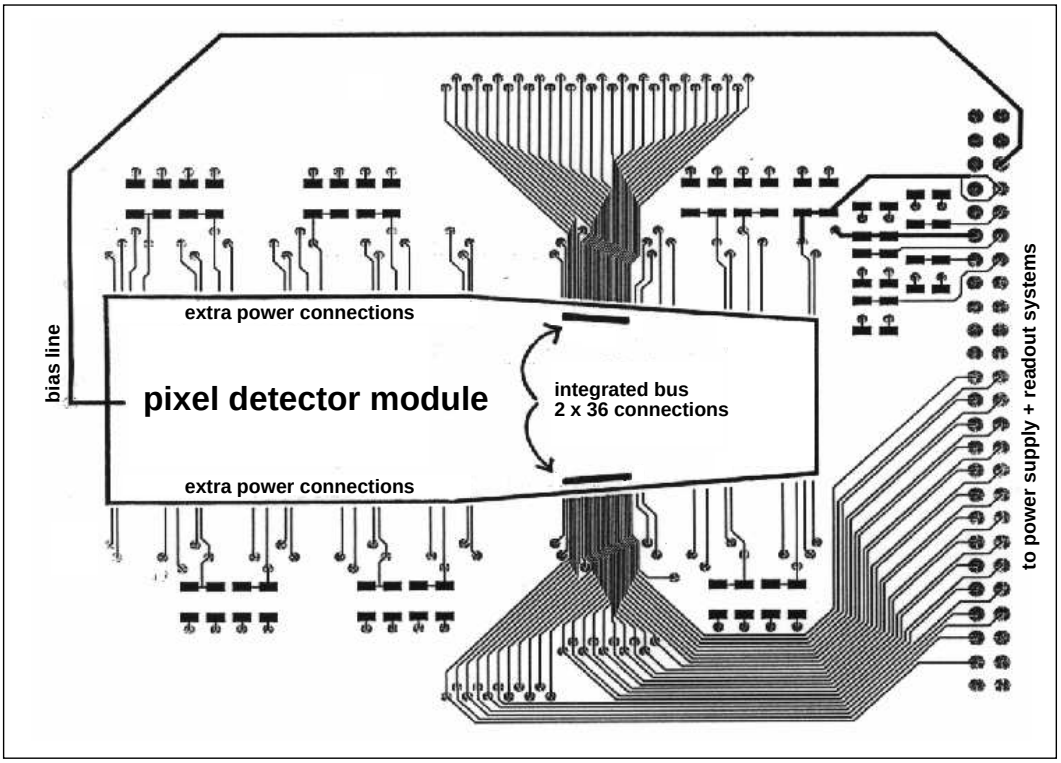

Figure 5.23: Circuit board with supplementary power bus for the test beam characterization of the first pixel detector prototype module.

The supplementary power bus was already taken into account for the test beam setup. Extra lines on the printed circuit board reached towards the rim of the detector. Wire bonds connected from there to the matching lines of the bus. A stable operation of the detector was yielded and 400 000 events recorded, involving the entire detector surface at three different thresholds 6.8, 8.9 and 14.3 $\pm$2.4 ke$^-$.

Noise: A fraction of 0.1% of the pixels in the tested module was systematically noisy. The largest part of them belonged to two entire chip columns which were affected by a short circuit. All noisy pixels were masked for the data analysis.

Cluster size: The remaining detector surface yielded clusters of hit pixels as expected by the particle tracks defined by the silicon microstrip detectors and the module's geometrical orientation in the telescope. Figure 5.24 shows the distribution of cluster sizes in both directions for three different threshold settings. The local x axis pointed along the long side of the module and was sensitive to its rotation with respect to the beam. The y axis along the short side of the module was perpendicular to the beam. In x direction, up to three pixels were traversed by a particle. One and two pixel wide clusters dominated. With raising thresholds, the fraction of one-

pixel clusters increased as expected, blinding out the effect from charge sharing with neighboring pixels. In y direction, a majority of one pixel wide clusters was measured, with a small fraction of events where tracks passed through the intermediate region between two pixels and released enough charge to be detected from both pixels. No significant threshold dependence was found there.

Efficiency: The detector proved to be efficient. The efficiencies for finding a single-pixel cluster and clusters of several hit pixels at the position expected from the track extrapolation are shown in figure 5.25 as a function of the threshold applied. It was noted that the thresholds of individual chips deviated significantly from the mean value which was adjusted for the module. This situation was taken into account for the detector performance study. After calibration in the laboratory, a wide threshold range could be covered finally. Efficiencies exceeding 99% were yielded at thresholds below 10 ke^- to find a cluster of hit pixels at the position expected by the track extrapolation. Single-pixel hits were found with the same result below 8 ke^- thresholds.

Spatial resolution: The spatial resolution obtained from the residuals between extrapolated track position and measured hit, i.e. the geometrical center of the clusters or single pixels, matched the expectation 330 $\mu m/\sqrt{12} \approx 95$ μm. Figure 5.26 summarizes the results for one-pixel clusters and two-pixel clusters. The resolution in x direction was sensitive to the rotation angle and the resulting particle track length in the detector. One-pixel clusters yielded resolutions of better than 70 μm. Two-pixel clusters allowed to determine the track position down to 30 μm by means of interpolation. In y direction, single pixel clusters yielded about 95 μm and double pixel clusters about 10 μm resolution perpendicular to the beam, independently from the threshold applied.

Assessment

The test beam results stated a working detector technology. High particle detection efficiency, small cluster sizes associated to particle tracks and a spatial resolution matching the design expectation were measured. It was shown that thresholds of less than 10 ke^- could be adjusted where the detector was still fully efficient and that the fraction of noisy pixels was negligible.

At the same time it became clear that a successful operation of a detector module could only be achieved with carefully selected components. The detector substrates had to be free from defects and the readout chips needed to be grouped for matching operating parameters. An extra component had to be designed to support the power supply of the readout chips, complicating the detector production but ensuring operational modules.

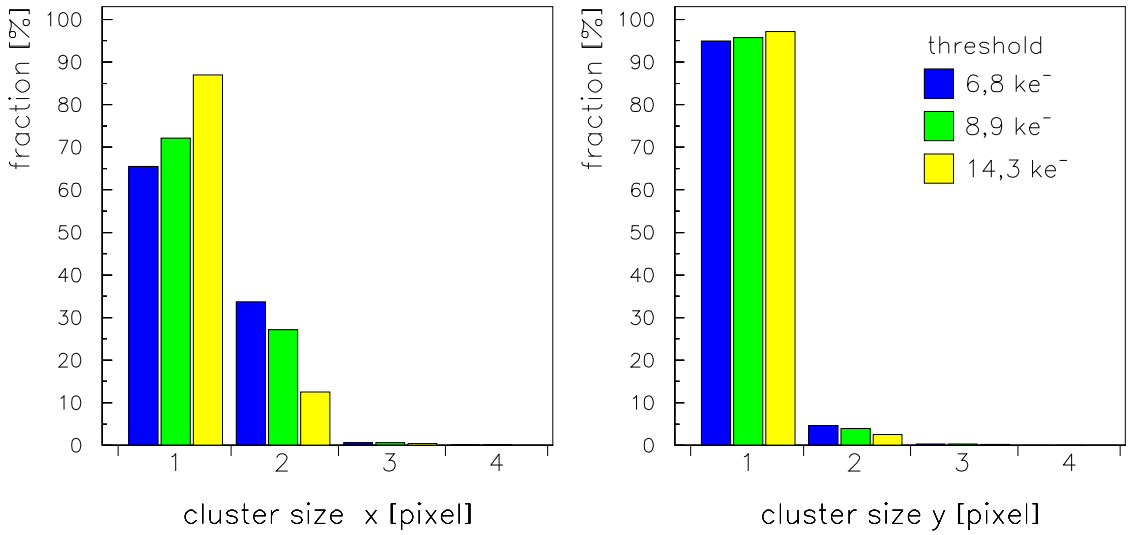

Figure 5.24: Pixel detector cluster size in local x and y direction at 40° angle of incidence for three thresholds applied.

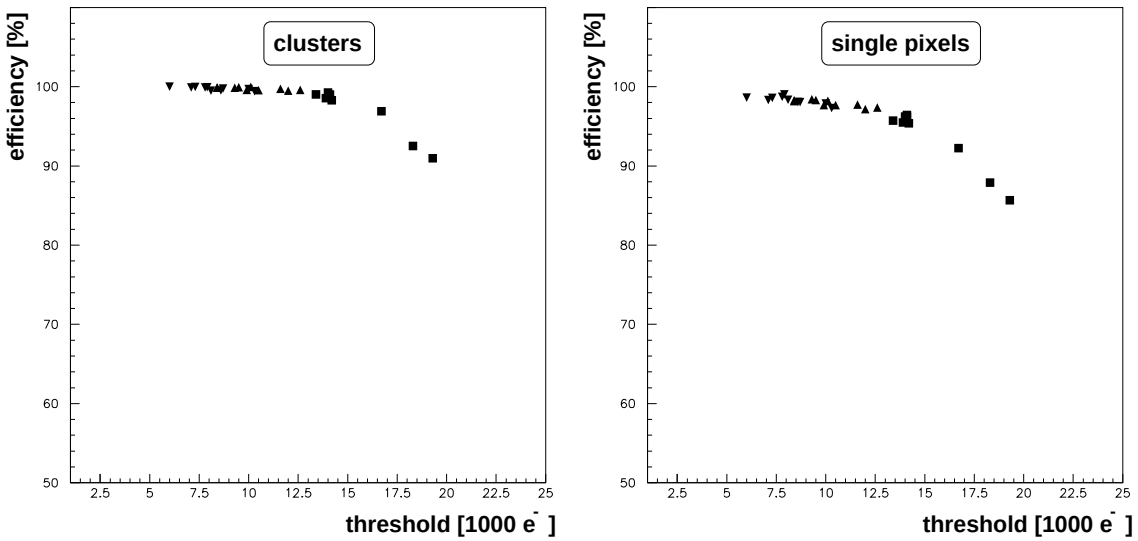

Figure 5.25: Detector efficiency as a function of the threshold.

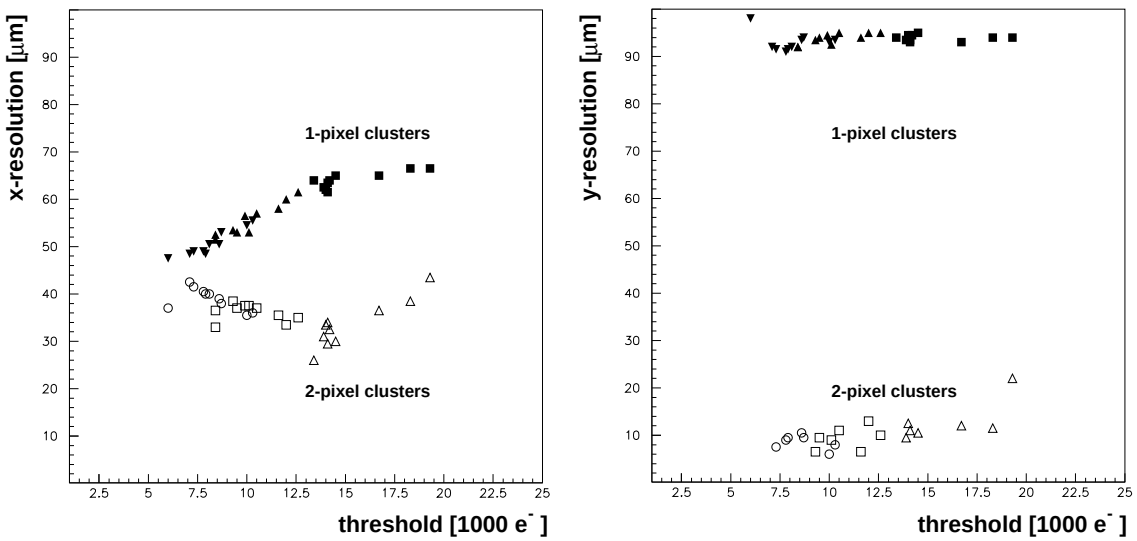

Figure 5.26: Spatial resolution as a function of the threshold.

5.6 Module production

Four physics institutes in three countries and six industrial partners were involved in the production of the DELPHI pixel detector modules. The sharing of tasks required logistic effort to match work flow and deadline for the detector assembly. Availability of components and processing in due time had to be assured, taking into account quality tests and shipping. The assembly sequence and procedures, functionality tests and the yield of the production are discussed.

5.6.1 Module assembly

The composition of a pixel detector module, equipped with all components, is schematically shown in figure 5.27.
The readout electronics is bump bonded to the detector substrate. A "flat" kapton[5] cable, glued on top of the readout chips, carries the additional power bus. A second "long" kapton cable connects the module to the data acquisition system. It is glued on top of the flat kapton. Wire bonds provide contact to an adapter layer in the flat kapton, from where another set of wire bonds addresses the bus pads on silicon. Extra wire bonds for the supplementary power connections of every readout chip are established along the detector rim. A ceramic piece glued to the small detector side serves to fix the module to the mechanic support.

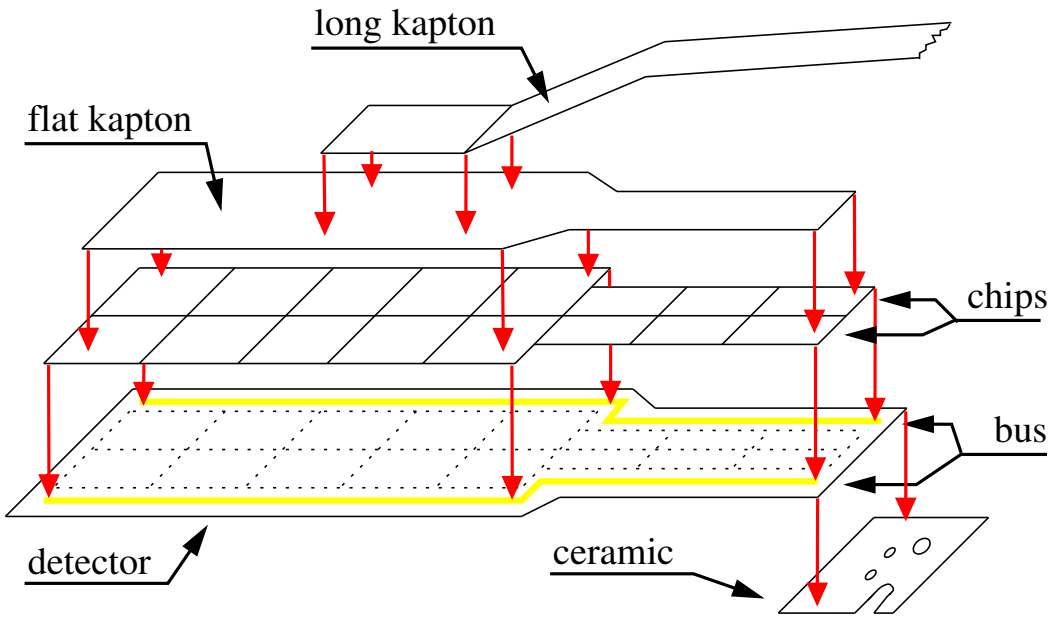

Figure 5.27: Components of a pixel detector module.

[5]polyimide film by DuPont, Wilmington, Delaware, USA

industrial supplier	module component or task
CSEM, Neuchâtel, CH	detector wafer
FASELEC, Zürich, CH	electronics wafer
IBM Corbeil + Montpellier, F	metallization + bump bonding
SCISEM, Aix-en-Provence, F	dicing
CHEVAL, Besançon, F	ceramic support
TELEPH, Meylan, F	"flat" + "long" kapton cable

Table 5.5: Industrial suppliers of components for the DELPHI pixel detector.

Assembly step 1: Wafer test and bump bonding
The module assembly started with the on-wafer tests of detectors and bumped readout chips, delivered from the suppliers (see table 5.5) to either CPPM Marseille or Karlsruhe University. The test procedures applied have already been described in chapter 5.5 when discussing the pre-production. Good detectors and chips were identified and the wafers sent for dicing. The detectors and sets of 16 readout chips with similar characteristics were then flip-chip assembled by IBM (see fig. 5.28) and returned to the laboratory in Marseille where a first test of analog and digital functionality was performed by probing the detector with a special test card. Working modules were sent to Wuppertal University where ceramic support and flat kapton cable were attached.

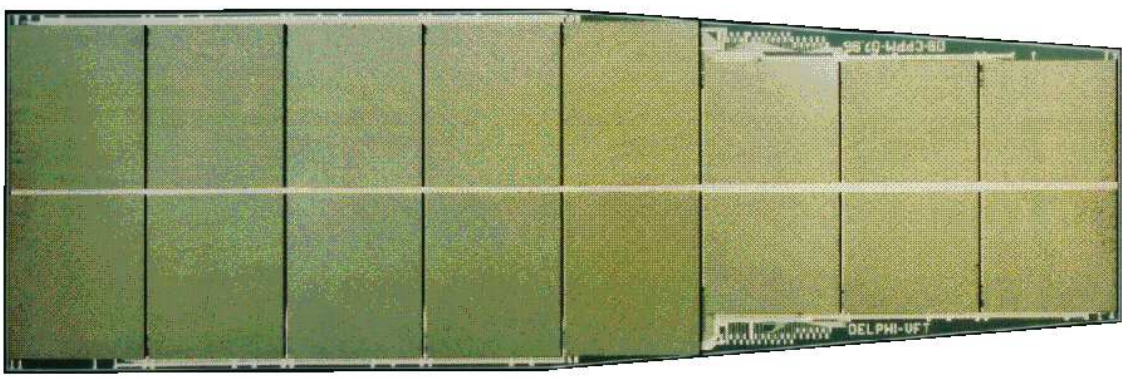

Figure 5.28: Pixel detector module with bump bonded chips.

Assembly step 2: Attachment of ceramic support and flat kapton
The ceramic support pieces are laser cut from 300 μm thick SHAPAL, an aluminum nitride ceramic chosen for its high electrical resistivity, mechanical strength equivalent to aluminum, high thermal conductivity and thermal expansion close to the one of

silicon [96]. High resistivity is important to insulate the modules electrically from DELPHI's common ground; the ceramic is glued to the detector backplane where the depletion voltage is applied. Mechanical strength is required since the modules are fixed at one end only and strong forces might apply. Thermal conductivity and expansion matching the one of silicon are required to drain heat from the detector module and to insure minimum mechanical stress.
Two ceramic shapes were designed to be used with the modules of the internal and external detector layers. The layout of the pieces is shown in figure 5.29. The ceramic for the external layer is more shallow than the one for the internal layer to match the reduced available space at the modules' support side there. Two precision pins fit into the accurately machined slit and one of the holes to define the final position of the modules. Screws through the remaining holes fix the module to the mechanical support.
The flat kapton hybrid is shown in figure 5.30. It consists of two 300 μm thick components. The component extending over the entire module length is copper-plated on both sides. A contiguous copper layer faces towards the readout chips. The copper layer on the opposite side is etched and forms the additional power lines as well as pads for decoupling capacitors. The second component is mounted on top of the first kapton near the central part of the module. It serves as an intermediate adapter piece and provides routing from a single set of input pads to the pads for the connection to the two bus systems on silicon.
The flat kapton cables were delivered to Karlsruhe where the surfaces were cleaned. The functionality of every line was verified and the capacitors were soldered to the pads. Batches of tested cables were sent to Wuppertal, where also the detector modules from Marseille and the ceramic supports arrived for the assembly. The attachment of ceramic and flat kapton to the silicon detector was performed in two steps in the Wuppertal laboratory, where specially designed and CNC-machined aluminum jigs were used to minimize production tolerances. Reference [97] provides a detailed description of setup and procedure applied. The technical layout of the jig is shown in figure 5.31. An aluminum block was counter-sinked to place, align and fix the components. Adequate spacing was taken into account with respect to the amount of glue applied. Pipes and drills machined in the aluminum allowed to apply vacuum to fix the pieces during the gluing process.
First the ceramic was placed in the sink visible in the right part of figure 5.31. Precision pins as in the final detector support fixed its position. Thermally conductive glue (E704, see table 5.6) was applied to the ceramics using a dispenser operating with clean and dry pressurized air. The droplets of glue are seen in figure 5.32. Then the detector was placed in the jig, horizontally aligned by positioning pins and vertically fixed by vacuum. Ceramic and silicon overlapped horizontally by 4 mm and were spaced by 100 μm. The jigs were equipped with an electrical heating. The application of 80 °C, controlled within ± 1°C, allowed for an accelerated hardening of the glue. The bump bonds were not affected at this temperature.

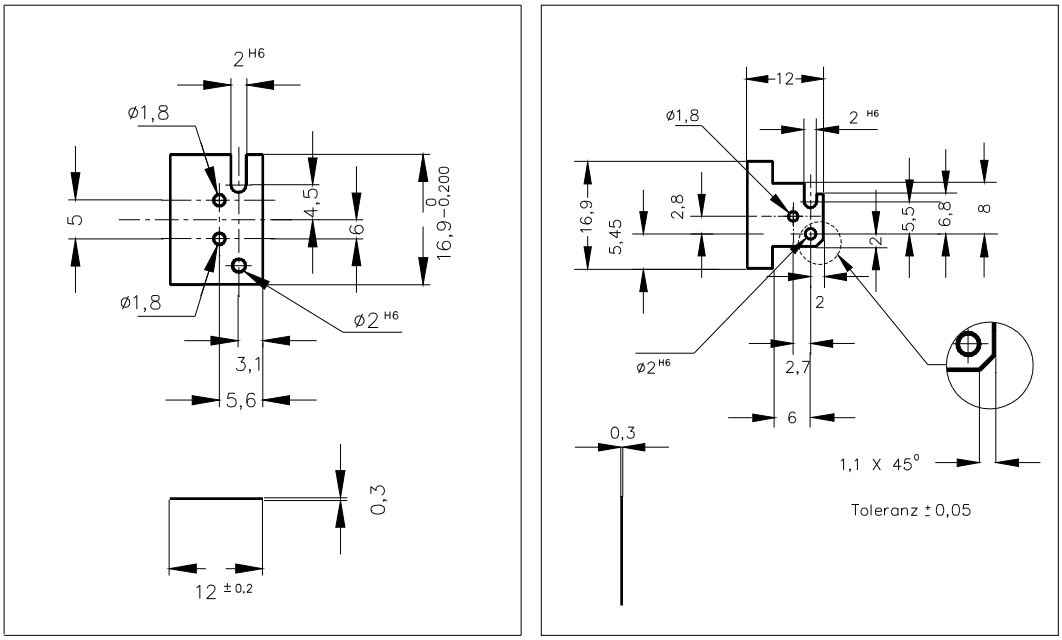

Figure 5.29: Layout of the ceramic supports. Left: modules of internal layer; right: modules of external detector layer.

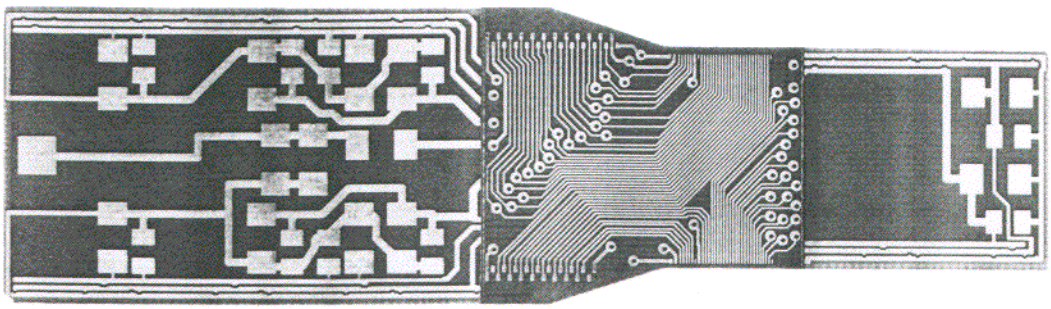

Figure 5.30: Flat kapton cable. The power bus is connected to the central adapter and distribution piece by through-connections. Decoupling capacitors fit onto the visible pads.

The flat kapton cable was glued to the chip side of the module then. During this operation, care was taken to avoid glue flowing in between the readout chips. The glue would have changed the capacitive conditions at the pixels' input stages – similar to misaligned bump bonds – and would have led to malfunctions. When applying droplets of A2015 glue, the inter-chip regions were covered by a stencil therefore. The adhesive hardened within 10 hours at room temperature. A weight matching the flat kapton's shape and its passive components ensured planarity and appropriate mechanical contact.

The photograph in figure 5.33 shows a detector module in the assembly jig, equipped with ceramic and flat kapton hybrid. A geometrical survey was performed and properties on every module filed as soon as the glues had hardened. The modules were packed in special transportation boxes then, fixed between free-running plastic foils to absorb stress, and sent to Karlsruhe University for the final assembly steps.

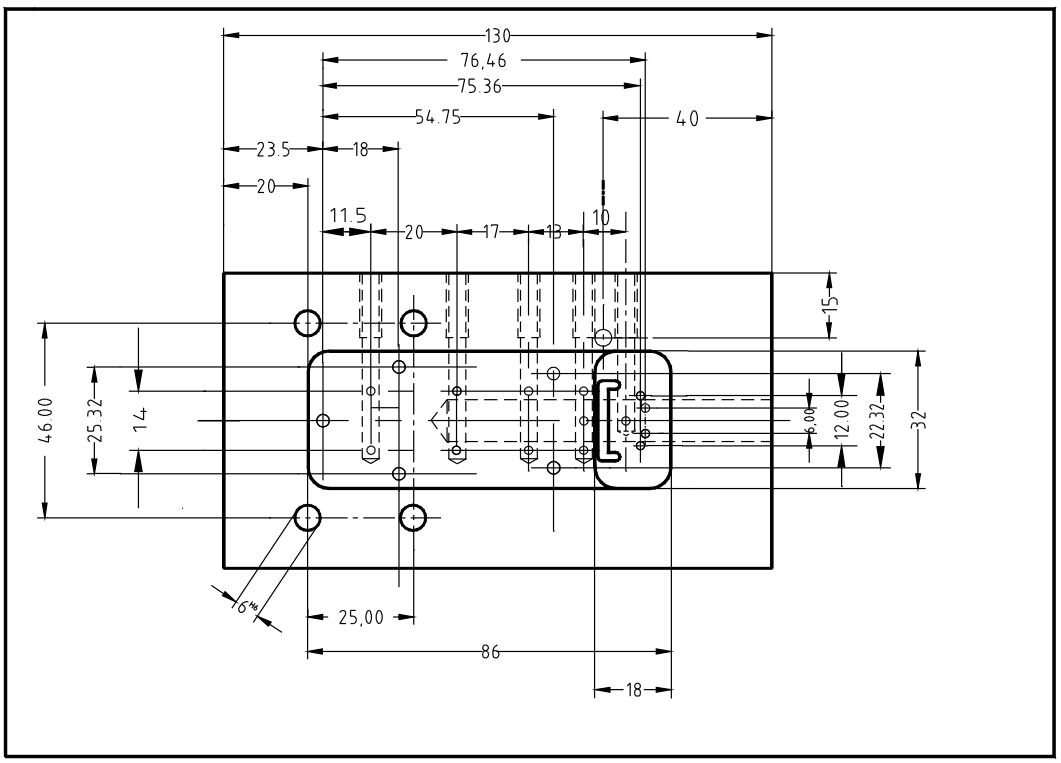

Figure 5.31: Layout of the jig for the module assembly.

glue	Epotecny E 704	Araldit 2015
type	tixotrophic two component	tixotrophic two component
potting time	24 h	30 - 40 min.
hardening time	120 min. @ 80 °C 15 min. @ 125 °C 5 min. @ 150 °C 2 min. @ 175 °C	10 h @ 20 °C
thermal conductivity	1.5 $\frac{W}{m°C}$	not required

Table 5.6: Characteristics of the applied glues [98].

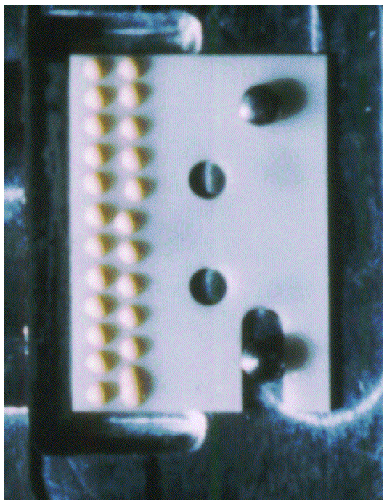

Figure 5.32: Glue deposited on the ceramic support.

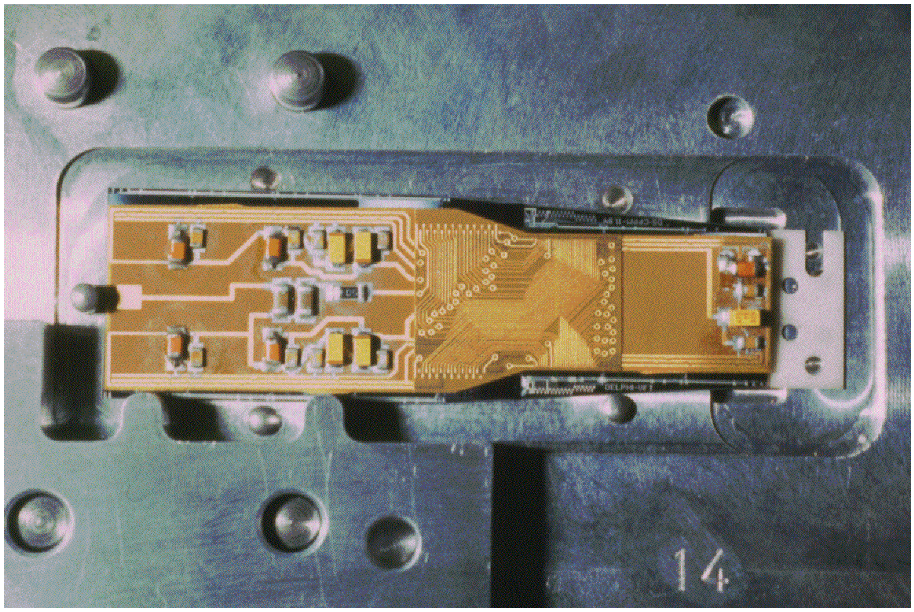

Figure 5.33: Ceramic support and kapton hybrid attached to the silicon module.

Assembly step3: Attachment of long kapton cable, wire bonding
The "long" kapton cables connect the detector modules to repeater electronics [99]. They provide 44 lines to route all voltages, currents and digital control and readout channels. Four different kapton designs were required for the different sub-layers of modules. The innermost detector layer needs the longest cable to connect to its repeater as shown in figure 5.43. In order to match the industrially available production technology, a design with two separate constituents was chosen which are connected

to form the final cable. The cable types are summarized in table 5.7 and one layout is shown in figure 5.34.

kapton type	detector layer	quantity	length
LK1	internal 1	36	295 mm
LK2	internal 2	40	280 mm
LK3	external 1	36	130 mm
LK4	external 2	40	120 mm

Table 5.7: Types of long kapton cables.

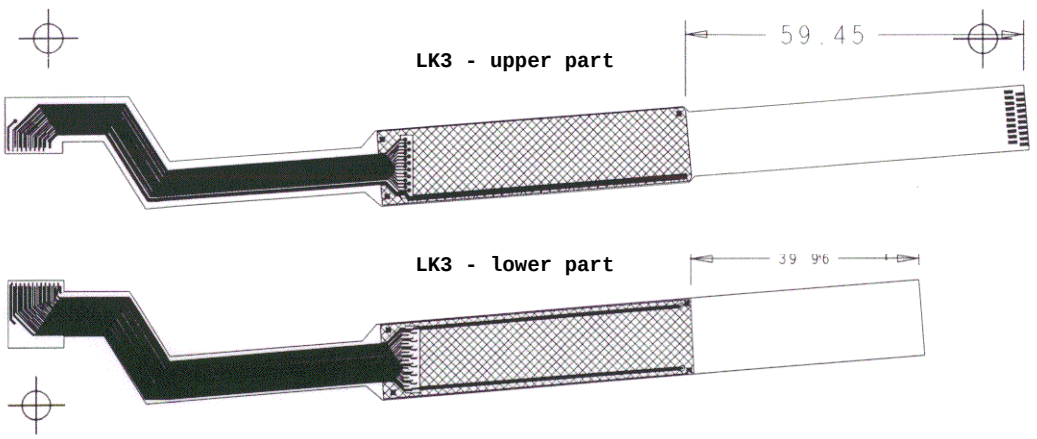

Figure 5.34: Long kapton cable, built from two components. The left part connects to the detector module and is about 500 μm thick. The right part is thinned. The two components are not attached to each others there and are flexible to allow to be bent and fit into the connectors on the repeater boards individually.

Before being released for assembly, also the long kapton cables were tested comprehensively and checked for short circuits and interrupted lines. The line for the depletion voltage turned out to be of special interest. Several cables showed a long-term instability there and developed unproportionally high dark currents. The situation is shown in figure 5.35 where a good and a faulty cable are compared. It was considered that insufficient etching between the depletion voltage line and a neighboring ground line was the cause for these instabilities, combining with humidity effects and the electric field applied. No optical evidence could be found, though, to support this conjecture. After initial problems with already assembled detector modules, the long kapton ca-

bles were tested to stand up to 130 V on the depletion line, even though only up to 60 V were applied during the later operation.

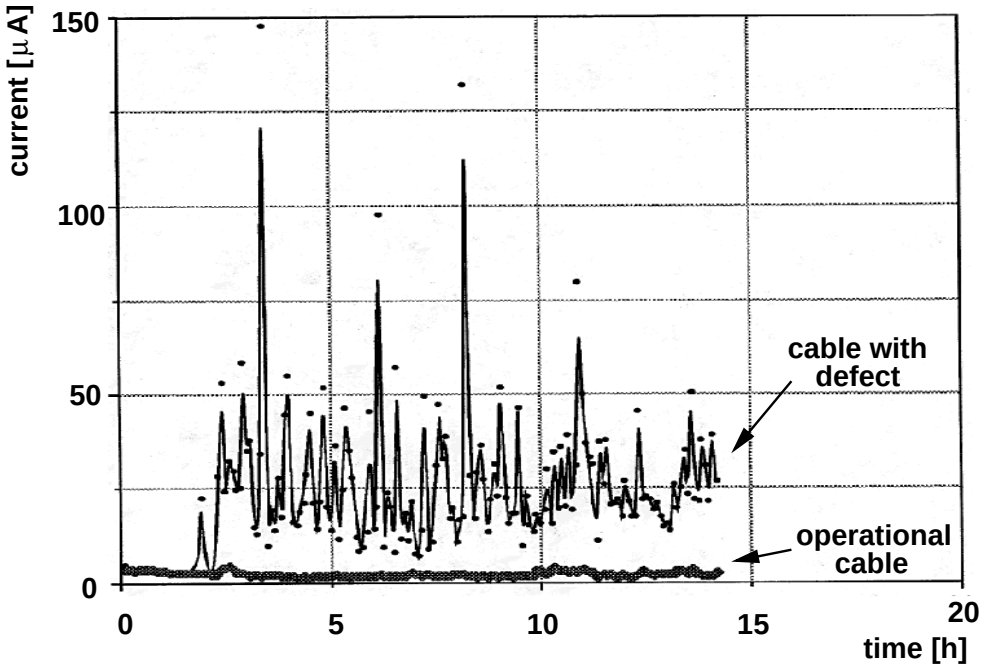

Figure 5.35: Dark current on the depletion line of an operational and a defect long kapton cable.

Both kaptons were attached to each others using Araldit 2015 adhesive. Clean surfaces were ensured and the components aligned with respect to their connector pads. After several hours of hardening, the modules were wire bonded. Three sets of bonds were applied, using a semi-automatic bonding machine which was used already for the construction of DELPHI's microstrip detector modules. The machine's parameters have been described in reference [100].
The first set of wire bonds established 44 connections from the long to the flat kapton cables. The contacts of every wire were applied under similar conditions, but strong forces with the bond needle had to be adjusted to match the indulging surfaces.
The second set of bonds to contact the integrated bus was more difficult to manufacture. One bond had to be placed on kapton, the other one on silicon with highly different mechanical conditions. Furthermore, a step of about 1 mm had to be bridged. The procedure required experience and skill from the assembly team.
The third set of wire bonds for the supplementary power connections was less affected by the step, but several pads and lines on the detector rim were arranged unluckily and facilitated damage to the silicon with slightly displaced bonds. The insulating oxide layer with the double metal layer was easily damaged during this process leading to short circuits with the integrated bus.

The photograph in figure 5.36 shows a close-up view of the wire bonded central part of a pixel detector module.

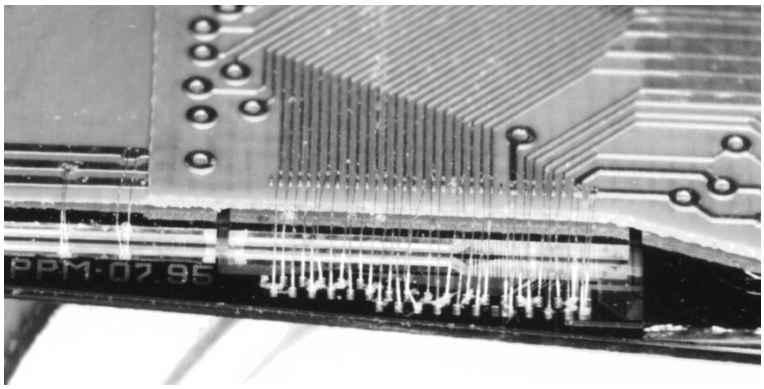

Figure 5.36: Wire bonds from the flat kapton's adapter layer to the integrated bus. On the left hand side supplementary bonds to the power lines are visible, applied in pairs.

With several types of modules the shape of the long kapton cable did not allow to reach all bond pads after its attachment. The order of the assembly steps had to be revised in this case. First the wire bonds between flat kapton and silicon were applied, than the kaptons joined and the remaining bonds placed. Special care was taken not to damage already existing wires which could not be repaired. An entire module would have been lost in such a case.

A very basic functionality test followed to ensure that no short circuit or unconnected line was present. The final modules as seen in fig. 5.37 were packed in specially designed transportation boxes, consisting of an aluminum body and a free-moving plastic cover. Loosely fixed screws and a piece of foam kept the modules in place and avoided (after some initial loss) damage to the detectors during transportation. Batches of boxes, containing the yield of the assembly of several days, were sent by express service to either Wuppertal University or INFN Milan who shared the final comprehensive and time consuming functionality tests.

5.6.2 Final functionality test

The functionality and performance of every assembled detector module was characterized in the final step of the module production, with all cables attached to the detectors and connections established. A test bench was concepted for this purpose, consisting of a PC-controlled CAMAC system, power supplies and pulse electronics with GPIB[6] interface. A custom designed test repeater card, provided by the elec-

[6]General Purpose Interface Bus

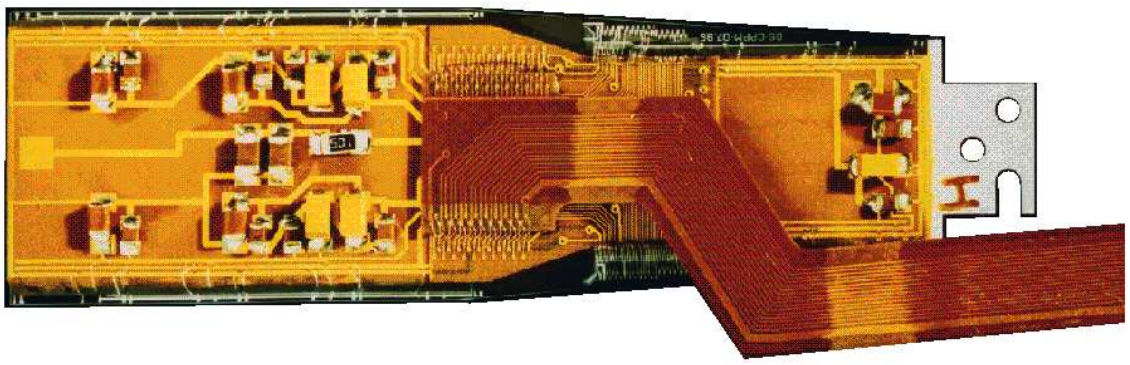

Figure 5.37: Photo of a fully assembled pixel detector module for the external layer.

tronics laboratory of CPPM, enabled to connect a single pixel detector module to the supply and readout devices. A LabVIEW[7] program, developed by the groups in Milan and Wuppertal, allowed to operate the detectors in test cycles under comparable conditions, even though different devices were applied [77]. Extra flexibility was gained by this procedure.

The acceptance test comprised the following measurements which enabled to judge the functionality of every module and its ability to work in a group of modules operated in parallel and sharing common supplies:

1.	detector leakage current at 30 V, 40 V, 50 V depletion
2.	power consumption; input voltages at nominal currents
3.	Sparse Data Scan: all pixels responding in test mode
4.	threshold at $\leq$1% noisy pixels
5.	measurement of the threshold's slope near the nominal setting
6.	mask of associated noisy pixels
7.	^{90}Sr β^- irradiation: mask of dead pixels

The leakage current and power consumption measurements provided information on the basic functionality. Very noisy detectors usually also drew an enlarged dark current. With several modules, however, the dark current was intercepted by the detector's guard ring, and did not affect the functionality itself. In such a case the concern was more if the power supply system would be able to drive such modules.
The test of the sparse data readout detected not responding chips or inactive address bits. Modules with such failures were rejected or considered as a backup.
The threshold at which less than 1% of the pixels were noisy was checked to be within

[7]trademark by National Instruments

the normal distribution that would allow to operate the modules at full detection efficiency. The slope of the threshold in the proximity of this setting was measured to ensure a known behavior in case of later fine tuning. The addresses of the noisy pixels were filed.
Sensitivity to ionizing particles was verified as the last step. A non-collimated electron source was moved across the detectors. Count rates for every pixel were accumulated applying a random trigger and dead pixels determined.

A form sheet was assigned to every detector module, containing the detailed results of all assembly and test steps and stating the ranking of the module's quality within three classes: A) good for DELPHI, B) spare, C) failed.

5.6.3 Production yield and breakdown of errors

The entire detector production has been evaluated and summarized in reference [101]. The graphical representation in figure 5.38 details the yield after the different production and assembly steps as a function of the detector batch number.

The total production comprised 426 detectors, delivered in 13 wafer batches of 10 to 46 detectors each. In a first production period during autumn and winter 1995/96, a high yield exceeding 90% according to the first on-wafer test could be achieved with the batch numbers 1 to 9. A few modules with high leakage currents and short circuits or interruptions in the double metal bus had to be rejected. In the second production period 1996/1997, the quality of the detector substrates degraded significantly, as seen with batches 10 to 13. Both the quality of the high-resistivity silicon itself and slightly modified details of the processing at CSEM were considered as an explanation for the lower yield. One batch of detectors which suffered from very high leakage currents and could not be used for further assembly at all was not taken into account in the overview. The replacement batch (no. 12 in the graph) was evaluated instead. It was produced as the last one and special care was taken to improve its quality. The test results confirmed the success of the effort and the yield reached the level of the initial wafers again. An average fraction of 84% of accepted detector substrates could be obtained after the production. During dicing, only a small fraction of detectors was damaged and 97% of the sent modules were accepted after this step.
The bump bonding was the next critical operation where the wafers had to undergo several processings for bond pad metallization, cleaning or opening of the passivation oxide layer and the bonding of the chips to the detector substrate itself. The tests performed after these operations comprised the functionality of the sparse data scan readout in test mode and provided information on the quality of the connections of the readout chips to the supply lines. With the exception of two batches yields of up to 95% were achieved, increasing with time as experience was gained with the handling of the modules at IBM. The mean yield of 80% matched the expectation according to the bump bonding failure rate of about 10^{-4} and 16 readout chips per

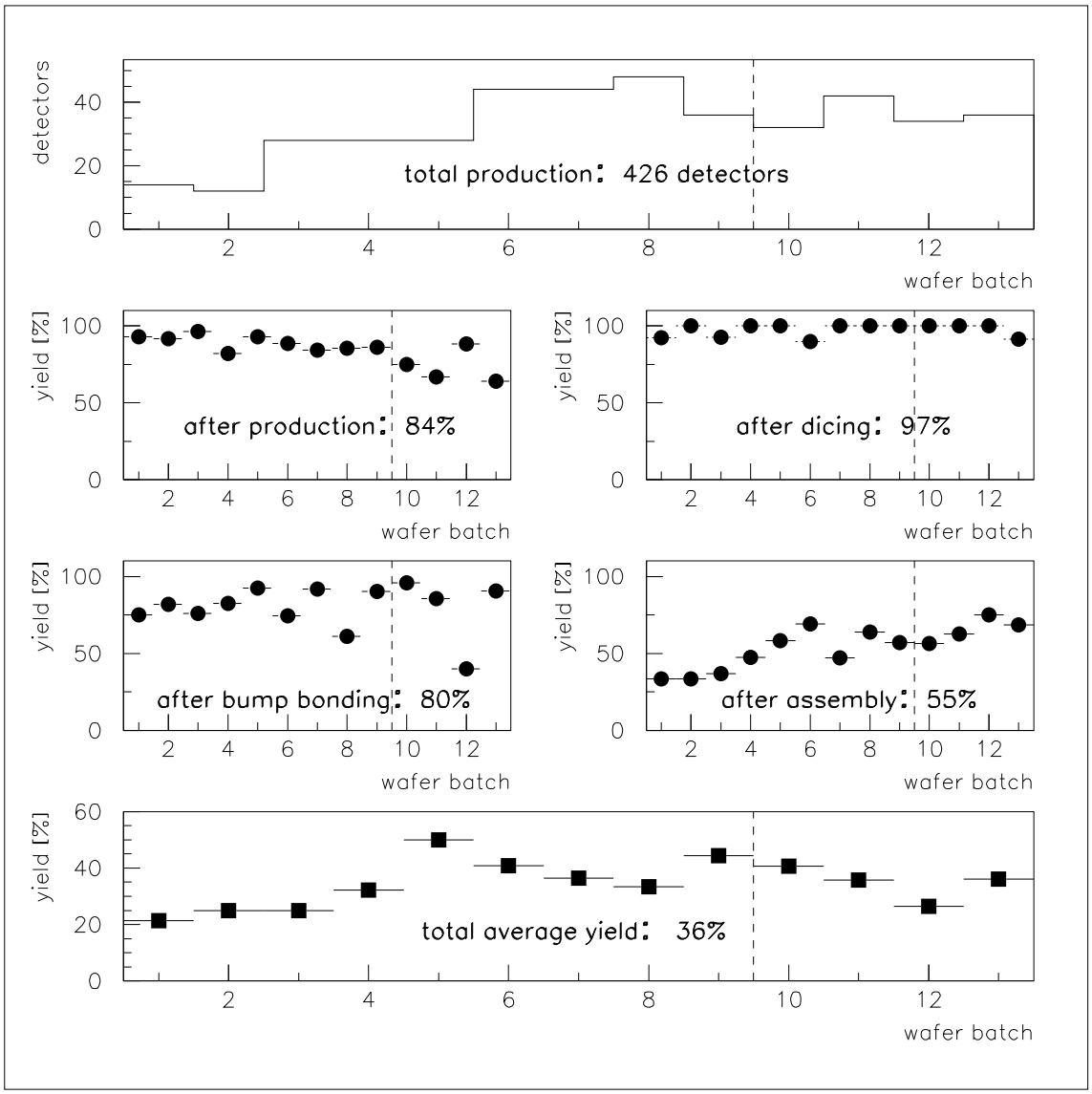

Figure 5.38: Yield of the module production. The graphics shows the percentage of working detectors after the different production and assembly steps. The vertical dashed line separates the two production periods in 1995/96 and 1996/97.

module. Unfortunately, the single replacement batch yielded a very low result after the bump bonding, most likely because of the elapsed time and different assembly machine settings since the previous productions.

The equipment of the accepted modules with ceramic support, kapton cables and wire bonds and the extensive shipping in between the laboratories involved in the construction was the most complex operation. This is reflected in the yield of fully assembled and working modules. In the beginning of the production, only about 30% of the modules which passed all the other steps before were classed as suitable for the application in DELPHI. Even though the assembly was tried with a few prototype

modules before, the handling of the components still had to be learned and optimized. Especially the wire bonding of the external power bus turned out to be difficult. Significant experience, however, was gained within the first 5 batches and the assembly yield increased to about 70%. A mean efficiency of 55% was reached in this step, applying the final functionality test to characterize the modules' performance.
The total efficiency after all assembly steps is summarized in the bottom plot of fig. 5.38. The efficiency per batch varied between 20% and 50%. The overall yield of the pixel detector production was 36%, just enough to obtain 152 working modules as required for the full pixel detector. The quality of 95 modules was considered only as appropriate for backup purpose. These modules mostly had an entire chip not responding or high noise. Further 179 detectors were misbehaving according to other criteria and could not be mounted in the Silicon Tracker.
The production yield from batches 1 to 9 allowed to equip the Silicon Tracker with 5 of 8 parts of the entire pixel detector for the physics period in 1996. The accepted 95 detector modules were installed. All cones of the internal layer were assembled and one half cone of the external detector layer present. The production was resumed (batches 10 to 13) and the pixel detector completed for the running in 1997[8].

The breakdown of errors for the fully assembled modules is detailed in figure 5.39. The largest fraction of faulty modules was affected by damage to the integrated bus during the wire bonding procedure. Decoding errors with the sparse data scan test were present with 52 of the assembled 271 modules; nearly 20% of the modules were affected by this failure. Pixel addresses were output in the wrong order, did not appear or occurred several times. High dark current and increased noise with another 20% of the assembled modules were probably due to the bump bonding process. Faulty wire bond or bump bond connections were most probably the cause for missing control or output signals of single chips. This error occurred with seven modules. In four modules the long kapton cable was not working reliably. Either no proper contact to the microconnector on the repeater side could be established, or the fault was within the cable and led to unsteady contacts with mechanical deformations. With a few modules, the ceramic support broke during the handling. Further 35 detector modules were lost because of various reasons, e.g. damaged corners in the assembly jig.

[8] A separate production of further 20 detector modules, intended as spares for possible future repair, was started in spring 1998.

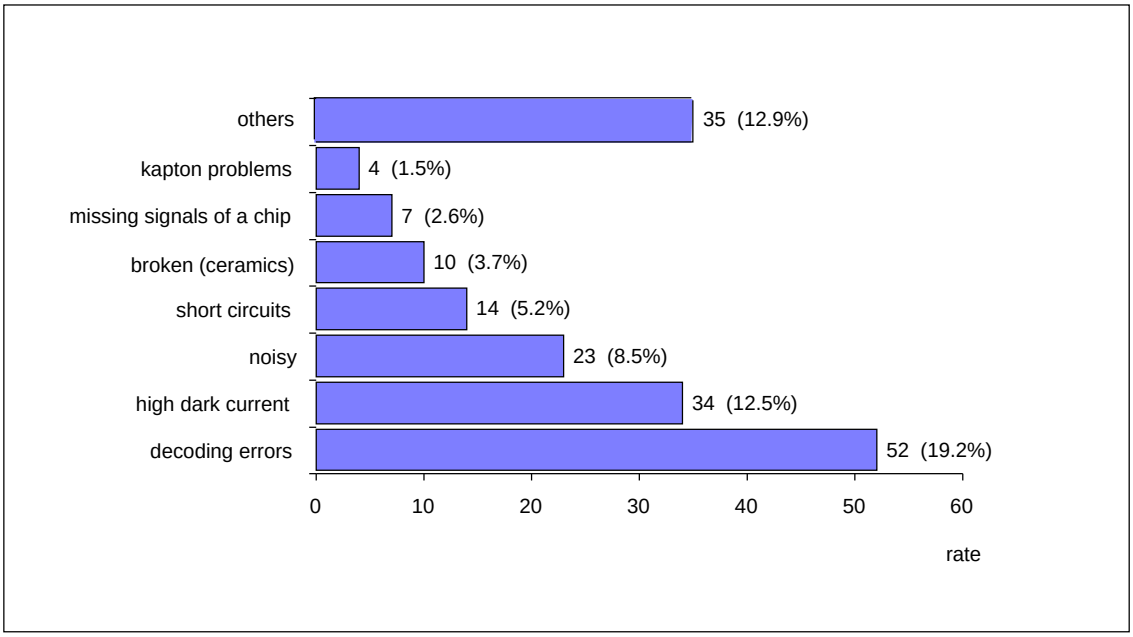

Figure 5.39: Breakdown of errors for the assembled detector modules.

5.7 Assembly of the detector layers

The basic unit of a pixel detector layer is a "half cone", an assembly of 19 detector modules mounted onto a half cylinder support with either 12° or 32° inclination. Eight half cones were built to be inserted into the Silicon Tracker, connected to two boards of repeater electronics with power distribution and driver circuits to receive and send signals to the supply and readout systems outside the DELPHI detector. Matching the Silicon Tracker's half shell structure, one half cone per detector layer, side and half shell was concepted.

The half cones were assembled at CPPM Marseille where also the mechanical support and tools for the handling and survey of the components were designed and available. Figure 5.40 shows a cone of the internal pixel detector layer, held by a jig during the assembly procedure. The 19 detector modules were staggered in two sub-layers with their chip sides repelling each others and the detectors being spaced by about 1 mm. The lower sub-layer contained 10, the upper sub-layer 9 detector modules. Gaps between neighboring modules were covered by the transposed arrangement. The support sides of the modules were mounted onto an aluminum ring with precisely machined pads to screw the ceramics to. A cooling pipe connected to the aluminum ring enabled to drain heat from the detectors by water flow. Inlet and outlet of the pipe are visible at the top and bottom of the photo. The modules of the lower sub-layer were put in place first, followed by the detectors of the upper sub-layer. The modules' ceramic support broke easily during this operation. Patience and skill were required by the assembly team to avoid damage. Despite of precautions, supports of a few modules on the outermost parts of half cones broke. Since the modules operated perfectly apart from the mechanical damage, the ceramic pieces were supported by aluminum replications.
The aluminum ring was screwed to a half cylinder support. Outside the detector's acceptance, an aluminum cylinder carries the modules of the external pixel detector layer and both ministrip detector layers. A composite piece forms the support of the internal pixel detector layer and also carries the modules of the innermost microstrip detector layer [102]. The material was chosen for its small radiation length. The layout is shown in fig. 5.41. The composite piece is built from three carbon/epoxy layers. The design took special care to minimize deformations caused by thermal stress and a thermal gradient of about 2 °C between the hybrids of the microstrip layer and the pixel detectors. Slits machined into the support served to route the long kapton cables, as seen in fig. 5.40 during the assembly.

The connection of the long kapton cables to the repeater boards turned out to be difficult. Even though the kapton cables were rather thin, the 500 μm material provided significant stiffness, and strong forces could apply to the pixel modules. In order to facilitate the handling during the assembly, the cables were already pre-bent in the region where the cooling pipe had to be bridged. The connection to the repeaters is

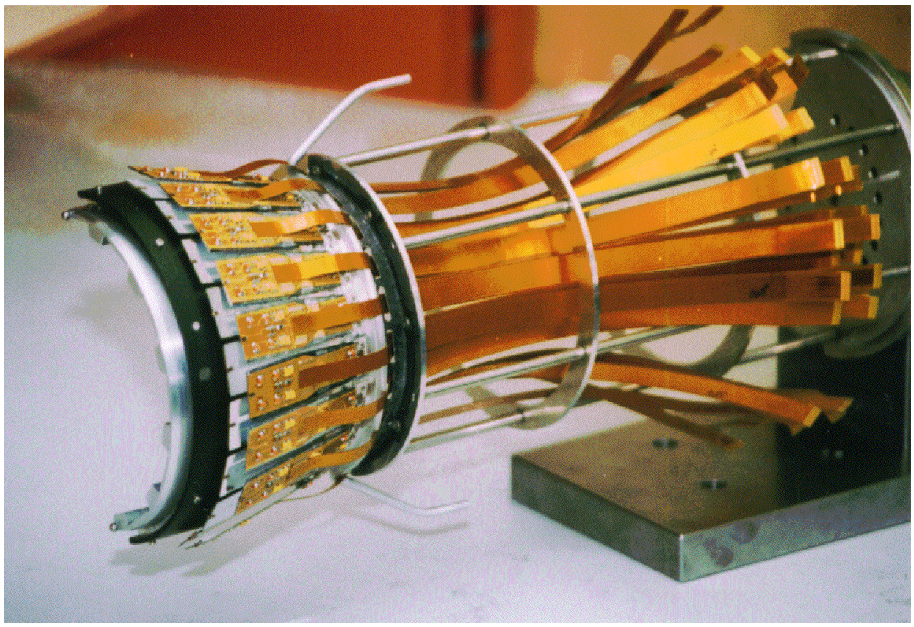

Figure 5.40: Assembly of a half-cone of the internal detector layer.

shown in fig. 5.42. The modules of every sub-layer are connected to a separate repeater board. The split ends of the kapton cables fit into two microconnectors, shifted by 17.3° on the repeaters and matching the arrangement of the modules on the cones. Contact needles inside the connectors pressed onto the kapton lines and a bar fixed the cable's position then. The procedure could be repeated only a limited number of times without damage to the kapton. A working ensemble of 9 or 10 detectors per repeater could be achieved only if the reliability of the contacts was checked immediately after a module was added to the repeater. If a non-working module was found with an already fully equipped repeater, a large fraction of cables had to be dismounted again in order to reach the faulty detector, imposed by the tight space. With high probability, another fault at a different position would have occurred during the reconnection. The detectors were operated therefore after every new module was added to the repeater and the basic functionality was checked. The detectors were shielded from the ambient light inside a box. Kapton cables not fitting perfectly into the connectors were often the cause for short circuits and increased currents on specific supply lines. High currents on the depletion line were measured frequently during the assembly. A few modules worked perfectly on their own but disturbed the parallel operation in a repeater and had to be replaced.

The long kapton cables needed to be strongly bent to reach the connectors on the repeater boards. The situation is shown in fig. 5.43. Sharp bends of nearly 90° occurred especially close to the connectors at lower radii. Little space between the repeaters in their final position resulted in additional pressure onto the cables. Microscopic

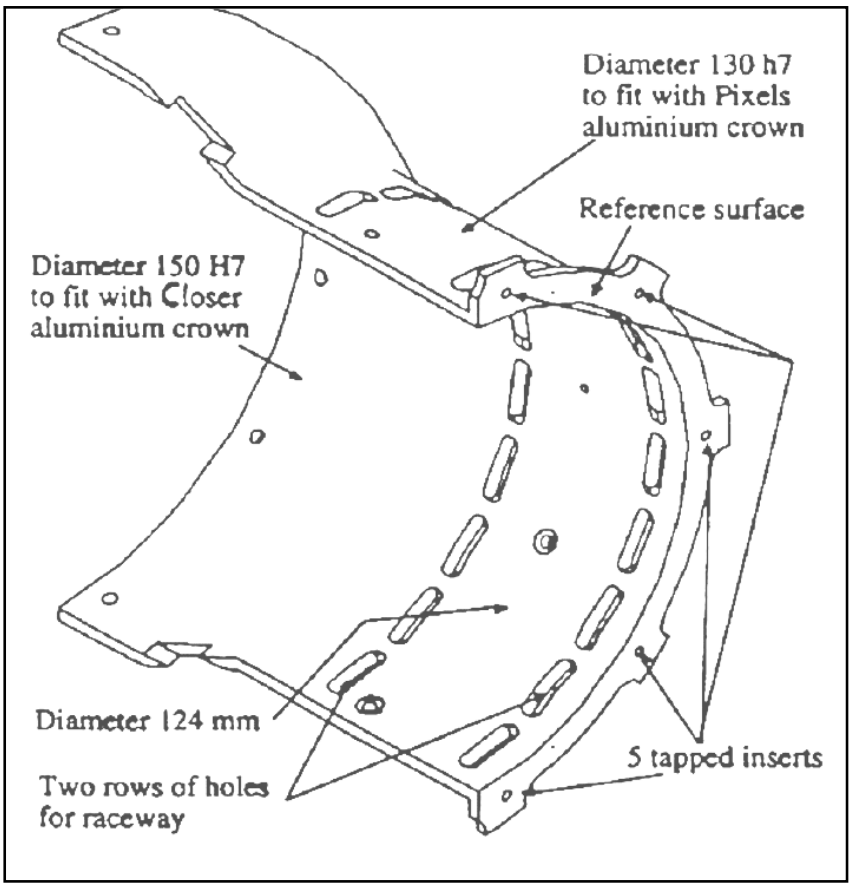

Figure 5.41: Layout of the composite support cylinder.

cracks in the kapton's copper lines have been identified as responsible for problems experienced during the running of the pixel detector in 1996 and 1997 (see chapter 6).

5.8 Integration into the Silicon Tracker and installation into DELPHI

The cones were assembled in timely correlation to the module production and the activities performed in the framework of the Silicon Tracker maintenance. A tight scheduling was imposed to enable the necessary dismounting, exchange, repair and remounting of the different detector, electronics and mechanics components. Common tools had to be used efficiently and enough time for comprehensive testing had to be foreseen. Finally, the date for the insertion into the DELPHI experiment set the limit for the assembly activities.

The assembly of a new cone started as soon as enough operational modules were available. The cones of the internal pixel detector layer were built first. After compre-

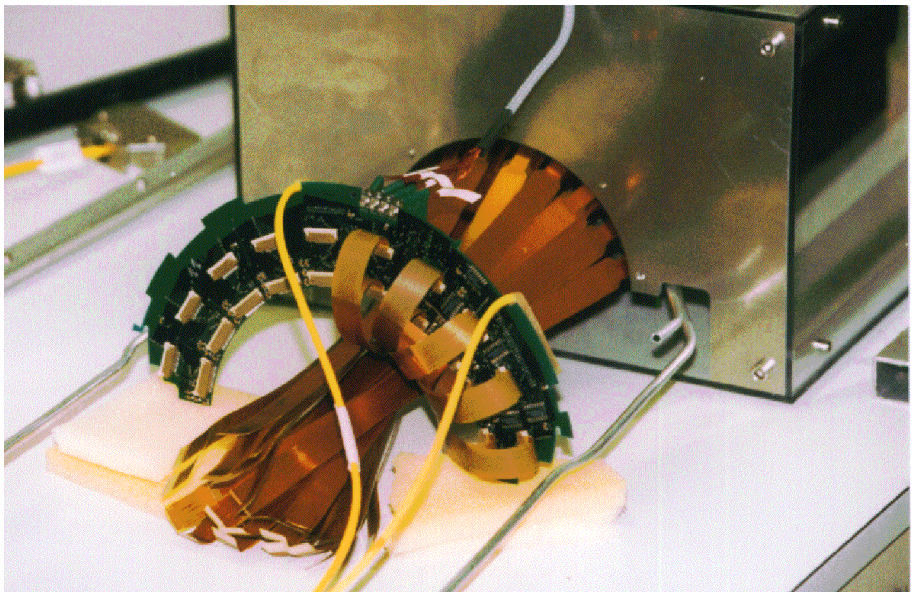

Figure 5.42: Connection of long kapton cables to the repeater boards.

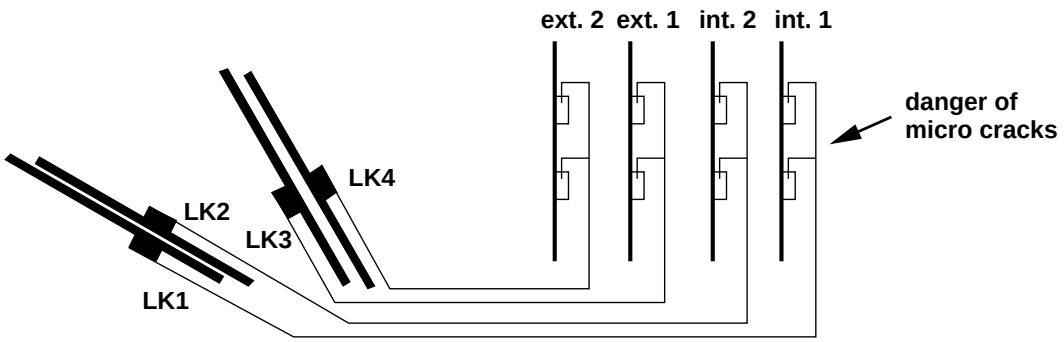

Figure 5.43: Routing of long kapton cables.

hensive tests with a readout system used later on in the DELPHI counting room, the cone was transported to the Silicon Tracker assembly laboratory at CERN. Work on the Silicon Tracker was done separately for every half shell there. A specially designed jig allowed to turn the entire structure around the "beam axis" to access the detector half shells from all sides.

Insertion of pixel detector half cones

The insertion of the pixel detector started with the internal microstrip modules (Closer Layer) dismounted. The half cones of the internal pixel layer were inserted in pairs. Connected by metal bars, the cylinders of both end-caps were placed on top of the

half shell and lowered with a special tool. A minimum distance of less than 0.5 mm to the microstrip detectors had to be passed without damaging the components. Up to six persons were involved in the demanding operation, taking care that no accidents occurred. Parallel to the half cones themselves, also the repeaters had to reach their final positions. Great care was taken that no cables got caught and no extra forces were imposed onto the pixel modules. After reaching the final position, the half cylinders were screwed to the Silicon Tracker's support structure and the bars removed. The half cones of the external pixel detector layer were mounted independently for every endcap and half shell. After the cones of the external pixel detectors were in place, the two mini strip cones were installed. The units of detectors and repeaters were placed on top of the cables already in place from the pixel detectors and screwed to the aluminum support. Slits in the cylinder served to route the cables. Comprehensive functionality and cross talk tests of all detector components were performed after every assembly step. Work on one of the Silicon Tracker's components could badly influence other parts, facilitated by the fragility and very proximity of the heterogeneous detector and electronics components. An operational cooling system in the laboratory was essential to avoid damage to the front-end electronics especially with the strip detectors.

Geometrical survey

A geometrical survey was carried out during the assembly which served as the starting point for the later alignment of the detector modules with particle tracks.
The survey of the pixel detectors shall be emphasized here. Unlike with the microstrip and ministrip detectors where spheres on top of the hybrids defined the position of every module in space, the touch probe of the 3D machine[9] used to measure the spheres with high precision was not appropriate for the survey of the pixel detector modules. Their mounting on just one side and the fragility of the ceramic support required a different approach.
In a first step the two-dimensional positions of the external detector corners and the ceramics with respect to pads close to the corners were determined during the module assembly. These pads remained visible. Their well known positions on the detector mask defined the position of the pixel array which was finally related to the coordinates of the external corners. A microscope set-up was used to scan the detectors' edges with 5 μm precision and to extrapolate the corners' positions from their directions [97]. A reference frame with its origin in one of the precision pins for the ceramic support was chosen. Figures 5.44 and 5.45 detail the procedure and show the result obtained with one pixel detector module.
In a second survey step, after the mounting of the modules into half cones, the position of every module in space was determined by applying a proximity measurement with a camera identifying the modules' corners. A touch probe measured the three-

[9]POLI S.p.A., Varallo Sesia, Italy

dimensional positions of the precision pin in the ceramic support and spheres glued to the half cone's support itself (see fig. 5.46).
The final survey was performed after the insertion of the half cones into the Silicon Tracker. The position of the half cone support with respect to the other components was measured and the final location of every detector module and sensor diode in space obtained. The three-dimensional coordinates of three distinguished pixel corners were calculated and entered into an alignment data base, describing the position and orientation of every sensor array in space [103, 104].

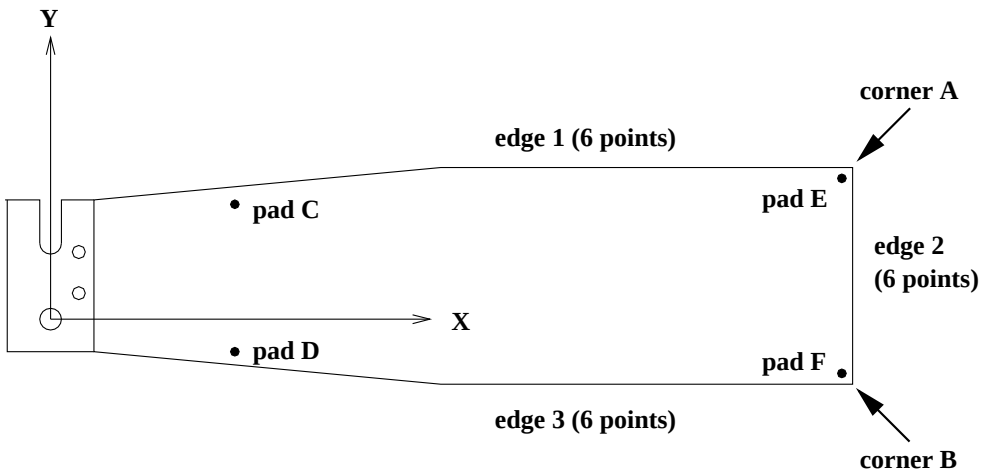

Figure 5.44: Scan of the pixel modules' geometry.

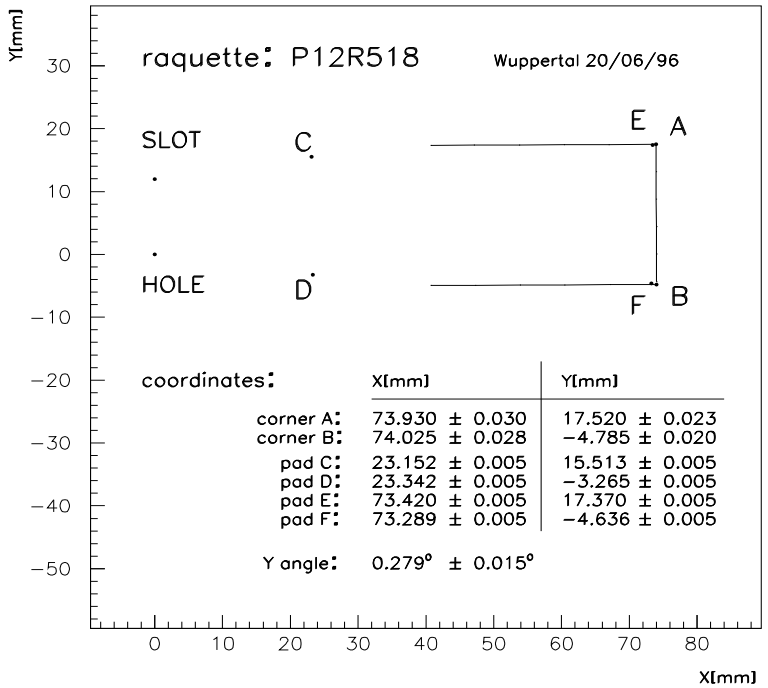

Figure 5.45: Geometry of a pixel detector module.

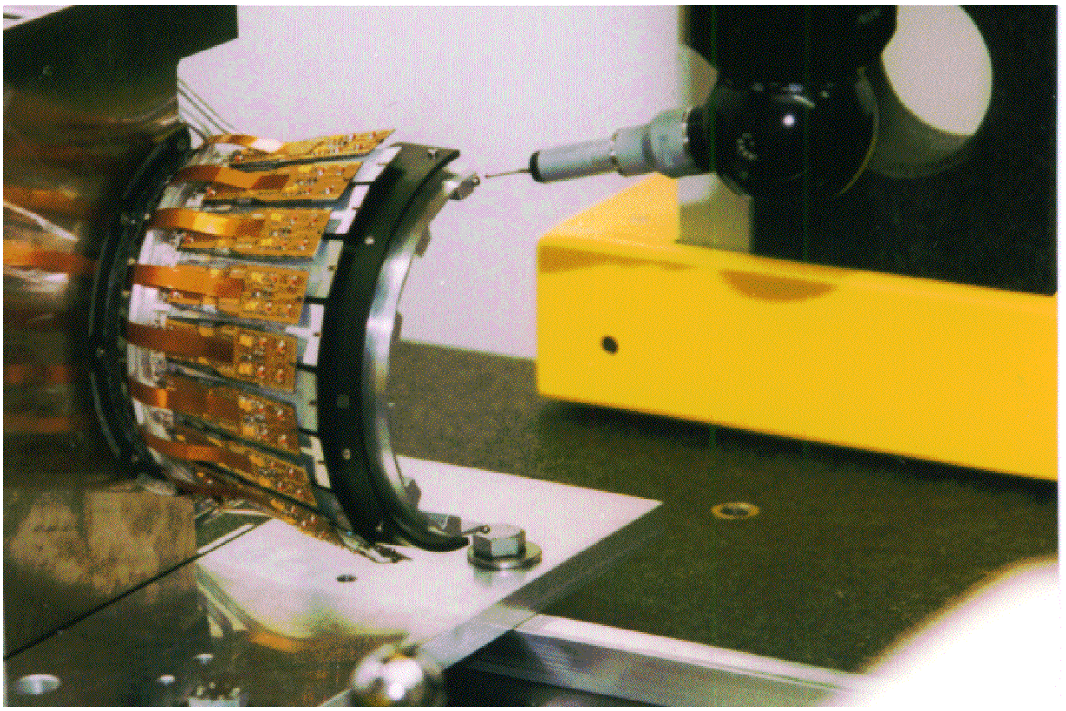

Figure 5.46: Geometrical survey of a pixel detector half-cone, using a 3D touch probe.

Installation in DELPHI

The photo in fig. 5.47 shows one half of the Silicon Tracker fully assembled and ready for the transport from the laboratory to the DELPHI experiment. The silicon detectors are protected by an internal and external cover. All cables are connected to the repeaters and the 20 independent cooling channels are equipped with tubes. A handle allowed to move the entire structure of about 1 m length and a weight of about 3.5 kg. The two half shells were installed in DELPHI while LEP's vacuum pipe was in place. The situation where the beam pipe enters the opening in the central part of DELPHI is shown in fig. 5.48. The half shells were arranged on both sides of the pipe and pulled into DELPHI, supported by carbon fibre rails and sliding on skates. Very tight space between the innermost silicon components and beam pipe's flange mounts was expected. The insertion was practised in the laboratory therefore using the original detector and a mockup of the relevant structures. A survey of the clearance in the interaction region of DELPHI itself was additionally performed before the installation, sliding a detector mockup through the opening and measuring the available space with capacitive probes [105].
While the modules of the vertex detector half shells overlapped during the installation procedure and covered the full azimuthal angle finally, the vertical gap between modules of the Very Forward Tracker's half cones was used to route the cables and cooling pipes to the outside. The cables and tubes on both end-caps of DELPHI were fixed to

the end-plates of the Time Projection Chamber and connected to their counterparts coming from the supply systems in the counting room outside the DELPHI detector.

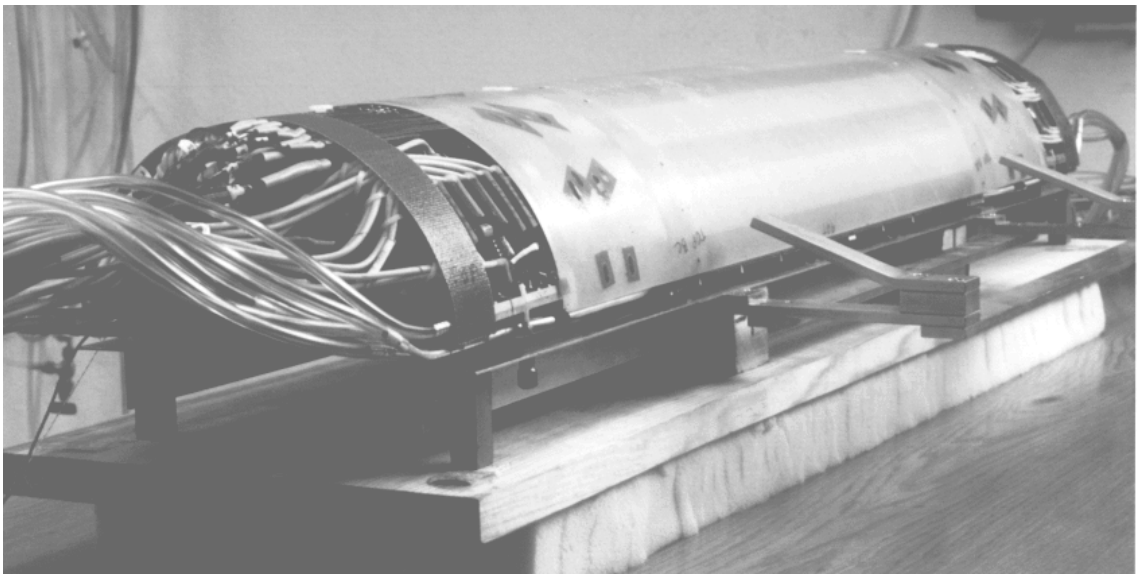

Figure 5.47: Silicon Tracker half-shell ready for the installation into DELPHI.

Figure 5.48: Beam pipe entering the central part of DELPHI [106].

Chapter 6

Experience with the pixel detector operation

From the point of view of the detector operation, the DELPHI pixel detector is subdivided into 16 parts, corresponding to the 9 or 10 detector modules, respectively, which are connected to a single repeater board. These subsets share a common power supply and are operated and read out together.
The power supply and data acquisition systems are introduced in this chapter and the detector control and monitoring tasks outlined. The operational status of the detector in its startup year and after its completion is discussed, problems experienced with module components are addressed and solutions to ensure stability and high data quality presented [10, 107].

6.1 The power supply system

The pixel detector's power supply system has been designed to operate and control the 152 detector modules with a minimum number of supply channels at maximum flexibility. Low and high voltages as well as control currents are provided in different granularity to the detector. 240 individual channels were considered to enable a flexible operation. Parts of the detector might be switched off in case of problems or their supply characteristics tuned.
The power supply system, shown schematically in fig. 6.1, consists of a commercially available 19" mainframe[1] equipped with multi-channel power supply cards of different specifications, and a custom-designed multi-channel digital-to-analog converter. The system is controlled by a front-end computer which enables to monitor and set individual channels or groups of channels and links to the DELPHI-wide slow control system for central operation [108, 109].

[1] CAEN SY527, C.A.E.N., Viareggio, Italy

Three low voltages for the operation of the front-end and driver electronics are distributed to pairs of repeaters. The depletion voltage as well as three currents to set basic parameters of the front-end electronics are supplied to every repeater separately. A fourth control current, defining the threshold of the detector modules, is most critical for the particle detection efficiency and therefore set and provided individually to every detector module by a high-resolution DAC system. Distribution boxes group and route the lines from the power supplies into cables connecting to every repeater over a distance of about 30 m. Sense lines allow to correct for voltage drops across this distance. The total power consumption of the pixel detector and its repeater electronics is about 50 watts.

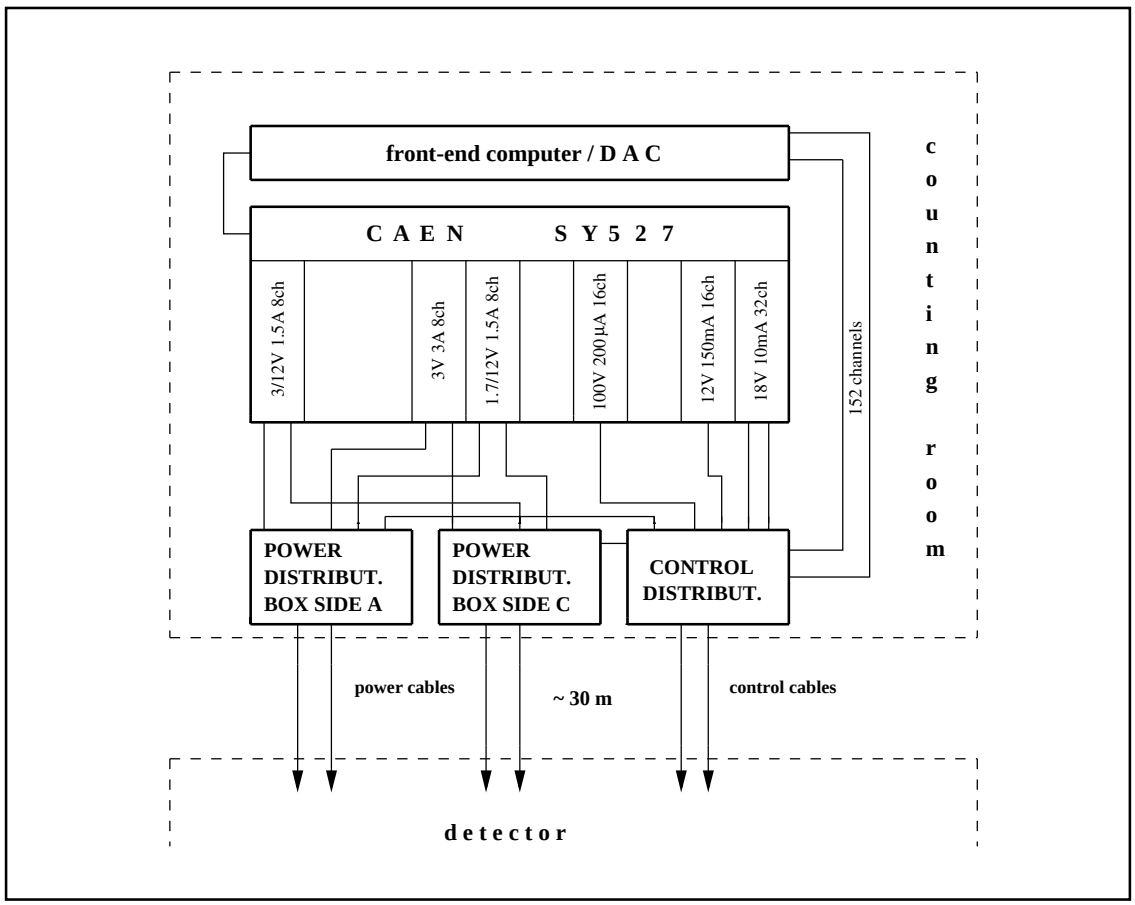

Figure 6.1: Outline of the power supply system.

6.2 The data acquisition system

DELPHI's data acquisition system is based on the Fastbus standard [110]. Digitized data in detector specific front-end buffers is read and pre-processed by a crate processor program running in a standardized front-end computer. The data stream is written to a detector specific "partition" and finally combined with data from other partitions to form the entire event as recorded by DELPHI.
The readout system of the pixel detector integrates into the DELPHI online system. Next to the crate processor and modules receiving LEP timing and DELPHI trigger information, it comprises the front-end buffers on four Fastbus cards [111]. Fig. 6.2 shows the scheme of the readout organization. On a positive trigger decision, data from 9 or 10 pixel detector modules, i.e. one repeater, is transferred sequentially to its front-end buffer (PIROU) in the counting room. All repeaters are treated in parallel. The front-end chips are addressed one by one in order to allow to skip malfunctioning chips. The addresses of hit pixels are transferred with a 5 MHz clock rate. The buffers are large enough to store up to 9 consecutive events, assuming a maximum detector occupancy of 1%. The local storage of hit information in every pixel cell, however, does not require to keep several events in the buffer memory. Four buffers are comprised in one fastbus module (PIROM). The content of all 16 buffers is accessed sequentially by the crate processor and joined to the Vertex Detector partition.

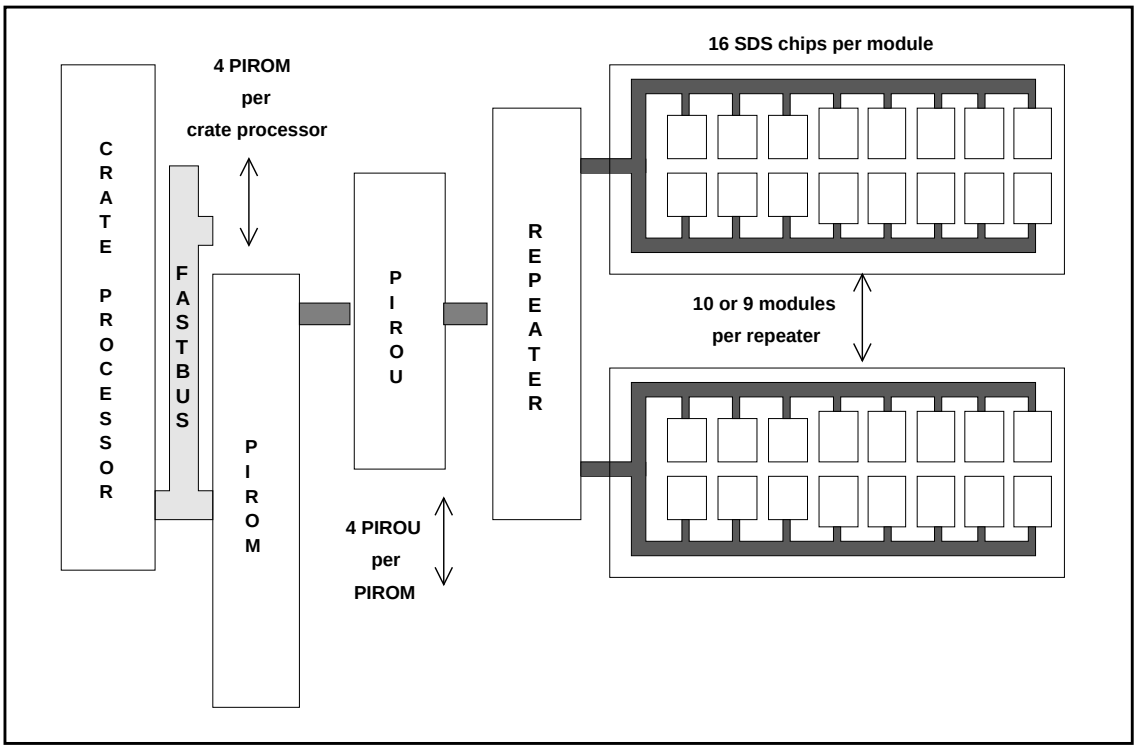

Figure 6.2: Pixel detector readout organization.

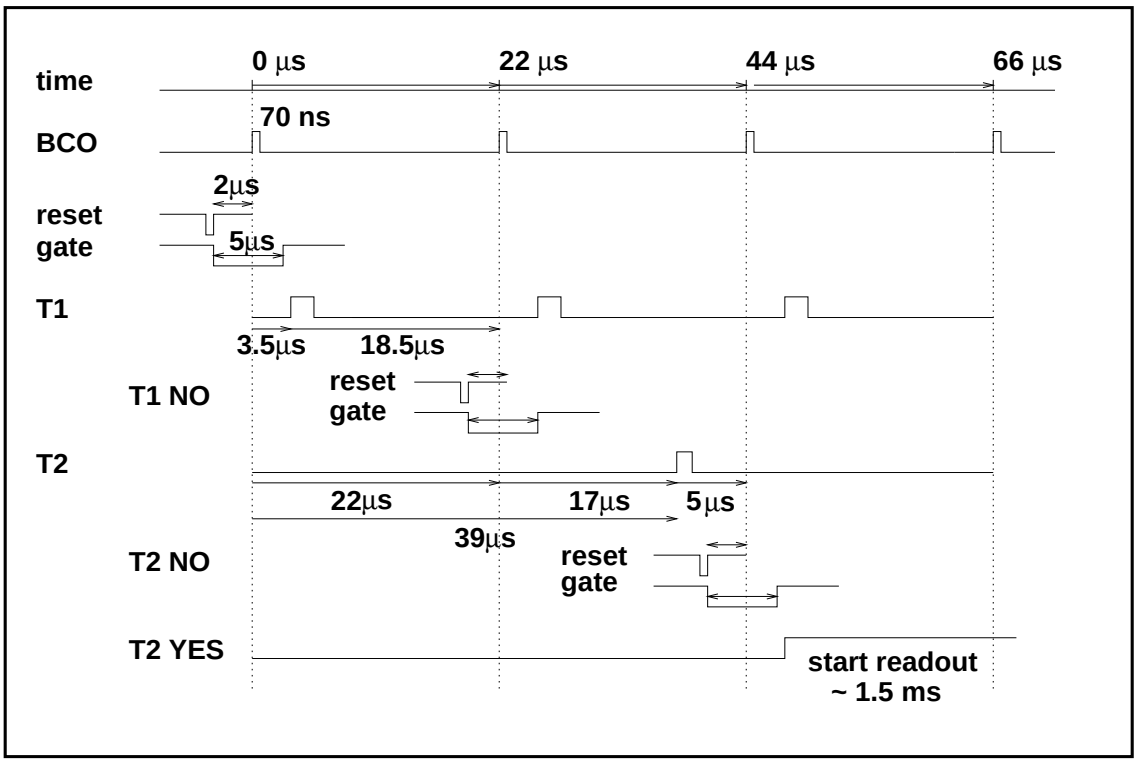

Figure 6.3: Timing of the pixel detector readout wrt. the DELPHI trigger.

The timing of the readout sequence is shown in fig. 6.3. During LEP operation, bunches of electrons and positrons cross DELPHI's interaction region every 22 μs. The memories of all pixels are reset 2 μs before the bunch-cross-over (BCO) and a gate signal is sent to the pixel detector. Stable thresholds are reached right in time when particles cross the detector (see fig. 5.5 in chapter 5.1). Pixels with a detector signal during the BCO switch the state of their memory flip-flop at the end of the gate signal and the hits can be retrieved with the next readout.
DELPHI's trigger system is composed of four successive levels T1 - T4. The first two levels are synchronous with the respect to the BCO signal. While T1 acts as a pre-trigger with input from DELPHI's fast tracking detectors and scintillation counters, T2 uses complementary information from different sub-detectors and initiates the readout of the data collected by the front-end electronics [112]. With a negative T1 decision, the data is discarded; the acquisition systems switch to a free front-end buffer and the detectors are ready for the next bunch-cross-over. Following a positive T1 decision, either one BCO is lost in case of a negative T2 and the detector reset for the next BCO, or the clocking is activated with a positive T2 and the readout started 39 μs after the BCO concerned. About 1.5 ms are required for the readout of one repeater, mostly for addressing of chips and bus transfer. The entire readout time fits into the 27 ms required by the readout of most of the other DELPHI detector systems. During

the running in 1997 and 1998, T1 rates of up to 500 Hz and T2 rates of up to 10 Hz, mostly around 5 Hz were applied.

The crate processor program fulfills three important tasks during the detector readout:

1. A certain fraction of all pixels, depending on the detector threshold, is noisy and appears as always or frequently hit. The dummy data exceeds the real information from particle hits by far. A suppression is therefore already applied during the readout. Suppression masks are obtained during calibration runs outside LEP physics and updated every few months and in case of major changes in the detector settings.

2. The pixel addresses are re-arranged from an on-line convention, based on front-end chip coordinates, to an off-line convention with module coordinates as later on in the DELPHI raw data stream.

3. The data integrity is checked with control words. Corrupt structures, e.g. not matching the modules' physical readout order, or events with buffer overflows are either rejected or marked as faulty to be taken into account for the data processing.

6.3 Detector control and data quality monitoring

Stable detector operation is essential for high data quality and the safety of the entire Silicon Tracker. Several tasks are running in the Silicon Tracker's workstation within the DELPHI online computer system and enable continuous control. The pixel detector is embedded in this survey. Parameters on power consumption, threshold setting and temperatures are recorded as well as the ambient humidity monitored. The operational parameters are entered into DELPHI's data base and the states of the different sub-systems displayed in several levels. Automated response to possible misbehavior of the detector or to changes in the data taking conditions is enabled within DELPHI's slow control system.

A monitor task for online data quality checking spies the Silicon Tracker's raw data stream from the Vertex Detector partition and performs a first real-time analysis [113, 114, 115]. Routines were set up to quickly detect dead, noisy or inefficient modules. The raw data is separately processed for the Silicon Tracker's sub-systems, various variables histogramed and displayed matching the detector's modularity as controlled by the supply systems. The online data quality monitor was an essential tool during the commissioning of the detector and provides fast feedback during LEP physics conditions. Detailed histograms are filled by a "local" monitor and intend to inform the detector experts about a variety of detector performance aspects. A few overview histograms characterizing the basic operational status of the Silicon Tracker are filled by the "central" monitor program, checked by the central shift crew of DELPHI during LEP operation. The pixel detector related histogram page of the central quality checking is shown in fig. 6.4. The data quality as analyzed during one LEP fill

is displayed before and after the suppression of additionally masked pixels. The top histograms show the event size distribution of the entire detector. The mean occupancy per repeater and module is shown below as well as the number of noisy pixels. While analog quantities as signal heights, pedestals and noise are available to characterize the operation of strip detectors from their distributions, the binary pixel data needed a different approach. Furthermore, it was not possible to handle histograms with bins for every of the 1.2 million pixels. The pixel detector is monitored down to the level of readout chips instead, recording the occupancies per event and number of noisy pixels. Trace plots document the development with time. Reference histograms allow to compare the current situation to a nominal operation and are updated in certain intervals. Help pages for every histogram provide the shifter with information on the meaning of the histograms and on actions to be started in case of disagreement with the references.
A noise analysis, identifying single pixels with unproportionally frequent response, is performed on-line. Updates to the mask of noisy pixels as used for the noise suppression during the detector readout are written to the DELPHI data base [116] and are taken into account for DELPHI's raw data processing.

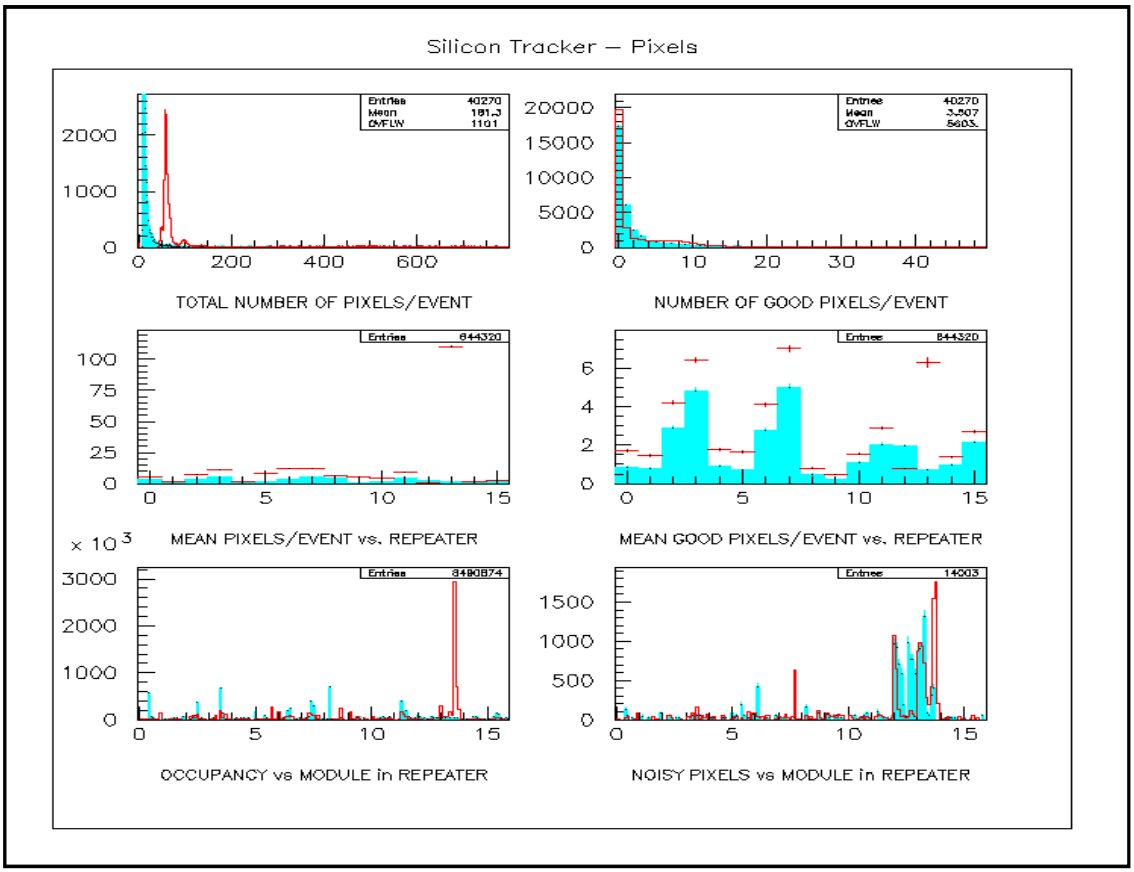

Figure 6.4: Pixel detector quality checking histograms.

6.4 Operational status

6.4.1 Detector configuration in 1996

First experience with the operation of the DELPHI pixel detector was gained in 1996 when LEP started its high energy period at 161 and 172 GeV center-of-mass energies. The yield of the module production (detailed in chapter 5.6.3) allowed to assemble five of eight parts of the full detector. All half cones of the internal pixel detector layer and one quarter of the external detector layer were installed into the Silicon Tracker. All detector systems were new. The supply and the readout systems were already laid out for the full detector but their modularity allowed the operation of the partially equipped system.
During the final detector tests in the assembly laboratory at CERN, 94 of the 95 pixel detector modules were operational. The result was confirmed after the installation of the Silicon Tracker into the DELPHI experiment and stated no mechanical damage or disconnected cables during this demanding procedure. After about one week of operation with all bias voltages applied, technical problems started to degrade the performance. The situation is shown in fig. 6.5. Short circuits appeared on bias lines of two of the innermost repeaters. The overflow current exceeded the power supply characteristics even at very low voltages and prevented from depleting all detector modules associated to these repeaters. A third repeater, also located in the innermost sub-layer, developed high but unstable currents on the depletion voltage line and needed to be switched off most of the time. A fourth repeater was missing one of the control signals and could not be read out. A fifth repeater suffered from readout errors with most of its detector modules leading to unreliable data. The situation remained unchanged for the rest of the year. The detector quarter AD, however, equipped with both pixel detector layers, was operational throughout the 1996 data taking and enabled to study the performance to be expected for the fully equipped detector [117]. Investigations on the origin of the short circuits led to the conclusion that the bias line with the kapton cables of type LK1 was most likely to be weak. Shorts on the detector modules themselves were unlikely since they were decoupled from the common supply. Faulty wire bonds could not be excluded at that time but further inspection was restricted to the next maintenance period. No observation was made then, however, which supported the conjecture of shorts caused by loose wire bonds.

6.4.2 Detector configuration in 1997/98

The full pixel detector was installed in spring 1997 with the missing three half cones added and faults with its initial configuration repaired. The faulty kapton lines for the bias voltage of the innermost pixel detector modules were bypassed and the supplies performed via the modules of the neighboring sub-layer. Fig. 6.6 summarizes the

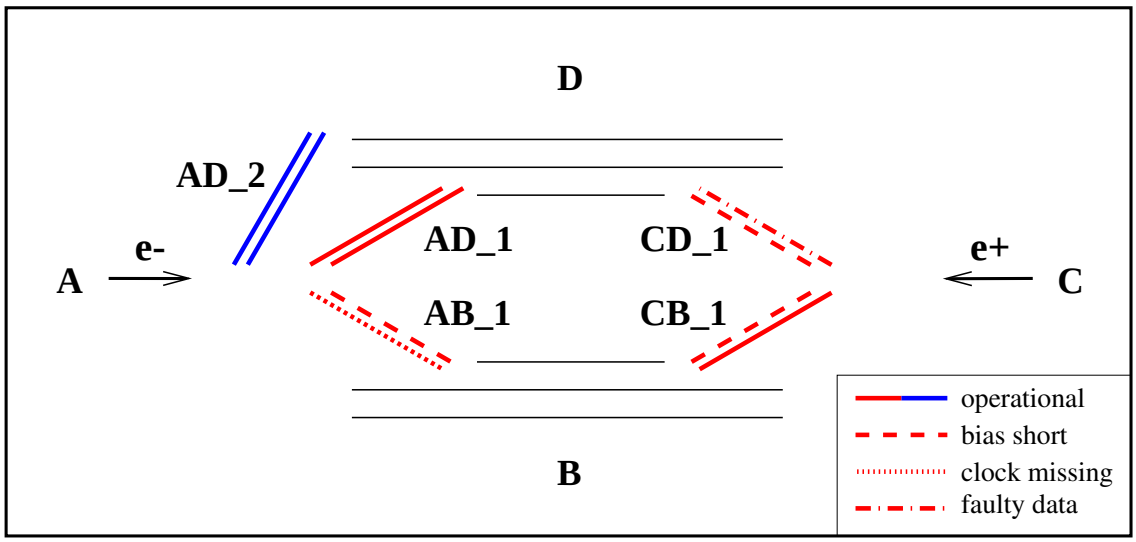

Figure 6.5: Operational status 1996.

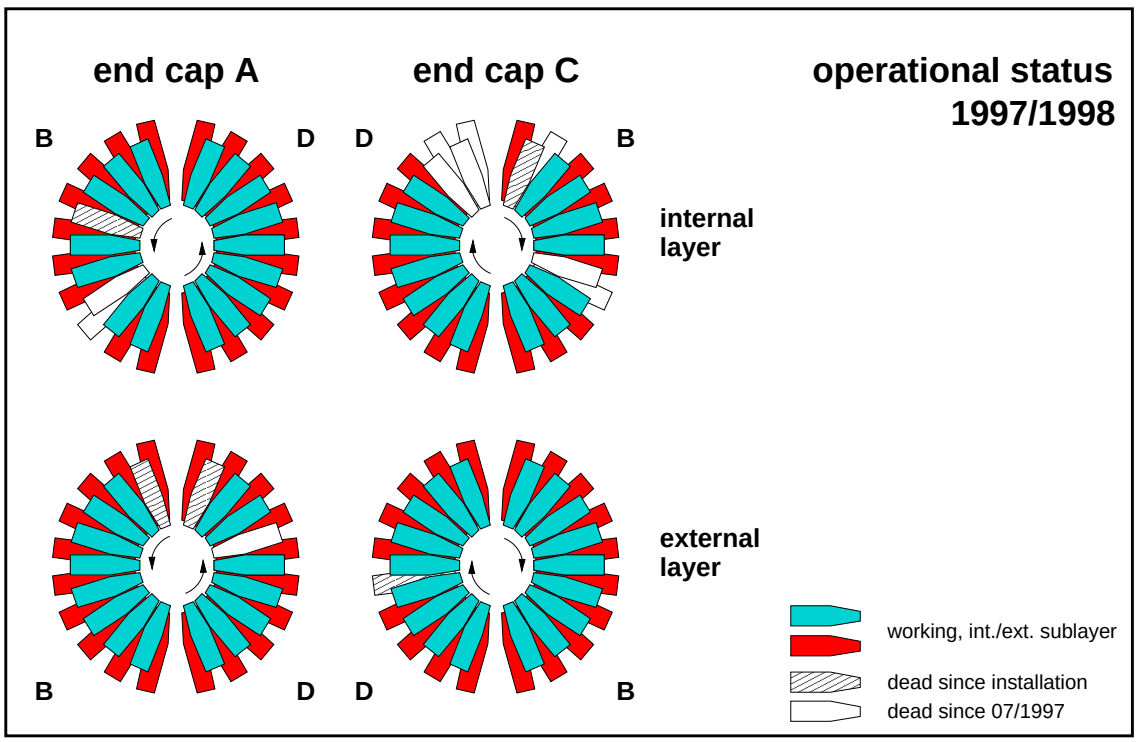

Figure 6.6: Operational status 1997/98.

operational status for every of the 152 pixel detector modules since the installation in 1997.
Five detectors were already known not to work during the assembly. One module in the internal layer of end-cap A was not replaced. The risk of more damage than repair during the dismounting was considered as very high. One module in the external layer of side C was installed despite of a known unsteady contact in its long kapton cable, motivated by the lack of good detectors. This module turned out to be problematic and is responsible for corrupted data in its repeater. Three other modules exposed on the corners of three half cones were damaged during the insertion into the Silicon Tracker and were disconnected from the supplies. No extra module was lost during the installation in DELPHI and the detector 96.7% operational at the beginning of DELPHI's startup.

After six weeks of operation, a major incident unfortunately led to the loss of further 7% of the pixel detector prior to physics data taking. At least five detector modules of the internal pixel detector layer and one module of the external layer developed shorts on the bias line, coinciding with a spike in the relative humidity of the ambient air. The situation is shown in figures 6.7 and 6.8 where the relative humidity and the reverse currents of the internal half cones are plotted versus the day number in 1997. Three periods can be distinguished:

I. The first period is characterized by the startup of DELPHI early April. The detector systems were subsequently switched on and the increase of the temperature resulted in dropping relative humidity. Stable temperatures and humidity in the Silicon Tracker's environment were reached during DELPHI's cosmics data taking when all sub-systems were fully operated to perform measurements for alignment purpose.

II. On May 13 (day 133), just before LEP physics was scheduled to start, a fire accident in the SPS radio frequency power supply room enforced to stop all beams and to postpone the LEP operation [118]. After the official news was published that several weeks of cleaning work were required, the DELPHI collaboration decided to switch off its experiment again to save resources and man power on shifts (day 152). The Silicon Tracker, however, stayed powered on in order to maintain its geometry as measured during the alignment data taking. The period in june was characterized by hot and humid weather conditions in the Geneva area. On June 11th (day 162) the relative humidity exceeded 80% in the DELPHI cavern for a short time. Just at that time all half cones of the internal pixel detector layer started to draw very high currents on the depletion lines and the power supply system switched off. No effect was seen with the external detector layers. It was not possible to deplete half of the pixel detector any more. For safety reason it was not switched on until DELPHI was operated again.

III. DELPHI resumed operation on July 7th (day 188), one week before first beams circulated in LEP. The internal pixel layer recovered from the accident but most of

the half cones showed higher currents than before. Ten detector modules could not be depleted any more. In the internal detector layer, pairs of modules were lost which were supplied commonly. One module of the external layer failed, too. It is supposed that moisture induced shorts in parts of the long kapton cables first and very likely lifted off bond wires finally.

After this accident, 90% of the detector was operational with 94% of the detector's surface covered by the overlapping modules.

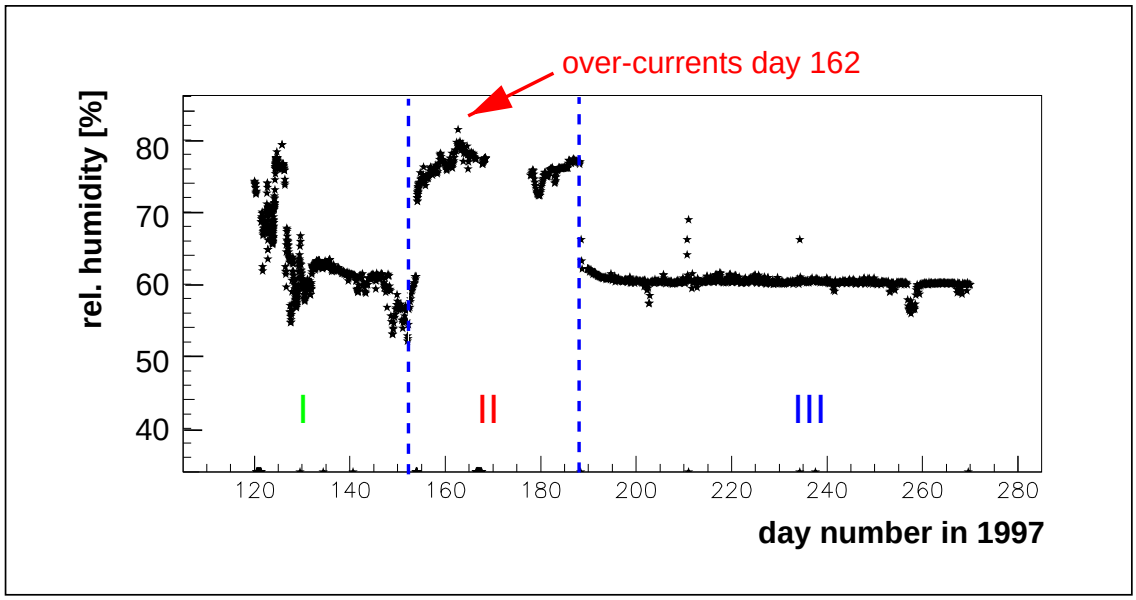

Figure 6.7: Humidity inside DELPHI 1997.

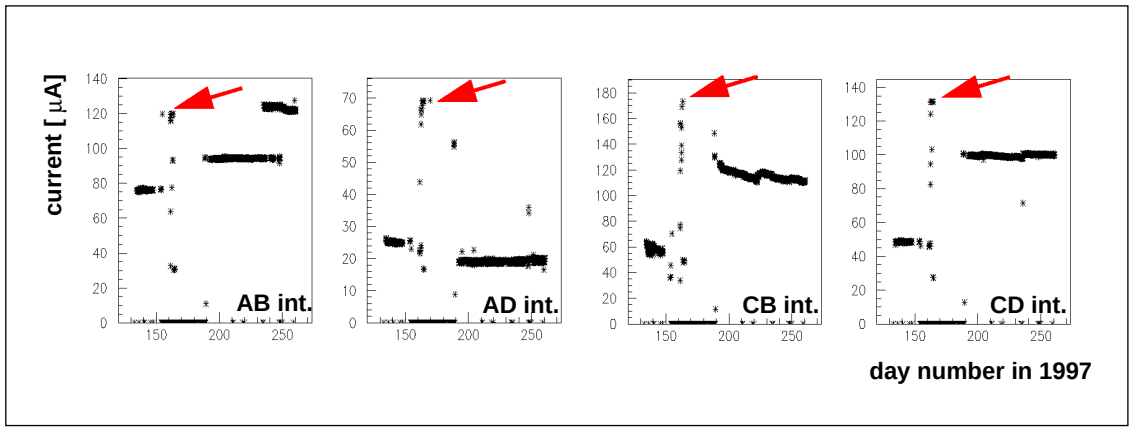

Figure 6.8: Detector currents of the internal layer in 1997.

6.5 Threshold setting and detector noise

Next to the operational status of the detector modules themselves, the applied thresholds and the fraction of remaining noisy pixels are most important for the detector's particle detection and tracking efficiencies.
Noisy pixels are always present with pixel detectors and binary readout, predominantly caused by non-uniformities in CMOS structures of the front-end electronics. An individual noise pattern is expected for every readout chip and module. High thresholds generally suppress this noise but yield reduced signal efficiency. The thresholds are therefore optimized for every module individually, aiming at a balance of low thresholds to obtain high signal efficiency and reduced noise with sufficiently raised thresholds.
For an individual event recorded by the acquisition system, noisy pixels usually can not be distinguished from real hits associated to particle tracks, especially if single pixels are concerned. Knowledge on the detector's noise behavior is therefore essential to yield high data purity.

Fig. 6.9 details the noise in the detector modules of one repeater, as measured during its commissioning after the installation in DELPHI. The nine modules were operated at nominal settings and repeatedly read out applying a random trigger. No beams were circulating in LEP. The retrieved pixels responded with different rates. The top plot shows their frequency distribution, i.e. the rate how often individual pixels were active within a certain number of readout cycles. The pixels' positions are visualized in the bottom plot, overlaying all addresses in one module's coordinate system. Most of the noisy pixels responded to nearly every trigger and could therefore be clearly identified. Nearly all pixels equipped with injection capacitors for threshold calibration purpose turned out to pick up noise and belonged to this class. The calibration procedure, intended to cross check the modules' efficiencies in certain intervals with simulated detector signals, could not be performed therefore. Two of such calibration pixels are implemented in the corners of every front-end chip. The pedestal of all noisy pixels is basically determined by these test pixels. Apart from isolated regions with increased noise, as one noisy chip in module number 2, the positions of further noisy pixels are distributed randomly.
A certain fraction of pixels was noisy to a smaller extent. For the threshold adjustment, pixels with frequencies exceeding 10% were considered. The goal was to reproduce the modules' behavior as characterized during the acceptance tests after the production. Thresholds between 9 and 10 ke^- were adjusted finally (see fig. 6.10), ensuring full particle detection efficiency. About 0.3% noisy pixels are identified and suppressed during the readout.

A more detailed study on the systematics of the noise was performed to enable further data cleaning. Several consecutive noise frequency measurements were performed and the systematics of the results considered. Fig. 6.11 shows the fraction of how often individual pixels with a given noise probability appeared within all measurements.

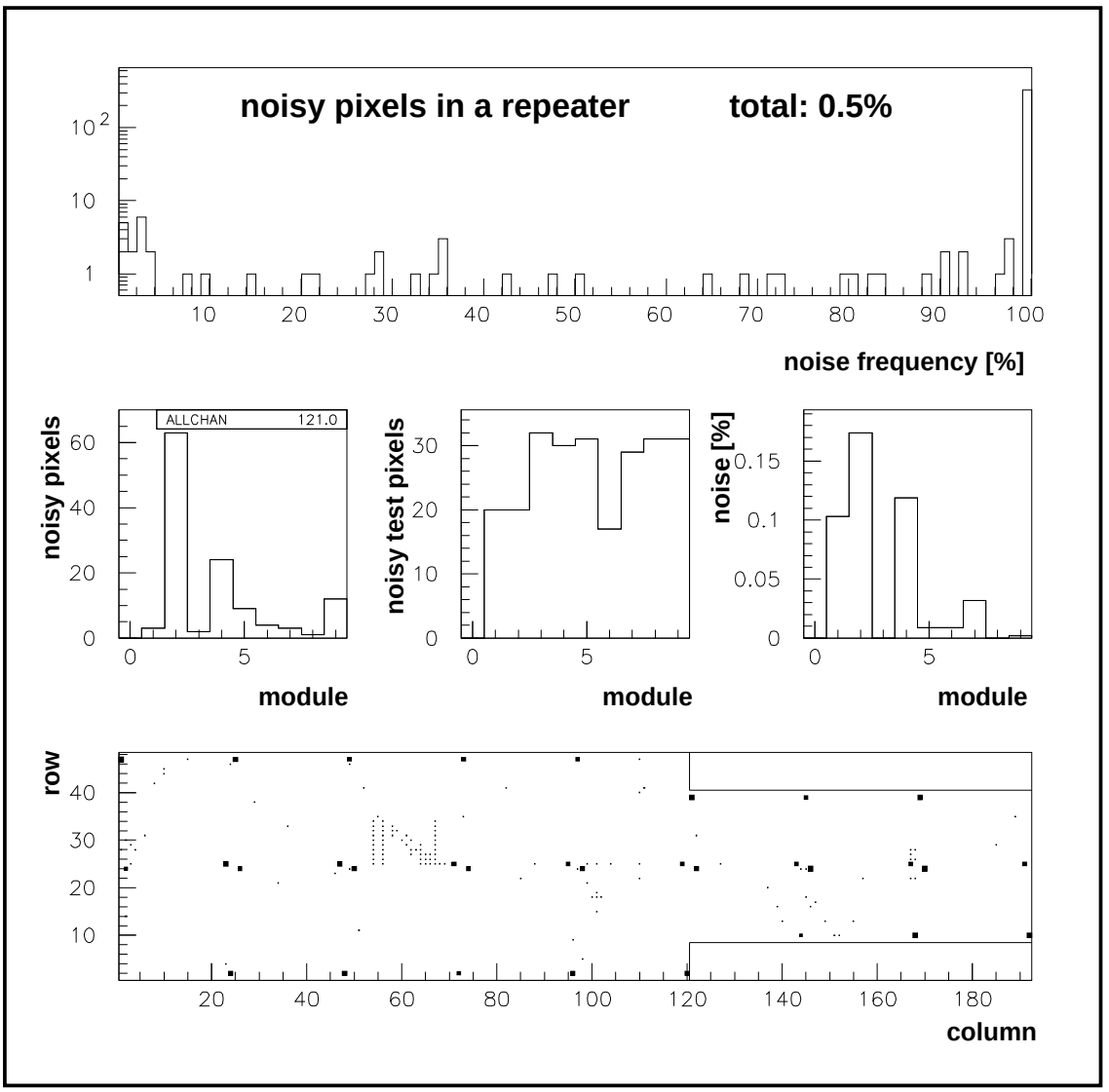

Figure 6.9: Noisy pixels in a repeater.

The individual measurements are shown in the left part and the mean values in 0.5% bins in the right part of the figure. As a result of this study, pixels with a relative response of less than 1% can be considered to contribute randomly to the noise. Pixels responding to more than 1% of the triggers were active with the same frequency in all measurements and are systematically noisy.

Fig. 6.12 summarizes the noise level after threshold optimization. Up to several hundred noisy pixels are present with every repeater. With the lowered limit for the noisy pixels definition applied, about 4×10^{-3} of all pixels were systematically noisy. The remaining random noise is of the order of 10^{-6}, low enough to enable stand-alone tracking with the Very Forward Tracker.

A procedure was added to the online data quality monitor to keep trace of the response

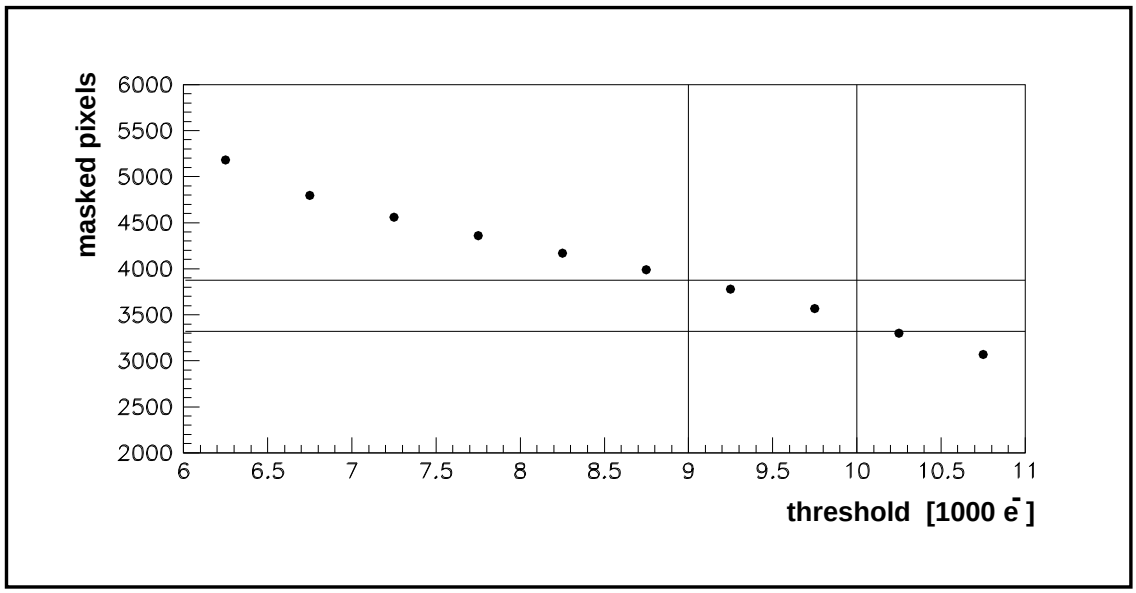

Figure 6.10: Number of masked pixels as a function of the applied threshold.

of every pixel and provide additional noise suppression for the data acquired during physics fills. Without carefully documented noise the pixel detector's data is hardly usable and would present too many possible space points to the track reconstruction algorithm. The number of noisy pixels recorded additionally to the crate processor suppression masks in 1997 is shown in fig. 6.13. For every LEP fill which reached physics conditions, the pixel detector's data was spied and pixels responding to more than 1% of the second level triggers identified. Filled circles represent the sum per fill, outlined circles new noisy pixels which were not identified in the previous fill. The total number of noisy pixels stays rather constant at the 10^3 level but changes dynamically by up to several hundred pixels.

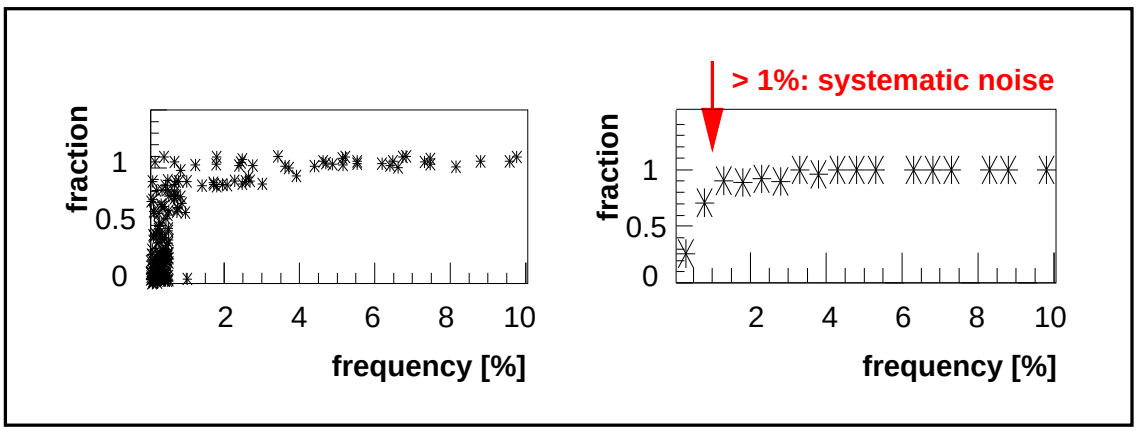

Figure 6.11: Determination of systematic and random noise.

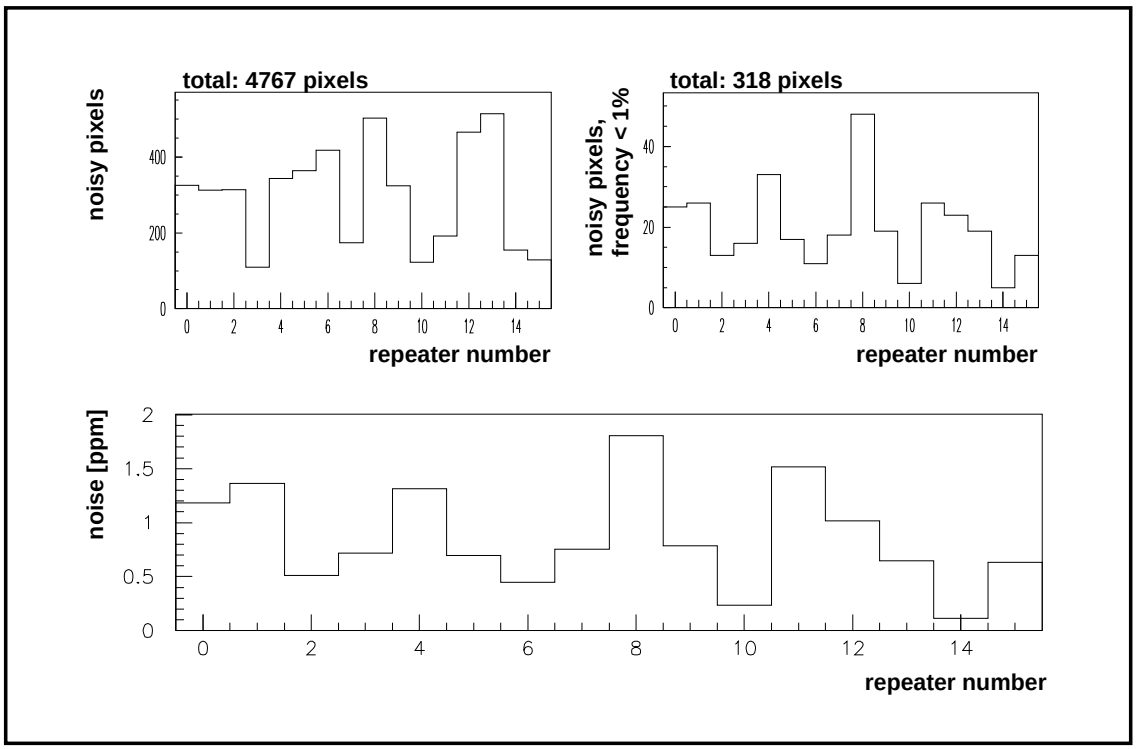

Figure 6.12: Random noise vs. repeater number.

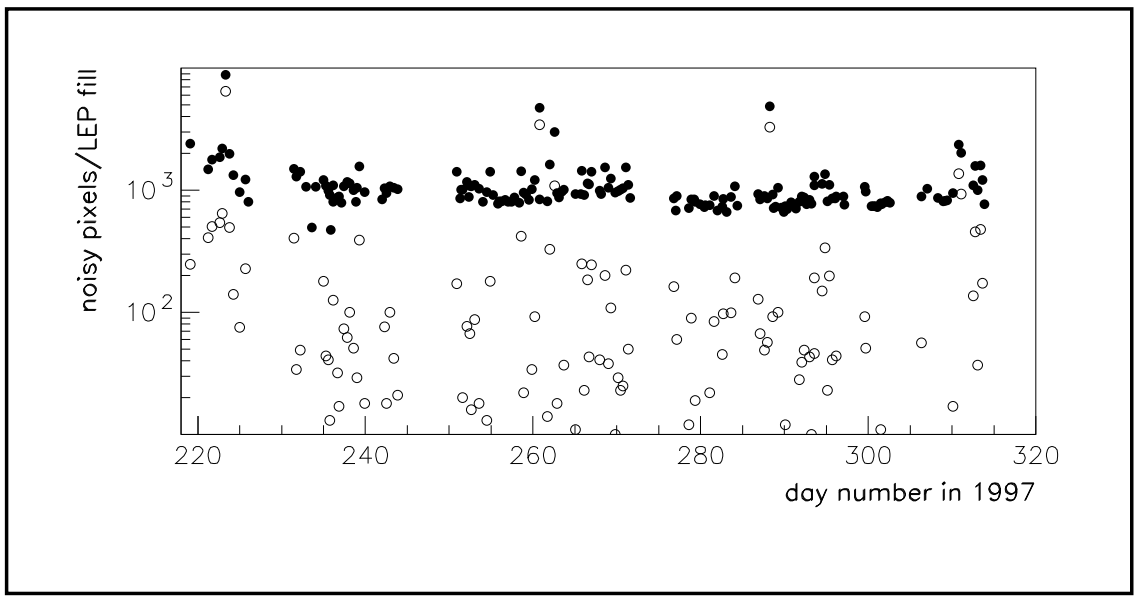

Figure 6.13: Trace plot of noisy pixels in 1997.

6.6 Event size and protection against excess occupancy

Stable detector operation is a critical issue both for high data quality and the detector's safety. The importance of appropriate thresholds and noise suppression for the data quality has been emphasized in the previous chapter. Typical event sizes of up to several hundred pixels are obtained during physics data taking with well collimated beams. Most of the recorded pixels belong to single pixel clusters and are either noise or related to particle tracks. Off-momentum particles from the beam halo move parallel to the beam axis. Showers of such particles cross the detector horizontally and show up as correlated activity in one hemisphere on both detector sides (see fig. 6.14). The charge released by off-momentum particles is collected by up to 2×8 neighboring pixels in the internal detector layer. Clusters of 2×3 pixels are seen with the external detector layer, matching the modules' orientation with respect to the beam axis (see fig. 6.15).
During the commissioning of a new fill, when particles are injected into the LEP collider, occupancies may increase by several orders of magnitude. DELPHI's data acquisition is kept running with internally generated triggers during this period to ensure functionality anytime. Protection against excess occupancy is required since the power consumption of active pixels increases by a factor of 10 with respect to the standby state. The supply's safety limits may be exceeded, enforcing the power supply supervisor to switch off the detector parts affected to prevent from damage. The modules' temperatures drop by up to 12°C in such a case (see fig. 6.16) and affect badly the detector's stability [119].
A LEP related detector state was therefore introduced to the pixel detector operation to prevent from excess power consumption. Thresholds are automatically raised outside physics data taking by the detector control system and lowered to their nominal settings again if LEP and DELPHI's background monitors declare acceptable beam conditions. The situation is shown in fig. 6.17 where the trace of the pixel detector's event size was monitored for one LEP fill. The fill was in coarse for 5 hours and 17 minutes. At the beginning of physics data taking, the thresholds were lowered and mean event sizes of about 225 pixels recorded. Standby thresholds at the end of the physics conditions resulted in suppressed sensitivity during LEP's filling activities.

Accidentally high occupancies during physics data taking are monitored by the data acquisition system. Locally increased hit rates are identified and communicated to the power supply controller which raises the thresholds in the modules concerned. Fig. 6.18 shows exemplarily what happened frequently during the first year of data taking without this control procedure regulating the detector's stability. High occupancy in two modules induced crosstalk in two readout chips, facilitated by the threshold oscillation after the reset of the pixels' comparator circuits. With increasing occupancy, these chips started to activate more and more pixels and were fully blinking finally,

similar to the situation show in fig. 6.19. Increasing the module's threshold enabled to interrupt the cross talk and to return the module to a nominal operation.
The "Anti Blink Command" (ABC) issued by the data acquisition system goes even a step further and tries to avoid blinking readout chips. First indications for increasing noise with consecutive readout cycles are observed and the threshold is increased by a certain value in the module affected. After typically 10 seconds the thresholds are decreased to an intermediate state and finally released to its standard settings again (see fig. 6.20). The ABC activities are stored for every channel. If a maximum number of re-trials is exceeded, the threshold is raised permanently and intervention by the detector experts is required.
Stable detector operation has been achieved with the active detector control system and power supply switch-offs widely avoided.

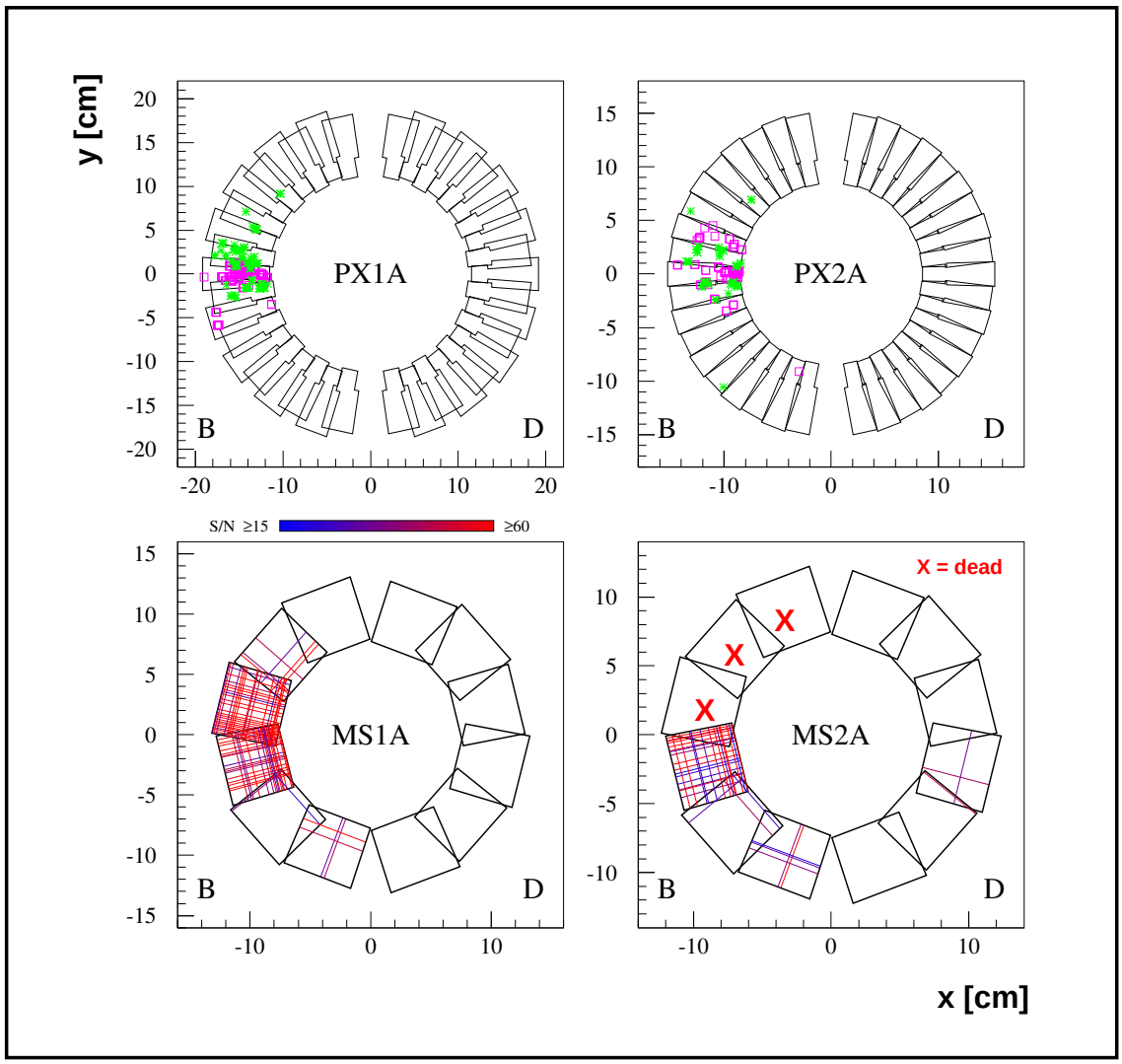

Figure 6.14: Correlated activity in the detector layers of the Very Forward Tracker.

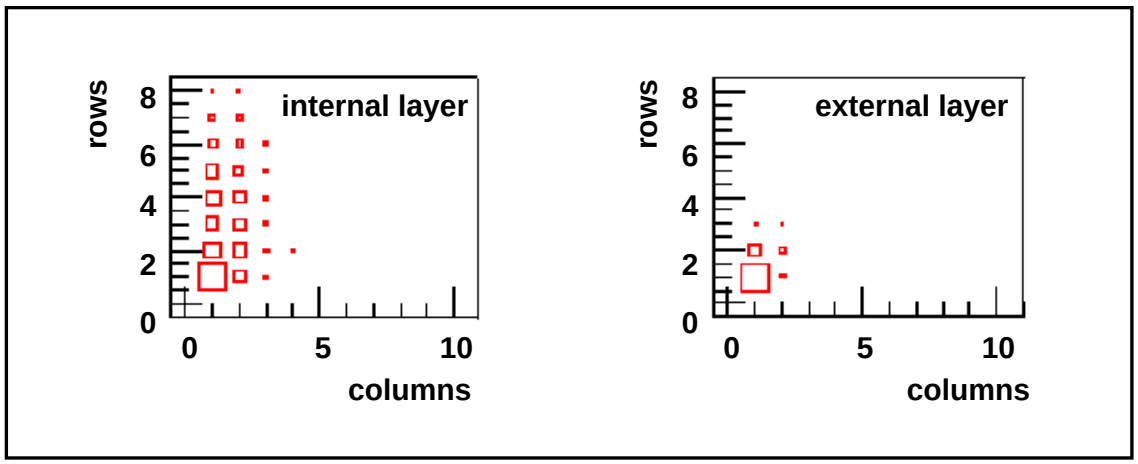

Figure 6.15: Cluster size as recorded online, mostly originating from particles parallel to the beam.

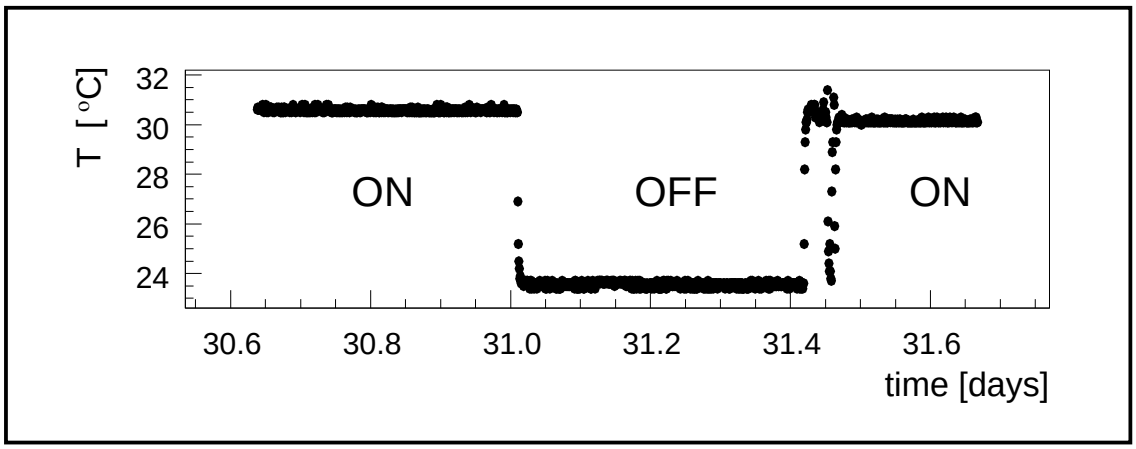

Figure 6.16: Temperature variation with the pixel detector in on/off states.

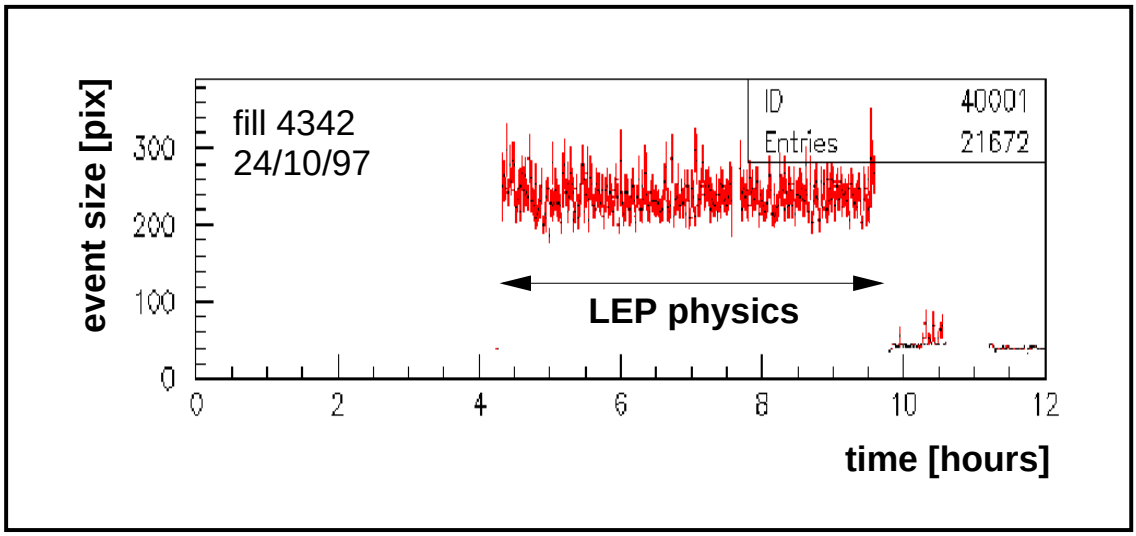

Figure 6.17: Trace plot of the event size during a LEP fill.

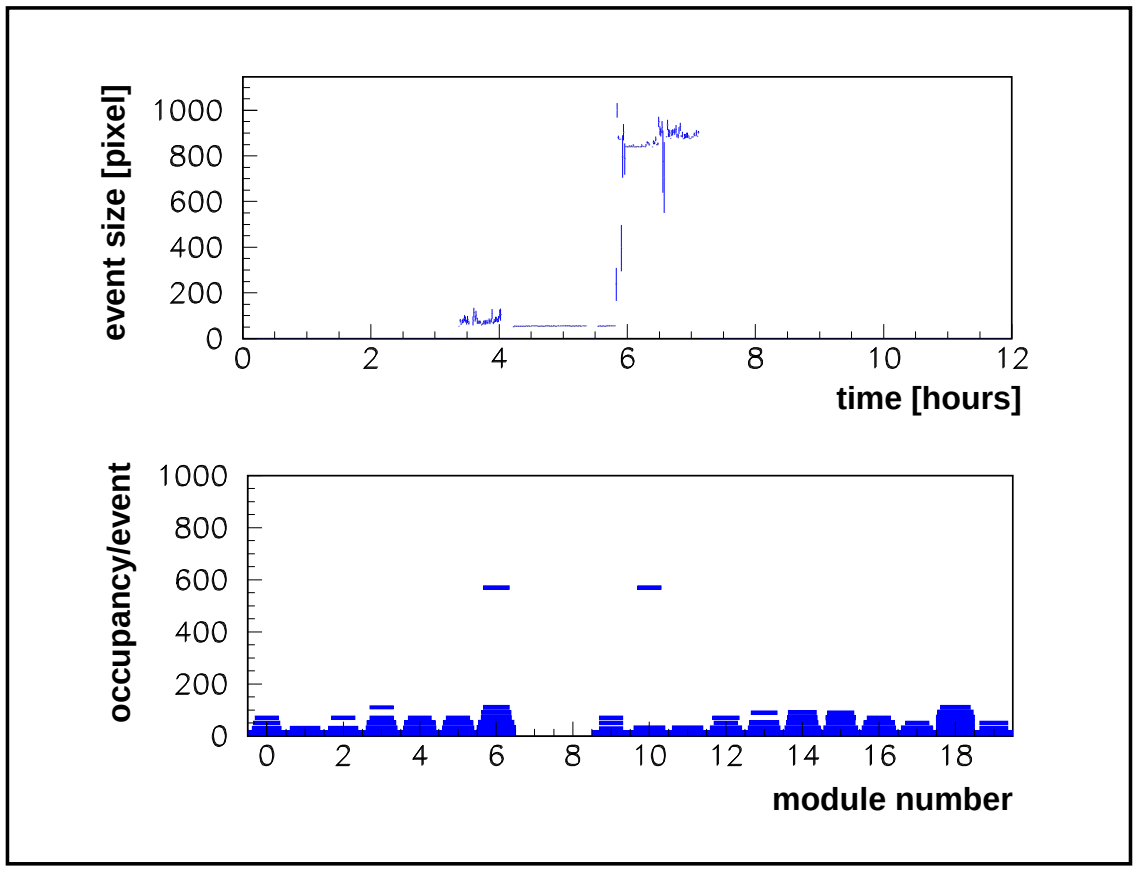

Figure 6.18: Increased event size by background induced chip blinking (top plot). Occupancy distribution for the 19 modules of a repeater pair; two modules developed blinking chips (bottom plot).

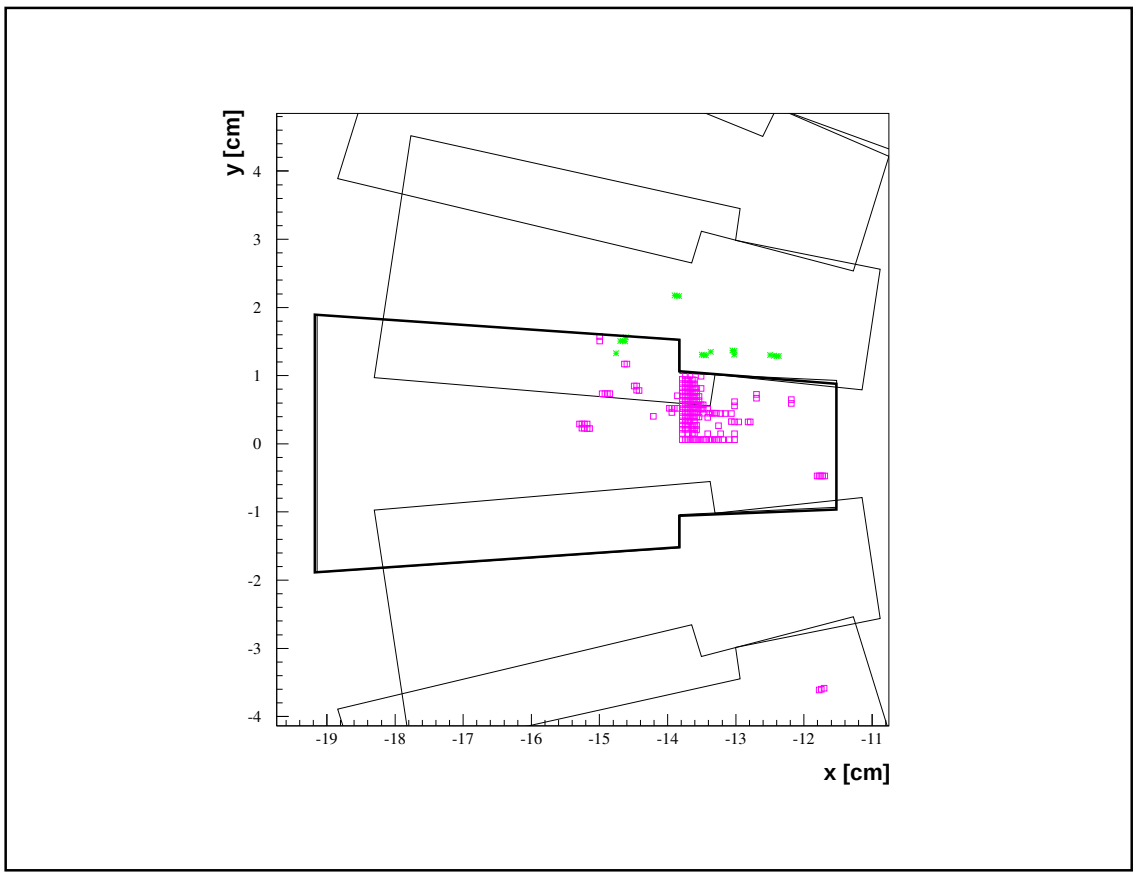

Figure 6.19: Blinking chip on a module.

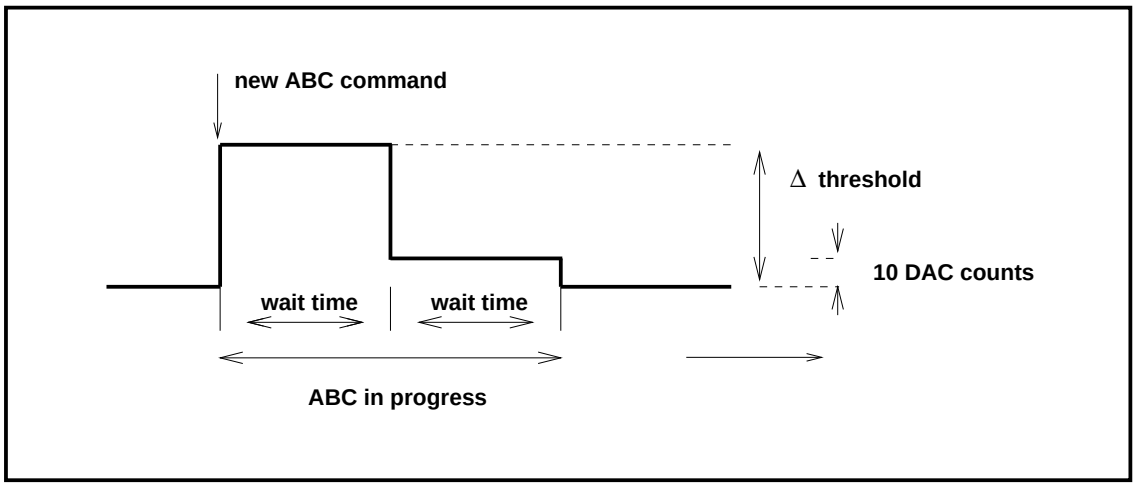

Figure 6.20: Sequence of automatic threshold rising and decrease.

6.7 Protection against high radiation dose

Active and passive radiation monitors are installed in the proximity of the Silicon Tracker [120]. The active detectors are built from four solar cells, mounted on a plastic ring surrounding the beam pipe at $z = 1.455$ m on side C of DELPHI. The radial distance from the beam is 9.5 cm. Thermo luminescent and radio photo luminescent devices mounted on some of the detectors provide an absolute calibration and can be accessed during maintenance periods.
DELPHI's radiation monitor has been designed to protect the microstrip vertex detector against high background integrating to a dangerous level. It is also of great importance for the pixel detector's safety. The limiting factor on the radiation sensitivity comes from the total dose acceptable for the detector electronics. The pixel detector's front-end electronics is especially endangered. The non-radiation hard CMOS process used for the SP8 chip's design stands doses up to 10 krad while the strip detectors' front-end chips MX6 and TRIPLEX tolerate up to 50 krad integrated dose. The microstrip detectors themselves with integrated coupling capacitors as well as the directly coupled pixel detectors are less sensitive to spikes of radiation.
The radiation monitor reacts on the time scale of tens of seconds. Counters are incremented depending on the background level and react fast to increase seen with single sensors. The information from the solar cells is combined to trigger warnings at several levels before dumping the beam. Figure 6.21 shows the integrated dose as measured in 1997 by two of the detectors. Monitor 1 is located above the beam pipe and monitor 2 on side B of DELPHI, measuring the horizontal component of the background. The accumulated dose in 1997 was 60 rad, which has to be scaled by about a factor of 10 at the radius of the pixel detector.

Figure 6.22 shows a long term trace-plot of the dose in correlation with the background monitored by the Time Projection Chamber and the Very Small Angle Tagger. The scale extends over more than a day. Four LEP fills can be distinguished. Especially at the beginning of a fill, during the acceleration and ramping, the background is usually high and spikes from increased off-axis particle flux are recorded by the radiation monitors. The pixel detector electronics has been accumulating about 1 krad per year since the start of its operation.
Locally the dose might be much higher. Uncontrolled, abrupt changes of the beam orbit ("beam loss") and the subsequent intense particle fluxes are critical for the pixel detector. LEP lost the beam a least once close to or even inside DELPHI since 1996. During fill number 4410 of November 6th, 1997, one pixel detector repeater developed a corrupted data structure, originating from one module sending uncorrelated data to the readout bus. This misbehavior continued to stay and is associated with increased occupancy. It was supposed that a hardware failure might have been caused by localized radiation damage, i.e. very high ionization in one chip affecting the oper-

ation of CMOS transistors or logic circuits. A readout procedure was established that minimizes the effect on the data.

During the prototyping period of the pixel detector project, a study on the general response of the front-end electronics to irradiation was performed. Figure 6.23 shows a result on the threshold shift with β irradiation. Two pixels per chip dispose of injection capacitors for analog pulses simulating detector signals, so that the thresholds could be probed. With doses exceeding 10 krad, a significant relative increase of the thresholds was measured. The resulting loss of particle detection efficiency sets the limit to the total dose acceptable.

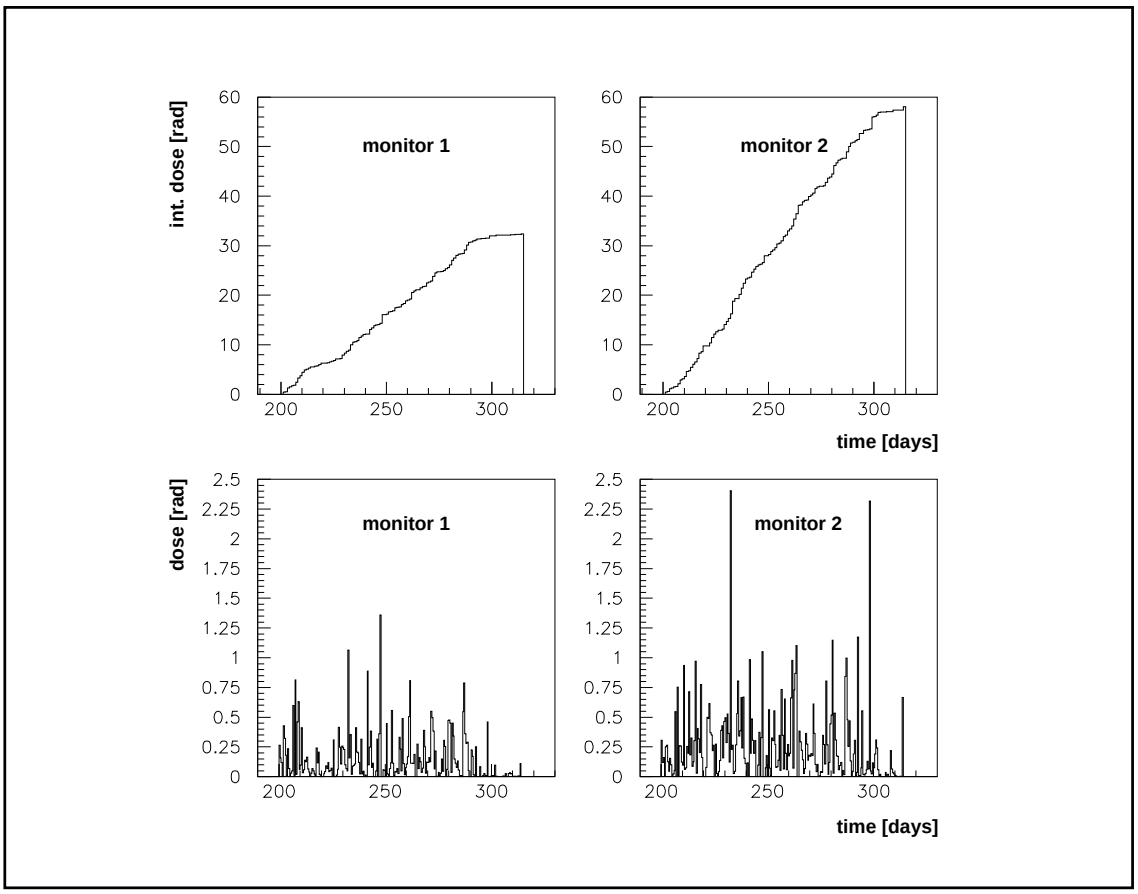

Figure 6.21: Integrated dose measured with the Silicon Tracker's radiation monitors.

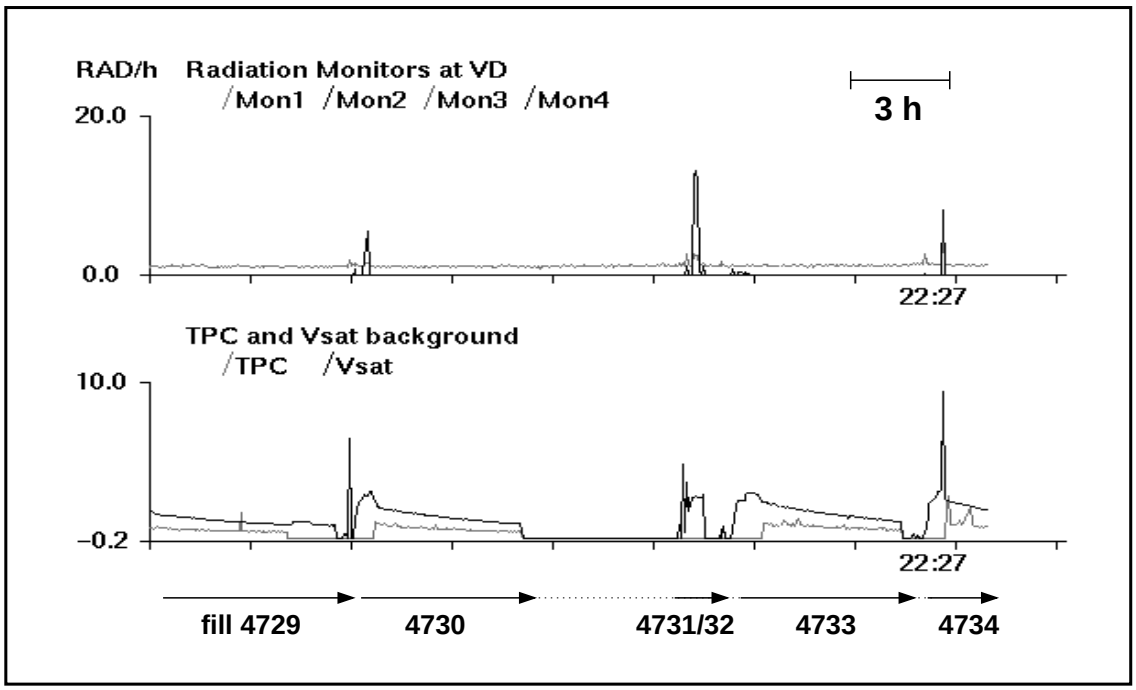

Figure 6.22: Online trace-plot from radiation and background monitors.

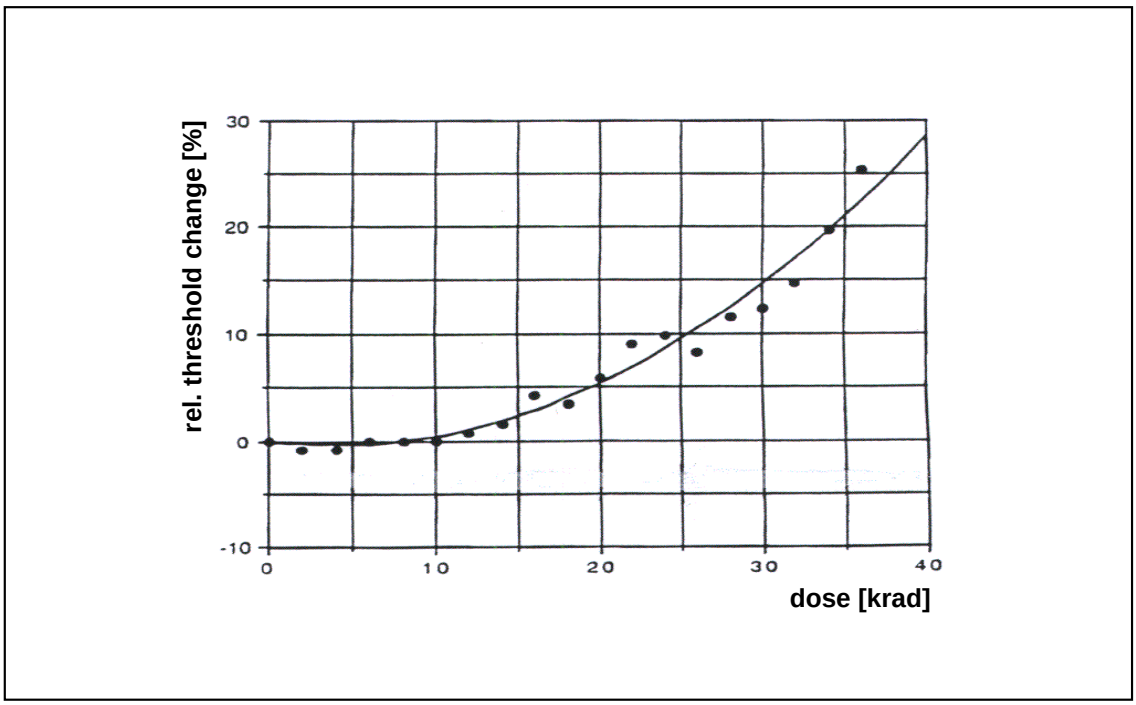

Figure 6.23: Relative threshold change with the readout electronics as a function of the radiation dose.

Chapter 7

Performance of the pixel detector

Stable detector operation and full integration of its supply systems into the real time control of DELPHI enabled to meet the performance required for successful contribution to physics measurements. Detector noise with different event tags, geometrical stability, spatial resolution and the contribution to the track reconstruction are summarized here referring to [67].

7.1 Detector noise

After the masking of noisy pixels during data acquisition and off-line event reconstruction, remaining hits originate either from particles traversing the detector or from random noise. Fig. 7.1 shows the number of pixels for three classes of events as tagged by DELPHI's event reconstruction program.
Hadronic events with high track multiplicity are likely to involve tracks also at low polar angles. A mean number of about 4.5 hit pixels was measured for this class of events. Much higher activity is seen with background events, defined as triggered events with no tracks pointing to the primary vertex. Beam-gas interactions belong to this category. Very large numbers of hit pixels are obtained from showers developing at small angles and traversing the pixel detector layers. Such background events are easily identified and excluded from analyses.
The most important information on the pixel detector's data quality is provided when tagging a third class of events with just two charged tracks reconstructed in the central region of DELPHI. No physics background is expected in the forward region, distinguishing this class of "cosmics" events for an upper estimate on the random noise. A mean number of 0.6 pixels was measured requiring the cosmic tag which corresponds to a fraction of 0.5×10^{-6} of all pixels.

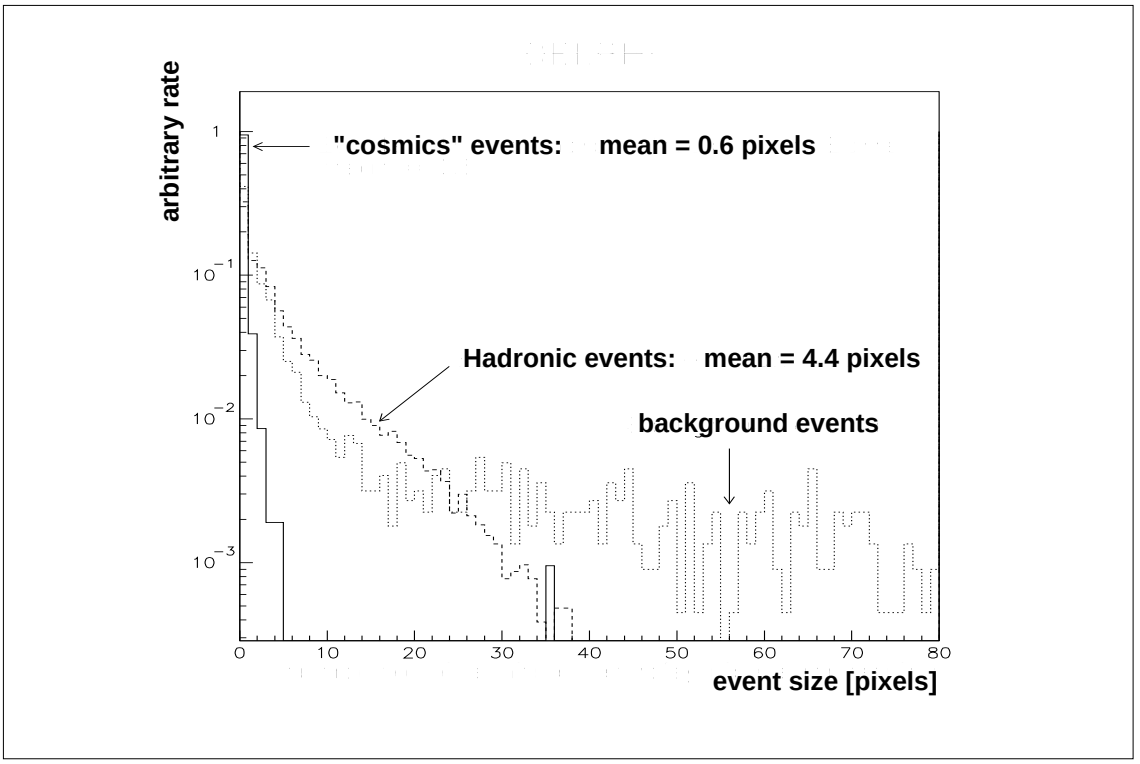

Figure 7.1: Pixel detector event size for different event tags.

7.2 Alignment, detector stability and spatial resolution

The alignment of the pixel detector is based on the geometrical survey performed during the detector assembly and the measurement of track residuals after the installation in DELPHI. Tracks from e^+e^- collisions as provided by the other end-cap tracking detectors are used to refine the survey. This procedure allows to correct for mechanical deformations of the support structure resulting from stress during the installation process. Three steps are distinguished. A global alignment of entire pixel detector half cones is performed first. The relative position of the sub-layers in every half cone is determined in a semi-global alignment then. The final module positions are obtained by considering the overlap regions of neighboring modules and the track residuals there taking into account the constraint of the primary vertex. Tracks are re-fitted over all track elements and the χ^2 minimized.
Mechanical deformations of the support structure are parameterized and provided to the track reconstruction program. Distortions of the pixel detector's geometry with respect to the survey in the assembly laboratory are seen with fig. 7.2. The top plot visualizes a torsion of the Silicon Tracker's support. This biggest movement found is visible as a relative change of the radial position of pixel and ministrip modules de-

pendent on their z positions. The deformations are of the order of several millimeters. A rotation of the half cones around the vertical axis is shown in the bottom plot. Systematic translations of up to half a millimeter were measured as a function of the modules' azimuthal positions.
Considerable movements also occur with individual pixel detector modules. The modules are bound to the support at one end only and experience tractive forces by the kapton cables. Fig. 7.3 shows the relative change of the bending angles for the 40 and 38 pixel detector modules, respectively, of upper and lower half cones in every detector layer. The kapton side of the modules points either towards the beam spot or away from it. The effect of pulling kapton cables is seen from the distribution of intersection point residuals, shifting the modules to either larger or smaller inclination angles. The shifts correspond to a few hundred micrometers at the top of the modules.

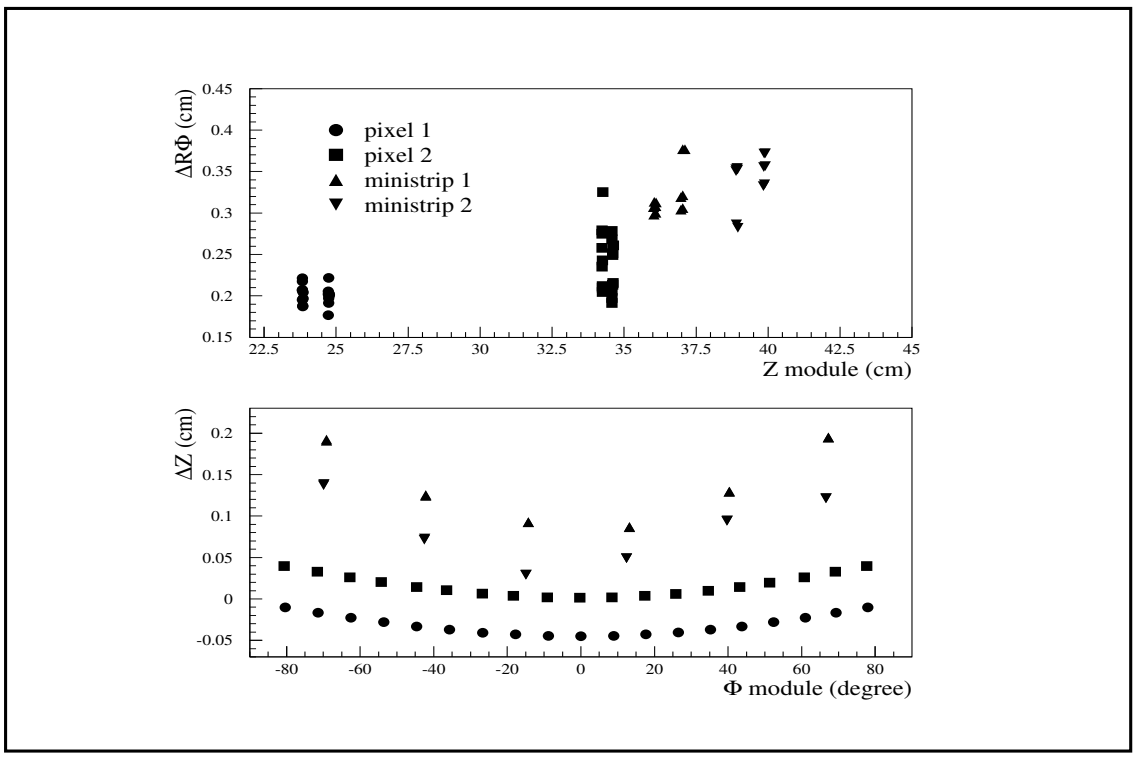

Figure 7.2: Difference between survey and final VFT alignment for quarter AD in 1996. Top: torsion of the structure. Bottom: rotation of the cones around the vertical axis results in systematic translations of the modules' z positions.

The quality of the alignment is reflected in the spatial resolution and the detector efficiency measured. Tracks from the primary vertex intersect the first and second pixel detector layers at 57.5° and 40.5° angles of incidence, respectively. Released charge in the detector substrate yields a majority of single-pixel hits or clusters of two pixels neighboring in radial direction. The expected spatial resolution from these hit patterns has been parameterized according to geometrical considerations. With

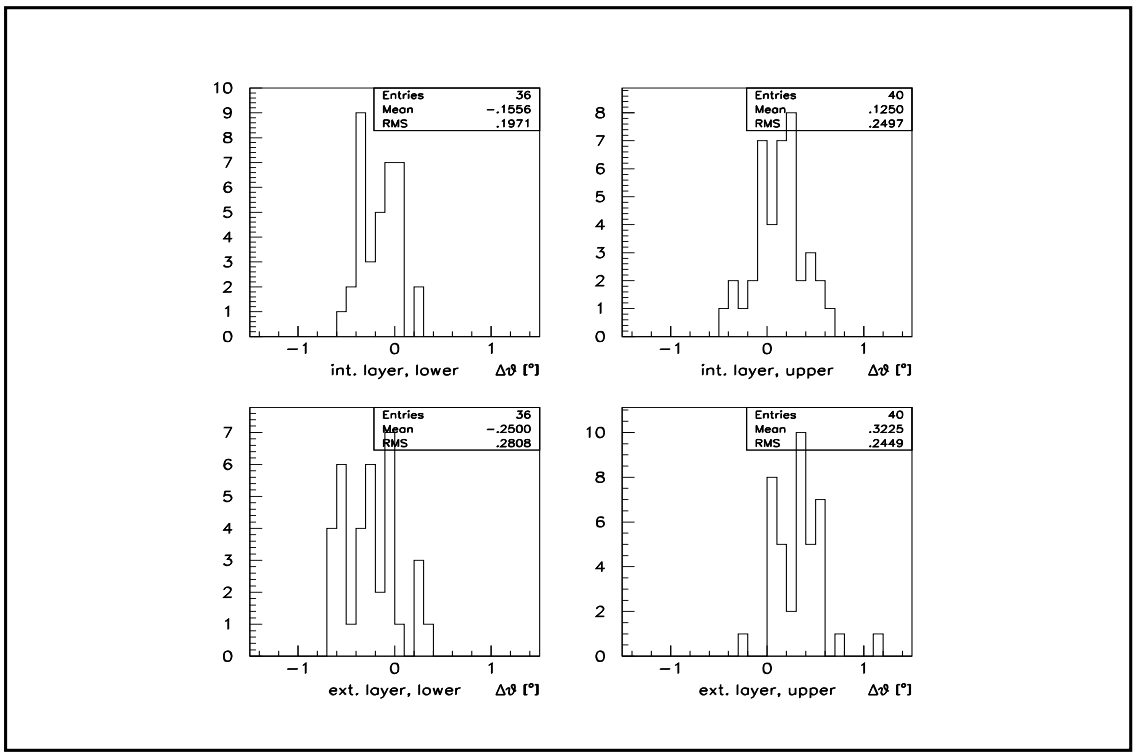

Figure 7.3: Relative change of the modules' inclination angles as measured in 1998 with respect to the geometrical survey after the assembly in 1997.

increasing angles of incidence, the ratio of two-pixel clusters to single-pixel clusters grows. Resolutions from 100 μm with single pixels down to 70 μm are expected. The distribution of track residuals as measured in 1997 is seen in fig. 7.4 and matches the expectation and design goal.
The modules in all detector quarters and layers contributed efficiently to the space point measurement. The mean efficiency was 97% for finding hits in a 3σ window around the predicted position. Non-working modules were excluded from this study.

7.3 Contribution to the track reconstruction

Since 1997 a revised track reconstruction strategy is applied to DELPHI's end-cap region that uses to the full extent the detector upgrades for LEP2 operation. The updates to the forward tracking have been summarized in refrence [65]. A stand-alone pattern recognition is performed with the space points measured by the Very Forward Tracker and track elements are created. At this point pixel detectors and ministrip detectors are not distinguished any more. Two of ten track search strategies in the end-caps start with the Very Forward Tracker. Track elements from this detector are combined with track elements provided by other detectors at larger radii. Ambiguities

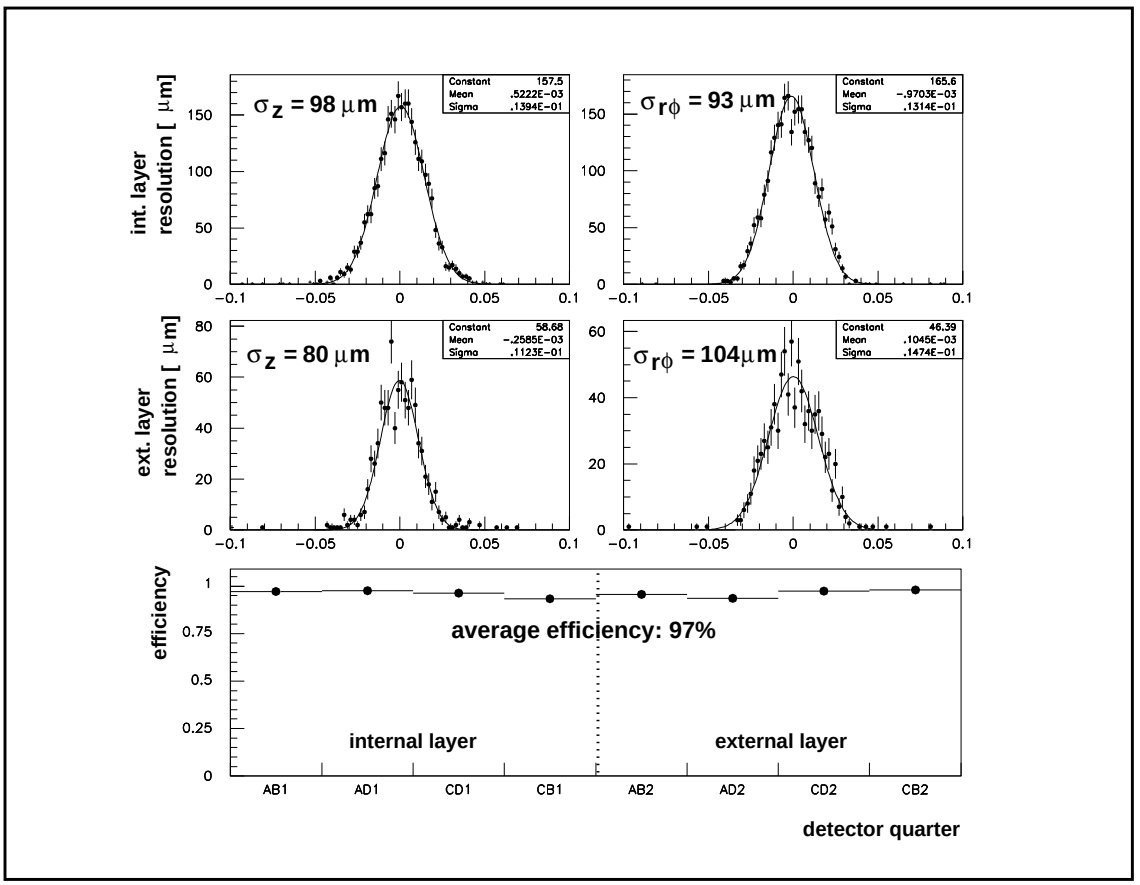

Figure 7.4: Spatial resolution and efficiency measured in 1997.

are resolved and the best fitting candidates used to form a track. A second search uses track elements measured by the Inner Detector and extrapolates to the Very Forward Tracker. The combined track elements from Inner Detector and Very Forward Tracker are the seed for finding the track then.

The Very Forward Tracker usually contributes among other tracking detectors to the formation of a track. In certain cases, however, a good VFT track element might not be linked to other candidates if no clear association is possible. The track element is then treated as a track on its own. Such VFTONLY tracks reach purities exceeding 95% if hits in three of the four VFT layers are considered. VFTONLY tracks usually have a poor momentum resolution due to their small length and almost parallel orientation to the magnetic field. Their direction, however, is measured with one to two millirad precision.

The Very Forward Tracker contributes efficiently to the track reconstruction in DELPHI as shown in fig. 7.5. The overall efficiency increases considerably at polar angles below 20° including this silicon detector into the track search. A gain of factors two to three is reached. The importance of VFTONLY tracks in the proximity of the interaction region to the track measurements at small polar angles is clearly visible.

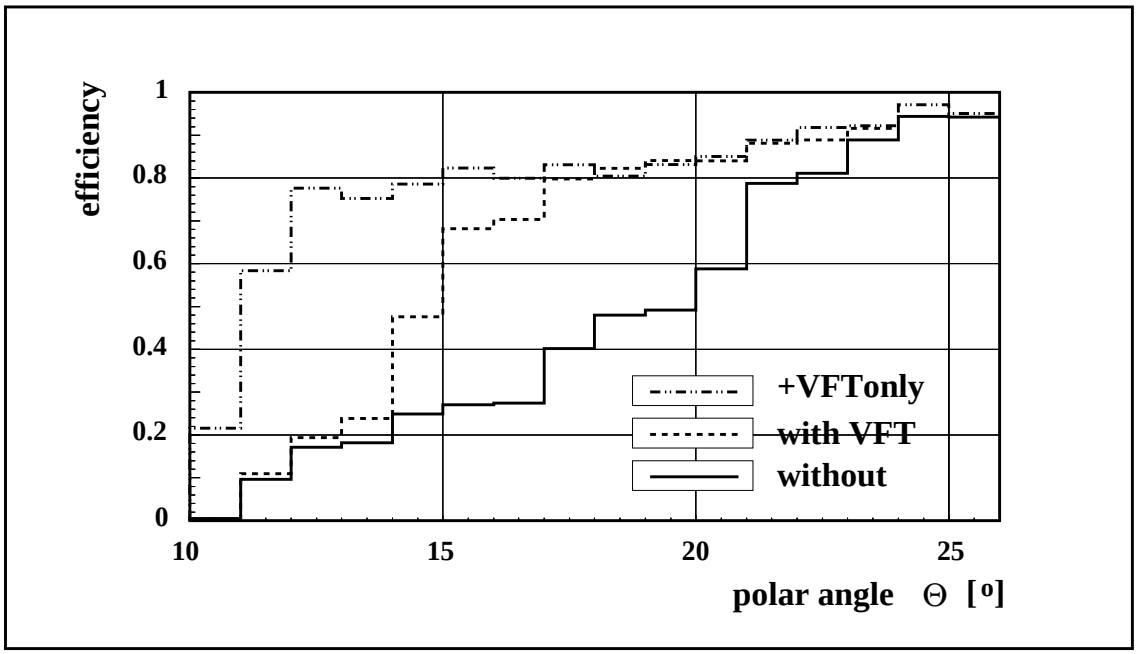

Figure 7.5: Track reconstruction efficiency in the forward region with and without Very Forward Tracker.

Chapter 8

Application of DELPHI's forward tracking detectors to electron identification in semi-leptonic W events $e^+e^- \rightarrow q\bar{q}e^+\nu_e$, $q\bar{q}e^-\bar{\nu}_e$

Studies of W bosons, the charged exchange particles of the weak force, belong to the most relevant physics topics at LEP2. Precision measurements on W mass, width and coupling parameters provide essential and complementary information on the validity of the Standard Model. The dominant W boson production mechanisms are overviewed in this chapter. With a design luminosity of 500 pb^{-1} per experiment, a rate of about 9000 W-pair events and 400 single W events was expected within three years of LEP2 operation. The rates are considerably smaller than with Z physics items at LEP1. Detector hermeticity and high efficiency are therefore essential requirements as outlined already in previous chapters.
Aspects of the reconstruction of W events with electrons in the semi-leptonic channel are described and the application of DELPHI's forward tracking detectors to the electron identification is discussed.

8.1 Production of W bosons at LEP2 energies

W bosons are predominantly produced in e^+e^- collisions according to the diagrams shown in fig. 8.1 [121]. The top plots describe the lowest order graphs for W boson pair production $e^+e^- \rightarrow W^+W^-$. The "t-channel" diagram on the left hand side visualizes the conversion of the initial e^+e^- pair into a W^+W^- pair involving a neutrino exchange. With the "s-channel" diagram on the right hand side electron and positron annihilate and produce an intermediate photon or Z boson. A positively and a negatively charged W boson are produced in a double resonance and decay into

fermion-anti-fermion pairs. The graphs shown here focus on semi-leptonic decays. One W boson decays hadronically (here: u and $\bar{d}$ quarks), the other one into a lepton (here: electron) and its associated neutrino.
Further contributions with the same initial and final states but different intermediate states arise from other graphs. The bottom diagrams of fig. 8.1 describe the dominant contributions to single W boson production $e^+e^- \rightarrow We\nu$. A t-channel photon exchange is involved in (from left to right) "fusion", "Bremsstrahlung" and "multiperipheral" graphs. The graphs lead to the final production of a W boson or quark-antiquark pair, a scattered electron and its associated neutrino. The study of single W boson events is attractive because they enable to measure properties of the triple gauge boson vertex γWW [122]. In event samples containing decays of W boson pairs a mixture with ZWW vertices is present.

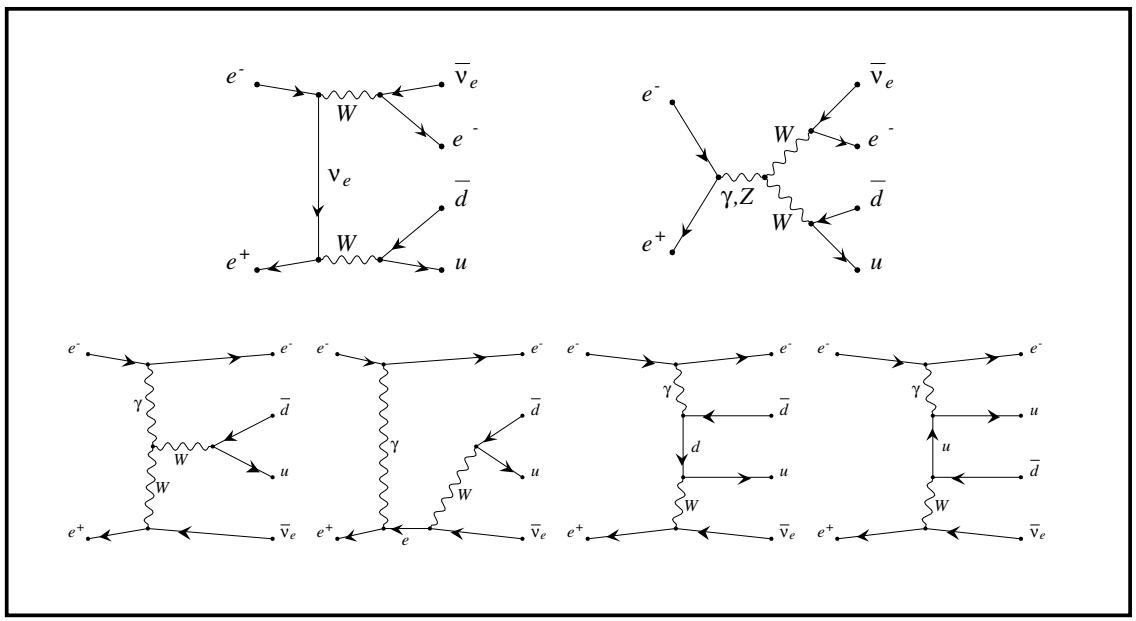

Figure 8.1: Top graphs: Lowest order Feynman diagrams for semi-leptonic decays of W boson pairs. Bottom graphs: Dominant diagrams for single W boson production.

The cross sections of W boson pair production and single W boson production versus the center-of-mass energy as predicted by Standard Model calculations have already been shown in chapter 3.2, fig. 3.3. The production of W boson pairs requires to exceed approx. $\sqrt{s} = 160$ GeV. Single W bosons are produced already below the W^+W^- threshold. The cross sections are significantly lower, however.
Recent preliminary measurements by the four LEP experiments on W pair cross sections, W mass and W decay branching ratios have been summarized in reference [123]. At 183 GeV center-of-mass energy the combined average cross section is specified as $\sigma(e^+e^- \rightarrow W^+W^-) = (15.86 \pm 0.40)$ pb. The combined mass measurements from direct reconstruction yield $m_W = (80.32 \pm 0.10)$ GeV/c^2. The branching ratios $W \rightarrow e\nu$, $\mu\nu$, $\tau\nu$, hadrons up to 183 GeV center-of-mass energy were determined as

$(10.92 \pm 0.49)\%$, $(10.29 \pm 0.47)\%$, $(9.95 \pm 0.60)\%$ and $(68.79 \pm 0.77)\%$.
The predicted cross sections for single W boson production $e^+e^- \rightarrow We\nu$ range from 0.35 pb at 172 GeV to 0.51 pb at 183 GeV center-of-mass energies and agree with measurements from all LEP experiments [124].

The experimental signature of the topology in semi-leptonic W events is characterized by two hadronic jets, i.e. groups of contiguous tracks in space associated to activity in the hadron calorimeters, one isolated lepton and missing momentum resulting from the undetected neutrino. The lepton is an electron or muon, originating either directly from a W decay or from a cascade decay via τ production.
The production of electrons is considered in the following discussion. The distribution of electron energies and production angles in semi-leptonic W events is shown in fig. 8.2. W^+W^- and $We\nu$ Monte Carlo data was used, generated with PYTHIA for 183 GeV center-of-mass energy. Electrons from semileptonic decays of W pairs are produced predominantly in the central detector region and fade out towards the direction of the incoming beams. Their energies extend up to about 70 GeV. Electrons from single W production are produced mostly at very low polar angles. The cross section peaks at $\theta < 2^\circ$ where the electron remains undetected. Only a small fraction of electrons is emitted at larger angles which are covered by tracking detectors. Calculations with the EXCALIBUR generator on the expected cross section of single W events with electrons produced at polar angles $\theta \geq 10^\circ$ yield $\sigma \approx 0.08$ pb. Single W events have been studied therefore by tagging events with either a two-jet structure in the central detector, no lepton detected and large missing momentum (hadronic W decay) or with a single lepton found at large missing momentum (leptonic W decay). The new tracking detectors in DELPHI's forward region, especially the Very Forward Tracker, can help to tag such kind of events by detecting the electron and relating it to additionally measured coplanar and very acollinear hadronic jets.

8.2 Electron identification with the DELPHI detector

Different procedures are applied to identify electrons in the central part and the end-cap region of DELPHI [51, 125]. Performance aspects of calorimeters and detectors for track reconstruction are taken into account. Electromagnetic interactions in support material located in front of the calorimeters complicate the task. In the central region the material is described as $0.8\ \chi_0/sin\ \theta$. Several radiation lengths of support material are involved in the end-caps.

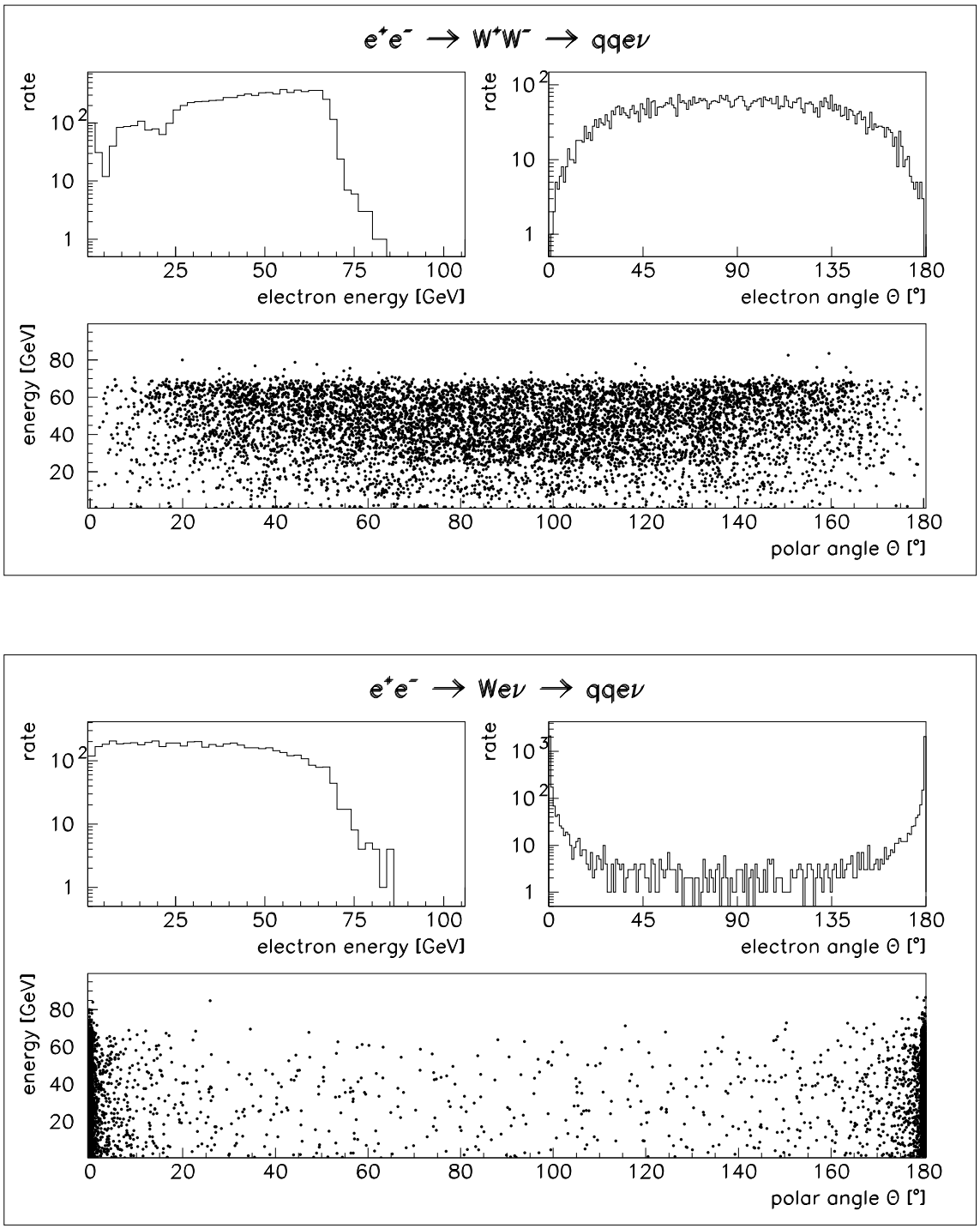

Figure 8.2: Electron energies and production angles in semi-leptonic decays of W boson pairs (top) and single W boson production at 183 GeV center-of-mass energies (bottom).

Central detector

Electron identification in the central part of DELPHI is based on two independent and complementary measurements. The central electromagnetic calorimeter (High Density Projection Chamber) enables to measure the energy deposition E of electromagnetic showers. The energy deposition is compared to the independently measured momentum p as determined by the track reconstruction detectors. The variable E/p is converted into a probability for the electron hypothesis. A ratio close to 1 is expected for electrons, correcting the measurements for several detector effects and taking into account calibrations. Additional information is provided by the measurement of the specific particles' energy loss dE/dx inside the Time Projection Chamber, exploiting the high track point density and spatial resolution of this tracking device. An average efficiency of 55% at 45% purity is achieved within the polar angles $50° \leq \theta \leq 130°$. The tagging result is expressed in four qualities "very loose", "loose", "standard" and "tight".

Detector end-caps

In the end-cap region other strategies are applied. The main problem with electron identification in the intermediate region between central detector and end-caps results from material located before and after the Time Projection Chamber (see the region around $\theta = 40°$ in fig. 3.7, chapter 3.3). But also below $\theta = 15°$ the material adds up considerably. Electrons suffer from radiation loss there and photons convert with high probability into electron-positron pairs, leading to smeared signals and low detection purity.
The selection criterion for electron identification in the end-caps is the ratio of the electromagnetic energy associated to a track and the track momentum. Tracks fulfilling quality criteria as constraints on the measured momentum and its relative error, the impact parameter and minimum track length are extrapolated to the Forward Electromagnetic Calorimeter EMF, covering the polar angles $8° \leq \theta \leq 35°$ in every end-cap. Showers in the calorimeter are associated to them taking into account the specific energy spread created by the electrons. Information from the Time Projection Chamber on specific energy loss is used only to a small extent. The standard forward electron tag limits per end-cap to the polar angles $20° \leq \theta \leq 32°$ and yields efficiencies of about 50% at $\geq$ 20% purity.

Use of the new forward tracking detectors

With the increased importance of the forward region at LEP2, several DELPHI physics teams have developed own approaches for refined electron search in the end-cap region. The new and upgraded tracking detectors in DELPHI's forward region enable the possibility to measure track points or track elements of electrons close to the interaction region before they shower in the support material. The geometrical acceptance of

end-cap calorimeters and tracking detectors is overviewed in table 8.1. Even though the very forward calorimeter STIC is equipped with layers of silicon veto counters which enable to measure several track points, the large amount of support material in front of it limits its efficiency for electron-photon separation considerably due to the subsequent conversion processes. The design goal of this detector aims at photon detection instead.
Two tools for electron-photon separation involving Vertex Detector and Very Forward Tracker shall be discussed. Polar angles above 10° were considered.

polar angles θ [°]	calorimeters and tracking detectors
1.7 – 2.5	STIC
2.5 – 10	STIC + VETO
10 – 11	STIC + VETO + EMF + VFT
11 – 15	EMF + FCA + FCB + VFT
15 – 20	EMF + FCA + FCB + ID + VFT
20 – 25	EMF + FCA + FCB + ID + TPC + VD + VFT
25 – 32	EMF + FCA + FCB + ID + TPC + VD
32 – 37	EMF + FCB + ID + TPC + VD
37 – 39	EMF + ID + TPC + VD

Table 8.1: Acceptance of calorimeters and tracking detectors in the end-caps of the DELPHI detector.

Isolated electron-photon separation based on VD-VFT space points Electron-photon separation based on hits in the Silicon Tracker is performed by the SIVETO package[1], intended to be used in topologies where electrons and photons are isolated and highly energetic. Showers in the forward and central electromagnetic calorimeters are backward extrapolated to the beam spot, taking into account the bending by the magnetic field. Space points in Vertex Detector and Very Forward Tracker are searched along the trajectories. The photon tag that provides a veto to the electron hypothesis fails if at least one of the following requirements is met:

- at least two Vertex Detector rϕ hits in two different layers are found within 300 μm distance from the trajectory
- at least one space point in the Very Forward Tracker was measured with all coordinates within 300-400 μm from the trajectory
- at least one Very Forward Tracker space point matches the trajectory in the xy plane together with one Vertex Detector hit in the outermost silicon detector of the Inner Layer. With the silicon strip detector cuts on the signal-to-noise ratio are applied.

[1]provided by M. Verlato, INFN Padova, Italy

The SIVETO code is part of the FORWARD_EM package[2] that also links to the calorimeter information.

Electron and photon identification based on VFT tracks Track information provided by the Very Forward Tracker is used in the FREGIT package[3] to distinguish between electron and photon signatures. Tracks with VFT participation or tracks only built inside the VFT are related to additional information from other end-cap detectors and intend to characterize the event. Energy deposition in the Forward Electromagnetic Calorimeter is considered as well as unassociated track elements in the Forward Tracking Chambers and the Forward Ring Imaging Cherenkov detector. Additional tracks mainly from Bremsstrahlung and photon conversion are supposed not to have hits in the Silicon Tracker.
The basic idea for establishing an electron identification is to create a variable describing the detector activity with several positive and negative contributions:

positive contribution	negative contribution
tracks in VD or VFT	no tracks in VD/VFT
energy deposition in EMF	energy in Hadron Calorimeter
additional tracks in EMF	hits in muon chambers
unass. TEs in FCA,FCB,FRICH	
total elmag. energy/p ≈ 1	total elmag. energy/p $\rightarrow 0$

Table 8.2: Signatures of detector activities to be used with the electron tag.

Hits in the Silicon Tracker are required to state the passage of a charged particle close to the interaction region. The energy deposition in the Forward Electromagnetic Calorimeter provides the particle's energy. Hits in the Forward Muon Chambers would reject the electron candidate. Multiple tracks and unassociated track elements (TEs) in the forward tracking chambers and the Forward Ring Imaging Cherenkov detector are considered to take into account Bremsstrahlung and showering. The ratio of total measured electromagnetic energy to the momentum is required to be close to unity for electrons.
Tests of the algorithm with hadronic, semi-leptonic and fully leptonic W^+W^- Monte Carlo data as well as bhabha events provided information on electron, muon and pion separation. Appropriate cuts on the discriminating variable were determined to be applied with real detector data.

[2] provided by V. Hedberg et al., CERN

[3] "Forward region electron and gamma identification tool" provided by S. Garcia, CERN

Electron identification efficiencies The tagging efficiencies for isolated electrons were determined with bhabha Monte Carlo data. Back-to-back electrons generated within polar angles $9° \leq \theta \leq 171°$ at 183 GeV center-of-mass energy were used; angles below 40° were considered separately for every end-cap.
Fig. 8.3 shows the efficiencies yielded by the FREGIT, FORWARD and the standard tags as a function of the polar angle. A cut on $E_e > 15$ GeV was applied to the measured electron energy. The direction of the electrons were reconstructed within $\Delta\theta = \pm 0.7°$ and $\Delta\phi = \pm 1.2°$ r.m.s. The standard tag is of almost no importance and restricts to the polar angles from 20° to 32°. Both the FREGIT and FORWARD tags reach much higher efficiencies, exceeding 80% in the region $26° \leq \theta \leq 36°$. While FREGIT's efficiency drops rather continuously towards lower polar angles, the FORWARD tool shows a dip in the acceptance region near $\theta = 24°$ where Vertex Detector and Very Forward Tracker overlap and provide just one pixel hit and each one $r\phi$ and one rz hit in the microstrip detector. The combined average efficiency of all tools is about 70%.

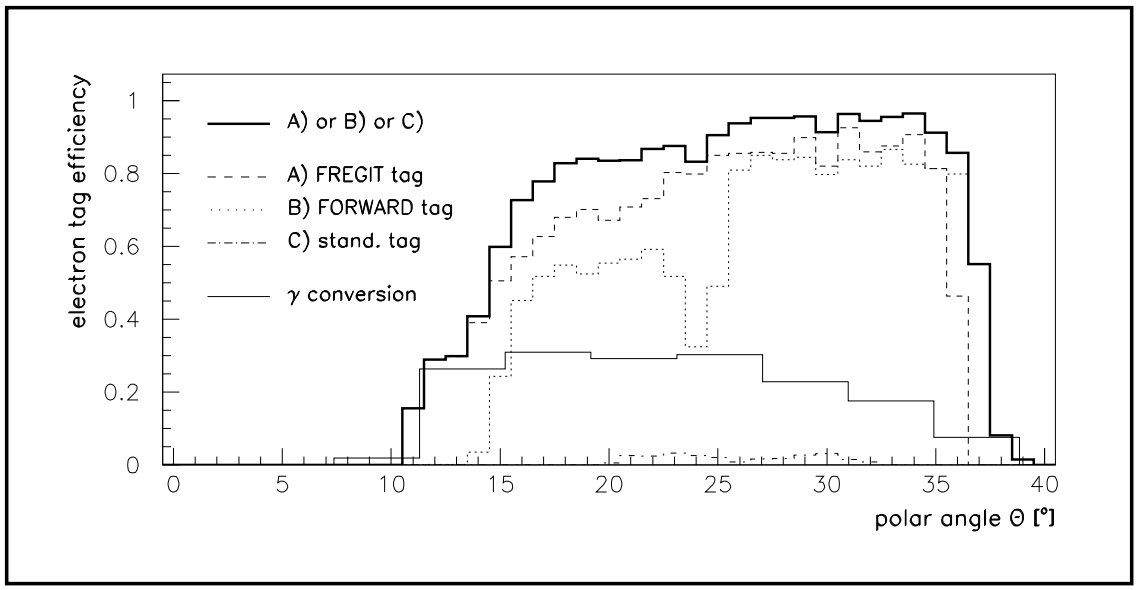

Figure 8.3: Electron identification efficiencies yielded with three tagging routines.

Energetic photons, however, are likely to be mis-identified as electrons if they convert into electron-positron pairs close to the interaction region. The most severe background to semi-leptonic W events is expected from radiative return events $e^+e^- \to Z\gamma$. Such processes occur with high cross section at LEP2 energies (see chapter 3.2). The energies and angular distribution of initial state radiation photons as obtained from HERWIG $Z\gamma$ Monte Carlo data for 183 GeV center-of-mass energy are shown in fig. 8.4. Mainly low polar angles are concerned but nearly the entire end-cap region is affected by the emission of photons of predominantly 70 GeV energy (top). The rz coordinates of conversion vertices in the Silicon Tracker region are shown in the bottom plot, re-

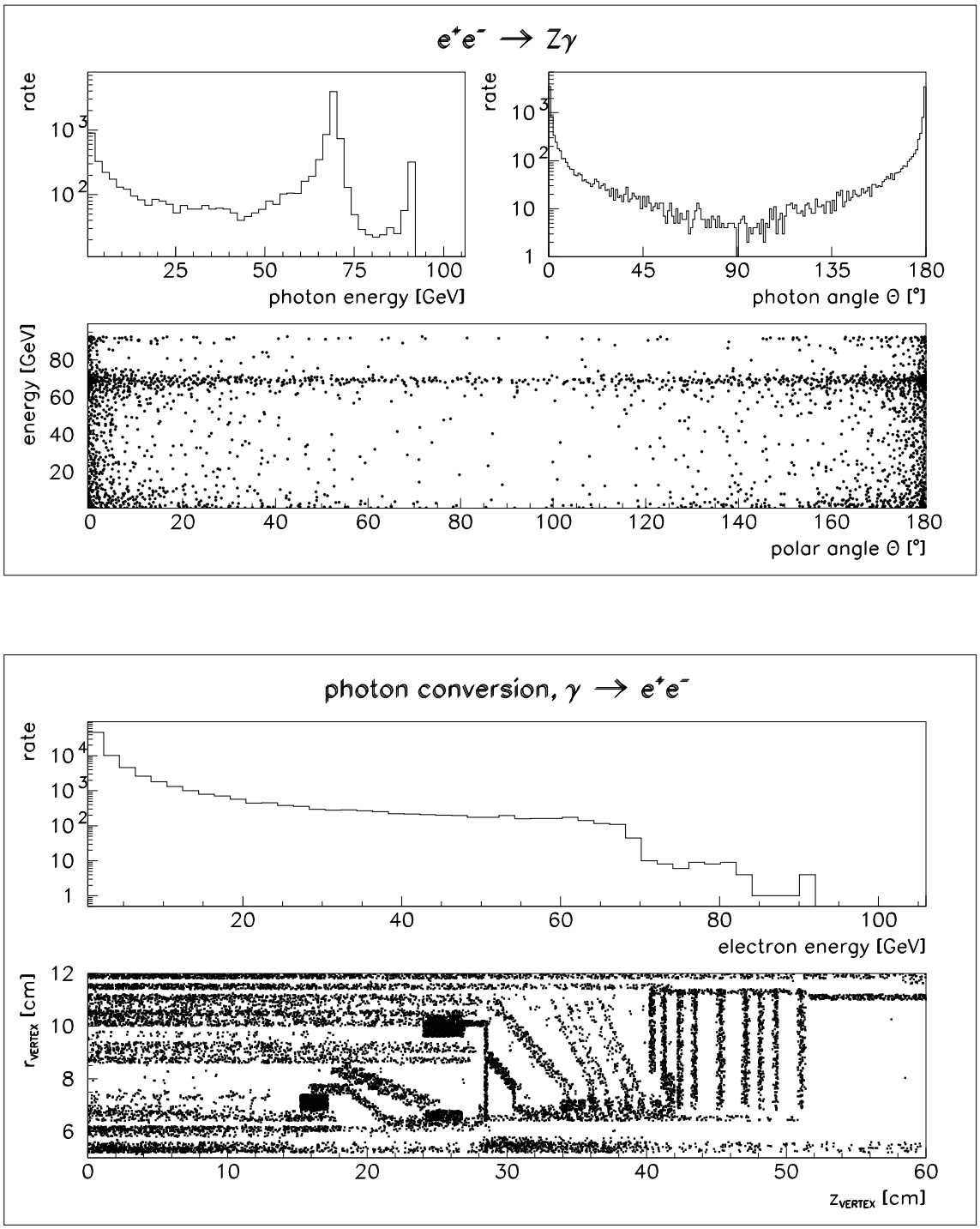

Figure 8.4: Photon energies and production angles in events with initial state radiation and return to the Z resonance (top). Positions of photon conversion vertices in the Silicon Tracker region and distribution of conversion electron energies (bottom).

producing the entries in DELPHI's material data base. The beam pipe, the modules of all three Vertex Detector layers, the pixel and ministrip detectors can be recognized as well as the support structures of Vertex Detector and Very Forward Tracker.
The energies of conversion electrons cover the range expected for electrons from W events. An efficiency of 30% has been measured for tagging initial state radiation photons as electrons.

8.3 Event selection from the data sample at $\sqrt{s} = 183$ GeV

The electron identification tools were applied to the data sample of 54 pb^{-1} integrated luminosity, recorded by DELPHI in 1997 at 183 GeV center-of-mass energy. Candidates for semi-leptonic W events were selected according to the following strategy:

Events with more than 6 reconstructed charged tracks were selected, with a total visible energy exceeding 50 GeV, more than 25 GeV energy associated to charged tracks and hadronic activity exceeding 5 GeV. Bhabha events were rejected by requiring less than 90% of the beam energy measured with the Forward Electromagnetic Calorimeters in both end-caps. A veto electron tag was applied in DELPHI's central detector part for $40° < \theta < 140°$ as well as a veto on tagged muons in the entire solid angle.
Electron tagging in the forward direction was performed by the *or*-combination of the three algorithms "FREGIT", "FORWARD" and "standard tag". Electron candidates with energies of more than 15 GeV were considered for polar angles from 8° to 40° and details on the tagging results logged. Events were accepted if just one electron was identified in one of the end-caps.
Tracks in a cone of 15° opening angle around the electron direction were masked and excluded from the track clustering to obtain information on the hadronic jets. The DURHAM cluster algorithm was applied with a standard distance variable $y_{cut} = 0.08$ and the remaining tracks forced into two jets. The four-vector of the jets was used to calculate jet masses and the invariant mass of the jet system. The direction of the W boson candidate was obtained from the momentum vector of the jet system. The sum of momentum components of electrons and jets was used to characterize size and direction of the missing momentum. From Monte Carlo data a back-to-back topology of electron and neutrino in the laboratory system is expected. Details on the cuts applied are summarized in table 8.3.

Figure 8.5 shows the polar angle distribution of electron candidates after application of these cuts. The rate in bins of two degrees is compared to Monte Carlo data of the expected signal[4,5] and the most important background[6]. The Monte Carlo

[4] qqeν four fermion processes at 183 GeV generated with GRACE
[5] qq$\tau\nu$ events generated with EXCALIBUR and subsequent simulation of the DELPHI detector
[6] Zγ events generated with HERWIG

charged tracks	≥ 6
E_{total}	> 50 GeV
$E_{charged}$	> 25 GeV
$E_{hadronic}$	> 5 GeV
$\sqrt{(E_{EMF_A})^2 + E_{EMF_C})^2}$	< 80 GeV
$E_{electron}$	> 15 GeV
$\theta_{electron}$	$8^\circ \leq \theta$ or $180^\circ - \theta \leq 40^\circ$
$\min(\theta_{jet\ 1}, \theta_{jet\ 2})$	$> 5^\circ$
$\max(\theta_{jet\ 1}, \theta_{jet\ 2})$	$< 175^\circ$
tracks in jet 1,2	> 5
charged tracks in jet 1,2	> 2
miss. transvers momentum	> 10 GeV/c
$\mid \theta_{electron} - \theta_{p_miss} \mid$	$> 20^\circ$
$E_{hadronic}$ in jet 1,2	> 1.5 GeV
invariant 2-jet mass	> 10 GeV/c^2
angle jet 1, jet 2 ("acollinearity")	$\leq 170^\circ$

Table 8.3: Cuts applied for the event selection.

data result was normalized to the integrated luminosity of the detector data and the average efficiencies for electron identification and photon mis-identification measured in advance taken into account.

A total number of 149 events satisfied the cuts in both end-caps. The rate is well explained by radiative return events, however, giving rise to restrict more variables. The detector participation as provided by the FREGIT tag is shown in fig. 8.6. All tracking detectors are present. Hits in the Very Forward Tracker outside the detector's acceptance $10.5^\circ \leq \theta \leq 25^\circ$ are striking and can be explained by particles showering already in the innermost region of DELPHI. The distributions of three variables shown in fig. 8.7 provide further information. The top plots detail the electron energies in detector data, Zγ and qqeν Monte Carlo data. The expected reconstructed electron energies in qqeν events range from 15 to about 70 GeV with a broad maximum around 50 GeV. Electrons from Zγ events, however, peak at 70 GeV with a tail towards very low energies. The measured electron energies are more related to the distribution from radiative return events than from qqeν events. The distributions of the invariant jet masses and missing momenta also leads to the conclusion that a large fraction of events is compatible with radiative return events.

Refined cuts were applied restricting the electron energies to 30 GeV $< E_e <$ 65 GeV. With the electron tags, hits in the Vertex Detector or tracks in the Very Forward Tracker were explicitly required. The minimum missing transverse momentum was set to 20 GeV/c. A reduced list of event candidates was obtained. The polar angle

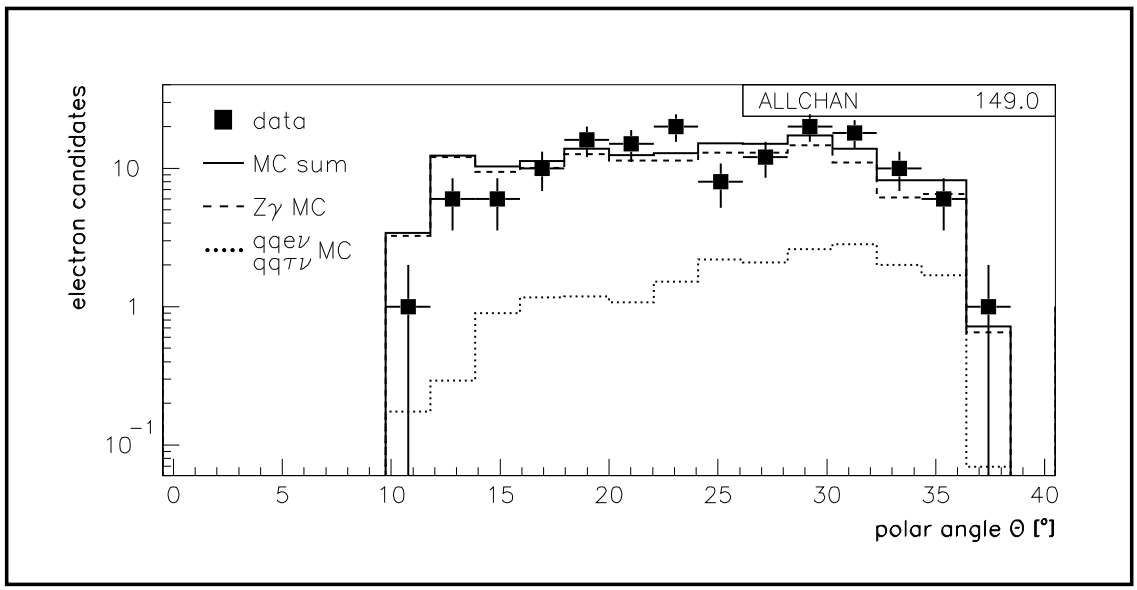

Figure 8.5: Polar angle distribution of electron candidates.

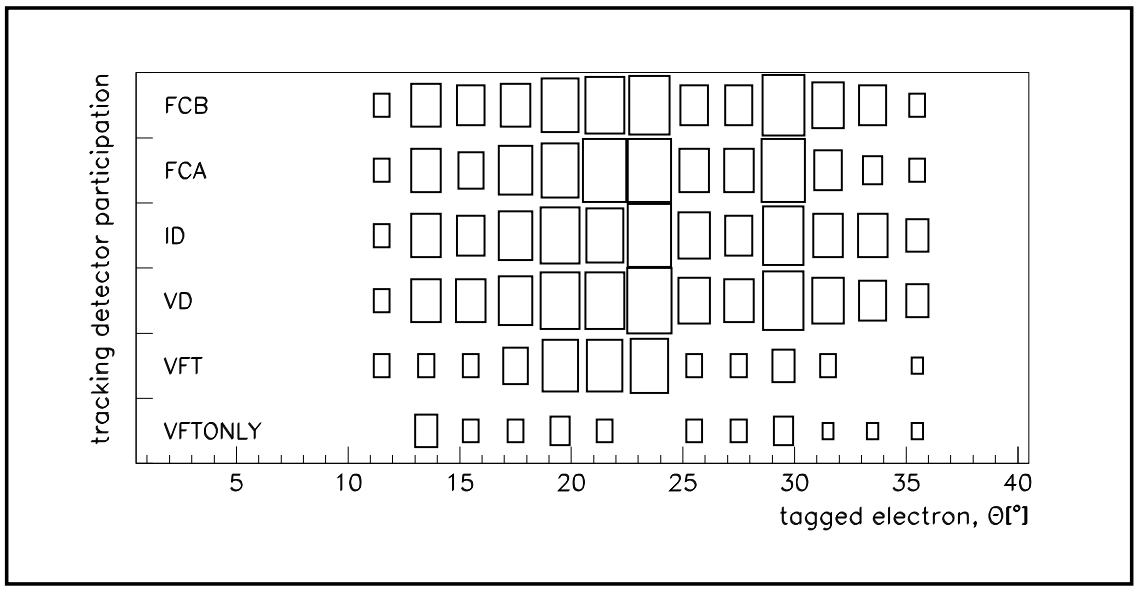

Figure 8.6: Detector participation with the FREGIT electron tag.

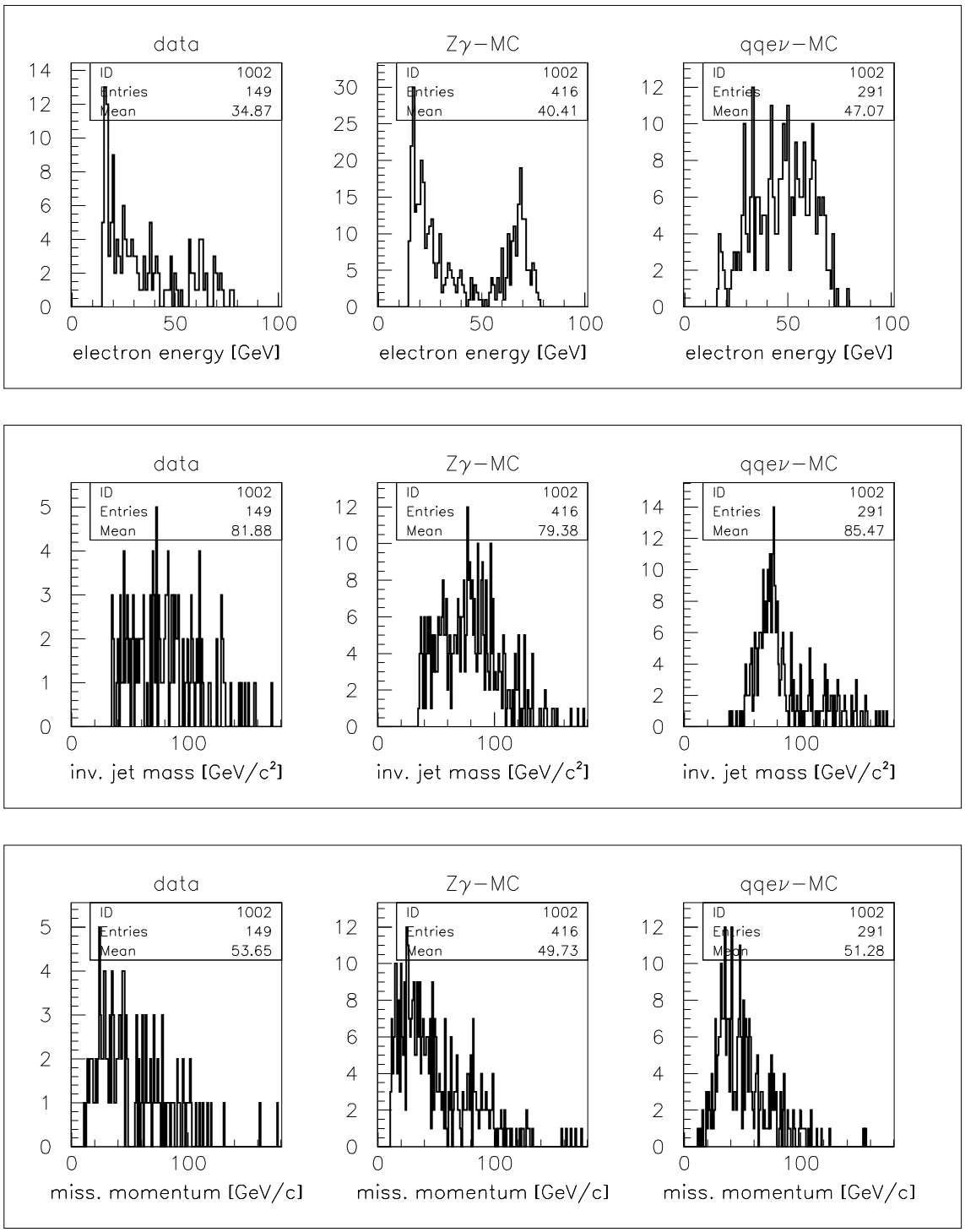

Figure 8.7: Distribution of measured electron energies (top), invariant mass of the jet system (middle) and missing momentum (bottom) for detector data, Zγ and qqeν Monte Carlo data.

distribution of 15 tagged electrons is shown in fig. 8.8. The rate agree better with the expected signal and indicates a reduced content of radiative return events. The event list was compared to an independently obtained list of semi-leptonic W events[7]. From the 15 events six were also tagged as qqeν events and one as a qq$\tau\nu$ event.

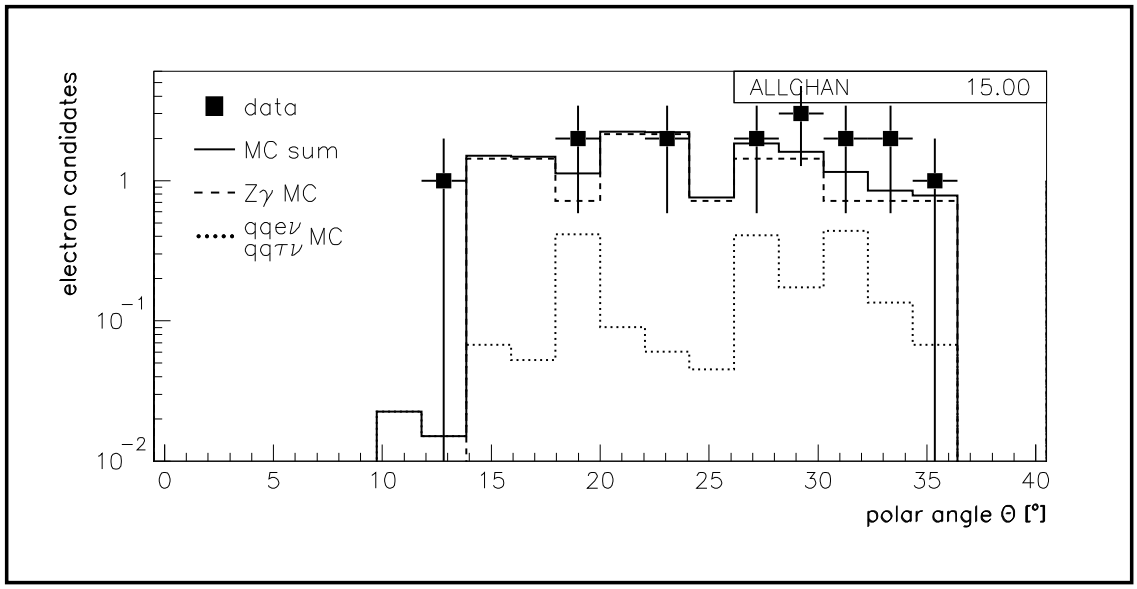

Figure 8.8: Distribution of electron polar angles after application of refined cuts. Hits in Vertex Detector or Tracks in the Very Forward Tracker were required.

The topologies of three events shall be presented in more detail. Fig. 8.9 compares the reconstructions of a radiative return event with hadronic Z decay to a semi-leptonic W-pair event. The momenta of jets, electrons and missing momenta are plotted in three projections. Information on the tagged objects is provided as well as the longitudinal and transverse missing momenta and the jet-to-jet geometries.
With the event shown in the topology display on the left hand side, an electron of nearly 20 GeV energy was detected in the forward direction. The two-jet system has an invariant mass of 90.5 GeV/c^2. Together with rather little missing longitudinal and transverse momentum a hadronic Zγ event is likely to be present. The event on the right hand side has an energetic electron tagged. Large missing momentum both in longitudinal and transverse direction indicates a semi-leptonic W event where the neutrino carries away a considerable fraction of the momentum. Even though the polar angles of the W boson agrees well with the measurement by the TGC team, the invariant jet mass was not measured sufficiently.
A new candidate for a semi-leptonic W event is shown in fig. 8.10 where the measured topology is compared to the DELPHI event graphics. An isolated electron is tagged at $\theta = 13°$ with an energy deposition of 41 GeV in the Forward Electromagnetic

[7]provided by the DELPHI TGC team

Calorimeter. A VFT hit is present there as well as hits in Vertex Detector and the forward tracking chambers. Only minor activity is seen in the calorimeters on the opposite side. The invariant mass of the two jets is 70 GeV. Considerable missing momentum is stated. The jets are almost coplanar with respect to the direction of the electron; an angle of 85° was measured between the electron direction and the plane of the two jets. Two coplanar jets ($\theta_{ACOP} = 89.4°$) were also obtained with the DELPHI event graphics and the DURHAM algorithm applied. The jet axes are indicated in the graph on the right hand side. Since the jets are clearly acollinear, the event might originate from single W production. Improved aspects of the event classification, however, are required to substantialize this conjecture.

8.4 Assessment and further improvements

Electrons from semi-leptonic W events have been tagged in the end-cap region of DELPHI applying search algorithms which base on the use of the Silicon Tracker to find information on tracks close to the interaction region. The new tagging routines extend the acceptance of the standard tag considerably towards low polar angles. Matching hadronic jets were clustered away from the electron and an event sample with 15 candidates selected from the data acquired at 183 GeV center-of-mass energies. Though the electron tagging was efficient and half of those events were also independently characterized as semi-leptonic W events, contamination with radiative return events is still present. Several improvements to increase the purity are considered.

The most powerful way to separate signal from background is the electron identification itself. Hit information from the internal layers of Vertex Detector and Very Forward Tracker are essential hints for passing electrons. Additional information on photon conversion already before the first detector layers might be obtained from the detector signal heights. The traces of electron-positron pairs in the forward direction are likely to be very close to each others and will appear as single tracks at the radii of the silicon detectors. The specific energy loss dE/dx in micro- and ministrip detectors can help to distinguish single from double tracks. The binary hit information from the pixel detector might be useful if the cluster sizes differ from single tracks to pairs of very close tracks.

Improved jet reconstruction will enable to discriminate the invariant jet mass to allow W and Zγ event separation. Different cluster algorithms might be used. The CAMJET algorithm [126] for instance provides good jet momenta and jet energies by re-weighing to the visible energy. More reliable jet masses are obtained. It is not possible, however, to cluster the tracks into a specified number of jets. The DURHAM algorithm was therefore used. Application of constraint fits is required then to impose energy conservation. Furthermore, the invariant mass of the jet system can be fixed to the W boson mass.

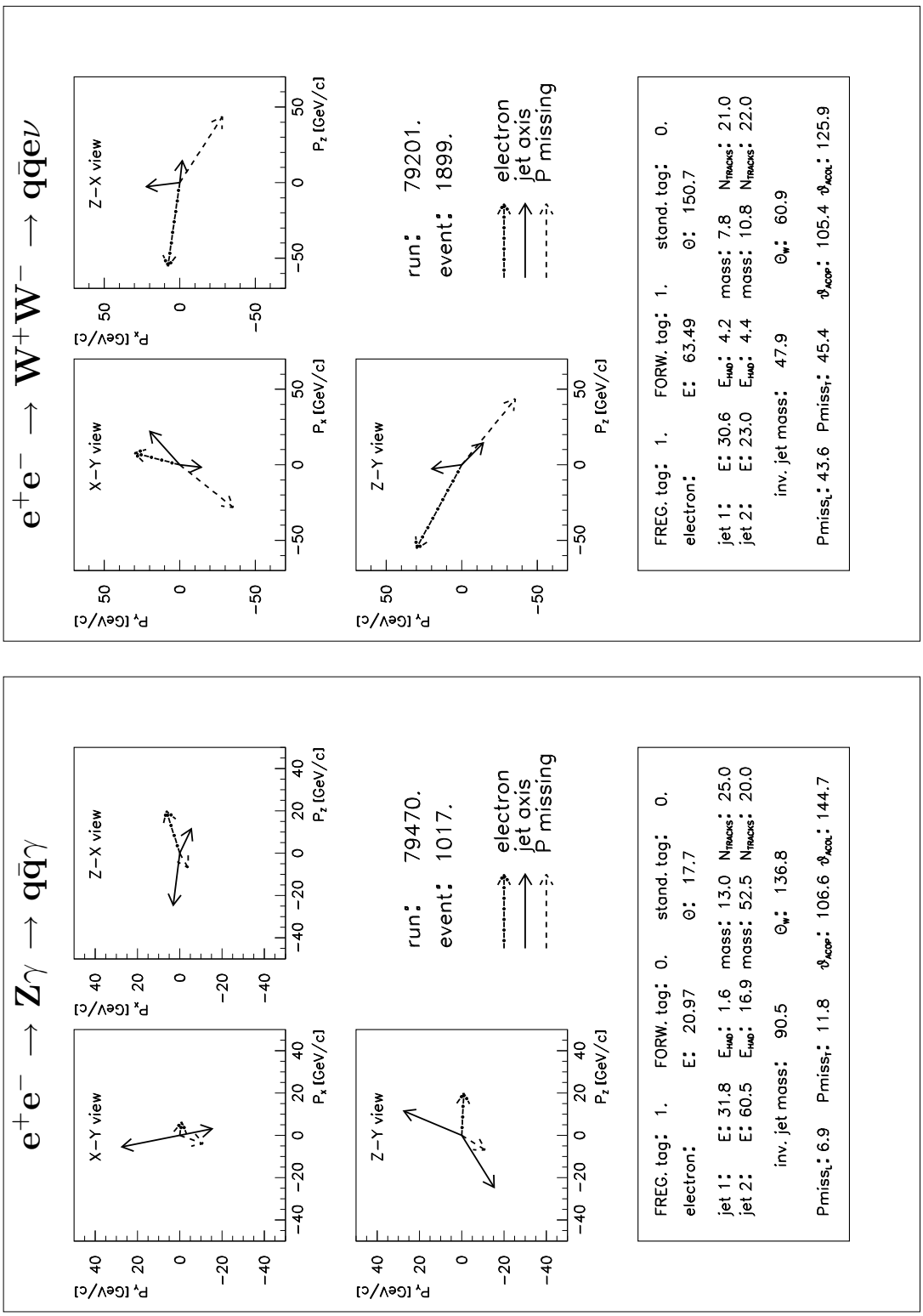

Figure 8.9: Topologies of a Zγ event and a q$\bar{\text{q}}$eν event from W-pair decay.

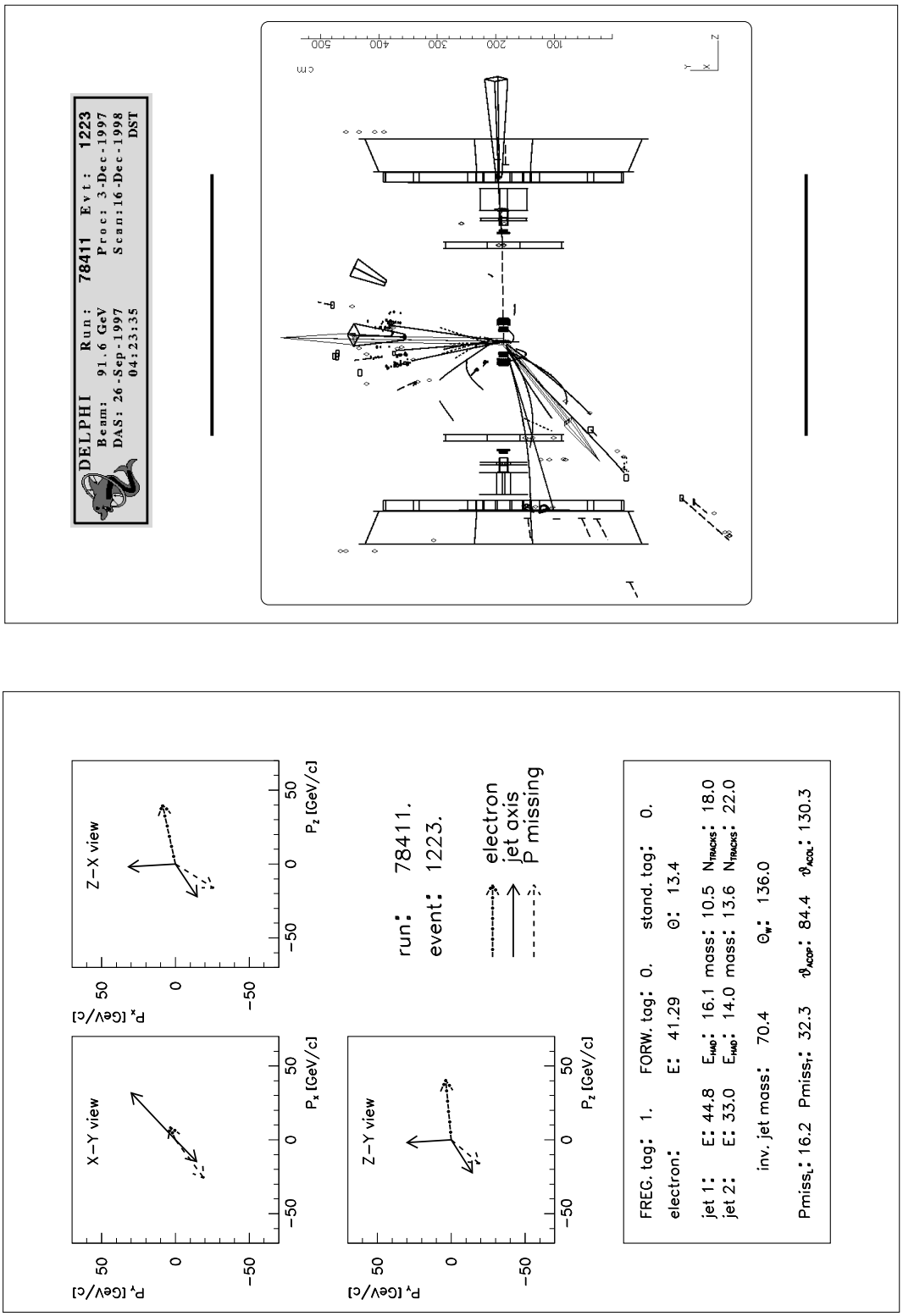

Figure 8.10: Candidate for a semi-leptonic W event. The electron tag is supported by a VFT hit at $\theta = 13°$. Left: display of the reconstructed topology. Right: display of the event as obtained from the DELPHI event reconstruction.

Chapter 9

Conclusions

The DELPHI detector comprises the first application of a hybrid silicon pixel detector to a collider experiment. The detector was built as one of the upgrades of the DELPHI experiment to optimize its track reconstruction at LEP2, the high energy period of CERN's Large Electron Positron collider aiming at e^+e^- collisions at 200 GeV center-of-mass energies.

Pixel detectors are two-dimensionally segmented semiconductor tracking detectors which provide unambiguous space points along the trajectories of charged particles. The development of such detectors is one of the important research activities with the experiments at CERN's forthcoming collider LHC. High track densities with high-luminosity proton-proton collisions demand for advanced track reconstruction capabilities. Pixel detectors provide the required performance. High spatial resolution in two dimensions, advanced signal treatment and pattern recognition are the outstanding characteristics of pixel detectors. Their development, however, is technologically pretentious and involves latest microelectronics and interconnection techniques.

The DELPHI collaboration decided to participate in the development of a pixel detector and to apply it to its track reconstruction. Physics considerations at LEP2 demand for detector hermeticity and overall high efficiency. Several radiation lengths of unavoidable support material in front of the existing tracking detectors limited the track reconstruction in DELPHI's end-caps by subsequent multiple scattering and showering of charged particles. A new tracking device close to the interaction region, the Very Forward Tracker, was designed to initiate the track reconstruction by providing stand-alone pattern recognition. Constraints were imposed by the tight available space. The Very Forward Tracker is a silicon detector, built from ministrip and pixel detectors arranged in cone-shaped layers. The ministrips base on an approved technology and are highly efficient at low noise. The pixel detectors envolve new technologies and procedures. They are essential to resolve the ministrips' space point ambiguities and yield the stand-alone pattern recognition.

Experience was gained with the construction of a large-scale pixel detector. The development of a multi-chip module that matched the requirements of DELPHI and could be produced with sufficient yield was the most important aspect for the success of the project. A hybrid module was designed that carries 16 readout chips bump bonded to the detector substrate. The entire detector requires 152 modules each comprising 8064 pixels, providing a total number of more than 1.2 million pixels. A squared pixel geometry of 330×330 μm^2 was chosen to yield 100 μm spatial resolution. The total active area is 0.15 m^2. Bus lines on the detector substrate minimize the number of external lines and connections. The thin-film double-metal aluminum design was not appropriate for the power supply lines, however. A supplementary power bus on a separate kapton layer takes over this task. The front-end electronics comprises binary signal processing; on-line zero-suppression yields the addresses of hit pixels.
A production chain was established involving four physics institutes in three countries as well as industrial suppliers. Even though a failure rate of the order of 10^{-4} was achieved with the bump bonding process, the complicated handling of the modules themselves resulted in a yield of only 36% for the fully assembled modules.
The pixel detector was therefore installed into DELPHI during two maintenance periods. First experience with the operation of the detector was gained with a partially equipped system when LEP2 operation started in 1996. Failures due to short circuits were avoided with the fully equipped detector by insuring sufficient modularity also with the supply systems. Stable operation was achieved with an active detector control system that prevents from excess hit rates. The detector noise is analyzed on-line and suppressed to yield high data quality. A random noise of 0.5×10^{-6} was achieved after the suppression of systematically noisy pixels.
The pixel detector contributes efficiently to the track reconstruction in DELPHI's end-cap region. It is used as a starting point to join track elements of different detectors in the forward track finding and improves the forward tracking efficiency by factors two to three.
The Very Forward Tracker was applied to electron identification in DELPHI's end-caps. Showering in the support material complicates this task there. Photon conversion from initial state radiation yields very similar characteristics. Track points measured by the Very Forward Tracker in front of most of the support material enable to distinguish between photons and electrons. Several physics analyses can profit from improved electron-photon separation performed with the help of the Very Forward Tracker.
A sample of event candidates for semi-leptonic W decays involving electrons in the forward direction was selected from the data acquired by DELPHI at 183 GeV center-of-mass energy. The performance of three tagging routines was studied. High efficiency to electron identification was achieved and the tagging considerably extended down to $\theta = 10^\circ$. Radiative return events, however, still require special attention if photon conversion occurs in the material up to the Silicon Tracker. Signatures and procedures for further electron-photon separation have been discussed using to the full extent information on energy loss and cluster sizes provided by the Very Forward Tracker.

List of Figures

2.1 ATLAS event simulation H(130 GeV) → ZZ' → 4e 6

2.2 Principle of hybrid pixel detectors 8

2.3 High multiplicity event with CERN experiment WA97 12

3.1 LEP Collider and CERN's accelerator complex 18

3.2 Layout of the DELPHI Detector 19

3.3 Total hadronic cross section from LEP1 to LEP2 energies 21

3.4 Cross sections of Standard Model processes at LEP2 22

3.5 Event candidate for the process $e^+e^- \rightarrow ZZ$ or HH at $\sqrt{s} = 189$ GeV . 25

3.6 Event candidate for the process $e^+e^- \rightarrow ZZ \rightarrow e^+e^-e^+e^-$ at $\sqrt{s} = 189$ GeV 26

3.7 Material distribution in the end-cap region of DELPHI 28

3.8 Nb. of coordinates measured by DELPHI's forward tracking detectors . 29

4.1 Outline of the DELPHI Silicon Tracker 32

4.2 Cross section of a quadrant of the Silicon Tracker 33

4.3 Material of the Silicon Tracker 33

4.4 End-cap of the Silicon Tracker 34

4.5 Cross section of the 3-layer vertex detector 35

4.6 Arrangement of ministrip detectors 38

4.7 Arrangement of pixel detectors 38

4.8 Assembly of a ministrip module 40

5.1 Layout of the readout chips CDFSP8/8b 47

5.2 Block diagram of the electronics components in every pixel 47

5.3 Layout of the pixel electronics 48

5.4 Threshold behavior of the CDFSP6 chip 50
5.5 Timing of the pixel detector threshold 50
5.6 Calibration of the threshold current 51
5.7 Spectrum of ^{109}Cd γ lines 52
5.8 Particle detection efficiency vs. detector threshold 53
5.9 Principle of 2-dimensional sparse data scan readout 55
5.10 Pattern of light spots projected on a CDFSP3 chip 57
5.11 Sequence of output signals 57
5.12 Film bonding technology 59
5.13 Schematics of the flip-chip bonding process 61
5.14 Principle of the C4 bump bonding technology 61
5.15 Process of self aligning and bonding 62
5.16 SP8 readout chip with bump bonds 63
5.17 Layout of the pixel detector substrate with integrated bus 64
5.18 Detector region with integrated bus 64
5.19 Selection of chips for the first prototype modules 67
5.20 Shifted bumps on electronics chips 68
5.21 Asymmetric hit rates with a CDFSP6 chip 68
5.22 Failure classes of the integrated bus 70
5.23 Circuit board with supplementary power bus 71
5.24 Pixel detector cluster size 73
5.25 Detector efficiency vs. threshold 73
5.26 Spatial resolution vs. threshold 74
5.27 Components of a pixel detector module 75
5.28 Pixel detector module with bump bonded chips 76
5.29 Layout of the ceramic supports 78
5.30 Flat kapton cable 78
5.31 Layout of the jig for the module assembly 79
5.32 Glue deposited on the ceramic support 80
5.33 Ceramic support and kapton hybrid attached to the silicon module . . 80
5.34 Layout of long kapton cables 81

5.35 Dark current on the depletion line 82
5.36 Wire bonds from flat kapton to integrated bus 83
5.37 Fully assembled pixel detector module 84
5.38 Yield of the module production 86
5.39 Breakdown of errors for assembled modules 88
5.40 Assembly of a detector half-cone 90
5.41 Layout of the composite support cylinder 91
5.42 Connection of long kapton cables to the repeater boards 92
5.43 Routing of long kapton cables 92
5.44 Scan of the pixel modules' geometry 94
5.45 Geometry of a pixel detector module 94
5.46 Geometrical survey of a detector half-cone 95
5.47 Silicon Tracker half-shell 96
5.48 Beam pipe entering the central part of DELPHI 96

6.1 Outline of the power supply system 98
6.2 Pixel detector readout organization 99
6.3 Timing of the pixel detector readout wrt. the DELPHI trigger 100
6.4 Pixel detector quality checking histograms 102
6.5 Operational status 1996 104
6.6 Operational status 1997/98 104
6.7 Humidity inside DELPHI 1997 106
6.8 Detector currents of the internal layer in 1997 106
6.9 Noisy pixels in a repeater 108
6.10 Number of masked pixels vs. threshold 109
6.11 Determination of systematic and random noise 109
6.12 Random noise vs. repeater number 110
6.13 Trace plot of noisy pixels in 1997 110
6.14 Correlated activity in the VFT 112
6.15 Cluster size vs. detector layer 113
6.16 Temperature variation with on/off state 113

6.17 Trace plot of the event size during a LEP fill 114
6.18 Increased event size by background 114
6.19 Blinking chip on a module 115
6.20 Sequence of automatic threshold rising and decrease 115
6.21 Integrated radiation dose 117
6.22 Online trace-plot from radiation monitors 118
6.23 Relative threshold change vs. radiation dose 118

7.1 Event size with different event tags 120
7.2 Mechanical deformation of the Very Forward Tracker 121
7.3 Inclination angles of pixel detector modules 122
7.4 Spatial resolution and efficiency measured in 1997 123
7.5 Tracking efficiency with and without Very Forward Tracker 124

8.1 Feynman graphs for W^+W^- and single W production 126
8.2 Electron energies and production angles in W boson decays 128
8.3 Electron identification efficiencies 132
8.4 Photon energies and production angle in $Z\gamma$ events 133
8.5 Polar angle distribution of electron candidates 136
8.6 Detector participation with the FREGIT electron tag 136
8.7 Distributions of measured variables 137
8.8 Distribution of electron polar angles and refined cuts 138
8.9 Topologies of a $Z\gamma$ event and a $q\bar{q}e\nu$ event from W-pair decay 140
8.10 Candidate for a semi-leptonic W event, $\theta_{electron} = 13^\circ$ 141

List of Tables

2.1 RD19 pixel detectors. 9

4.1 Characteristics of the DELPHI microstrip detector 36
4.2 Track ambiguities with different Very Forward Tracker configurations . 37
4.3 Characteristics of the DELPHI Very Forward Tracker 39

5.1 Institutes and responsibilities within the pixel detector project 43
5.2 Chip development for the DELPHI pixel detector 45
5.3 IBM C4 bump bond process options 62
5.4 Basic functionality tests of readout chips 66
5.5 Industrial suppliers of components for the DELPHI pixel detector . . . 76
5.6 Characteristics of the applied glues 79
5.7 Types of long kapton cables 81

8.1 Acceptance of end-cap calorimeters and tracking detectors 130
8.2 Electron signatures in the forward region detectors 131
8.3 Cuts applied for the event selection 135

Bibliography

[1] E. H. M. Heijne, P. Jarron, *Development of Silicon Pixel Detectors: An Introduction*, Nucl. Instrum. Methods Phys. Res. A 275 (1989)

[2] A. Peisert, *Silicon Microstrip Detectors*, in: Instrumentation in High Energy Physics, F. Sauli, ed., World Scientific 1992

[3] J.M. Heuser, *Experience with the construction, operation and maintenance of vertex detectors at LEP*, Nucl. Instrum. Methods Phys. Res. A 418 (1998) 1-8

[4] E. H. M. Heijne et al., *The Silicon Micropattern Detector: A Dream?*, Nucl. Instrum. Methods Phys. Res. A 273 (1988)

[5] E. H. M. Heijne, P. Jarron, *Silicon Detector Development in Europe*, in: 1988 Snowmass Summer Study on High-energy Physics in the 1990-s, 739-747 World Scientific 1989

[6] International workshop on silicon pixel detectors, Louvain, Belgium, 1990, Proc. in Nucl. Instrum. Methods Phys. Res. A 305 (1991)

[7] International workshop on semiconductor pixel detectors for particles and X-rays, Bari, Italy, march 24-27, 1996, Proc. in Nucl. Instrum. Methods Phys. Res. A 395 (1997)

[8] International workshop on pixel detectors, Pixel98, Fermi National Accelerator Laboratory, Batavia, IL, USA, may 7 - 9, 1998, Proc. FERMILAB-CONF-98-196, 1998

[9] P. Delpierre, *Problems in building a pixel detector - examples from DELPHI and ATLAS*, Third int. symposium on the development and application of semiconductor tracking detectors, Melbourne, December 1997, submitted to Nucl. Instrum. Methods Phys. Res. A

[10] J.M. Heuser, *Running experience with the DELPHI pixel detector: Reflections on design characteristics and system features*, Proc. of the 6th International Conference on Advanced Technology and Particle Physics, October 1998, Como, Italy, submitted to Nucl. Phys. B

[11] E. H. M. Heijne et al., *R&D Proposal: Development of hybrid and monolithic silicon micropattern detectors*, CERN DRDC/90-81, DRDC/P22, 15 December 1990

[12] A. Zichichi, *The LAA project*, ICFA Instrum. Bull. Vol. 3 (1987) 17-23, 1987;
F. Anghinolfi et al., *Development of integrated CMOS circuits and silicon pixel detectors in the CERN-LAA project: progress report 1988-1989*, CERN LAA SD 89-11 CERN EF 89-14, 1989

[13] The ATLAS Collaboration,
http://atlasinfo.cern.ch/Atlas/ATLASFIGS/ATLASPIC/atlaspic_withgif.html

[14] G. Vanstraelen, *Monolithic integration of solid-state particle detectors and read-out electronics on high resistivity silicon* Doctoral Thesis, Katholieke Universiteit Leuven, Belgium, 1990

[15] W. Snoeys, *New integrated pixel detectors for high energy physics*, Doctoral Thesis, Stanford University, California, 1992

[16] F. Pengg, *Monolithic silicon pixel detectors in SOI technology*, Doctoral Thesis, Universität Linz, Austria, 1996

[17] G. Riley, *Flip Chip Interconnection: Dream or Nightmare?*, Proc. 3rd workshop on electronics for LHC experiments, London 22-26 September 1997, CERN/LHCC/97-60 107-111, 21 October 1997

[18] B. Dierickx, *XYW detector: a smart two-dimensional particle sensor*, Nucl. Instrum. Methods Phys. Res. A 275 (1989) 542

[19] M. Campbell et al., *From a 50 μm readout element to a 50 million cell detector: design aspects of a pixel system*, Proc. 3rd workshop on electronics for LHC experiments, London 22-26 September 1997, CERN/LHCC/97-60 203-207, 21 October 1997

[20] M. Campbell et al., *A 10 MHz Micro Power CMOS Front-End for Direct Readout of Pixel Detectors*, Nucl. Instrum. Methods Phys. Res. A 290 (1990)

[21] P. Middelkamp, *Pixeldetektoren*, Diploma Thesis, Bergische Universität-GH Wuppertal, Germany, WUD-93-37, July 1993

[22] J.M. Heuser, *Untersuchungen an Silizium-Pixel-Detektoren und Vorstudien zum Einsatz im Very Forward Tracker bei DELPHI*, Diploma Thesis, Bergische Universität-GH Wuppertal, Germany, WUB-D 94-05, February 1994

[23] F. Anghinolfi et al., *A 1006 element hybrid silicon pixel detector with strobed binary output*, IEEE Trans. Nucl. Sci. NS-39 (1992) 650

[24] F. Anghinolfi et al., *Design and performance of the OMEGA-Ion hybrid silicon pixel detector*, Nucl. Instrum. Methods Phys. Res. A 326 (1993)

[25] M. Jacob, E. Quercig, *The CERN OMEGA Spectrometer - 25 years of physics*, CERN 97-02, 12 June 1997

[26] H. Beker et al., *A hybrid silicon pixel telescope tested in a heavy-ion experiment*, Nucl. Instrum. Methods Phys. Res. A 332 (1993) 188-201

[27] M. Campbell et al., *Development of a pixel readout chip compatible with large area coverage*, Nucl. Instrum. Methods Phys. Res. A 342 (1994) 52-58

[28] E.H.M. Heijne et al., *Development of silicon micropattern pixel detectors*, Nucl. Instrum. Methods Phys. Res. A 348 (1994) 399-408

[29] E.H.M. Heijne et al., *First operation of a 72k element hybrid silicon micropattern pixel detector array*, Nucl. Instrum. Methods Phys. Res. A 349 (1994) 138-155

[30] F. Antinori et al., *Experience with a 30 cm^2 silicon pixel plane in CERN experiment WA97*, Nucl. Instrum. Methods Phys. Res. A 360 (1995) 91-97

[31] E.H.M. Heijne et al., *Construction and characterization of a 117 cm^2 silicon pixel detector*, IEEE Trans. Nucl. Sci. 42(4), 1995, 413-418

[32] P. Middelkamp et al., *Studies on a 300k pixel detector telescope*, Nucl. Instrum. Methods Phys. Res. A 377 (1996) 532

[33] D. Di Bari et al., *Performance of 0.5 $\times$ 10^6 sensitive elements pixel telescope in the WA97 heavy ion experiment at CERN*, Nucl. Instrum. Methods Phys. Res. A 395 (1997) 391-397

[34] The WA97 Collaboration, *Proposal: Study of baryon and antibaryon spectra in lead-lead interactions at 160 GeV/c per nucleon*, CERN/SPSLC 91-29, 263, 1991

[35] P. Middelkamp, *Tracking with active pixel detectors*, Doctoral Thesis, Bergische Universität-GH Wuppertal, Germany, WUB-DIS 96-23, December 1996

[36] E.H.M. Heijne et al., *LHC1: A semiconductor pixel detector readout chip with internal, tunable delay providing a binary pattern of selected events*, Nucl. Instrum. Methods Phys. Res. A383 (1996) 55-63

[37] D. J. Pedder, *Flip chip solder bonding for advanced device structures*, Plessey Research Review 1989, Plessey, United Kindom, 1989, 69-81

[38] W. Snoeys et al., *Layout techniques to enhance the radiation tolerance of standard CMOS technologies demonstrated on a pixel readout chip*, 8th European Symposium on Semiconductor Detectors, Schloß Elmau, Germany, June 14-17, 1998, submitted to Nucl. Instrum. Methods Phys. Res. A

[39] The ALICE Collaboration, *ALICE - Technical Proposal for A Large Ion Collider Experiment at the CERN LHC*, CERN/LHCC/95-71, LHCC/P3, 15 December 1995

[40] The FELIX Collaboration, *FELIX : a full acceptance detector at the LHC : letter of intent*, CERN-LHCC-97-45, LHCC-I-10, 1997

[41] K. Eggert, *FELIX - A full acceptance detector at the LHC*, in: Proc. 27th International Symposium on Multiparticle Dynamics, ISMD '97 Frascati, Italy, 8 - 12 Sep 1997, hep-ex/9801021

[42] The LHCb Collaboration, *LHCb – technical proposal*, CERN/LHCC 98-4, LHCC/P4, 20 February 1998

[43] T. Gys et al., *A new position-sensitive photon detector based on an imaging silicon pixel array (ISPA-tube)* , Nucl. Instrum. Methods Phys. Res. A 355 (1995) 386-389

[44] M. Campbell et al., *Development of pixel hybrid photon detectors for the RICH counters of LHCb*, LHCb 98-035 RICH, 30 January 1998

[45] The ATLAS Collaboration, *ATLAS inner detector technical design report*, CERN/LHCC/97-17, 30 April 1997

[46] The ATLAS Collaboration, *ATLAS pixel detector technical design report*, ATLAS TDR 11, CERN/LHCC/98-13, 31 May 1998

[47] The CMS Collaboration, *The Compact Muon Solenoid - Technical Proposal*, CERN/LHCC 94-38, LHCC/P1, 15 December 1994

[48] The CMS Collaboration, *CMS - Tracker Technical Proposal*, CERN/LHCC 98-6, CMS TDR 5, 20 April 1998

[49] The DELPHI Collaboration, *DELPHI - Technical Proposal*, DELPHI 83-66/1, CERN/LEPC/83-3, 17 May 1983

[50] P. Aarnio et al., The DELPHI Collaboration, Nucl. Instrum. Methods Phys. Res. A 303 (1991) 233

[51] P. Abreu et al., The DELPHI Collaboration, Nucl. Instrum. Methods Phys. Res. A 378 (1996) 57-100

[52] LEP design report, Vol. 2, CERN-LEP/84-01, 1994

[53] CERN SL division, http://www.cern.ch/CERN/Divisions/SL/welcome.html

[54] LEP design report, Vol. 3, CERN-AC/96-01 (LEP2), June 1996

[55] S. Myers, C. Wyss, *Prospects for energy and luminosity at LEP2*, in G. Altarelli, T. Sjöstrand, F. Zwirner (Ed.), Physics at LEP2, CERN 96-01 Vol. 1,2, 19 February 1996

[56] G. Altarelli, T. Sjöstrand, F. Zwirner (Ed.), *Physics at LEP2*, CERN 96-01 Vol. 1,2, 19 February 1996

[57] DELPHI collaboration, http://delphiwww.cern.ch/delfigs/export/pubdet4.html

[58] P. Bambade et al., *Neutral current four-fermion production in e^+e^- collisions at $\sqrt{s}$ = 130-183 GeV.*, submitted to ICHEP'98, Vancouver, June 22-29, paper 230, DELPHI 98-104 CONF, 22 June 1998

[59] The DELPHI Collaboration, *An Upgrade of DELPHI in the Forward Region*, CERN/LEPC/92-5,LEPC/I-11, 25 May 1992

[60] The DELPHI Collaboration, *Proposal for the Upgrade of DELPHI in the Forward Region*, DELPHI 92-142 GEN 135, 16 October 1992

[61] A. Benvenuti et al., *STIC - the new DELPHI Luminosity Monitor*, DELPHI 94-31 CAL 112, 23 March 1994

[62] The Delphi Collaboration, *Proposal for the DELPHI Surround Muon Chambers*, DELPHI 92-139 TRACK 71, 21 October 1992

[63] C. de Clercq, *A Study of Muon Identification in DELPHI with the Surround Muon Chambers*, 92-148 PHYS 241 TRACK 72, 12 November 1992

[64] The DELPHI Collaboration, *Proposal for the DELPHI Very Forward Tracker*, CERN/LEPC/93-6, LEPC/P2/Add.3, 15 May 1993

[65] M. Elsing, *Summary of the updates in the DELPHI forward tracking to include the VFT*, DELPHI 98-5 PROG 227 TRACK 91, 20 January 1998

[66] H. Wahlen, Bergische Universität-GH Wuppertal, Germany, priv. communication

[67] P. Chochula et al., The DELPHI Silicon Tracker Group, *The DELPHI Silicon Tracker at LEP2*, Nucl. Instrum. Methods Phys. Res. A 412 (1998) 304-328

[68] A. Zalewska, *Conventions for the barrel part of the Delphi Silicon Tracker 1996*, DELPHI note 96-146 MVTX 18, 24 October 1996

[69] V. Chabaud et al., *Alignment of the DELPHI vertex detector*, DELPHI 95-177 MVX 10, 12 December 1995

[70] H. Pernegger, *The silicon ministrip detector of the DELPHI Very Forward Tracker*, Doctoral Thesis, Institut für Hochenergiephysik, Wien, Austria, February 1996

[71] M. Krammer, *The construction of the DELPHI Very Forward ministrip detector*, Proc. 4th International Workshop on Vertex Detectors - Vertex '95, ed. E. Gross and R. Mir, Weizmann Inst. Sci., WIS-96-18 (41-52), 1996; DELPHI 96-11 MVX 11, 12 February 1996

[72] C. Boutonnet, J.J. Jaeger, J. Waisbard, *Notice d'utilisation circuit CDFSP5/5b*, Collège de France, LPC, Paris, December 1993

[73] M. Solal, J.C. Clemens, *Electronics for pixel detectors*, Nucl. Instrum. Methods Phys. Res. A 380 (1996) 335-341

[74] J.M. Heuser, *Status of SPARSE chip tests in Wuppertal*, RD19 general meeting, CERN, 2 September 1994

[75] J.C. Clemens, *Latest news on chip testing - SP5*, DELPHI pixel electronics meeting, Collège de France, Paris, 6 February 1996

[76] M. Solal, *SP5 electronic test*, technical note CPPM Marseille, 19 June 1994

[77] P. Gerlach, *Messungen an VFT Pixeldetektoren*, Diploma Thesis, Bergische Universität-GH Wuppertal, Germany, WUB-D 96-27, July 1996

[78] K.H. Becks et al., *Progress in the construction of the DELPHI pixel detector*, Nucl. Instrum. Methods Phys. Res. A 395 (1997) 398-403

[79] J.J. Jaeger et al., *A sparse data scan circuit for pixel detector readout*, IEEE Transactions on Nuclear Science, Vol. 41, No. 3, June 1994, 632-636

[80] J.M. Heuser, *Electrical and laser measurements with CDF2 readout chips, + addendum*, RD19 technical note, 19 May 1993

[81] J.M. Heuser, *Sparse Data Scan test with CDF SPARSE3 pixel detector readout chips, + addendum*, RD19 technical note, 19 October 1993

[82] P. Kind, J.M. Heuser, *Sparse Data Scan test with CDF SPARSE4 pixel detector readout chips, + addendum*, Bergische Universität-GH Wuppertal, Germany, January 1994

[83] 3M Corporation, data sheet 5303R z-axis adhesive film

[84] Y. Saitoh et al., *Development of novel fabrication techniques for a silicon micro vertex detector unit using the flip-chip bonding method*, IEEE Trans. Nucl. Sci. NS-41 (1994) 1192

[85] D. Sauvage et al., *A pixel detector for the '95 upgrade of the DELPHI micro vertex detector*, Proc. 4th International Workshop on Vertex Detectors VERTEX 95, June 1995, CPPM Marseille CPPM-95-05

[86] V. Bonvicini et al., *Screen printing and chip flipping techniques for large area hybrid pixel detectors bonding*, Nuclear Physics B 44 (1995), 409-413

[87] L.F. Miller, *Controlled Collapse reflow chip joining*, IBM J. of Res. and Dev. 13, no. 3 (1969), 239-250

[88] IBM Corporation, *C4 product design manual*, C4 product design center, Hopewell Junction, New York 12533, USA

[89] IBM seminar on flip chip and ball grid array technology, IBM Germany, Stuttgart, 17 - 18 October 1994

[90] J.M. Heuser, P. Gerlach, CPPM group, *SP5 wafer test at CPPM*, Report on automatic chip testing and chip selection, technical note, Bergische Universität-GH Wuppertal, Germany, July 1995

[91] W. de Boer, D. Knoblauch, A. Koerpert, G. Maehlum, *Tests of the first pixel detectors for the DELPHI upgrade*, DELPHI 95-118 TRACK 82, 24 July 1995

[92] W. de Boer et al., *Wafer Tests of the Pixel Detectors for the Upgrade of the DELPHI Vertex Detector*, 96-60 MVX 16, 17 May 1996

[93] J.M. Heuser, *DELPHI pixel detector test beam*, Report on data analysis results, technical note, Bergische Universität-GH Wuppertal, Germany, 15 September 1995

[94] CPPM Marseille, http://marpix1.in2p3.fr/Delphi/Delphi.html

[95] L. Roos, *Analysis of beam test data with beam incidence angle of 30 and 45 degrees*, Technical note, ISN Grenoble, 2 March 1995

[96] *SHAPAL Translucent aluminum nitride ceramic*, Technical bulletin, Tokuyama, Japan

[97] K.H. Becks et al., *Progress in the assembly of the DELPHI VFT pixel detector*, Bergische Universität-GH Wuppertal, Germany, Technical Note WUB 96-8, June 1996

[98] data sheet E 704 glue, Epotecny, Velizy, France;
data sheet Araldit 2015 glue, Ciba Geigy, Wehr/Baden, Germany

[99] M. Raymond, *Spécification Technique du Besoin Kapton Longs*, CPPM Marseille, DELPHI-STB-1019/B, 16 October 1995

[100] D. Knoblauch, *Aufbau und Test der Mikrostreifen-Detektor-Module für den Upgrade des DELPHI-Vertexdetektors*, Diploma Thesis, Universität Karlsruhe, Germany, IEKP-KA/96-1, 26 February 1996

[101] K.H. Becks et al., *Commissioning of the DELPHI Pixel Detector*, Nucl. Instrum. Methods Phys. Res. A 418 (1998) 15-21

[102] M. Raymond et al., *Design and manufacture of an accurate composite piece* Proc. International Workshop on Advanced Materials for High-precision Detectors, Archamps, France, 28-30 Sep. 1994, CERN 94-07, 179 - 187

[103] B. Überschär, *The concept of the VFT geometrical database*, DELPHI internal documentation, 28 March 1995

[104] DELPHI Silicon Tracker group, *Conventions for the VFT align files*, DELPHI internal documentation, 1996

[105] M.Caccia, C.Combi and W.Kucewicz, *A precise survey of the clearance in the interaction region at DELPHI*, DELPHI internal note 98-33 MVX 23, 16 April 1998

[106] CERN libraries, photo ref. CERN-EX-9304072

[107] K.H. Becks et al., *The DELPHI Pixels*, Nucl. Instrum. Methods Phys. Res. A 386 (1997) 11-17

[108] S. Kersten, *Slow control for the DELPHI pixel detector*, Bergische Universität-GH Wuppertal, Germany, internal documentation, 4 May 1998, available on: http://www.uni-wuppertal.de/FB8/groups/Drees/paper/slowcon_vft.ps.gz

[109] The DELPHI Collaboration, *The Design and Operation of the Slow Controls for the DELPHI Experiment at LEP*, Nucl. Instrum. Methods Phys. Res. A 349 (1994) 160-182

[110] Ph. Charpentier et al., *The DELPHI Fastbus Data Acquisition System*, Proc. Int. Conf. on Computing in High Energy Physics 1991, Y. Watase and F. Abe eds., Universal Academy Press, Tokio, 1991, p. 643;
M. Jonker et al., *Architecture and Performance of the DELPHI Data Acquisition and Control System*, same proceedings, p. 691

[111] C. Aubret et al., *DELPHI pixel detector readout*, internal documentation, Collège de France, Paris, 26 September 1997, available on: http://cdfinfo.in2p3.fr/Experiences/Delphi/VFT/documents.html

[112] V. Bocci et al., *Architecture and performance of the DELPHI trigger system*, Nucl. Instrum. Methods Phys. Res. A 362 (1995), 361-385; *Basic concepts and architectural details of the DELPHI trigger system*, IEEE Trans. Nucl. Sci. 42 (4), 1995, 837-843

[113] V. Chorowicz, *The real-time data monitoring in DELPHI*, DELPHI internal note 95-31 DAS 164, 21 March 1995

[114] T. Camporesi and L. Beneteau, *The DELPHI Histogram Presenter*, DELPHI internal note 92-100 DAS 129, 8 July 1992

[115] J.M. Heuser, M. Caccia, L. Roos, *Online monitoring of the DELPHI VFT pixel detector*, DELPHI internal note 96-150 MVX 19, 24 October 1996

[116] L. Roos, F. Ledroit, S. Kersten, *The VFT pixel calibration database*, 97-161 MVX 22, 7 October 1997

[117] L. Roos et al., *First results from the DELPHI pixel detector*, Nucl. Instrum. Methods Phys. Res. A 409 (1998), 229-231

[118] CERN press release, *Fire in SPS surface building*, 16 May 1996

[119] M. Raymond, *Détermination du gradient de température dans les détecteurs pixels*, DELPHI-TTE-1005, IN2P3-CPPM, Marseille, 26 November, 1993

[120] P. Collins et al., *The DELPHI Beam Dump*, DELPHI 95-170 LEDI 4, 22 November 1995

[121] W. Beenakker and F.A. Berends, *WW cross-sections and distributions*, in G. Altarelli, T. Sjöstrand, F. Zwirner (Ed.), Physics at LEP2, CERN 96-01 Vol. 1,2, 19 February 1996

[122] G. Gounaris, J.L. Kneur and D. Zeppenfeld, *Triple Gauge Boson Couplings*, in G. Altarelli, T. Sjöstrand, F. Zwirner (Ed.), Physics at LEP2, CERN 96-01 Vol. 1,2, 19 February 1996

[123] LEP electroweak W mass working group, *LEP WW cross-section and W mass for '98 summer conferences*, LEPEWWG/MW/98-02, CERN, 29 September 1998

[124] M. Acciarri et al., L3 Collaboration, *Production of Single W Bosons at LEP*, Phys. Lett. B403 (1997) 168-176;
M. Acciarri et al., L3 Collaboration, *Production of Single W Bosons in e^+e^- Interactions at at 130 $\leq$ $\sqrt{s}$ $\leq$ 183 GeV and Limits on Anomalous $WW\gamma$ Couplings*, Phys. Lett. B436, 3-4 (1998) c417-27;
Opal Collaboration, *Limits on anomalous γWW couplings from single W production in e^+e^- collisions at $\sqrt{s}$ = 161-172 GeV*, OPAL physics note PN308, 13 August, 1997;
ALEPH Collaboration, *Search for single W production at LEP2*, ALEPH contribution to 1998 winter conferences, ALEPH/98-023 CONF/98-013, 11 March 1998;
DELPHI Collaboration, *Measurement of Trilinear Gauge Couplings in e^+e^- collisions at 161 GeV and 172 GeV*, Phys. Lett. B423 (1998) 194-206

[125] K.D. Brand, *Electron identification in the forward region*, DELPHI internal note, 30 August, 1994

[126] Y. Dokshitzer, G. Leder, S. Moretti, B. Webber, *Better Jet Clustering Algorithms*, Cavendish-HEP-97/06;
S. Bentvelsen and I. Meyer, *The Cambridge jet algorithm: features and applications*, CERN-EP/98-043, 11 March 1998

Acknowledgements

The DELPHI pixel detector project has been a unique opportunity to participate actively in various steps of the construction, commissioning and operation of a novel semiconductor tracking device for a high energy physics experiment. I thank the DELPHI collaboration for supporting the project from the prototyping phase to the detector's integration into the experiment. My group at Wuppertal University joined the pixel detector project at the beginning of the planning. I thank especially my supervisors Prof. Dr. J. Drees and Prof. Dr. K.-H. Becks for this decision and the continuous support of my work. Laboratory equipment, the possibility of frequent travels to and participation in collaboration meetings and international conferences as well as a long-term stay at CERN enabled to take over responsibilities and interesting tasks within the project. Lasting and valuable contacts have been established in an international community.

The success of the project has been achieved in a common effort of many colleagues of the collaborating institutes. I would like to mention a few representative names. The roots of the detector concept in CERN's RD19 collaboration are acknowledged. I thank spokesman Dr. E. Heijne and Dr. M. Campbell for the opportunity to gain experience with pixel detectors in laboratory and test beam measurements.

The Silicon Tracker project of DELPHI has been led by Dr. H. Dijkstra and Dr. P. Collins, CERN, and Dr. M. Caccia, representing the group at INFN Milan and taking especially care of the pixel detector. I thank them for their outstanding coordination and "integrating" work to realize the pixel detector as an important part of DELPHI's final silicon tracking detector.

The detector module and its mechanical support were designed in the group of Prof. Dr. P. Delpierre at CPPM, Marseille. Essential organizing work was done in the laboratory to realize the detector production. The detector layers were assembled there. I thank especially Dr. J. C. Clemens, Dr. M. Raymond and Dr. D. Sauvage for their comprehensive work.

The assembly of the detector modules was performed at Karlsruhe and Wuppertal universities. I thank the team of Prof. Dr. W. de Boer, Karlsruhe, and my Wuppertal colleagues Dr. K.-W. Glitza, Mr. P. Gerlach and Mrs. I. M. Gregor for their skill. They contributed essentially to the required module yield. Mrs. S. Kersten, Wuppertal, provided important contributions to the pixel detector's supply and control system.

The team at Collège de France, led by Dr. G. Tristram, designed and supported the front-end readout and the data acquisition system. I thank the team for the comprehensive and important work especially during the commissioning of the detector.